2018

High Pressure Torsion of Polycrystalline and Single Crystal Aluminium

Yu Liu
University of Wollongong

High Pressure Torsion of Polycrystalline and Single Crystal Aluminium

A thesis submitted in fulfilment of the requirements

for the award of the degree of

Doctor of Philosophy

from

University of Wollongong

by

Yu Liu

School of Mechanical, Materials and Mechatronic Engineering

Faculty of Engineering

August, 2018

Declaration

I, YU LIU, declare that this thesis, submitted in fulfilment of the requirements for the award of Doctor of Philosophy, in the school of Mechanical, Materials and Mechatronic Engineering, University of Wollongong, Australia, is wholly my own work unless otherwise referenced or acknowledged, and has not been submitted for qualifications at any other university or academic institution.

YU LIU

August 2018

Acknowledgements

I wish to express my sincere gratitude to my supervisors A/Professor Cheng Lu (University of Wollongong), Professor Anh Kiet Tieu (University of Wollongong) for their excellent supervision and guidance, continuous encouragement and invaluable advice during my PhD study. All my supervisors' implicit trust in my research abilities not only allowed me to freely pursue my goals, but also gave me an opportunity to learn how to manage time and allocate resources. Without their help I could never have finished this work. I am grateful to Dr. Lihong Su, Dr. Azdiar Gazder, Dr. Guanyu Deng, Dr. Shao Dai (Sydney Univeristy), Dr. Hui Wang, Dr. Ramdzan Buyong and Dr. Jingtao Li for their invaluable advice on my study. My thanks are also extended to Rui Wang and Dongzhi Luo. I enjoyed all the coffees, dinners, movies and trips together with you. I feel very lucky to have you guys during my study in Wollongong and I will never forget the time we spent together. Special thanks go to my wife Liaoni He for the help and encourage. Finally, I would like to offer my heartfelt thanks to my parents for their continued love, understanding and devotion. Their encouragements always kept me going forward during my study.

Thank you all,

Table of Contents

Table of Contents

Table of Contents

Abstract

As a technique to produce ultrafine grained (UFG) materials, severe plastic deformation (SPD) has engaged considerable investigation over last two decades. HPT is one of the most important SPD techniques because of its unique advantages, including the extreme grain refinement capability, over other SPD techniques. In this work, the evolution of microstructure, texture, hardness and grain boundary (GB) migration in the one-layer and two-layer stacked polycrystalline Al and Al single crystal processed by HPT have been investigated in detail.

The one-layer polycrystalline aluminium was employed to study material flow behaviour for a wide range of strains. The morphology, texture and hardness were used to characterise the material flow. It was found that the grain refinement is not a linear function of shear strain. The UFG structures were obtained at both middle position and edge position after HPT with the rotation angle of 1800°. The distribution of hardness was inhomogeneous throughout the diameter of the disc, even after a large number of HPT revolutions. The central hardness was significantly lower than the hardness at the periphery of the HPT deformed discs. Initial shaped grains, band-shaped structures and small equiaxed grains dominate at the stages with the low, medium and high strains, respectively. The intensities of textures in HPT were weak, due to the change of the shear direction (SD). The gradients of the microstructure and texture were observed at the low strain stages, but the gradients disappeared at the stages with the high shear strain.

The two-layer polycrystalline aluminium was processed by HPT. It was found that the evolution of microstructure in the two-layer specimen is similar to that of the one-layer specimen. But the gradient of the morphology, grain size and texture along the specimen thickness was reduced compared with the one-layer specimen, indicating that the material flow in the two-layer specimen was more stable. In terms of grain refinement, no advantage could be found in the two-layer specimen at the low and high strain levels. However at the stages with the medium strain, the grain size of the two-layer specimen was obviously smaller, especially after the rotation angle of 720°. Strong evidences of shear-induced GB migration were observed in the HPT processed specimens. The GB migration along the preferred orientation resulted in shrinkage or expansion of the particular grains.

The one-layer and two-layer Al single crystals were deformed by HPT with low strains. At

the centre position of the specimen, the deformation does not follow the typical simple shear mode. The material flows around the shear plane normal (SPN) axis. At the middle position, the band-shaped structures prevailed. At the edge position, the band-shaped structures were fragmented into the relatively equiaxed grain. The GB migration was observed in the HPT processed specimens. It is found that the magnitude of the shear strain affected the GB migration. The GB migrations occurred at the HAGBs, whereas the $\Sigma 41a$ and $\Sigma 5$ GBs were stationary.

List of Abbreviations

ARB-accumulative roll bonding

C2S2-continuous confined strip shearing

CSL-coincidence site lattice

CT-cryogenic temperature

CDRX-continuous dynamic recrystallisation

CPEFM-crystal plasticity finite element method

DIGM-diffusion induced grain boundary migration

DSC-displacement shift complete

ECAP- equal channel angular pressing

EBSD-electron backscatter diffraction

ED-electron deposited

EDS-energy dispersive X-ray spectroscopy

FCC-Face Centred Cubic

FSD- fore-scatter detector

GND- geometrically necessary dislocation

GB- grain boundary

GNBs-geometrically necessary boundaries

HPT-high pressure torsion

HPTT- high-pressure tube twisting

HAGB-high angle grain boundary

HRTEM-high-resolution transmission electron microscopy

List of Abbreviations

IPF-inverse pole figure

IDBs-incidental dislocation boundaries

LAGB-low angle grain boundary

MD-molecular dynamics

MCF-multipass coin-forging

nc-nanocrystalline

ODF-orientation distribution function

PF- pole figure

RCS-repetitive corrugation and straightening

RT-room temperature

RSSR-resolved shear strain rate

SFE-stacking fault energy

SE-secondary electron

SEM-scanning electron microscopy

SPD-severe plastic deformation

SSE-Simple Shear Extrusion

TEM-transmission electron microscopy

TB-twin boundary

TE-Twist Extrusion

UFG-ultrafine grained

XRD-x- ray powder diffraction

List of Figures

List of Tables

Chapter 1 Introduction

Grain size generally plays an important role in the mechanical properties of polycrystalline materials. According to the Hall-Petch relationship [1, 2], the decrease of grain size can increase the strength of materials. Thus ultra-fined grained (UFG) materials with grain size of 100 nm ~ 1 μm are capable of possessing excellent strength.

As effective methods to produce UFG materials, SPD techniques have engaged considerable interest over the last several decades. All of these SPD methods are capable of providing high plastic strains and causing severe grain refinement. High pressure torsion (HPT) has unique advantages over other SPD techniques. For example, HPT is able to continuously offer extremely high shear stain in one step compared with other SPD techniques. Therefore, HPT has recently attracted extensive research interest for various materials.

Generally speaking, the properties of materials are correlated to the microstructure and crystallographic texture. Numerous experiments and simulations were undertaken to observe the evolutions of microstructures and textures and to understand the deformation mechanism in HPT. However, there are still some controversies. For instance, it is generally believed that it is impossible to obtain completely homogeneous hardness distribution in any condition because the shear strain at the centre of the disc is theoretically zero [3]. However studies shown that shear strain deviates from the ideal rigid-body model at the very early stages of HPT deformation [4], and the hardness distribution became reasonably homogeneous in the situation with high strains [5-7]. In this work, the microstructural and textural evolutions during HPT of polycrystalline and single crystal aluminium will be investigated for the full strain range to address these controversies.

According to the classic deformation mechanism, the dislocation nuclear and movement are the bases of plastic deformation. Generally, finer grains have a higher fraction of the grain boundaries (GBs). These GBs could play the role of barriers to obstruct the dislocation slip. As a result, the strength and hardness of the materials are improved. A decrement of grain size results in an increment of the grain boundary fraction. When the grain size decreases to a certain value, the high density GBs constrain the dislocation nucleation and movement. In this condition, the GB mediated processes including the GB rotation and the GB migration become the alternative approaches to accommodate plastic deformation.

It is widely accepted that GB rotation prevails in nanocrystalline (nc) materials and GB migration is the predominant GB mediated process in UFG materials. The specimens processed by HPT are ideal for studying the underlying mechanisms of the GB migration. In this work, the two-layer polycrystalline and single crystal Al were processed by HPT to investigate the mechanism of the GB migration.

This thesis consists of 7 chapters as follows:

Chapter 1 introduces the research background.

Chapter 2 presents a brief overview of the SPD techniques and HPT, and reviews the literatures on microstructure, mechanical properties, texture and GB motion in the HPT processed samples.

Chapter 3 describes the starting materials, equipment, experimental procedures and experimental parameters used in the study.

Chapter 4 presents the results of the commercial purity (CP) Al one-layer discs subjected to HPT with various rotation angles. The microstructural and textural evolutions as well as the hardness are investigated in detail.

Chapter 5 shows the results of the CP Al two-layer discs deformed by various HPT rotations. The evolution of microstructure and texture, hardness and GB motion in the UFG materials produced by HPT are analysed and compared with those of the one-layer discs.

Chapter 6 demonstrates the results of the Al <100> single crystal specimens after HPT processing. The microstructural and textural evolution at the centre, middle and edge of the discs are investigated. The GB motion during HPT is discussed.

Chapter 7 summarises the conclusions of the present study, and gives recommendations for future work.

Chapter 2 Literature review

SPD as an effective method to produce UFG materials or nc materials, is becoming more and more appealing. As shown in Fig 2.1, UFG materials refer to those materials which have completely equiaxed and homogeneous microstructures with the average grain sizes in the range of 0.1-1 μm; the nc materials are defined as the materials with the grain size of less than 0.1 μm [8, 9].

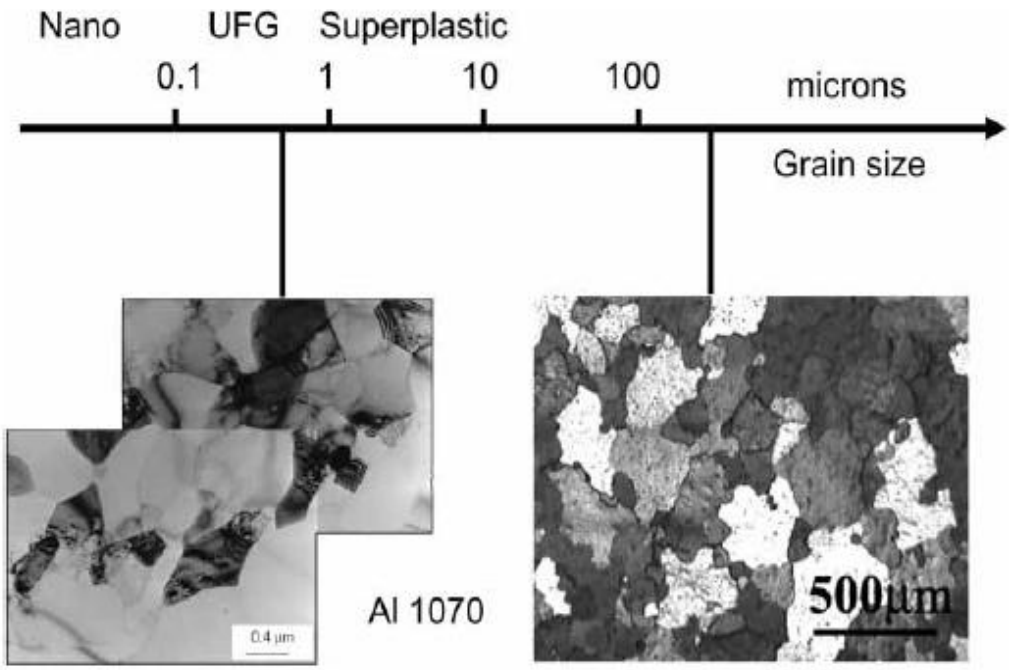

Figure 2.1 Typical microstructure of Al 1070 before and after SPD [8].

Ultra high strains produced by SPDs give rise to significant grain refinement, thereby improving the mechanical properties of materials. High pressure torsion (HPT) is one of the most widely used SPD techniques.

Aluminium is a typical Face Centred Cubic (FCC) metal and has good formability. Pure Al is widely used as the starting material in a great number of studies. In this study, purely polycrystalline Al and Al single crystals are employed to study the microstructural and textural evolutions, hardness, grain refinements and GB mediated processes in HPT.

2.1 SPD and HPT

Generally, grain size plays a significant role in dictating material properties. It is well known

from the Hall-Petch relationship [1], as described by Eqn. (2.1), that the grain refinement may dramatically improve the strength of materials.

$$\sigma = \sigma_0 + kd^{-\frac{1}{2}} \tag{2.1}$$

where σ is the strength, d is the grain size, σ_0 and k are material constants.

According to Eqn. (2.1), the strength of the fine-grained materials has great advantages over their coarse grains counterparts. Therefore extensive research has been carried out worldwide during the past two decades on various grain refinement techniques in order to understand the strengthening mechanism of different types of materials [2, 3].

Compared with conventional coarse grained materials, UFG materials show some excellent properties without the need to change the chemical composition. These properties include high strength [9-12], premium corrosion resistance [13-15] and even good ductility [16]. However, the materials with the submicron grain size cannot generally be produced by conventional plastic deformation processes.

SPDs are extremely effective techniques for producing bulk UFG materials. Nowadays, various techniques have been developed, such as Equal Channel Angular Pressing (ECAP) [17-19], HPT [20-22], High-Pressure Tube Twisting (HPTT) [23-25], Multipass Coin-Forging (MCF) [26], Repetitive Corrugation and Straightening (RCS) [27, 28], Simple Shear Extrusion (SSE) [29-31], Twist Extrusion (TE) [32-34], Accumulative Roll Bonding (ARB) [35-37], Conshearing Process [38, 39], Continuous Confined Strip Shearing (C2S2) and ECAP-Conform [5].

Among them the most widely used SPD techniques are ECAP, ARB and HPT. The specimens produced via these techniques can easily achieve exceptionally high strain. In addition, these processing methods are more feasible and economical. Equivalent Von Mises strain gives a measure of the amount of permanent strain in an engineering body. In order to compare the continues strain in HPT with the accumulated strains produced by ECAP and ARB, the equivalent Von Mises strain Ɛ is introduced in Fig. 2.2.

Process name	Schematic representation	Equivalent strain ε
HPT [40]	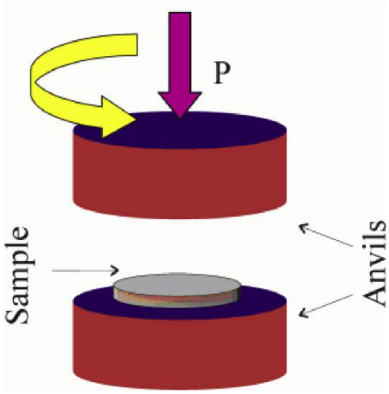	$\varepsilon = \frac{\gamma(r)}{\sqrt{3}}$
ECAP [41]	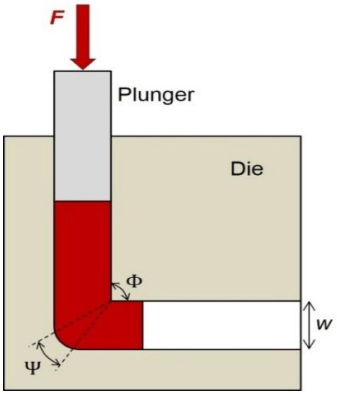	$\varepsilon = n\frac{2}{\sqrt{3}}\cot(\varphi)$
ARB [42]	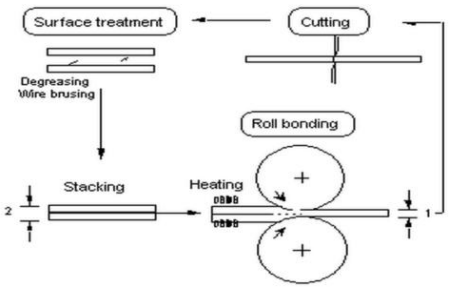	$\varepsilon = n\frac{2}{\sqrt{3}}\ln(\frac{t_0}{t})$

Figure 2.2 Summary of major SPD processes.

HPT is a kind of material processing method used to attain UFG structures. The principles of HPT processing are depicted schematically in Fig. 2.3. As shown in Fig. 2.3, the specimen in the form of a disk is located between two anvils in HPT and subjected to a torsional strain imposed through the rotation of one anvil, concurrently a compressive pressure is applied [6]. The process can be carried out at either room temperature or elevated temperatures. The disc is deformed by both high quasi-hydrostatic pressure and by the frictional force between the anvils and the disc [7].

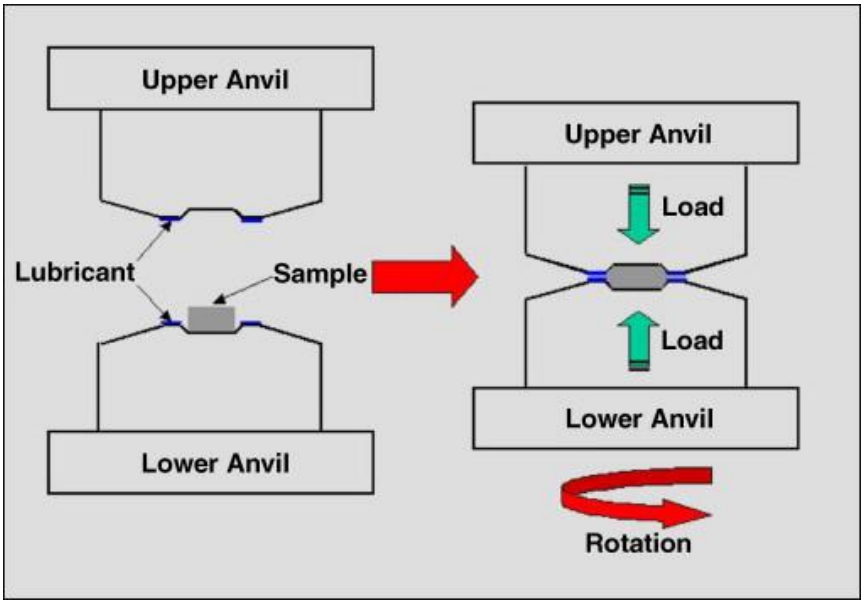

Figure 2.3 Schematic illustration of the principle of HPT process [6].

HPT has been attracted significant research interest since 1993[43]. However, it was first proposed by Bridgeman earlier in 1943[44]. There are two distinct types of HPT [3, 45]. One type is the unconstrained HPT. Under this condition, the material is free to flow outwards and only a minor back-pressure is introduced into the system, as shown in Fig. 2.4 (a). Another type is the constrained HPT, where there is no outward flow during the torsional staining or limited outward flow, as shown in Fig. 2.4 (b) and Fig. 2.4 (c). In unconstrained HPT, the materials between two anvils can flow freely and only relatively low hydrostatic pressure can be applied to the sample under this situation. Fig. 2.4 (b) shows a fully constrained HPT. Fig. 2.4 (c) demonstrates a kind of semi-constrained HPT, and the materials could flow outwards from the gap between two anvils. All the two modes can produce extremely high hydrostatic pressure during deformation.

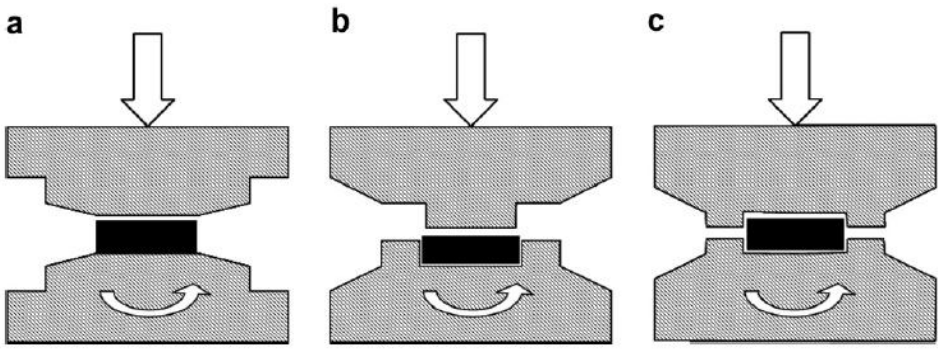

Figure 2.4 Two types of the HPT processes, a) Unconstrained HPT, b and c) constrained HPT [46].

2.2 Shear strain and equivalent strain imposed in HPT

As described in Section 2.1, the disc-shaped sample is placed between the two massive anvils in the constrained HPT. The upper anvil is fixed and the lower anvil is able to move up to provide the sample with extremely high compressive pressure of several GPa and the shear strain concurrently imposed through the lower anvil rotation anticlockwise viewed from the top at the room or elevated temperature. The sample is deformed by the surface frictional forces under a quasi-hydrostatic pressure.

The material deformation mode of HPT is usually classified as the simple shear [47]. As shown in Fig. 2.5, the applied shear strain γ can be given by an equation in the idealized condition where the disc thickness (h) remains constant during HPT [5, 16] :

$$\gamma = \frac{r\,\varphi}{h} \tag{2.1}$$

where r is the distance from the disc centre, φ is the rotation angle, and h is the thickness of the disc.

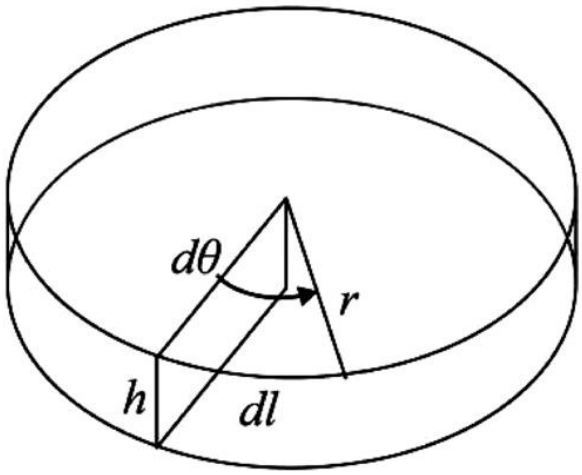

Figure 2.5 Parameters used in estimating the total strain in HPT [5]

Several equations have been used to calculate the equivalent strain in HPT. The equivalent von Mises strain, ε, is given by the following expression if the disc thickness is assumed to be constant [48-51]

$$\varepsilon_{eq} = \frac{2\pi N r}{\sqrt{3}h} \tag{2.2}$$

where N is the number of rotated revolutions.

According to Eqn. (2.2), it is apparent that a pronounced strain gradient exists in the sample. The equivalent strain is zero at the centre of the disc, while it reaches a maximum value at the edge of the sample. Thus it is anticipated that the equivalent strain is not identical along the radial direction (RD), and the inhomogeneous microstructure across the disc RD should be observed.

An alternative equation has been proposed for large shear strains ($\gamma \geq 0.8$), based on the Hencky strain criterion [52, 53]:

$$\varepsilon_{eq} = \frac{2}{\sqrt{3}} \ln \left(\frac{1}{2}\gamma + \sqrt{\frac{1}{4}\gamma^2 + 1} \right) \tag{2.3}$$

Degtyarev et al. [5, 16, 54] developed Eqn. (2.4) by taking the thickness change into account:

$$\varepsilon_{eq} = \ln \frac{h_0}{h} + \ln \left(\sqrt{\left(\frac{r\varphi}{h}\right)^2 + 1} \right) \tag{2.4}$$

where h_0 is the initial thickness of the specimen.

The equivalent strain could also be further simplified to the form [54, 55]:

$$\varepsilon_{eq} = \ln \left(\frac{2\pi N r h_0}{h^2} \right) \tag{2.5}$$

The above equations can be used to estimate the strain distribution within the disc deformed by HPT. They have respective advantages and disadvantages and are suitable for different conditions. Eqns. (2.3)-(2.5) give rise to a divergence of strain at the centre of the specimen where r=0. They do not incorporate the incremental rotation of the principal axes of the strain tensor [56], whereas Eqn (2.2) leads to a significant strain gradient in comparison with Eqn (2.3)-(2.5), which is not in agreement with the phenomenon of saturation in grain size and hardness at high strain levels [57-59]. In addition, all these equations assume that the strain is uniformly distributed across the disc thickness. In practice, as a simple and effective method, Eqn (2.2) is the most widely used equation to estimate the equivalent strain during HPT [59-62].

2.3 Hardness of materials processed by HPT

As a promising SPD method to produce UFG and nc materials, HPT is expected to give rise to a significant change in hardness. A great number of studies reported that generally the hardness of materials after HPT were considerable higher than that prior to HPT. However, in terms of hardness distribution, there were still many controversies. In order to investigate and

evaluate the mechanical properties of the disc samples processed by HPT, microhardness (mostly by taking measurements of the Vickers's microhardness, HV) or nanoindentation examinations were usually carried out for various applied pressures and numbers of revolutions.

As stated in Section 2.2, there is a significant strain gradient along the RD. As a result, inhomogeneous hardness is distributed throughout the disc diameter. Fig. 2.6 shows that the hardness at the edge of the specimen was about 3.5 times higher than that at the as-received condition, whereas the hardness at the central region increased by about 70% after 1 revolution. Even after 20 revolutions, homogenous hardness across the diameter had not been achieved. This conclusion was confirmed by many previous research [63-66] . Vorhauer et. al. [3] found that the less deformed area at the centre decreased with increasing HPT revolutions. The grains with the initial sizes were still visible at the central region even after 16 revolutions. In addition the hardness at the centre was apparently lower than other areas, and increased with number of revolutions. The increased hardness at the centre has been attributed to misalignment of the axes of the two anvils or other deviations.

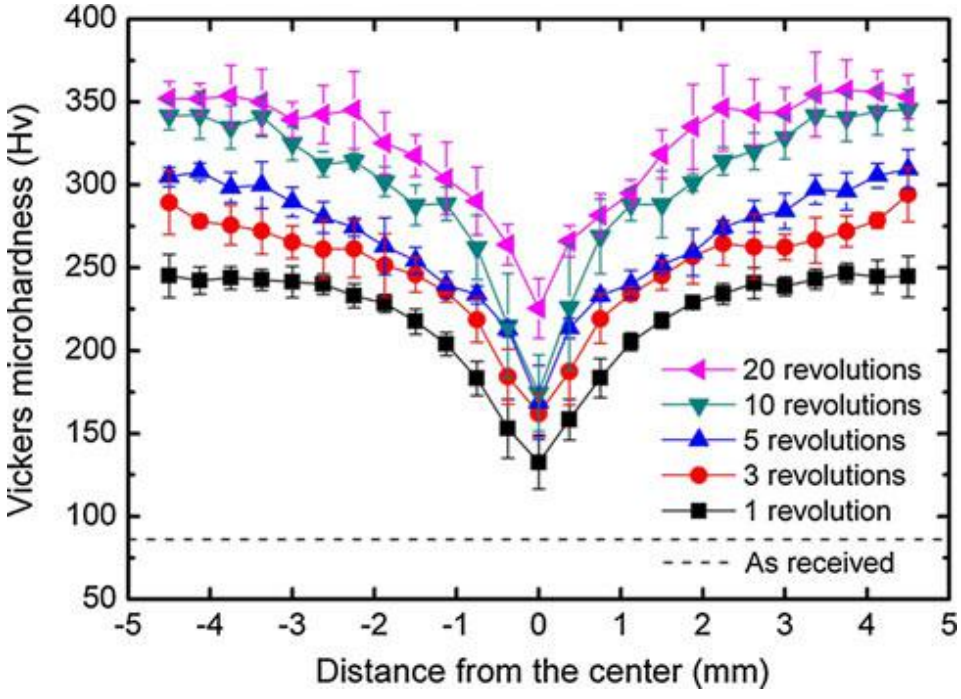

Figure 2.6 Microhardness distribution across the diameter of a Cu–28 wt % Ag processed by HPT under the 6 GPa pressure through total 20 turns, where the lower broken line shows the initial annealed condition [66].

However, on the other hand, many studies shown [5-7] that despite the existence of large

inhomogeneity on hardness at the centre of the sample for low revolutions of HPT, the hardness of the whole disc seemed to become reasonably homogeneous when the torsional strain increased to a sufficiently high level. As depicted in Fig.2.7, under the compressive pressure of 1 GPa, the hardness at the centre of the specimen only increased slightly to about 370 MPa, and at the edge the hardness increased dramatically to around 600 MPa after 1 turn HPT. But after 4 turns, homogeneous hardness across the diameter was achieved. A simple model was proposed to explain the development of a homogeneous microstructure in HPT based on the premise that shearing in a favourable area within the disc led to local hardening and the subsequent transfer of shearing to an adjacent position [6].

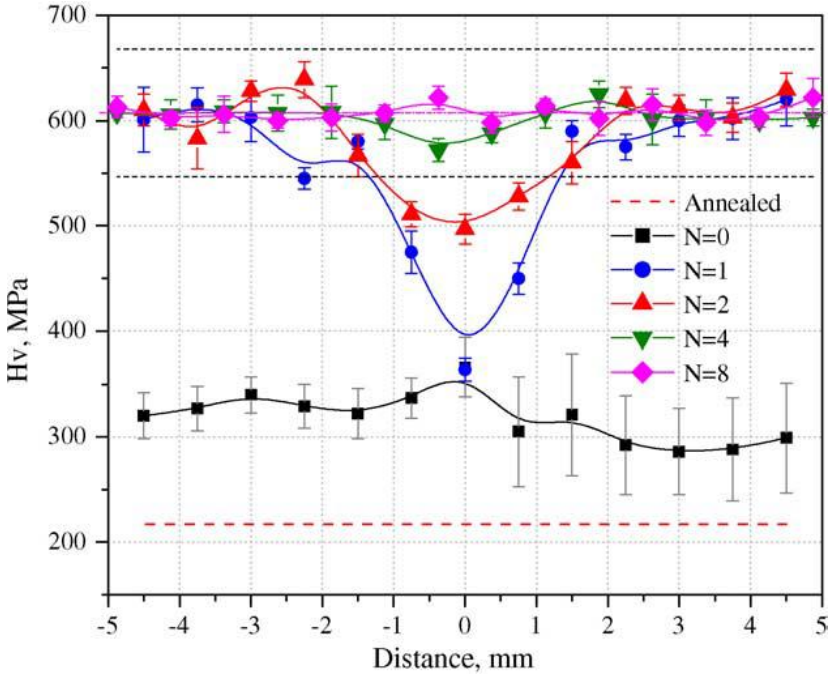

Figure 2.7 Microhardness distributions across the diameters of aluminium discs subjected to a pressure of 1GPa and up to eight revolutions. The lower broken line shows the initial annealed condition [6].

Although there is conflict between the preceding two views of the central hardness, it is reasonable to expect that the periphery of the disc sample is stiffer than the centre of the sample due to strain hardening at the edge of the sample. This assumption was supported by much published research [67-72]. However, a great number of measurements [62, 73-76] found that values of hardness at the central vicinity of the disc were obviously higher than values at the edge of the disc in many materials at least at the low strain stage, i.e. softening is occurred at the edge of the disc. As shown in Fig. 2.8, in the high purity Al processed by HPT under the 6 GPa pressure, it was found that the central hardness were obviously higher than the

peripheral hardness after 0.5 and 1 turn. With the increase of revolutions, the microhardness ultimately became reasonably homogeneous through the diameter of the disc.

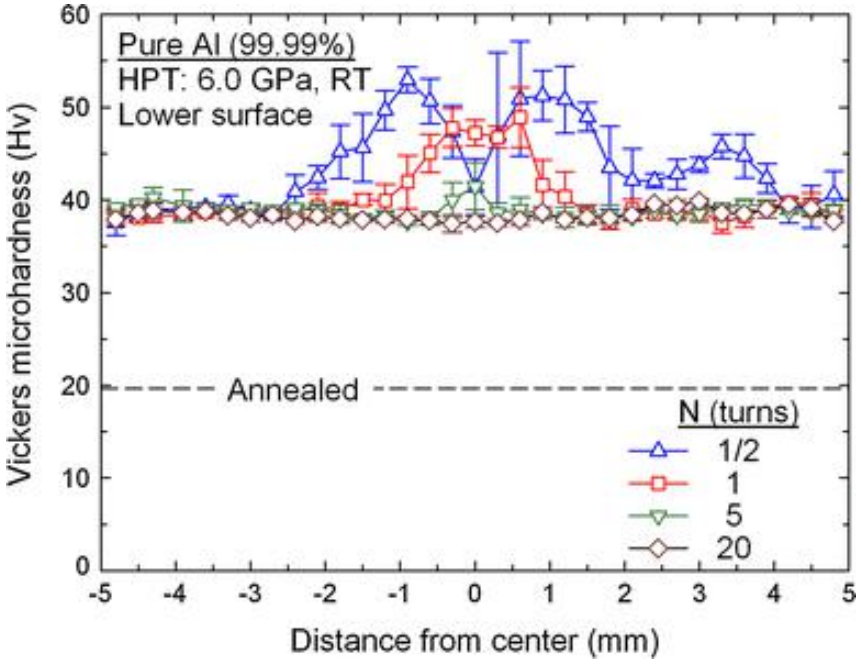

Figure 2.8 Variations of the average Vickers microhardness as a function of the distance from the centre of the high-purity Al disc after HPT with the pressure of6.0 GPa for 1/2, 1, 5 and 20 turns. The dashed line shows the average hardness in an annealed condition without processing and the error bars denote the 95 % confidence limit [77]

Stacking fault energy (SFE) is one of determinants causing the discrepancy between the hardening and softening during HPT. Distribution of microhardness in the materials processed by HPT depends upon the SFE and thus upon the nature of recovery within the materials. High SFE tends to result in cross-slip and rapid microstructural recovery. In materials with high SFE and high recovery rate including high purity aluminium [62, 73-75], softening behaviours caused by recovery occur more easily, especially at the periphery with relatively higher shear strain. Therefore, a lower microhardness will be attained at the edge of the HPT sample during the early stages of deformation [78]. In the materials with low SFE, such as copper and their alloys [79-81], low recovery rate results in that the hardness approach the minimum at the centre of the samples. Then due to strain hardening the hardness gradually increases until the saturation as the shear strain increases. Interestingly, regardless of the recovery rate of materials during HPT, homogenous microstructure is achieved when the materials experience high shear strain, leading to a saturation of hardness.

Significant softening in measured hardness after HPT processing has been also observed in

Zn-Al alloy [82]. The overall hardness across the diameter in these alloys samples after HPT are obviously lower than those in the as-received condition. As shown in Fig. 2.9, the Zn-Al alloys were deformed by HPT under 6 GPa. After 1 revolution, all hardness values of Zn-Al alloys were lower than that in the annealed condition. Noteworthy the decreasing amplitude of the hardness at the edge was greater than the hardness at the centre of the specimen. With additional numbers of revolutions, both central and peripheral hardness tended to decrease to the same level [83]. This phenomenon is hardly explained because severe grain refinement is inevitably introduced by HPT, which generally gives rise to a strengthening in hardness. Furukawa et al. studied the microstructural evolution of Zn-22% Al alloy by TEM and found that the phenomenon was possibly due to the absorption of the stable precipitates during HPT [84]. The significant reduction of the precipitates was related to the significant weakening behaviour.

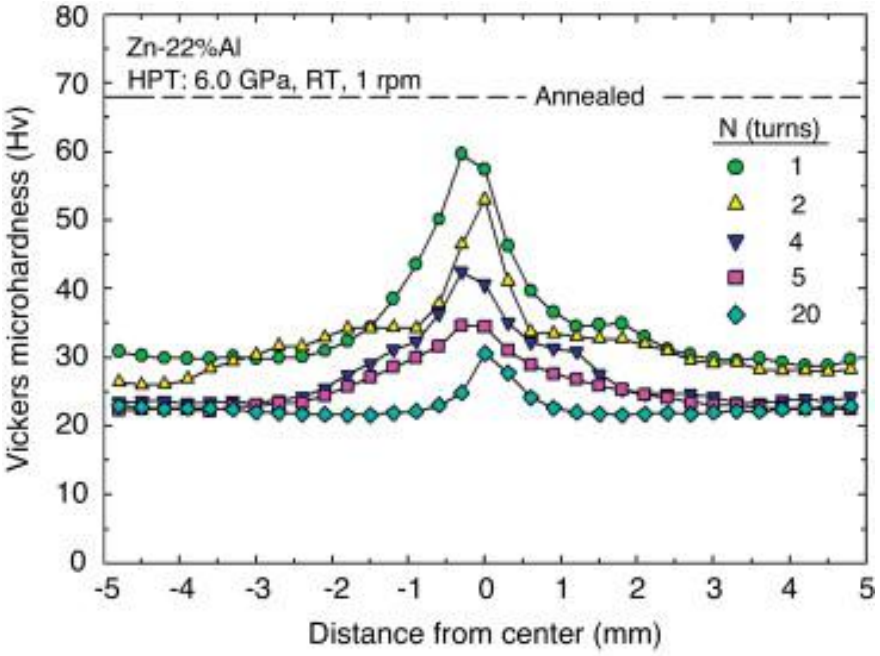

Figure 2.9 Microhardness distributions along the diameters of discs processed by HPT under 6.0 GPa for 1, 2, 4, 5 and 20 turns. The upper dashed line denotes the microhardness value of Hv ≈68 in the annealed condition prior to HPT [83].

According to the SFE of materials, there are three types of microhardness profiles as a function of the equivalent strain [85]. In Fig. 2.10, the hardness of the annealing condition was demonstrated by the horizontal bar on the vertical axis. As shown in Fig. 2.10 (a) for the materials lack of recovery, the hardness ascended with the increase of equivalent strain and finally stabilized at saturation value. As illustrated in Fig. 2.10 (b), in the materials with high

recovery rate, the hardness increased with the rise of equivalent strain at the low equivalent strain level, and subsequently decreased up to a saturation value at the high equivalent strain level. In the materials such as Zn-Al alloys and Pb-Sn alloys stated in the last paragraph, the hardness decreased after HPT and ultimately reached the saturation condition.

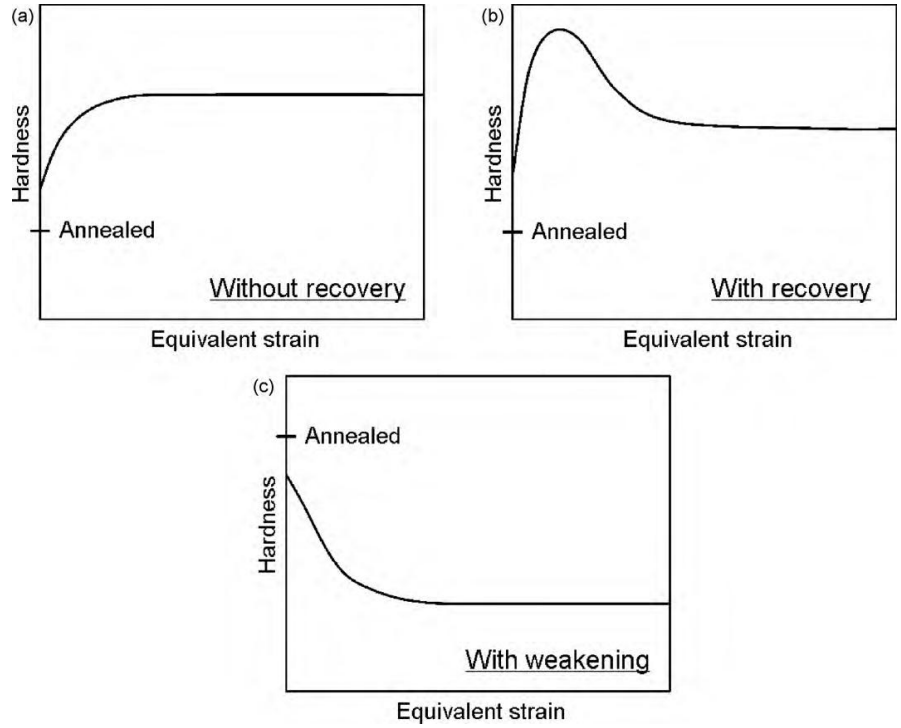

Figure 2.10 Schematic illustration of three types of the hardness as a function of the equivalent strain for materials processed by HPT: (a) without recovery as in most metals, (b) with recovery as in high-purity aluminium and (c) with weakening as in the Zn–22% Al alloy. The typical hardness levels for the initial annealed conditions are indicated [85].

It is found that microstructure of material [86] and grain growth [87] also play major roles in hardness evolution during HPT. At the early stage of HPT, working hardening which caused dislocation accumulation leaded to an increase in microhardness of material. With the development of plastic deformation, strain softening was observed at the subsequent stage. Specifically, high density of interior dislocations in nc grains is unstable, leading to the decrease of dislocations within nc grains. In addition, de-twinning and grain growth during HPT also make a contribution to strain softening at the second stage. At the final stage, the equilibrium between dislocation accumulation and dislocation annihilation were achieved. As a result, the hardness profiles as function of HPT strain as shown in Figure 2.11 is achieved.

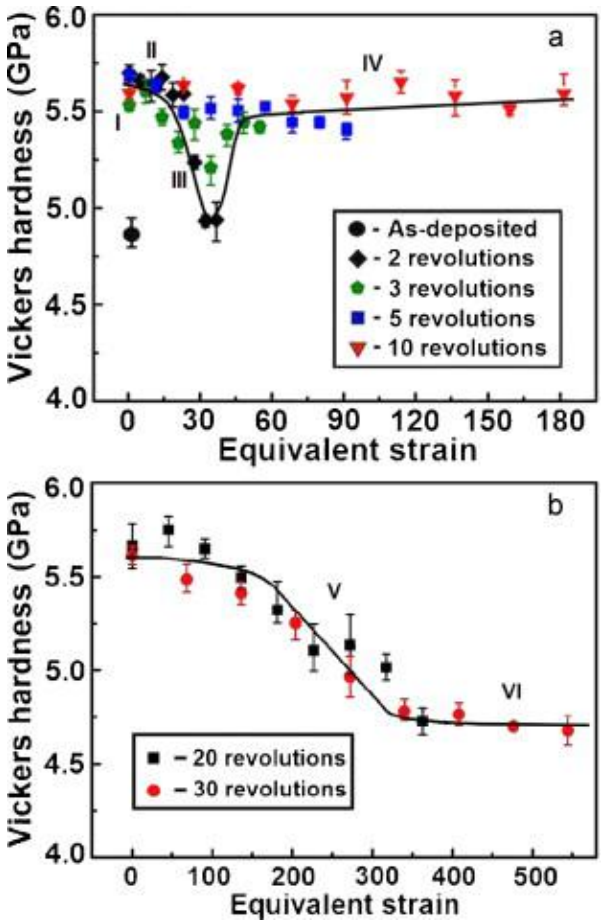

Figure 2.11 Vickers hardness plotted against von Mises equivalent strain for disks with HPT processing for 2, 3, 5, and 10 revolutions (a), and for 20 and 30 revolutions (b) [87].

The compressive pressure imposed on materials is another important parameter which influences the hardness of the deformed materials. Fig. 2.12 shows the relationship between the compressive pressure and hardness on commercial purity Cu processed by quasi-constrained HPT under the imposed pressures of 1, 4, 6 and 8 GPa, respectively [88]. It was apparent that the corresponding hardness values increased remarkably with the rise of the imposed pressure in the condition of the zero rotation up to the compressive pressure of 4 GPa. With the further increase of the compressive pressure, hardness was stable at the same level. It should be note that the strains were introduced by the compressive pressure before the torsion deformation in HPT. As a result, the obvious increase in hardness was detectable after the compressive force was applied.

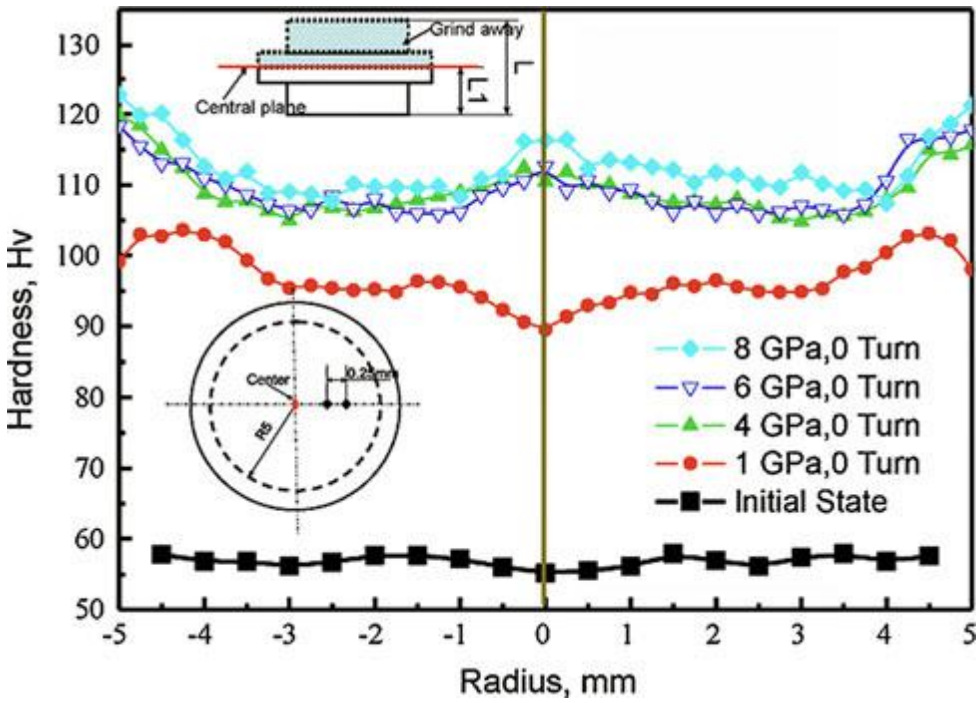

Figure 2.12 Hardness distribution across the diameter of CP Cu disks at the compressive stage of HPT under a series of applied pressures [88].

2.4 Microstructure evolution and grain refinement in materials processed by HPT

UFG and nc materials have been studied widely in the past due to their superior mechanical properties [75, 89-92] where the microstructural characteristics of materials play a significant role, such as high strength [10, 11], desirable corrosion resistance [13, 14] and favourable ductility [93, 94]. It is concluded from the early experiments that HPT can produce UFG and nc materials with the average grain size of ~170 nm [95] and 0.8 μm [5] in HP nickel; 300 nm [96], 140 nm [7], 260 nm [97] and even several tens of nanometres [98, 99] in copper; and less than 100 nm in Al alloy [100], Ni alloy [101] and Ti alloy [102]. As HPT is an effective method to produce materials with UFG and nc grains, it is crucial to study and understand the complicated microstructure evolutions and grain refinement mechanism during this process.

It is well known that the microstructure, grain size and grain shape, density and distribution of dislocations, as well as relative fraction and distribution of high angle grain boundaries (HAGBs) and low angle grain boundaries (LAGBs) undergoes drastic changes during the plastic deformation process, especially SPD. All of these characteristics are determined by the imposed strain, strain paths during deformation and the intrinsic properties of deformed materials. ECAP is easy to generate near equiaxed grains [103, 104] and ARB generally produces

pancake shaped structures over the whole deformed sample [105], while due to the variation in the shear strain along the RD, it is impossible to obtain homogeneous microstructure in the sample processed by HPT [106, 107]. Specifically, the grain sizes at the centre of the HPT processed disc are larger than that at the edge part in general.

Based on extensive investigations, several grain refinement mechanisms during HPT have been proposed [45, 60, 108, 109]. First a grain refinement mechanism primarily occurs in high SFE materials, including ferrite steel, aluminium and nickel, as schematically shown in Fig. 2.13 [74]. When the high SFE material is subjected to HPT deformation, the deformation is mainly caused by dislocation activities. As the imposed strain increases, some slip systems operate and a large amount of dislocations are generated within the grain. These dislocations tangle and kink with each other. Subsequently the dislocations accumulate to form thick dislocation walls at the low plastic strain. With the development of plastic deformation, the dislocation walls further agglomerate into the subgrain boundaries, which will block the dislocation propagation and motion (Stage I in Fig. 2.13). As the deformation proceeds the dislocations annihilate at the subgrain boundaries (Stage II in Fig. 2.13). The misorientation angles between subgrains increase, and the subgrain boundaries then evolve into the grain boundaries while the density of dislocations within the grains decreases, which leads to a clean grain interior (Stage III in Fig. 2.13). Therefore, after a series of dislocation accumulations, interactions, tangles and spatial rearrangements, the initial coarse grains are subdivided into a number of smaller ones with the high angle grain boundaries.

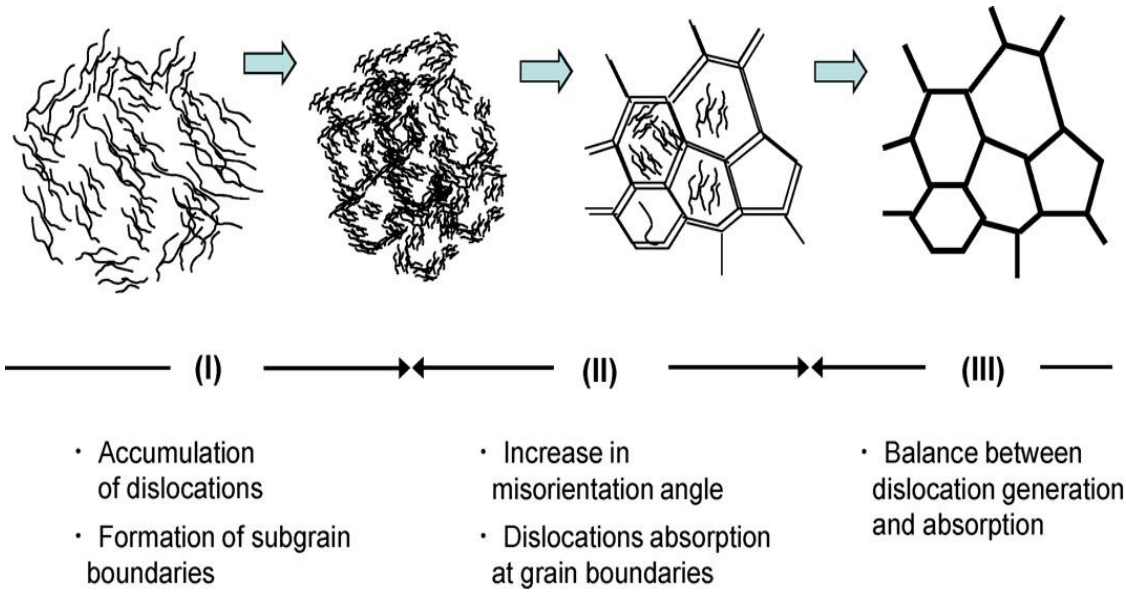

Figure 2.13 Schematic illustration of microstructural evolution with straining [74].

A representative result of the first grain refinement mechanism was reported by Xu et al. [62]. As shown in Fig. 2.14, the polycrystalline high purity aluminium was subjected to an applied pressure of 1 GPa and then strained by torsion through 1/8, 1/4 and 1 turn respectively. As illustrated in Fig. 2.14(a), at the early stage of HPT, the grain size at the centre of the specimen remained at the initial level of ~ 250 μm. However the network-shaped LAGBs had formed pronouncedly within the initial larger grains. The colour spread in the electron backscatter diffraction (EBSD) map indicated the presence of dislocations and/or sub-structures. The same grain shape was found at the edge of the same specimen in Fig. 2.14 (b). However, the new subgrains were born within the large grains. With the increasing imposed strain, the subgrains were well developed and the fraction of grains having the high angle boundaries has increased, as shown in Fig. 2.14 (c). Finally, most of the subgrains were transferred into small grains with the high angle grain boundaries. The grain size at the edge eventually reached ~2 μm as shown in Fig. 2.14 (d). The microstructural evolution is in good agreement with the first grain refinement mechanism.

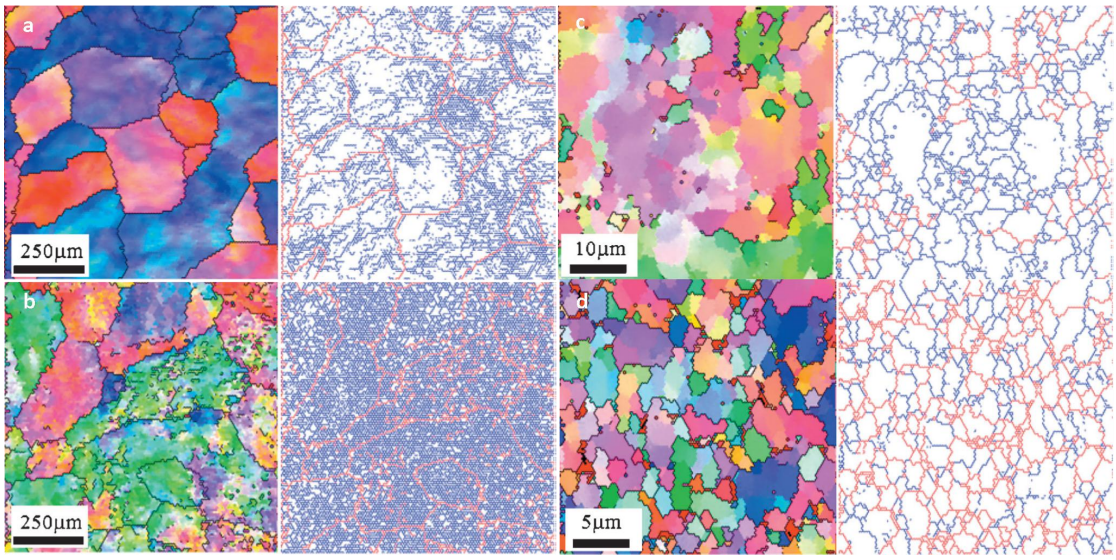

Figure 2.14 Images obtained by EBSD for disks processed by HPT where (a) shows 1/8 turn near the centre, (b) shows 1/8 turn near the edge, (c) shows1/4 turn near the edge and (d) shows 1 turn near the edge: the relevant boundary patterns are shown in the right column with red and blue lines used to identify high-angle and low-angle boundaries, respectively [62].

The second grain refinement mechanism primarily dominats in the low SFE materials such as copper [110, 111] , Cu alloys [112-114] and duplex stainless steel [60]. Deformation twinning or twin boundary (TB) subdivision and TB dislocation interactions are the determinants in microstructural characteristics of materials with low SFE during HPT.

The second grain refinement mechanism can generally be divided into several stages during HPT deformation [60]. As demonstrated in Fig. 2.15, at the beginning of HPT, the as-received materials have the coarse grained structures with low density of randomly distributed dislocations. At this stage, some twinning systems are activated and the deformation twins are generated immediately with the coarse grained structure after deformation. As the development of deformation, the formation of the second stage SFs/nanotwins and the interaction between the second stage SFs/nanotwins and the first stage twins result in the de-twinning process. At this stage (Stage 2), the remaining twin boundaries are converted into conventional HAGBs through the interactions between the dislocations and twin boundaries. At the next stage (Step 3), the decrease of twin density caused by the second de-twining process promotes the interaction between the dislocations and the twin boundaries. As a result, further grain refinement is achieved by the transformation of the remaining twin boundaries into HAGBs. During the HPT at Step 4, further grain refinement results from the interactions between the newly generated dislocations and the nanotwins.

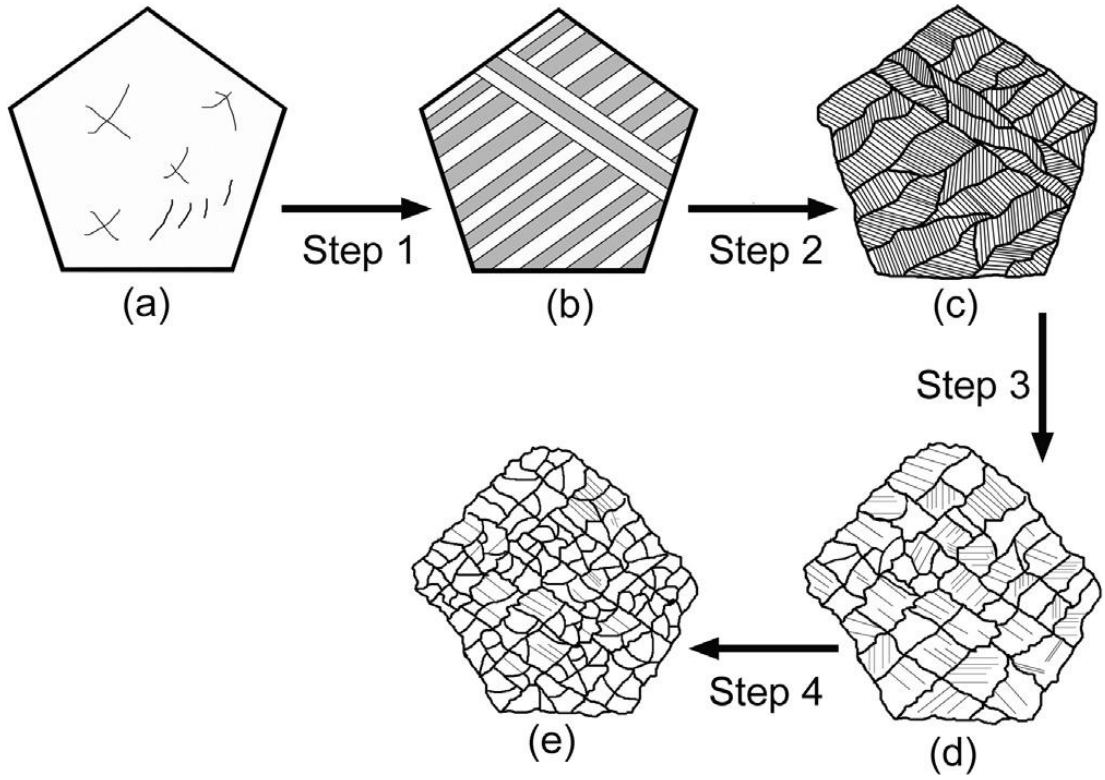

Figure 2.15 A schematic diagram of the HPT-induced grain refinement process in austenite [60].

Wang et al. [113] found that the initial coarse grain of Cu–Zn alloy was subdivided into smaller grains by primary and secondary twinning during HPT. Interactions between dislocations and TBs transformed the TBs into high angle grain boundaries. Fig. 2.16 showed the

microstructure corresponding to the stage in Fig. 2.15 (c) by TEM. A high density of stacking faults was demonstrated in Figs. 2.16 (a) and 2.16 (b). Fig. 2.16 (c) and (d) illustrated the nanotwins in a grain. The morphologies of stacking faults and nanotwins indicated that the most stacking faults and nanotwins were formed by the emission of the partial dislocations at the GBs.

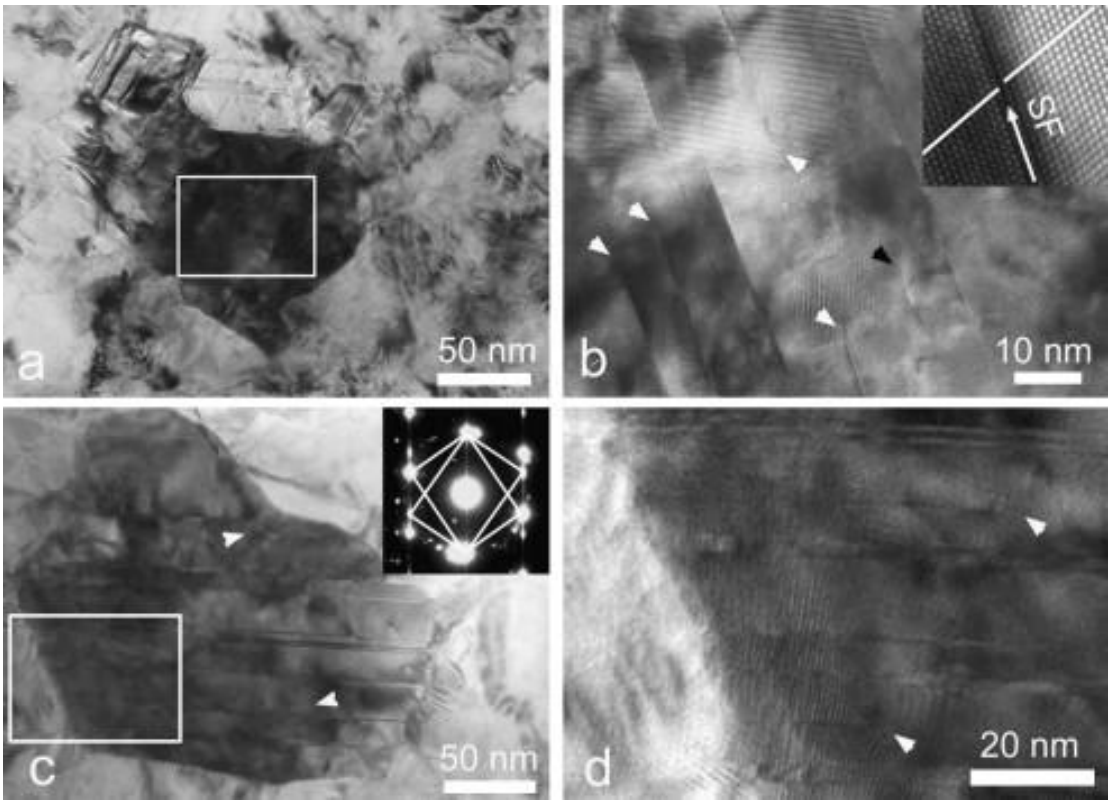

Figure 2.16 (a) TEM image of a grain with a high density of stacking faults, (b) a high resolution TEM image of part of (a), (c) a grain with a high density of nanotwins and its corresponding〈1 1 0〉 SAED pattern showing the twin relationship and (d) an enlarged image of the area marked with a rectangle in (c). White arrowheads mark the places where stacking faults and twins terminate in grains. A black arrowhead indicates a stacking fault with the two ends terminating within a grain.

Continuous dynamic recrystallisation (CDRX) is another grain refinement mechanism during HPT, especially at elevated temperature [115-117]. As shown in Fig. 2.17, the CDRX grain refinement mechanism generally consists of two steps [118]. At the first step, continuous LAGBs are formed by rearrangement of accumulating dislocations during the process of dynamic recovery. With the development of deformation, LAGBs can result in the formation of ultra-fine grained structures in the process of CDRX in the materials whose LAGBs with the misorientation close to 1° have low mobility. The elongated subgrains formed by LAGBs are easily generated during deformation because the LAGBs are produced at a higher rate if

they are located in favourable orientations, i.e. in the primary slip planes. The misorientation of LAGBs aligned in the SD tends to increase compared with transverse LAGBs at low strains [119-121]. Subsequently, these elongated subgrains transform into almost equiaxed grains by the formation of the transverse LAGBs with the elongated structures by dislocation rearrangement (Fig. 2.17a). The dislocation density decreases simultaneously. At the second step, the dislocations slide within the subgrains and are trapped by the subgrain boundaries, which give rise to the increase in their misorientations (Fig. 2.17b). The subgrains which contain parts of the original HAGBs are considered to be a nucleus (Fig. 2.17c), and finally the nucleus is transformed into a grain by converting all the LAGBs into HAGBs. Extensive grain rotations in the structure described in Fig. 2.17 (d) accelerate the evolution of LAGBs into HAGBs.

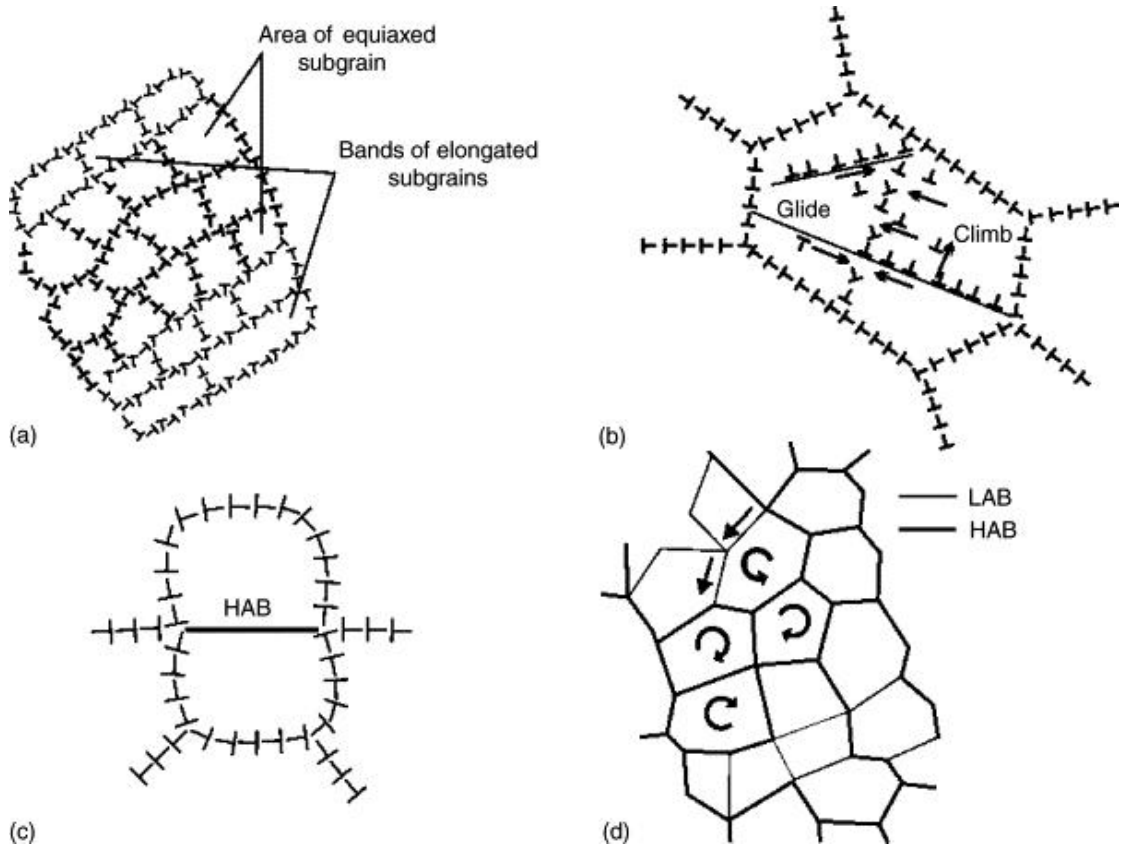

Figure 2.17 Schematic representation of grain refinement in AA1421 subject to SPD, (a) formation of arrays of equiaxed subgrains alternating with elongated subgrains, (b) interaction of LAGB with dislocations resulting in progressive increase in their misorientation, (c) a nucleus in 3D subgrain structure and (d) rotation of (sub)grains facilitates the transformation of LAGBs into HAGBs [118].

In the case of a single crystal, the deformation characteristics are totally different to those in polycrystalline. Because there are no grain boundaries within the as-received single crystal

and low density of dislocation at the early stage of deformation, the grain boundaries have little effect on the dislocation gliding. Therefore, the study of single crystals would aid in the further understanding of deformation behaviours and characteristics during HPT [122-126].

Most of previous researches on single crystals deformed by SPD focused on ECAP. There were only few research on single crystals processed by HPT [127, 128]. Nickel <111> single crystals were deformed by HPT to investigate the deformation mechanism of Face Cantered Cubic (FCC) high SFE materials [129]. As shown in Fig .2.18(a), at the beginning it is clear that few dislocations were observed in the as-received sample. With the development of HPT deformation, more dislocations were induced by plastic strain. The increase in the density of dislocations leads to substructures with LAGBs. As can be seen in Fig .2.18(b), the band shaped structures composed by these low angle subgrains were produced along the RD. In Fig .2.18(c), the band shaped structures was bordered by HAGBs. Under the equivalent strain of 2.25, the initial orientation of the single crystal was distorted slightly. With the increase in the applied strain, the band shaped structure was subdivided and transformed into a near equiaxed cell structure with LAGBs when equivalent strain reaches ~3. Subsequently these bands were converted into the elongated grains with HAGBs and subdivided into cell structure with LAGBs by further deformation. Eventually, at an equivalent strain of 12, the misorientations of cell structure increased into high grain boundaries, so that the corresponding grain size was reduced. It should be noted that the reduced grain size was in the order of magnitude of the cell structure presented at the last step and cannot be further decreased via higher deformation.

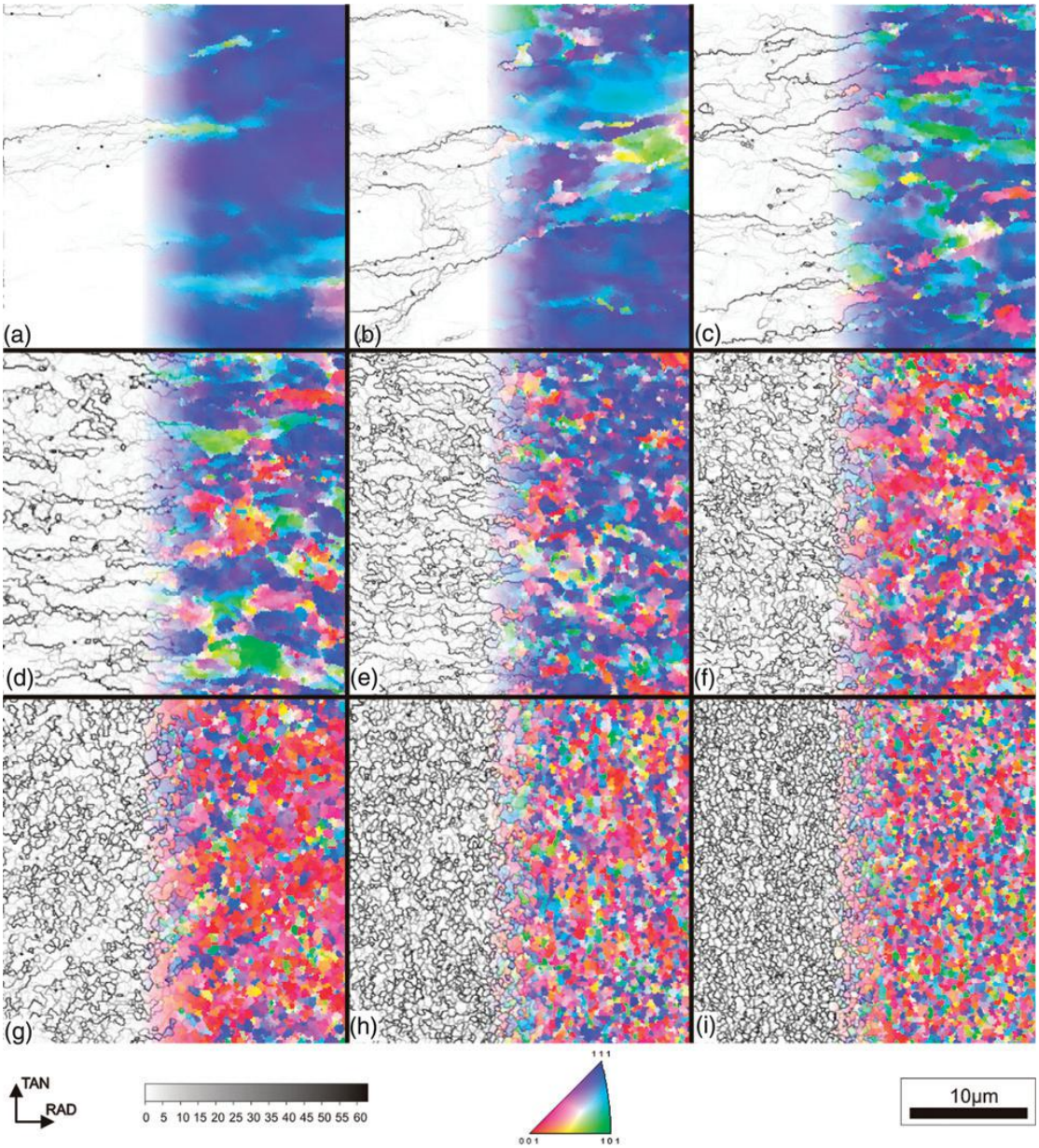

Figure 2.18 Structure development with increasing equivalent strain of the nickel <1 1 1> single crystal. The scans show the structure evolution in the RD with no sample rotation. The brightness of the boundaries correspond to the misorientation angle. The scans refer to the following equivalent strains (a) 1, (b) 1.5, (c) 2.25, (d) 3, (e) 4, (f) 5, (g) 8, (h) 12, (i) 32 [129].

More details on the band shaped structure are shown in Fig. 2.19. The bands having HGABs were composed of the elongated cells with LAGBs aligned in the RD, whereas the saturation microstructure in Fig. 2.19 (b) shows that the fragmentation did not influence the misalignment of the cell structure with respect to the SD.

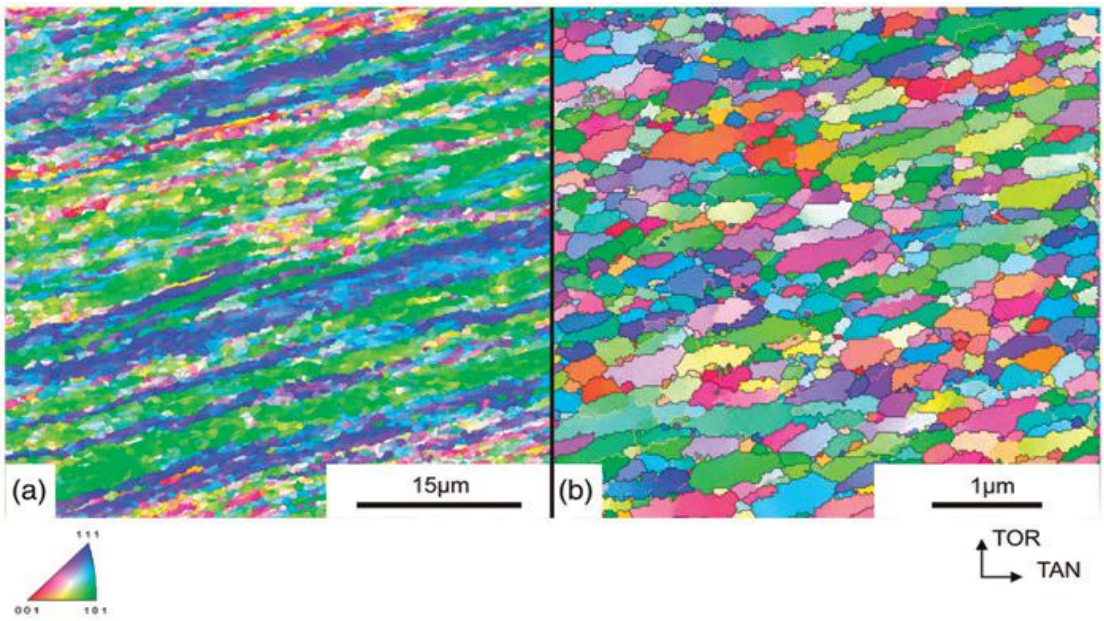

Figure 2.19 Comparison of the microstructure recorded in side-view of regions deformed to an equivalent strain of (a) 2.5 and (b) 32. Note the different scale bars [129]

2.5 Texture evolution in materials processed by HPT

The crystallographically preferred orientation in materials is called crystallographic texture. It has been found that crystallographic texture is certainly associated with many material properties, such as Young's modulus, Poisson's ratio, magnetic permeability and thermal electrical conductivity [130-135]. It is well known that the <001> direction is magnetically the softest in iron, so that the predominated Goss texture (110) [001] would minimise the magnetization losses, which is very useful in silicon steel used in transformer[130]. Taking advantage of these specific characteristics of materials caused by particular texture plays an important role in materials industries.

2.5.1 Representations of texture

Two kinds of ways are mainly used to represent the texture of materials: mathematical parameters way including Miller-Bravais Indices, Euler Angles, Angle/Axis of Rotation and Rodrigues vector, and graphic method including Pole figure (PF), Inverse pole figure (IPF) and Orientation Distribution Function (ODF).

Each representation has unique advantages over other representations. As an example, for the cubic crystal structured material in rolling deformation the Miller-Bravais Indices are able to demonstrate visually the orientation of the crystal with respect to the specimen in the form of

(h k l)<u v w>. (h k l) denotes the crystallographic plane parallel to the macroscopic deformation plane and the direction <h k l> is parallel to the normal direction (ND), and <u v w> strands for the crystallographic direction parallel to the rolling direction (RD)

PF, IPF and ODF are commonly used to represent textures of materials. PF is a two dimensional representation which is generated by the stereographic projection of the crystallographic orientations onto a circle plane of the reference sphere, as shown in Fig. 2.20. Usually the specific plane is chosen as the circle plane, For instance, the normal direction (ND) is typically chosen as the north pole of the sphere for the sample subject to rolling [136].

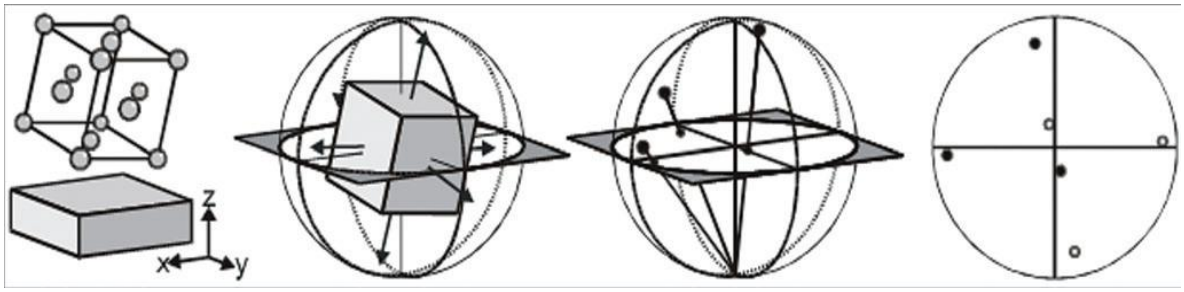

Figure 2.20 The production of a stereographic projection for a single crystal[137].

As shown in Fig. 2.21, IPF essentially is a representation in which the orientations of the sample coordinate system are projected into the crystal coordinate system. According to its characteristic, IPF is suitable to demonstrate the textures of axial symmetric samples. For cubic materials, IPF is normally presented in a unit triangle of <0 0 1>, <0 1 1> and <1 1 1> crystal directions

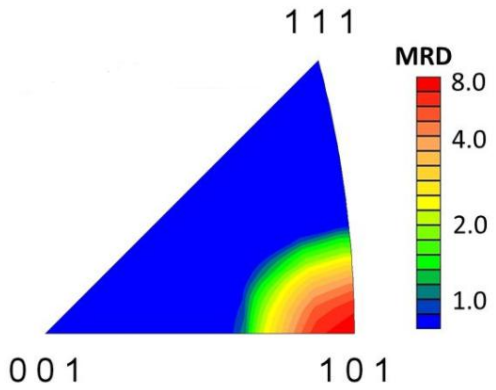

Figure 2.21 IPF with strong axial <110> texture where <100>//RD and <011>//ND [138].

Orientation distribution function (ODF) is a three dimensional representation of textures. ODF is able to provide quantitative information on the crystallographic orientations in the

form of three Euler angles (φ_1, Φ and φ_2) [139]. ODFs can separate the texture components and fibres clearly.

Euler angles refer to three notations which transform the specimen or sample coordinate system g_1 onto the crystal coordinate system g_2. They are defined commonly using Bunge's convention [140]. The rotation procedure is shown in Fig. 2.22. The coordinate system g_1 rotates first by an angle of φ_1 with respect to its ND direction, then rotates by an angle of Φ with respect to its new RD′ direction, and subsequently rotates by an angle of φ_2 with respect to its new ND′ direction. As a result, the coordinate system g_1 overlaps with the crystal coordinate system g_2.

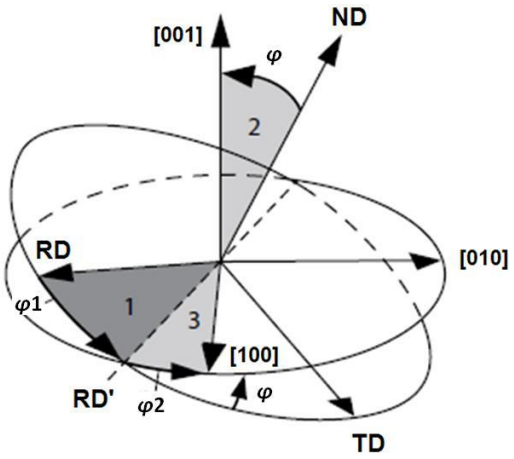

Figure 2.22 Diagram showing the rotations through the Euler angles φ1, φ, φ2, in the order 1, 2, 3 as shown describes rotation between the sample and crystal axes [130].

2.5.2 Texture measurement

Electron Backscatter Diffraction (EBSD) is a scanning electron microscope (SEM) based technique that collects the crystallographic information from the samples. In EBSD, a stationary electron beam hits a 60-70° angle tilted crystalline sample. The diffracted electrons form a specific Kikuchi pattern which contains the information concerning characteristics of the crystal structure and orientation, and discriminates between crystallographically different phases and characterise grain boundaries detected by a fluorescent screen. The data are analysed by EBSD software to establish a quantitative representation of the microstructure. The EBSD measurement process is shown schematically in Fig. 2.23.

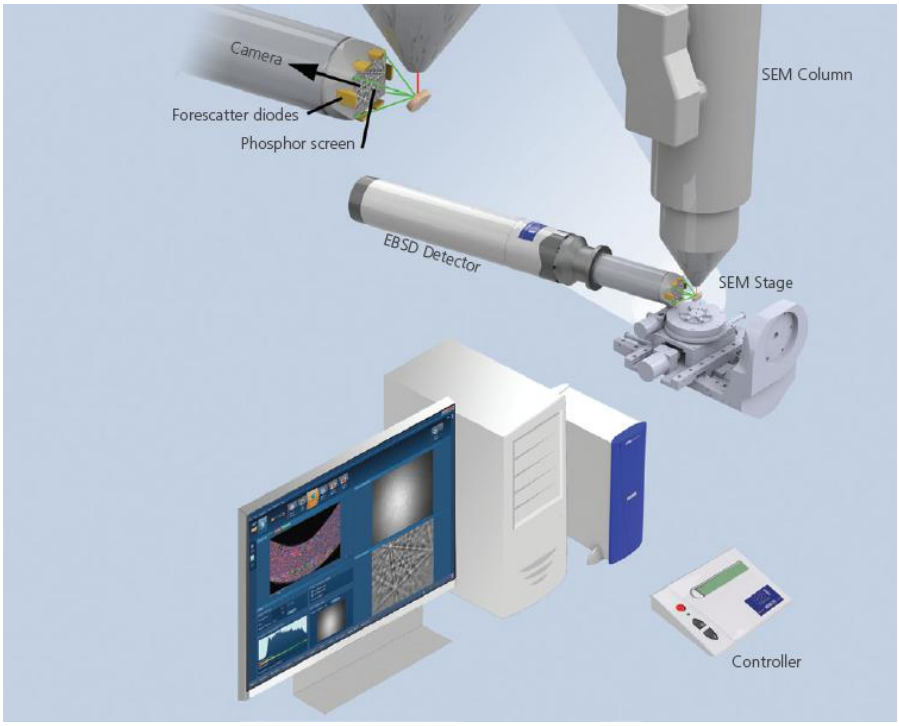

Figure 2.23 Schematic illustration of a typical EBSD system [137]

2.5.3 Microtextural evolution in torsion and HPT

Different fabrication methods will give rise to various textures. Hence the texture analysis is significant in the analysis of deformation behaviour [141]. Texture analysis makes it feasible to quantitatively compare between different modes of deformation.

However, in contrast to common plane strain or axisymmetric deformation textures such as rolling texture which has been undergone extensive studies in the past, little research has been undertaken to explore torsional deformation mechanisms. Stable texture is rarely observed in torsional deformation since all parts of the sample except the area near the sample centre are constantly rotated over the whole torsional deformation process. Therefore the development of torsional texture is considerably complicated.

In 1984, Canova et al. simulated torsional/simple shear deformation for FCC materials [142]. As shown in Fig. 2.24, three ideal orientations (i.e. Types A, B and C) were found in the simulations by FC (full constraints) and RC (relaxed constraints) Taylor methods under different shear strains γ. Type-B texture is a kind of transition texture between Type-A and Type-C textures. Type-C texture is a special orientation of Type-B texture. With the increasing shear strain, Type-B texture shows diminution, whereas Type-A and Type-C textures become stronger.

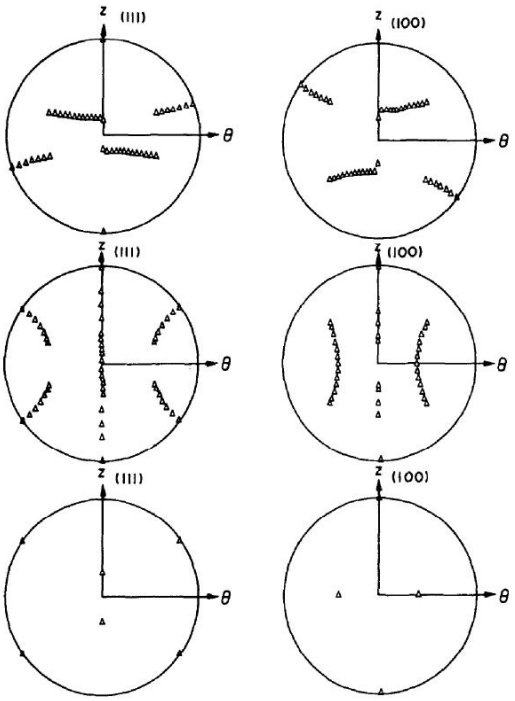

Figure 2.24 PF representations of the idealized Types-A, B and C texture components [142].

Subsequent studies [143] [144] define the shear strain orientations in detail in PF and ODF. All possible ideal texture components for the simple shear and the torsion deformation of FCC materials are listed in Table 2.1 [145].

Table 2.1 Euler angles and Miller indices for the ideal torsion texture components of FCC materials [146-148]

	Euler angles (°)			<u υ ω>	Taylor factor
	ϕ_1	Φ	ϕ_2		
A	0	35.26	45	{1-1-1} <1 1 0>	1
A_b	180	35.26	45	{-11-1} <-1-10>	1
A^*_1	35.26/215.75	45	0/90	{111} <-1-12>	1.15
	125.26	90	45		
A^*_2	144.74	45	0/90	{111}<11-2>	1.15
	54.74/234.74	90	45		
B	0/120/240	54.74	45	{1-12} <110>	$\sqrt{2}$
B_b	60/180	54.74	45	{-11-2}<-1-10>	$\sqrt{2}$
C	90/270	45	0/90	{001}<110>	$\sqrt{3}$
	0/180	90	45		
Cube	0/90/180/360	0	0	{001}<100>	$\sqrt{18}$
	45/135/225/315	0	45		

{111} fibre	{111}<uvw>
<110> fibre	{hkl}<110>

The ideal orientations are stable with little or no lattice rotation during the shear deformation [147]. All ideal simple-shear texture components are presented in the ϕ_2=45° ODF section and (111) PF [24, 149-153]. Thus the ϕ_2=45° ODF section and (111) PF are used to demonstrate the textural evolution in this study. It is known from Fig. 2.25 that the ideal simple-shear orientations are characterised by two kinds of ideal partial fibres in FCC materials, which are identified as A {1 1 1} <u ν ω> (or {1 1 1} - fibre in short) and B {h k l} <1 1 0> (or <1 1 0> -fibre in short). Type A consists of A/A_b (means A or A_b), A^*_1 and A^*_2 ideal components, and the {1 1 1} plane is the crystallographic slip plane parallel to the shear plane, i.e. A fibre has a common (111) shear plane with the rotation of the crystal around the shear plane axis. Type B fibre is comprised of the B/B_b and C components f and the <1 1 0> is their crystallographic slip direction, namely. The B fibre has a common <110> SD with the rotation around the SD.

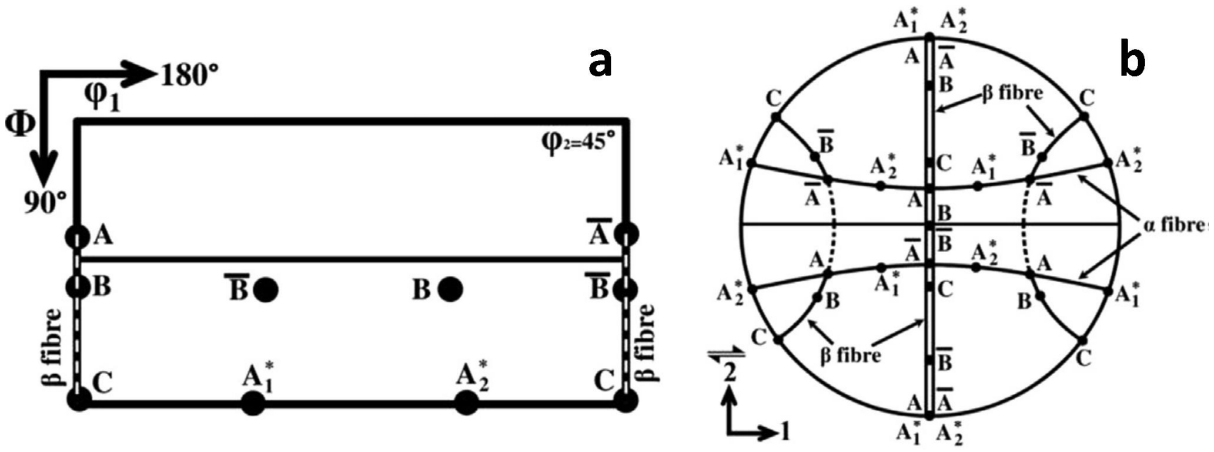

Figure 2.25 Ideal simple shear texture components shown in the ϕ_2=45° ODF section (a) and (111) pole figure (b) [149, 152]

Up to now, textures generated during HPT have been studied for a wide range of materials [154-159]. As shown in Fig. 2.26, Korznikova et al. studied the textural evolution in HPT nickel up to 5 turns[150]. It was found that A^*_2 prevailed after 0.1 turn (Fig. 2.26). With the increasing deformation (0.25 turn), a pronounced C texture component was observed in Fig. 2.26(c) due to the relaxed strain compatibility constraint associated with an elongated grain structure. At the strain equivalent to 0.5-5 turns (Fig. 2.26-f), the strength of textures decreased but the textural patterns were stable. The final textures were the typical simple shear textures.

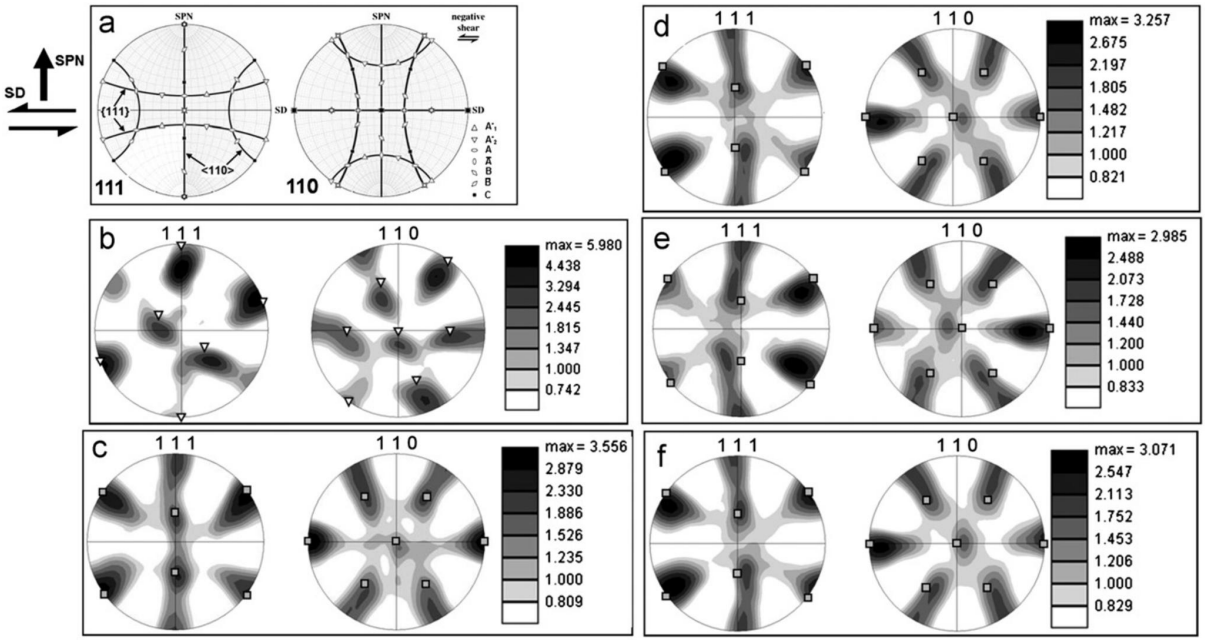

Figure 2.26 {111} and {110} PFs illustrating ideal simple-shear texture (a), as well as measured textures after accumulated strains of 0.1 rotation (b), 0.25 rotation (c), 0.5 rotation (d), 1 rotation (e) and 5 rotations (e). The open inverse triangles and grey squares in the measured pole figures indicate projections of A^*_2 and C ideal simple shear texture components. Note: all textures are arranged in conventional reference frame for simple-shear, i.e., SD is horizontal and SPN is vertical [150].

ODF is the most important method to illustrate the distribution of orientations in a quantitative manner [78, 146, 160-166]. The ϕ_2=45° ODF section contains all ideal simple-shear texture components. Therefore this ODF section is commonly used to represent the textures. Fig. 2.27 demonstrated that evolution of texture in HPT. The commercial pure (CP) Al was deformed by HPT at room temperature by Naghdy et al [78]. It was found that at the early stage of HPT, the straining which strengthens textures played a more important role than the grain fragmentation which weakens textures. At the strain of ~3.95 (Fig. 2.27), the B component accounted for the highest volume fraction. With the increasing strain, the A and A^* components continuously declined, whereas the C and B components became stronger (Fig. 2.27-e). At the strain level of ~12, the grain refinement led to a more randomised texture. From this stage onwards, the intensities of these components were changed slightly up to the final stage (Fig. 2.27) where these components were more randomised.

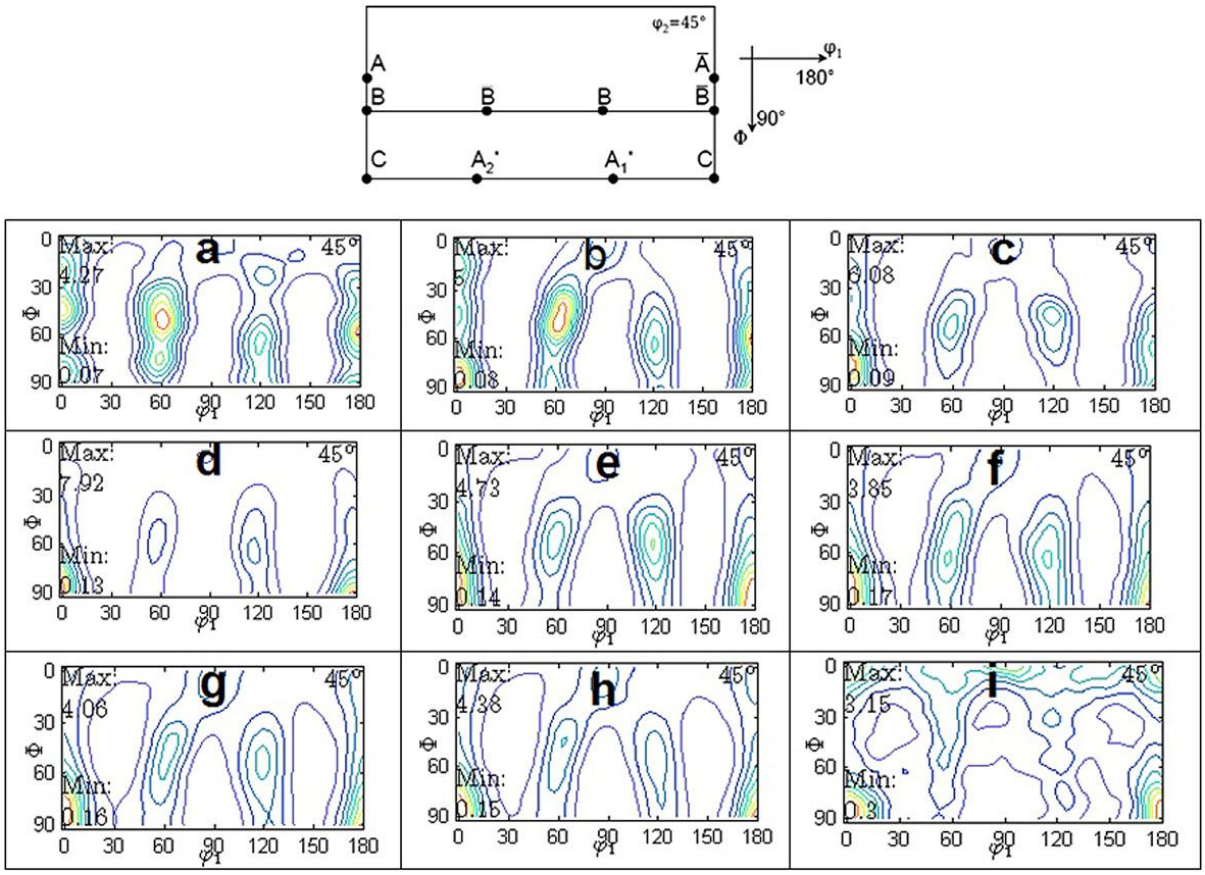

Figure 2.27 Experimental shear textures at equivalent strains of a-0.75; b-1.5; c-3.98; d-5.31; e-7.97; f-11.9; g-14.85; h-17.8; i-99 (φ2 = 45° sections of the ODF) [78].

2.5.4 Mechanism of texture evolution during HPT

Taylor model is one promising method to explain the texture evolution during the plastic deformation [167] and is extensively applied to study the texture evolution mechanism in the materials processed by torsion [168, 169]. In the Taylor model it is assumed that all crystallites are subjected to the same plastic strain, and the plastic deformation is achieved by the activation of the slip systems.

A simple model was developed in Refs. [127] based on the full constrained Taylor model to simulate the texture development of the <111> and <100> nickel single crystals subject to HPT. The results of the simulation were compared with the corresponding experimental results. It is found from Fig. 2.28 that the maximum density of poles occupied the same positions in Fig.2.28 (a) and Fig. 2.28 (b). The texture evolutions of the <111> and <100> nickel single crystals in experiment were in good agreement with the predictions of the model.

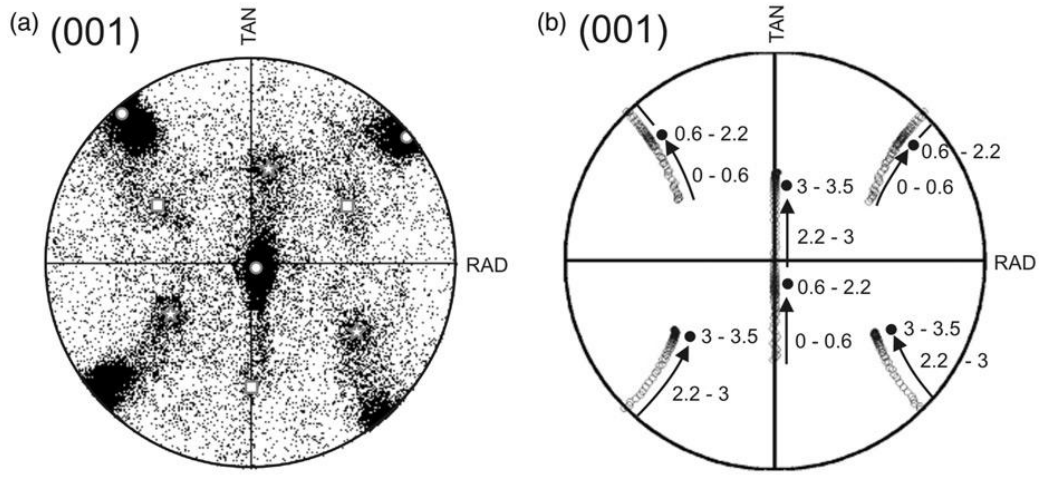

Figure 2.28 Comparison between texture measured for the <111> nickel single crystal subject HPT, (a) and texture predicted by the full constrained Taylor model, (b). The white squares in (a) mark the initial orientation while the white circles indicate the first preferred orientation and the white stars refer to the second preferred orientation. In the computation, (b), a rough scale is given referring the calculated texture evolution to the equivalent strain [127].

In order to understand the formation and properties of such fibres in polycrystals, it is necessary to study more information of the rotation fields (as show in Fig 2.29) on the ideal orientations [147, 170]. The preferred flow direction on the rotation field is the result of rigid body rotation rate, which plays a significant role in shear texture generation [171-174]. The crystallographic rotation field for torsion texture possesses a series of unique features [145, 147, 175]: One is the predominance of single sense rotations around the sample RD. In addition, the location of regions of crystallographic divergence adjacent to the main deformation texture components. The lattice rotation rate varies significantly as a function of the crystallographic orientation. Crystals oriented between the ideal shear orientations (along φ_1 in Bunge notation) have a high lattice rotation rate, while the rotation rate decreases to near zero for the orientations close to the ideal shear orientations. Therefore, the lattice rotation rate depends so strongly on orientation that the rotating grains near the particular ideal orientations can remain near those orientations over the appreciable strains.

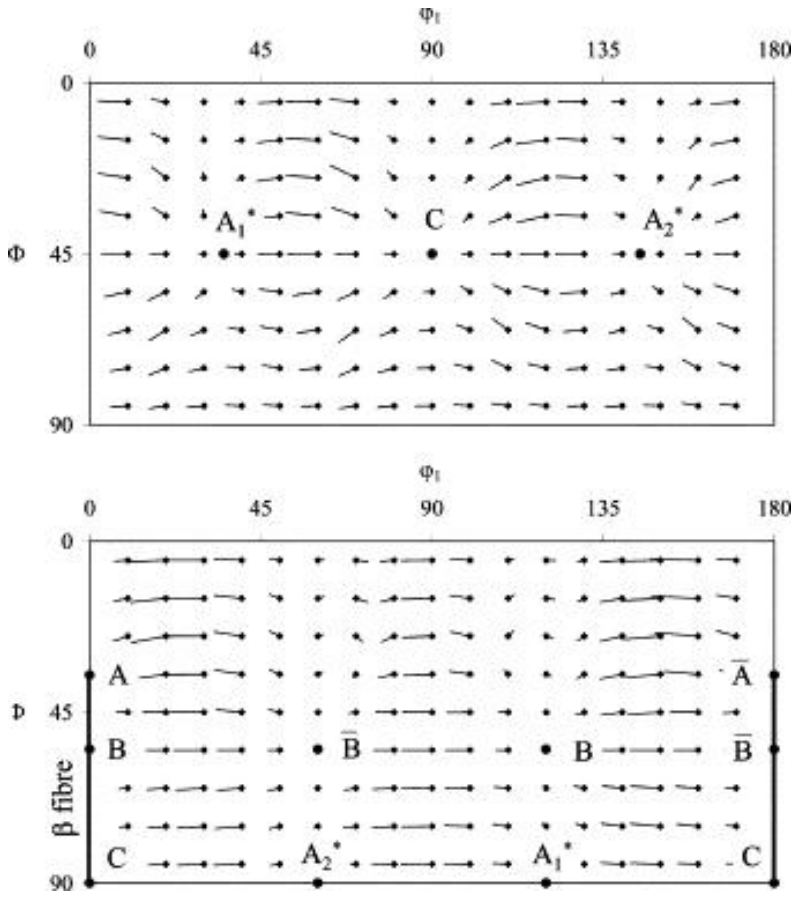

Figure 2.29 Rotation fields for fixed torsion of FCC material calculated using a full-constraint rate sensitive model (m =0.05) for {111} <110> slip. The plots are in the Bunge ODF notation for the Φ_2 = 0° and Φ_2 =45° sections [175] .

Wei et al. [176] developed a 3-dimensional crystal plasticity finite element method (CPEFM) model to study the texture evolution of the (100) nickel single crystal processed by HPT. As shown in Fig. 2.30, the simulation results were compared with related HPT experiments on (100) nickel single crystals undertaken by Hafok and Pippan [129]. It has been found that as the revolution angle of HPT deformation increased, a selected point at the edge of the sample surface with the initial C orientation transferred into the preferred A^*_1 component at the revolution angle of 60º around the torsion axis. In addition, the underlying mechanism of texture evolution in nickel single crystal during HPT was that the dominant slip and multi-slip accommodate the material deformation.

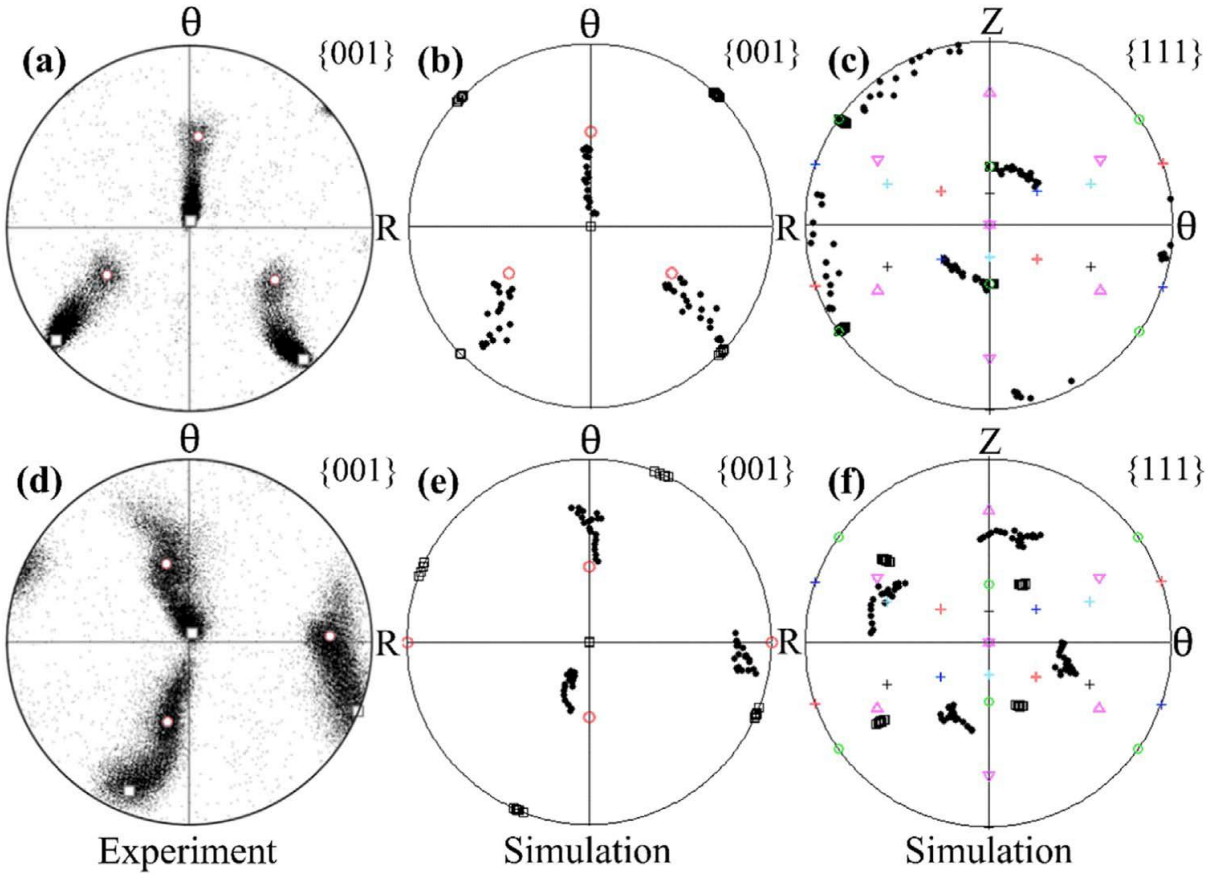

Figure 2.30 Comparisons of PFs between experiment and simulation of (001) nickel single crystal after HPT deformation of φ=30° (εeq≈1.5). Maps (a–c) and (d–f) are recorded after the same magnitude of plastic deformation but the initial crystallographic orientation changes [176].

Due to the high rigid body rotation rates of torsion, the high countervailing glide rotation rates are necessary for the texture stability during torsion. A number of studies investigated these effects on ideal orientation for various materials processed by torsion and HPT [145, 176-178].

The rate of the rotation of the crystallographic orientation during plastic deformation, which is defined as the lattice spin or lattice rotation rate, Ω*, is the difference between the rigid body spin (or rigid body rates), Ω, and plastic spin (or glide rotation rate), Ω^p. It follows that

$$\Omega^* = \Omega - \Omega^p$$

where Ω^p refers to the skew- symmetric part of the velocity gradient corresponding to plastic slip only.

For the velocity gradient, L, it follows that

$$L=D-\Omega$$

where D is the symmetric part of the velocity gradient L (called as strain rate tensor) and Ω is the skew-symmetric part of the velocity gradient L.

Ω^p involves the activation of slip systems and Ω* denotes the stability of texture, i.e. the ideal orientation, during deformation. Due to high Ω in HPT, in order to obtain stable texture, namely the minimum value of Ω*, high Ω^p requires to countervail the high Ω.

Wei et al. explored the influence of the factors of Ω*, Ω^p, Ω and D on ideal orientations of the <111> nickel single crystal after different HPT deformations [176]. As shown in Fig.2.31, it was revealed that in the nickel single crystal with the initial <111> plane parallel to the shear plane and $[11\bar{2}]$ parallel to the SD, there were 3 steady state stages, i.e. ideal orientations: A^*_2, C and A^*_1 and two transition stages between the steady state stages. During the steady state stages, the resolved shear strain rate (RSSR) magnitudes of the primary two slip systems were large, so that it generated the high Ω^p (Fig.2.31 c) to offset the high Ω (Fig. 2.31 b) at the same stages. Therefore, the corresponding Ω* was minimised at the 3 steady state stages (Fig. 2.31 d) causing the ideal orientations. On the other hand, appreciable lattice spins were detected at two transition stages. It should be noted that in Fig. 2.31 (d) the $\Omega^*_{\theta z}$, which stands for the rotation rate of the crystallographic orientation around the radial axis was dramatically higher than other two factors. The result indicates that the rotation of the crystal around the R axis played a more important role during HPT.

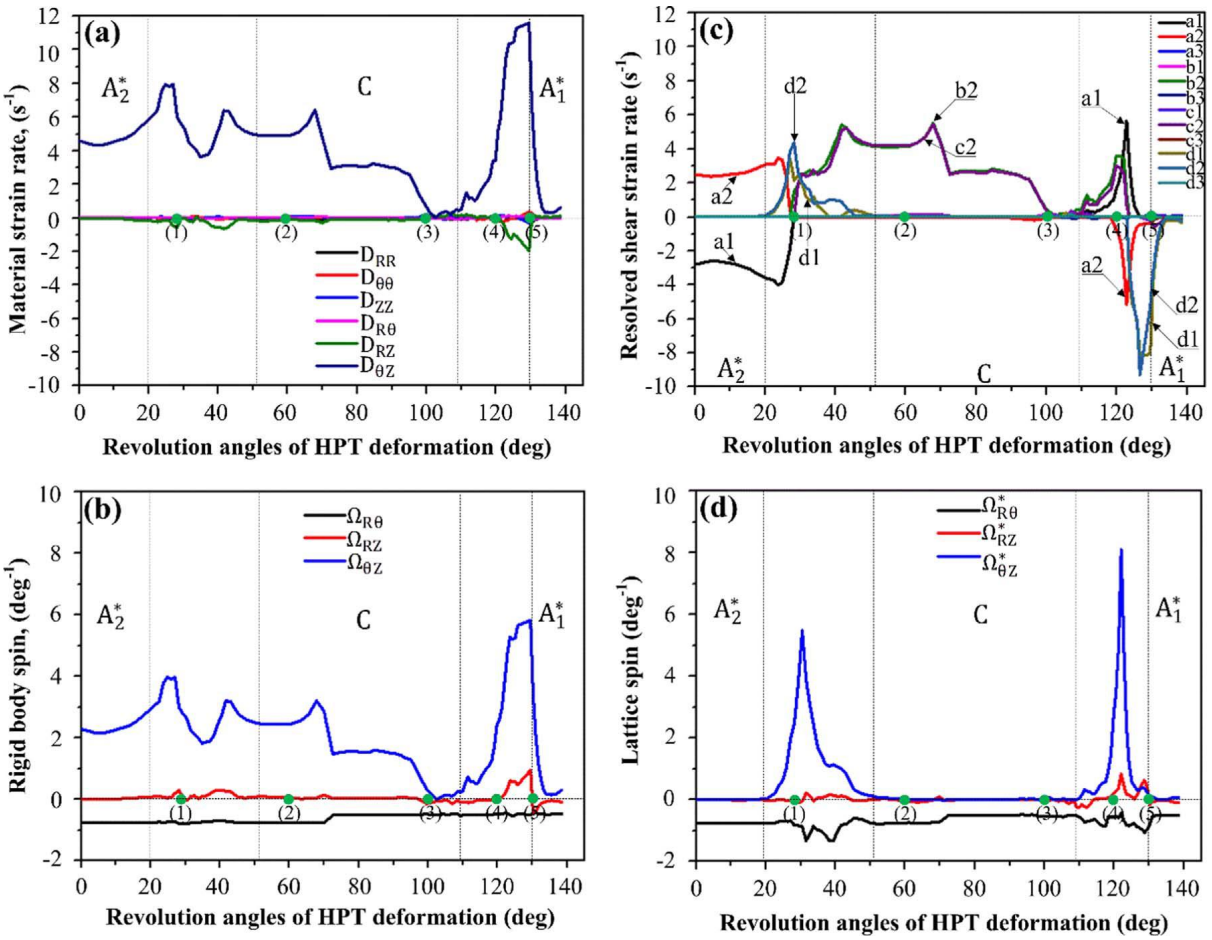

Figure 2.31 Results for the initial A*2 orientation of (111) nickel single crystal as functions of increasing revolution angles of HPT deformation: (a) material strain rate, (b) rigid body spin, (c)resolved shear strain rate, (d) lattice spin [176].

2.6 GB migration in materials processed by HPT

Conventionally, at room temperature, it is believed that the relationship between strength/ hardness and grain size in coarse-grained materials follows the Hall-Petch equation [1, 2]. This relationship is based on the fact that the grain boundaries act as barriers to prevent the dislocations from moving continuously, impeding the onset of plastic deformation， and hence enhance the strength/hardness of the materials. As demonstrated in Fig. 2.32, at Stage 1 finer grains accompanied with higher density of grain boundaries makes plastic deformation more difficult, thereby higher strength/hardness is acquired.

As shown in Fig. 2.32, when the grain size drops below the value in the range of Stage 3, softening has been observed in experiments for some alloys [179-181]. This indicates that the classic Hall-Petch relationship based on the dislocation-driven plasticity needs to be

reconsidered when the grain size decreases below a certain value. This is called “Inverse” Hall-Petch or Hall–Petch breakdown behaviour. The calculations by Chen et al. demonstrated the critical grain size for Ni was located in the range of ~11 to 22 nm [182]. Most previous studies believed that grain boundary (GB) mediated processes, such as GB migration, GB sliding, GB rotation or GB diffusion, might be responsible for this material softening behaviour [183-186]. Dislocation sources and pile-ups are hardly to be expected in the individual grain size, because of the limited grain size and higher density of GBs [181] in the nc materials. For instance, in a material with the average grain size of about 20 nm, 10% atoms are located at GBs [183]. Besides, large excess grain boundary energy in nc metals is able to cause instability in their internal structure, which would facilitate the grain boundary movement [187]. Therefore, in plastic deformation the GB mediated processes rather than the dislocation slip play a dominant role in nc with the grain size less than 10nm [188-190].

Between Stage 1 and Stage 3, there is a crossover regime where the grain size is in the range of 10 nm- 1μm, called Stage 2. In the plastic deformation at Stage 2, the volume fraction of GBs increases significantly and the effect of the dislocations gradually becomes weaker, whereas the GB mediated process becomes increasingly more important. At this stage, the homogeneous nucleation of the intragranular dislocation is hindered and the plastic deformation progressively falls short of the Hall-Petch relationship due to the heterogeneous nucleation and emission of dislocations from the GBs [191]. The partial dislocations emits, then the partial dislocations traverse the grain and are absorbed into the opposite grain boundary without multiplying or interacting with other dislocations [182, 192, 193].

As the grain size decreases, the plastic deformation mechanism is transited from the dislocation based mechanism to the GB based mechanism. However, there is no clear boundary between them. Dislocation activities were still detected in nanomaterials by experiments and molecular dynamics (MD) simulations with the grain sizes as small as 3-5 nm [188, 194]. This is because the GBs can act as the dislocation sources in nc materials [195-198].

The plastic deformation mechanisms that govern the grain mediated processes are still controversial. In order to clarify the ambiguity, various explanations have been proposed. Among them, DIGM, GB rotation induced GB migration and stress induced GB migration are the most promising mechanisms.

Grain rotation during SPD is considered as one of important GB mediated processes at the crossover stage (Stage 2) observed in nc materials [199, 200]. The phenomenon of discontinuous

grain growth seems to be related to grain rotation, i.e. grain rotation induced-grain coalescence and growth. In order to reveal this mechanism in detail, a series of MD simulations [200-202] and experiments [203-206] were carried out.

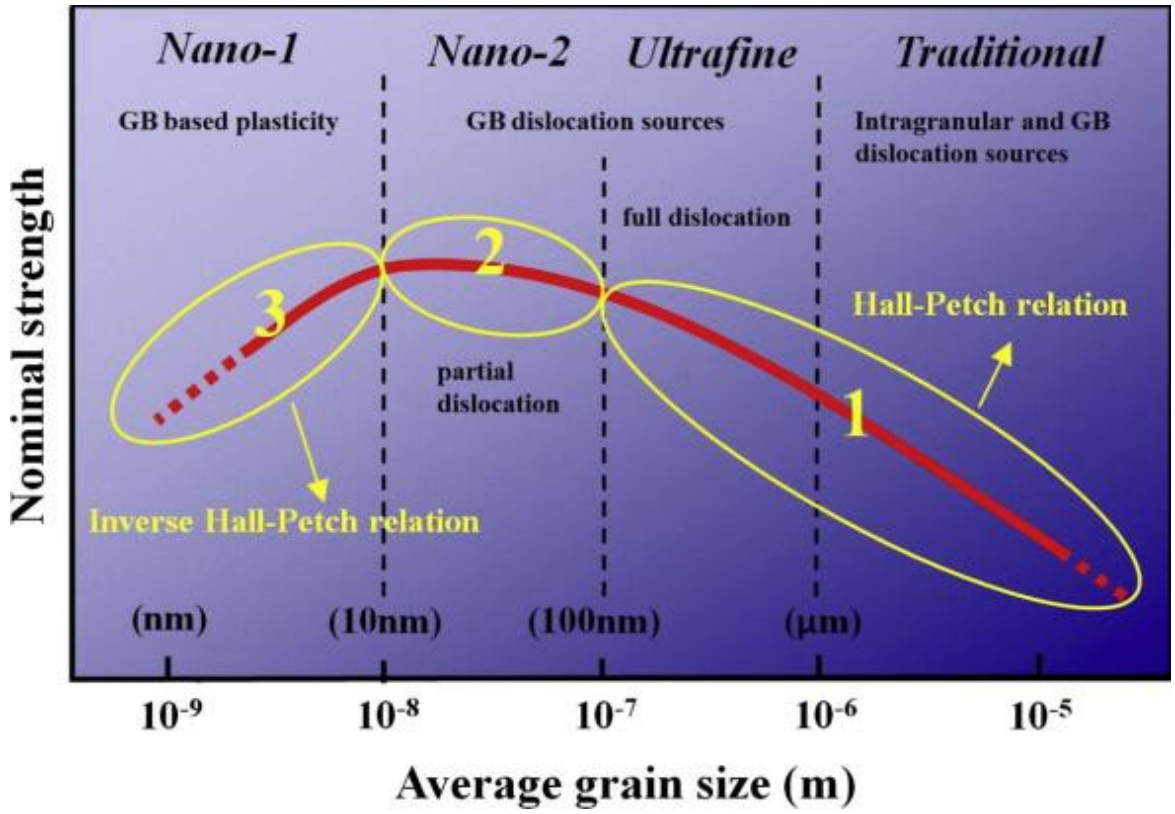

Figure 2.32 A mechanism map for deformation behaviour showing the nominal changes in the underlying mechanisms of plasticity at different grain sizes [191].

Obvious grain rotation was detected first in the experiment where the nc nickel films with the mean grain size of 9.7 nm deformed by in situ TEM tensile straining was studied at room temperature [181]. Evidence of individual grain growth and rotation with global rotation of the specimen was extracted from dynamic images (as shown in Fig. 2.33). In this study, it is assumed that the driving force of grain rotation is the energy from the misorientation of neighbouring grains and the grain rotation is achieved by mean of diffusion.

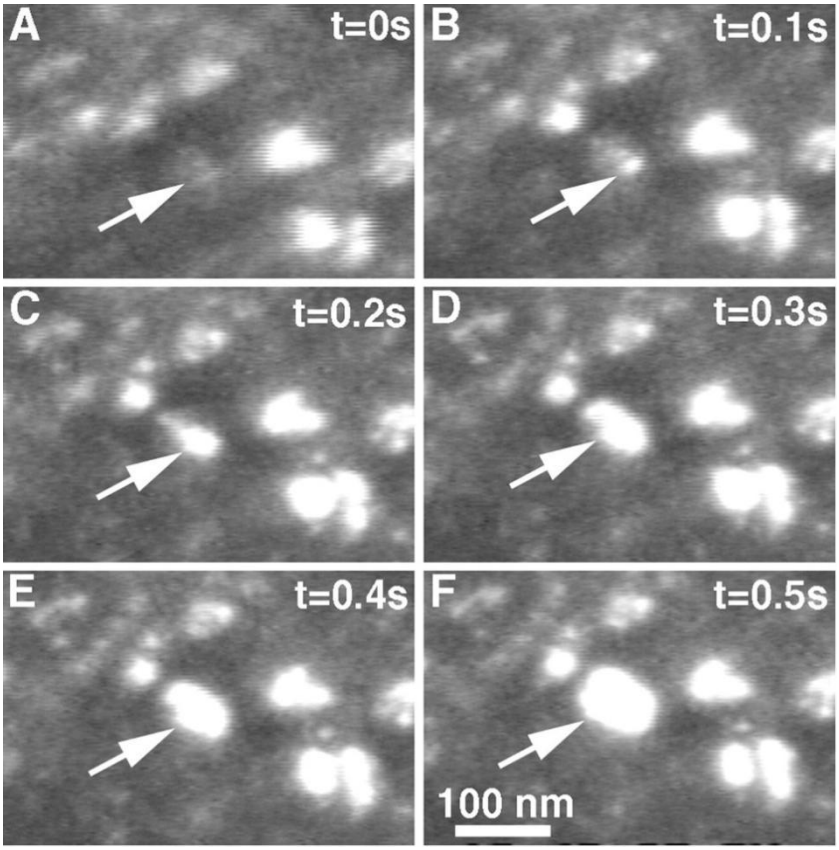

Figure 2.33 DFTEM observation of the rapid genesis of an agglomerate (e.g., white arrow) depicted by individual still frames extracted from a dynamic video sequence. (A) At t = 0 s, no grains in the strong diffraction condition are near the white arrow. (B) At t = 0.1 s, a grain in the strong diffraction condition with a size of about 6 nm is visible. (C) At t = 0.2 s, a group of grains in bright contrast with a size of about 28 nm is visible. (D) At t = 0.3 s, the group of grains has a nearly elliptical shape, with dimensions of 60 by 35 nm. (E) At t = 0.4 s and (F) t = 0.5 s, the size of the group of grains increases to maximum dimensions of about 80 by 60 nm [181].

Similar grain rotation during deformation was observed in an in situ experiment [204]. Electrodeposited nc Ni deformed by nanoidentation was deformed under tensile strain. During the deformation process, the average grain size increased from the initial 20 nm to 35nm. Noteworthy, the direct evidence of grain rotation was found in the experiment. Further inspection by high-resolution transmission electron microscopy (HRTEM) revealed that there were many sub-structures inside the selected grain, which indicated the large grain was generated by the coalescence of several neighbouring grains. Actually the grain rotation may decrease the GBs angles or lower the total GB energy in the system, thus relaxing the stress concentration. However, in contrast to the experiment conducted by Shan et al., the driving force is attributed to applied stress and the grain rotation in this experiment is approached by GB dislocation gliding.

The mechanism is schematically illustrated in Fig 2.34. The dislocations gliding along the GB introduces a relative shear between Grains 1 and 2, and then the gliding GB dislocation is split at the triple junction into two climbing GB dislocations. The rotation of Grain 3 is induced by the GB dislocation climbing. Hence the rotational deformation in Grain 3 can be effectively initiated by the preceding GB sliding. Finally the rotations of adjacent grains bring their orientations closer, resulting in the elimination of high angle GBs and the coalescence of nano-grains into larger grains.

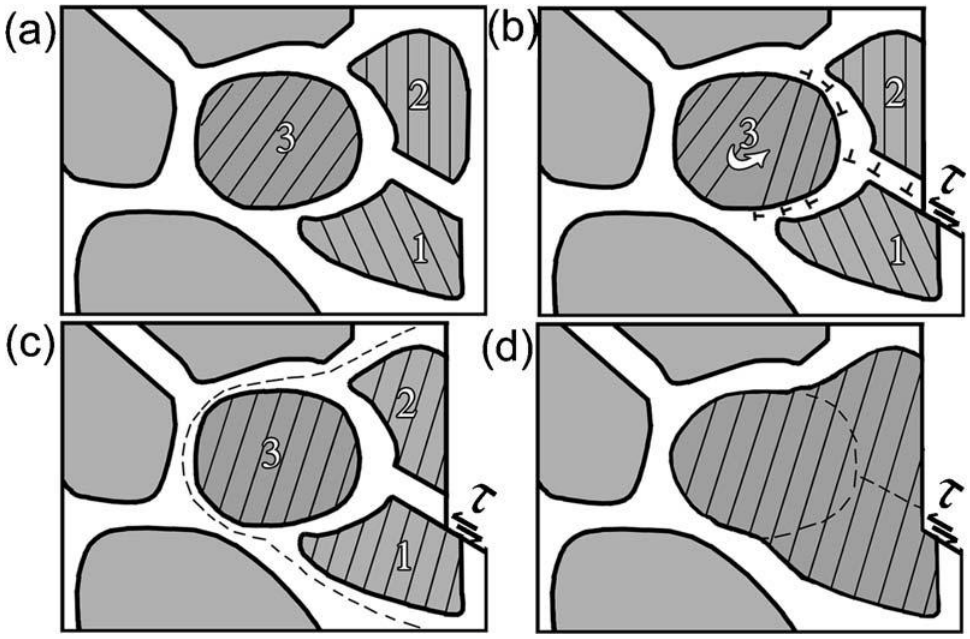

Figure 2.34 Proposed deformation mechanisms of nc materials: GB sliding transforms into crystal lattice rotation in neighbouring grain [204]. (a) Before plastic deformation, the nc Ni possessed high angle GBs. (b) Shear of two nc grains 1 and 2 by gliding GB dislocations, and subsequent occurrence of the crystal lattice rotation in the neighbouring nc grain 3 by climbing GB dislocations. (c) Multiple grain rotations leading to grain agglomerate. (d) A large grain formed with sub-GBs (highlighted by dotted line) due to incomplete grain coalescence.

Gutkin et al. [200] conducted the calculations on the energy characteristics of the splitting. It has been found that the splitting is energetically favourable in certain ranges of parameters of the system. Besides the dislocations are absorbed by GBs, climbs of GB dislocations caused by the splitting of gliding GB dislocations at triple junctions are also enhanced

GB movement includes GB migration, GB sliding and GB motion. The GB migration is referred to as GB movement towards its normal direction. GB sliding is considered as GB relative translation along the curve of GB. GB motion is the combination of the GB migration

and sliding. As an important GB mediated process, GB movement have been detected in a series of experiments.

It has been extensively observed that GB migration generally is associated with an external shear stress. Therefore this phenomenon is also called the stress-induced GB migration. The coupling effect means GB migration would be accompanied by the tangential translation of grains, which induces the shear deformation. Conversely, the shear stresses imposed on GBs can induce their migration. As shown in Fig. 2.35 [207], during the GB migration process the GB velocity v_n is parallel to the GB normal vector and perpendicular to the relative grain translation velocity $v_{//}$. The coupling effect is able to be characterised by a coupling factor β, i.e. $v_{||} = \beta v_n + \upsilon_s(\tau)$. This equation suggests that β is a geometric factor only depending on the misorientation angle θ between two grains [208]. Noteworthy, GB migration is not the only possible response of GB to the applied stress [209]. When β=0, GB motion is completely converted to the GB sliding. Particularly at high temperature, the response mode of GB to shear changes from GB migration to GB sliding as the temperature increases [207].

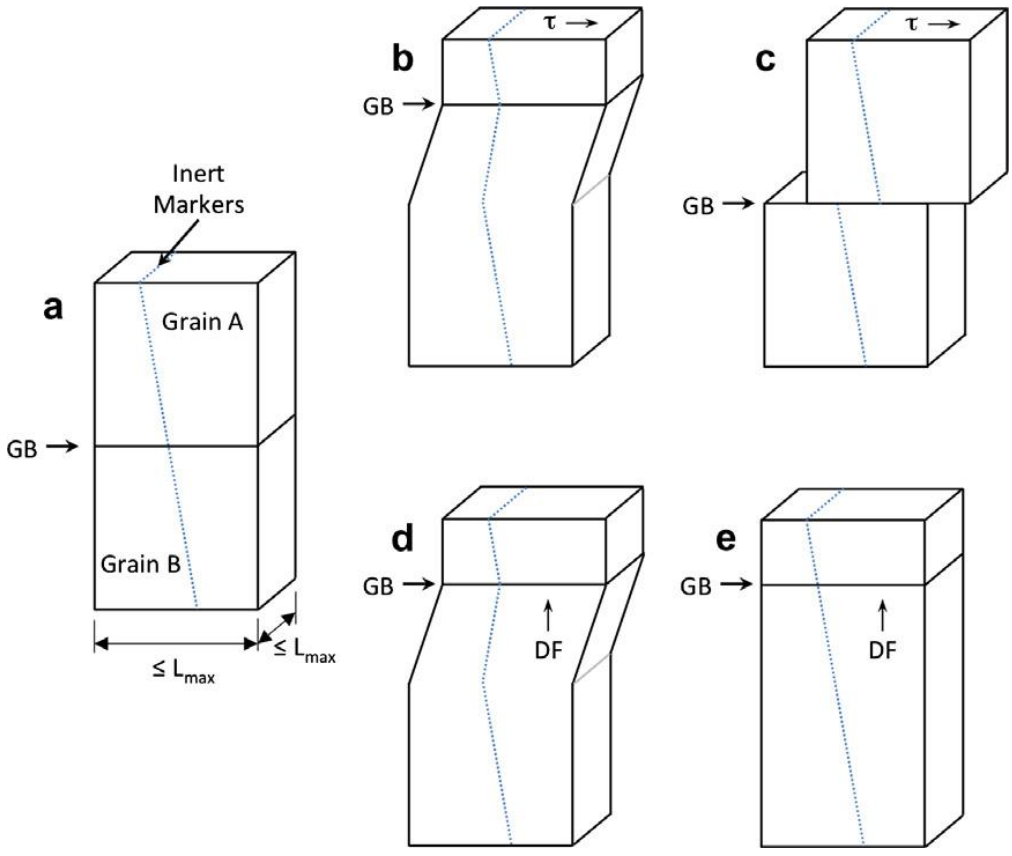

Figure 2.35 Illustration of the mechanical response of (a) a bicrystal with inert markers. Applied tractions can result in (b) shear-coupled migration of the boundary in the bicrystal or (c) sliding at the

boundary with no boundary migration normal to the interface. A driving force applied normal to the boundary can result in (d) shear-coupled migration of the boundary in the bicrystal or (e) migration of the boundary normal to the interface without any lateral motion [210].

In order to explore the potential mechanism responsible for the stress-induced GB migration, bicrystals with different symmetrically tilted grain boundaries were used in the experiments [209, 211-214] and then distinct GB migrations were observed. Winning and his colleagues found that GB migration occurred at the symmetrical tilt <112> and <111> planar boundaries [214, 215], <112> and <111> planar boundary [215], and <100> curved boundary [216] under external shear stress. The velocity of GB migration can be expressed by

$$\upsilon = m_0(c,\theta)exp\left\{-\frac{\Delta H(c,\theta)}{kT}\right\}\mathrm{p}$$

where ΔH is the activation enthalpy for the GB motion, c is chemical composition (concentration of impurities), θ is the angle of misorientation, T is the temperature and p is the driving force.

There is a transition between the activation enthalpy of LAGBs and HAGBs at a certain angle. For the symmetrical tilt <112>、<111> planar and <112> curved boundaries, the activation enthalpies close to the self-diffusion enthalpy at LAGBs and for HAGBs the activation enthalpies close to the GB diffusion enthalpy. On the other hand, for the <100> [216] and <111> [215] high angle curved GBs, their activation enthalpies are completely different. Strong dependence of the activation enthalpy on the misorietntation angle was found, which might be due to a strong misorientation dependence of the GB diffusion coefficient, i.e. activation enthalpy of GB diffusion.

It was generally believed that GB migration is driven by differences of free energy across the boundary, which results from stored energy, boundary curvature or anisotropy of physical properties such as magnetic susceptibility.

GB migration under an external shear stress involves a bulk diffusion process, i.e. the driving force on dislocation climbing is given rise by diffusion. In order to maintain the given boundary geometry, the dislocations climb with GB migration. These results are consistent with a mechanism called diffusion-induced GB migration (DIGM) proposed by Balluffi and Cahn [145, 217-220].

As illustrated in Fig. 2.36, the differences in the diffusion coefficients of the diffusing species

along the grain boundary cause a self-sustaining climb of grain boundary dislocations and motion of their associated grain boundary steps [221].

Noteworthy, the diffusion based mechanism is temperature-dependent because atoms become more active at higher temperature. In this mechanism, diffusion is given rise by variance of free energy caused by solute concentration, non-uniform stress states or GB surface tension on either side of GB. Extensive studies were carried out on the mobility of GBs [214, 215, 222]. It has been found that GB motion occured by a thermally activated process, promoted by an applied stress, with an energy of migration that was very close to that of either GB or bulk self-diffusion. The mobility of GBs adheres to a thermally activated equation

$$\mathrm{m} = \mathrm{m}_0 e^{(-E_m/kT)}$$

where m is the GB mobility, m_0 is the pre-exponential factor and E_m the activation energy for GB migration.

However, according to the calculation by Brechet [220], GB motion initiated by DIGM seems to occur when the initial grain size is small. The temperature dependence of this process is expected to be relatively weak. This is because two temperature dependent factors act in opposite directions and their influences are cancelled out somewhat by each other.

It is noteworthy that the dominant mechanisms during the GB migration should not be exclusive. In the experiment taken by Mompiou et al. [223], all velocities of GB motion were measured. It was found that the migration of GBs with more curvature was faster. This result indicated that GB migrations driven by the shear stress and capillarity forces were both active.

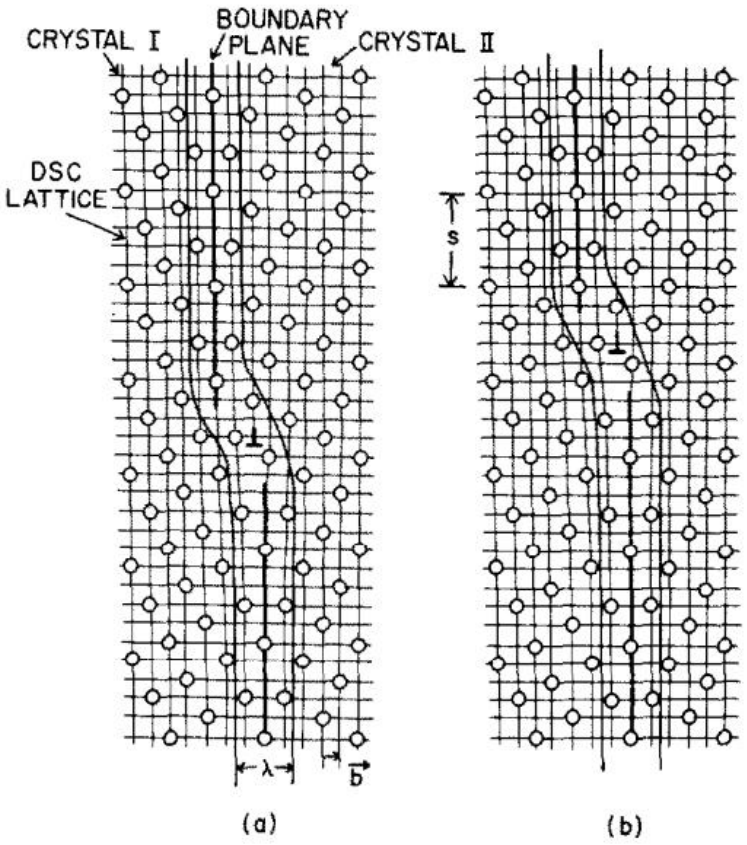

Figure 2.36 Climb of GBD in symmetric tilt boundary in simple cubic structure. Tilt angle = 36.9°; b = Burgers vector; 2, = grain boundary core width. (a) Initial structure. (b) GBD after climb by annihilation of a vacancy [221].

However, very fast grain growth or GB motion, which were orders of magnitude above the average velocities predicted by DIGM, have been detected in many studies [192, 223]. This suggests the diffusion-based mechanism might be not applicable in some conditions.

Rapid stress-driven grain coarsening in nc Cu at room temperature (RT) and cryogenic temperature (CT) was observed by Zhang and Weertmana [224]. As shown in Fig 2.37, the nc high pure Cu with the average grain size of ~20 nm was processed by microhardness indenter under RT and CT with different dwell times. It was found that the grain coarsening was faster at CT than that in at RT, which suggests that the predominant mechanism of grain growth was the stress-induced grain growth rather than one driven by diffusion. Legros and coworkers measured the velocities of GB by in-situ TEM observations under tensile testing [192]. The results demonstrated that the values of GB velocities were greater than the values which were able to be explained by diffusive processes. Besides, according to the diffusion based mechanism, the higher the density of dislocations the lower the GB migration rate is, and the

migration rate should be independent of the misorientation angle. However, the experiment conducted by Gorkaya et al. was not in agreement with the diffusion based mechanism [209].

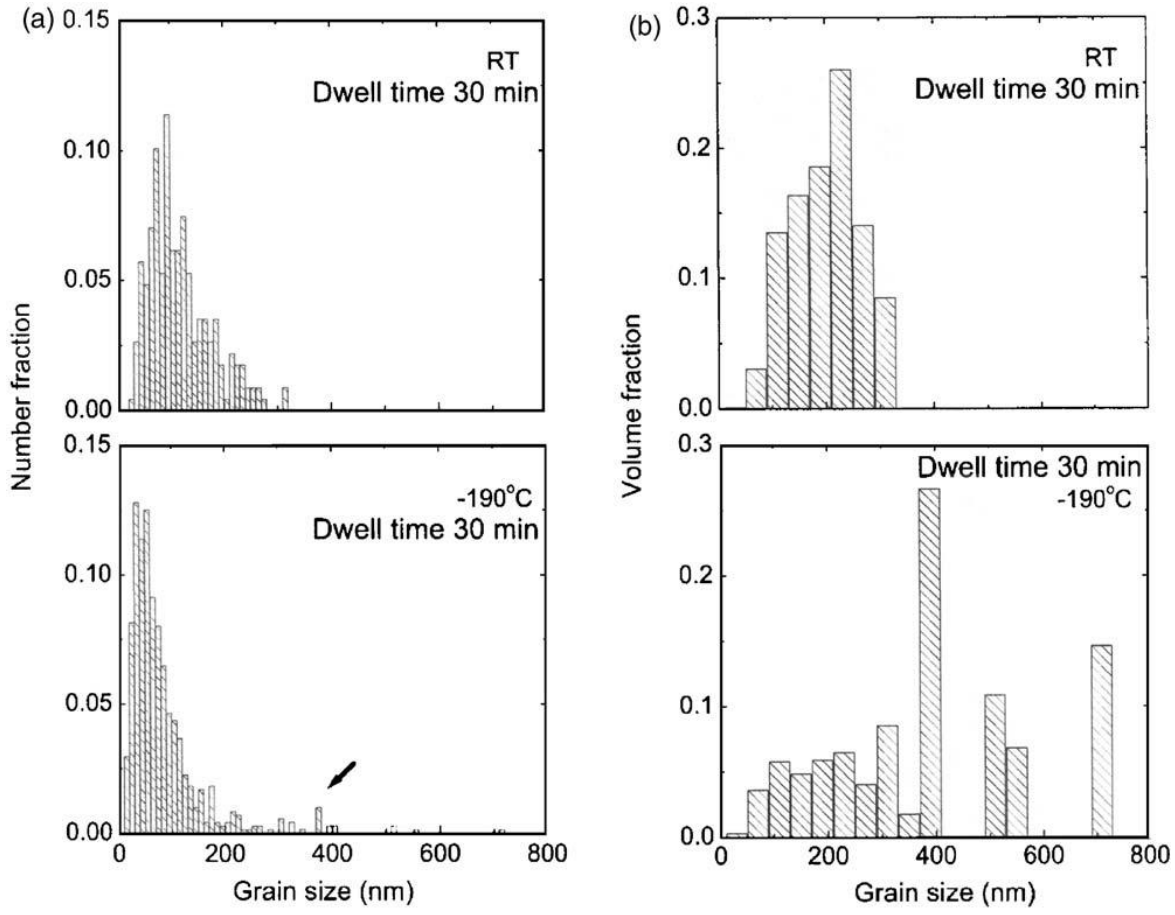

Figure 2.37 A comparison of (a) number fraction and (b) volume fraction grain-size distributions after 30min30min of indenter dwell time for indents made at RT and −190°C. The same sample as in Figs. 1 and 2. The arrow in (a) indicates the presence of the large grains after 30min dwell time at the low temperature. The presence of large grains is more evident in the volume distribution [224].

In a HPT experiment, the grain growth has been observed in the vicinity of the periphery of the HPT disc [225]. It was concluded that the grain growth was due to the GB diffusion caused by heating which was generated by friction between the upper and lower anvils during the intense torsional straining [226]. The high rotation speed in HPT could prevent heat from being conducted away effectively, subsequently resulting in a significant rise in temperature. However, the rotation speed was not mentioned [226]. The experimental results reported in Ref.[227] suggested that when the rotational speed was 1rpm, any heat generated during torsion could be quickly conducted away into the massive HPT anvils, and heat effect in the sample was negligible. This conclusion was supported by another HPT experimental measurement in which the temperature of the sample during HPT was lower than 40 ℃ [225]。

Another mechanism responsible for the GB migration induced by the shear stress is that the shear stress induced a coupling force on the dislocations; subsequently the movement of dislocations causes GB migration. This mechanism was extensively studied by experiments [209, 228] and atomistic simulations [207, 213, 229-231] for both low angle GBs and high angle GBs [211, 232]. The GB migration is caused by collective glide of edge dislocations which constitute the GB. The direction of the glide is perpendicular to the GB plane. The Peach- Koehler force, i.e. $F = (\sigma \cdot b) \times s$, imposed by the shear stress, results in a force on each edge dislocation and thus gives rise to a driving force, i.e. $p = \tau \sin\theta$, for the GB migration in the direction of the dislocation motion. The mobility of GB is determined as a relation between the GB migration rate υ and the driving force p: $m=\upsilon/p$ (Fig 2.38).

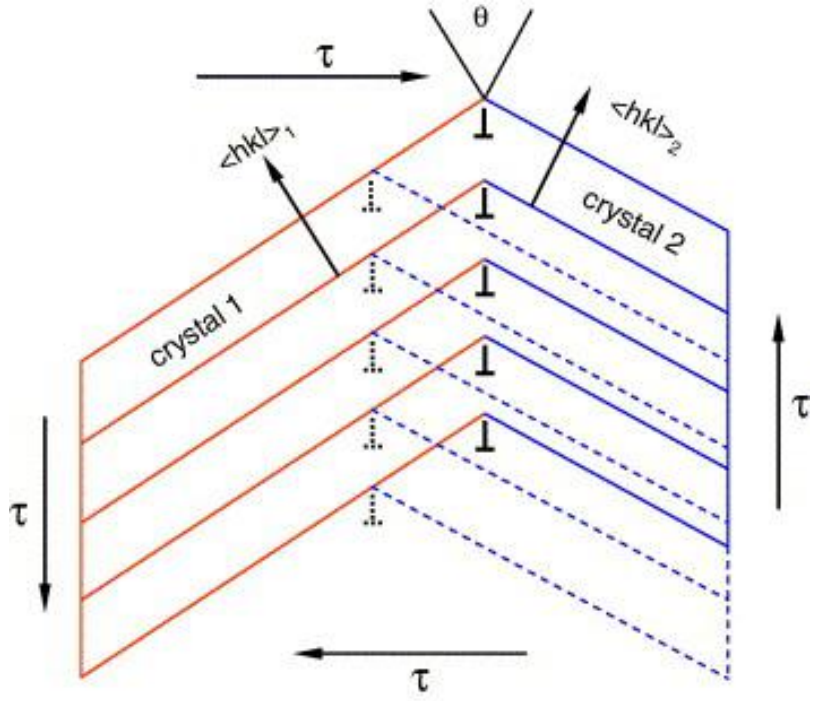

Figure 2.38 Bicrystal with a low angle symmetrical tilt grain boundary. Edge dislocations which compose the boundary move and produce a shear when subjected to a shear stress s. Dashed lines show crystal 2 before the loading [211].

According to this mechanism, the stress, not the strain, plays an important role in the GB migration [233]. In addition, the GB motion is no longer dependent on diffusion. Fast velocity of the GB motion which cannot be explained by the diffusion mechanism is allowed in this mechanism, especially under the shear applied at room temperature, i.e. athermal shear.

Observation using TEM is the most important experimental method to study the microstructure of the nanoscale materials. However the preparation of the TEM samples are

extremely difficult because the thickness of the TEM sample should be reduced to the order of the grain size, which might cause the GB structure to relax and change. Therefore, the numerical simulation is the best way to study the atomic-scaled GB mediated processes.

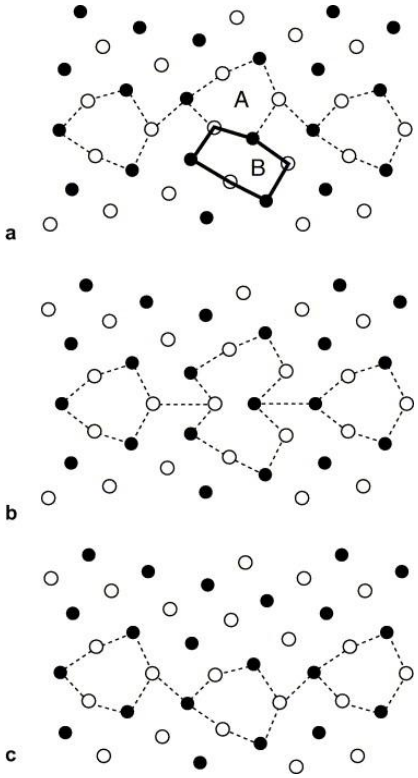

Figure 2.39 Atomic mechanism of coupled motion of the R17 (530) GB. (a) Initial state; (b) transition state; (c) final state. B is the lattice structural unit converting to the GB unit A [207].

The MD simulations of [001] symmetrical tilt GBs in copper were carried out by Cahn et al. [207, 208]. It was revealed that there were two atomic mechanisms of the shear-induced grain boundary migration, i.e. <110> mode and <100> mode. In Fig. 2.39, a typical <110> mode is demonstrated for a zigzag Σ 17(530) GB. Atoms are represented by white and black circles which are in different position depths. Fig 2.39 (a) shows the initial state. It should be noted that every GB A unit is adjacent to a B structure unit. The two units could be mutually transformed by slight atomic displacements. When this transformation occurs in each A unit, the whole GB moves one step downwards. Another mechanism of the GB migration in Ref. [207] is the <100> mode, as demonstrated in Fig. 2.40. Taking Σ 37 (610) GB as an example, in-plane and out-of-plane atomic displacements could bring atoms up or down, so that A-Unit is able to transform to C-Unit.

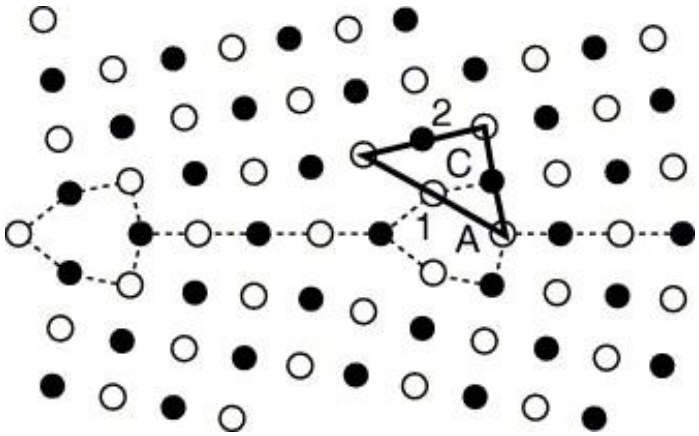

Figure 2.40 Atomic mechanism of coupled motion of the R37 (610) GB. C is the lattice structural unit converting to the GB unit A. 1 and 2 are atomic rows normal to the viewer discussed in the text [207].

The coupling factor predicted by the model was consistent with the measurements [211]. However the model is only applicable to the tilt symmetrical GBs. The extension of the model to non-symmetrical boundaries is possible but difficult. In addition, such transformations are unlikely to occur simultaneously in all units over a large GB area.

In real polycrystalline materials, GBs are not only pure twisted or tilted. In order to explore more general mechanism which is able to extend to the GBs without any specific orientation relationships, a geometrical model applicable to many ordinary GBs was proposed by Caillard et al. [234]. As shown in Fig. 2.41, external shape of Grain A is able to transform into Grain B by a rotation, followed by a shear deformation. This model suggests that a local reorganisation of small groups of atoms without long-range diffusion possibly occurs during the GB migration. The applicability of this model is extended from particular GBs to non-symmetrical and non-coincidence orientation relationship boundaries.

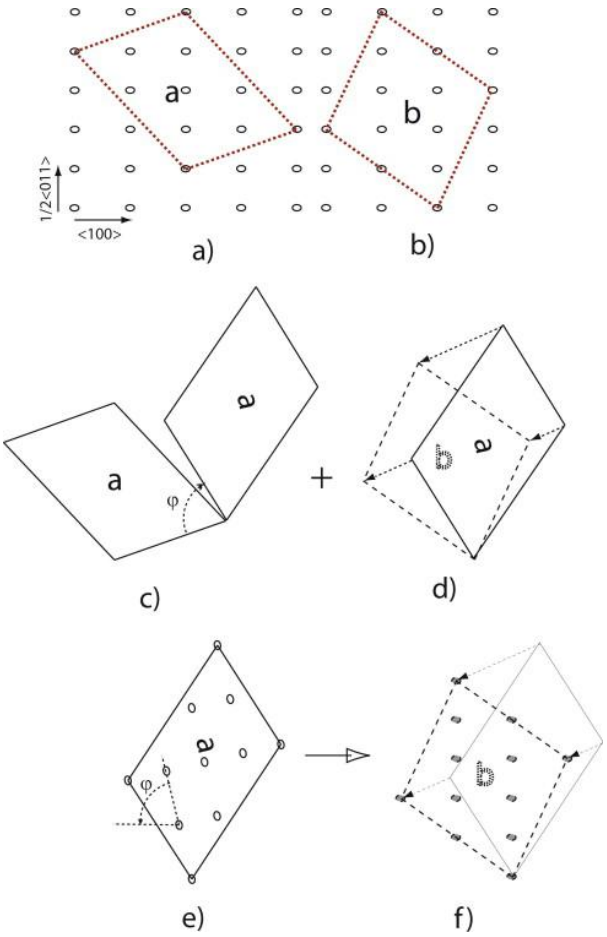

Figure 2.41 Description of the method used to determine shear–migration coupling mechanisms for general boundaries. (a and b) Selection of two parallelograms containing the same number of atoms. (c and d) Transformation of a into b, by a rotation of angle φ, and a shear. (e and f) Transformation of a group of atoms into another one by the same shear, accommodated by a shuffling rotating the lattice by the same angle φ [234].

A number of experiments were undertaken using polycrystalline materials deformed by indentation [203, 224], uniaxial loading [235, 236], tensile [204, 237] and HPT [225-227, 238]. Nc Al has been strained in an in-situ TEM at RT. Extensive GB migrations and grain growth occurred by the displacement of the oppositely facing boundaries of Grains A and B. The observations confirmed that the grain growth preceded the dislocation activity, and that the microscale dislocation activities were possible in the grains that had sufficiently grown. In addition, the rapid GB motion occurred during a non-straining period. Therefore the reason for the GB motion could be attributed to the stress-induced mechanism.

Most of the GB mediated processes in polycrystalline materials were observed in plastic deformation induced by indentation and tensile test. As HPT is a process that could produce

high stress, the GB mediated process is expected to occur in HPT.

As shown in Fig. 2.42, the HPT experiments were conducted by Liao et al. using electrodeposited (ED) Ni film. 5 HPT revolutions were applied to the sample under the pressure of 7 GPa at RT. Significant grain growth was observed and the average grain size of nc Ni sample grew from about 30 nm to 129 nm. As shown in PFs generated by XRD, the random texture in ED+HPT Ni was different to the duplex <111>/<001> texture in nc Ni produced by HPT from CG Ni. The difference indicates that the GB mediated processes play an important role in the deformation mechanism of ED+HPT Ni [227].

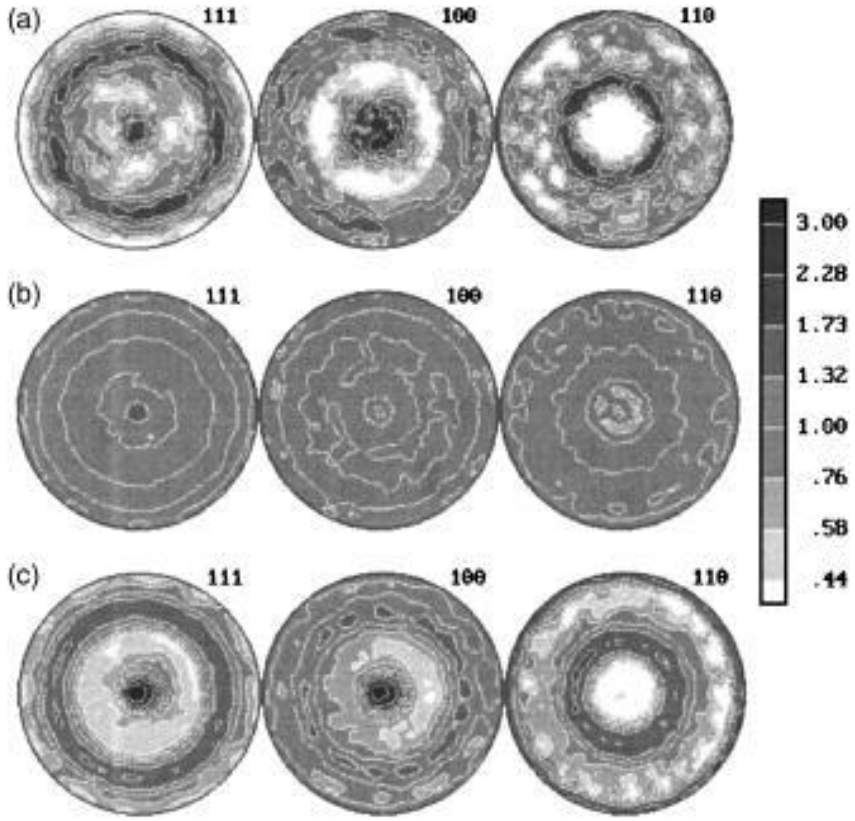

Figure 2.42 The texture of (a) as-electrodeposited nc Ni, (b) electrodeposition+HPT Ni, and (c) nc Ni produced by HPT processing of CG Ni. Equal-area projection pole figures displayed with normal direction aligned with either growth direction (a) or HPT compression axis [(b) and (c)] [227].

As described above, the grain rotation induced grain coalescence and the stress-coupled GB migration are two important mechanisms responsible for the GB mediated process. However, despite extensive studies having been performed, which mechanism plays a more important role in SPD, such as HPT, remains an open question.

Wen et al. summarised the previous studies in an effort to clarify which mechanisms govern

the plastic deformation [225]. The conclusion uncovered that the mechanisms governing the plastic deformation are grain size dependent. For the grains with size smaller than 100 nm, grain coalescence and growth is primarily due to the grain rotation induced grain coalescence, whereas the mechanism of the stress induced GB migration dominates for the grain sizes larger than 100 nm. The similar observation is found in the study by Wang [205].

However, the conclusion did not imply the two plastic mechanisms are mutually exclusive in nano and ultrafine grain size, especially the grain size is of the order of 100 nm. For instance, the observation in the preceding study [223] showed obvious GB migration in Grains A and B whose grain size is about 150 nm, while the grain rotation is demonstrated in the same study, as shown in Fig 2.43. The grain sizes of Grains A and B were slightly larger than 100 nm. In the in-situ TEM experiment the grain growth was observed to occur at very different rates, which indicated that the different mechanisms were active during the process [192].

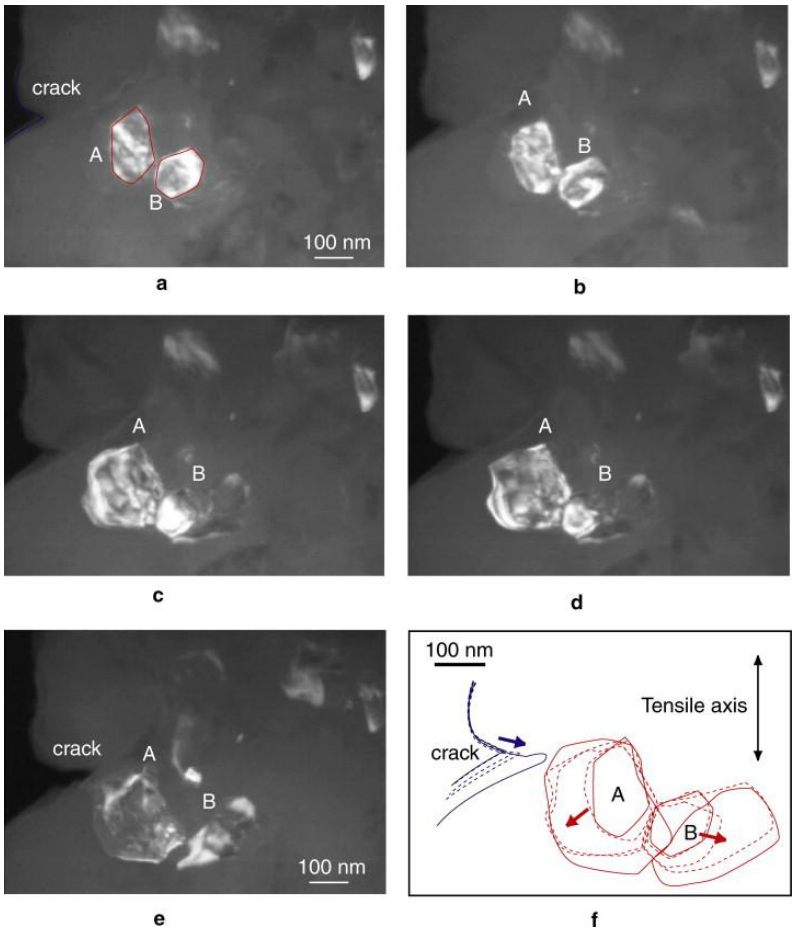

Figure 2.43 Growth by re-orientation and coalescence of grains. (a) t = 0 s (b) 6 s, (c) 20 s, (d) 22 s, (e) 49 s, and (f) sketch of the grain shape evolution from (a) to (e) [192].

Chapter 3 Experiment and equipment

3.1 Sample processing

3.1.1 Polycrystalline Aluminium specimen

One of the materials used in the present work was commercial purity (CP) aluminium containing Al of 99.9 wt% purity, and was in the form of the extruded rod with the diameter of 15 mm. The diameter of the extruded rod was reduced to 10 mm using lathing. Then the lathed rod was cut into discs with the thickness of 1.5 mm via wire cutting. These discs were pre-annealed at a temperature of 300℃ for 2 hrs in atmosphere, followed by air-cooling. The average grain size after annealing was ~11 μm.

3.1.2 Single crystal Aluminium specimen

The single crystal Al of 99.9999 wt% purity with a crystallographic orientation <001> parallel to the cylinder axis was employed in the present study. These single crystal specimens were purchased from MaTeck, Germany. In order to identify the location of initial crystallographic orientation after HPT deformation, one of the <001> directions was marked by a small notch on the side of discs as shown in Fig. 3.1 (a). The diameter of the single crystal Al disc was 10mm. and the thickness of the disc was 1.5 mm for the one layer HPT experiments, and 0.75 mm for the two layer stacked HPT experiments, respectively. In the case of two layer stacked HPT experiments, the two contact surfaces were polished gently by stainless steel wire brush to remove the oxide layer. The HPT processed specimen is shown Fig. 3.1 (b).

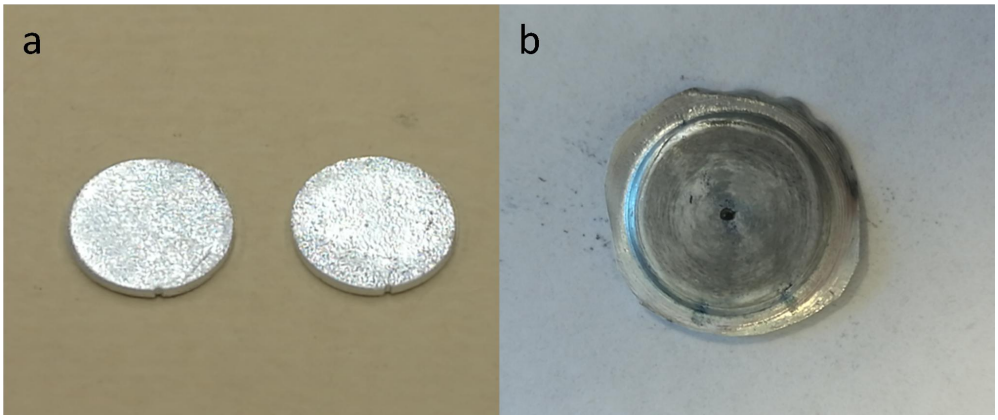

Figure 3.1 (a) as-received single crystal specimens and (b) HPT processed specimen

3.1.3 HPT processing

The disc-shaped samples were processed by HPT under a pressure of ~6.16 GPa at room temperature. In order to cover a wide range of applied shear strain, 9 different revolutions were conducted: 15° (1/16 turn), 30° (1/16 turn), 45°(1/8 turn), 90° (1/4 turn), 180° (1/2 turn), 360° (1 turn), 720°(2 turns), 1080° (3 turns), 1800° (5 turns).

The HPT machine used in the present study is shown in Fig. 3.2. In the experiments, the upper anvil was fixed and the lower anvil was rotated monotonously at a speed of 0.5 rpm. The low rotational speed was able to minimise the heat effect resulting from the friction between the upper and lower anvils and between the anvils and samples. It should be noted that although the HPT was undertaken under the so-called constrained conditions, some materials flowed out from the gaps between the two anvils, as shown in Fig. 3.1 (b). This is because the thickness of the specimen was slightly higher than the depth of the die cavity and the gap between two anvils was not fully close.

Figure 3.2 Photo of constrained HPT machine.

3.2 Hardness tests

Vickers hardness measurements were undertaken by a Struers Emco-Test DuraScan-70 equipped with a Vickers indenter, as shown in Fig. 3.3. Before the measurement, the tested disc surface was polished to a mirror-like surface. The small load of 0.025 kg was applied in the present study because Al is a soft metal. Hardness was tested along the diameter of the disc with a step of 0.5 mm from one edge to another edge. The 19 sets of points were selected to measure the hardness.

Figure 3.3 Photo of Struers Emco-Test DuraScan-70

3.3 Microstructure characterisation

3.3.1 Sample preparation for EBSD observation

The samples for the EBSD observations were mounted in particular sample holders. The sample polishing process consisted of grinding using 500#, 800#, 1200#, 4000# silicon foils, MD-Mol with abrasive of 3μm DiaPro suspensions and MD-Chem foils with 50% OPS step by step, according to the standards provided by Struer for pure aluminium.

It is necessary to conduct electrolytic polishing before EBSD (Electron Back-Scattered Diffraction) measurements to obtain the mirror-like surface. The electrolytic polishing were undertaken under the temperature of 9°C ~15°C. Other parameters such as voltage, flow rate

and processing time varied depending on the deformation degree of the specimens. For the specimens deformed by low shear strains (less than 1 turn), the voltage of 25V, the flow rate of 15 and the time duration of 60s were chosen as the parameters for the electrolytic polishing. For the specimens subjected high level shear strains (1 turn and more), the voltage of 20V, the flow rate of 13 and the time duration of 20-30s were used to obtain good quality surface.

3.3.2 EBSD observation

The characteristics of the HPT samples were observed by EBSD. EBSD measurements were carried out at JSM-7001F, as shown in Fig. 3.4, which is a thermal field emission scanning electron microscope equipped with EDS (Energy Dispersive X-Ray Spectroscopy) and EBSD detectors. EBSD was undertaken at an accelerating voltage of 15 kV and a working distance of 15 mm.

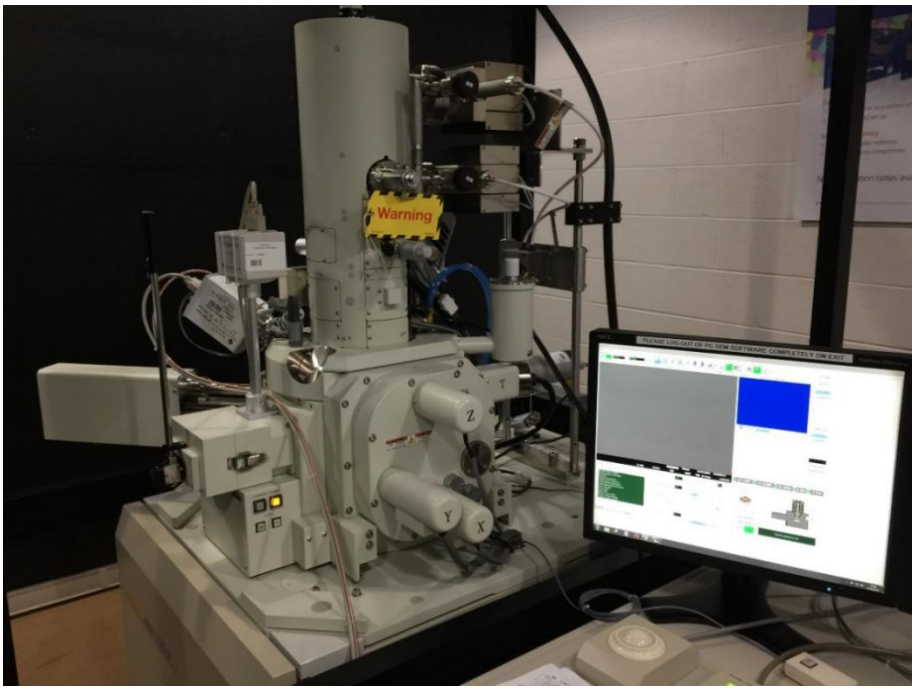

Figure 3.4 Photo of the EBSD machine.

Orientation mapping was measured using a triangular scanning grid. The size of mapping area and the corresponding scan step size were compromises between speed and quality. Specifically, a small step size was able to produce good quality maps, but accompanied by increased scanning time. In the present study, the scanning area and scanning step size at the M-position (at a distance of 2 mm away from the disc centre along the RD) and the E-position (at a distance of 4 mm away from the disc centre along the RD) are given in Table 3.1.

Table 3.1 Scanning areas and step sizes at the M-position and E-position of polycrystalline Al specimens processed by HPT.

Rotation Degree (°)	M-position		E-position	
	Mapping area/μm^2	Step size λ/μm	Mapping area/μm^2	Step size λ / μm
15	240x160	0.500	150x120	0.300
30	240x160	0.500	150x120	0.300
45	240x160	0.500	150x120	0.300
90	240x160	0.500	150x120	0.300
180	240x160	0.500	150x120	0.300
360	240x160	0.500	150x120	0.250
720	240x160	0.350	50x40	0.080
1080	120x80	0.200	50x40	0.075
1800	120x80	0.150	50x40	0.075

In the case of the HPT processed Al single crystal, the grains were very coarse. The scanning areas and the scanning step size are listed in Table 3.2.

To improve the reliability of orientation information, small grains composed of 10 or fewer pixel were removed automatically from the maps and a cleaning-up procedure was employed to reduce the noise on the EBSD maps using Channel 5 software [239]. In the meantime, 8 Kikuchi bands/ 50 Hough Resolution and Refined Accuracy indexing mode were used for indexing. The GBs with misorientation angle of $\theta \geq 15°$ are defined as HAGBs and depicted by black lines in the orientation map, while the GBs with misorientation angles of $2° \leq \theta < 15$ are referred as LAGBs and described by gray lines in the orientation map. The misorientation angle, grain size and aspect ratio were determined in the EBSD analysis.

Table 3.2 Scanning areas and step sizes at the M-position and E-position of single crystal Al

specimens processed by HPT.

Rotation Degree (°)	C-position		M-position		E-position	
	Mapping area/μm2	Step size λ/μm	Mapping area/μm^2	Step size λ/μm	Mapping area/μm^2	Step size λ / μm
15	1600x1200	4	1600x1200	4	1600x1200	3.5
30	1600x1200	4	1600x1200	4	1600x1200	3.5
45	1600x1200	4	1600x1200	3.5	1600x1200	3
90	1600x1200	1.5	1600x1200	1.5	1600x1200	1.5

3.4 Microtexture characterisation

3.4.1 Crystal and sample symmetry of HPT processed specimen

Crystalline is a kind of material whose structure can be idealized into having discrete translation symmetry at the atomic level [240]. Ions, molecules or atoms on a crystal lattice are extended in all 3 spatial dimensions periodically. There are totally 7 crystal systems and resultant 14 Bravais lattices with possible lattice centrings in various crystal lattices [241].

Symmetry is a critical property in crystals and plays an important role in texture analysis based on diffraction techniques. In diffraction experiments such as EBSD, for example, a point (x, y, z) is not able to be distinguished from another point (-x, -y, -z) if the crystal has an inversion centre [242], that is to say they are equivalent in terms of orientation. Therefore, in order to study orientations, it is very important to understand symmetry in various crystals. Only the centrosymmetric elements can be distinguished in diffraction experiments and the non-centrosymmetric subgroup can be transferred into the centrosymmetric subgroup by adding an apparent inversion centre [243]. In fact, most crystals are centrosymmetric and have an inversion centre. Al is classified as a FCC metal. Therefore Al has a cubic symmetry in terms of crystal symmetry.

Different sample symmetries will affect the Euler space employed in texture analysis. For the Al sample processed by HPT, the monoclinic sample symmetry is applied because the HPT deformed sample consists of a 2/m symmetry element, i.e. the cylinder axis is a twofold symmetry axis and the shear plane located at half thickness of the disc is a mirror plane

perpendicular to the cylinder axis [130]. As a result, the Euler space of 0°≤φ1≤180°, 0°≤φ≤90°, and 0° ≤φ2⩽90° is applied in texture analysis of the specimens deformed by HPT.

3.4.2 Shear convention of HPT processed specimen

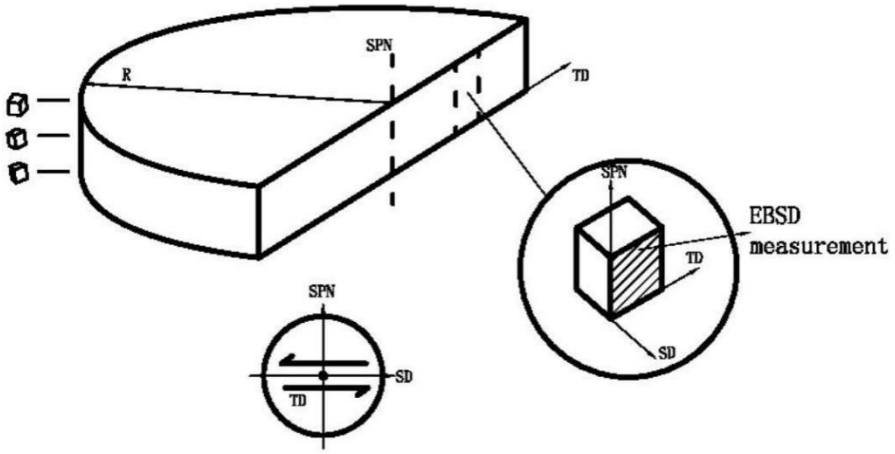

Figure 3.5 Shear convention of the HPT processed sample. TD, SPN and SD refer to the transverse direction, SPN direction (axial direction) and SD (torsion direction)

In order to define the geometry of the HPT processed sample, a typical shear convention is employed in this thesis: TD represents the transverse direction, i.e. RD; SPN denotes the shear plane normal direction which is parallel to the axial direction and perpendicular to the disc plane; SD is the shear direction, namely SD is tangential to the deformation rotation. Actually, the coordinate system is the same as the local polar coordinate system (R, θ, Z) [57] where R, θ, and Z denote the RD, SD and SPN, respectively.

3.4.3 Texture measurement

Texture of the HPT deformed specimens was analysed based on EBSD data. The EBSD specimens were ground and polished with a Struers Oxide Polishing Suspensions (OPS) to obtain a mirror-like surface. The EBSD detector operated with a voltage of 15 kV.

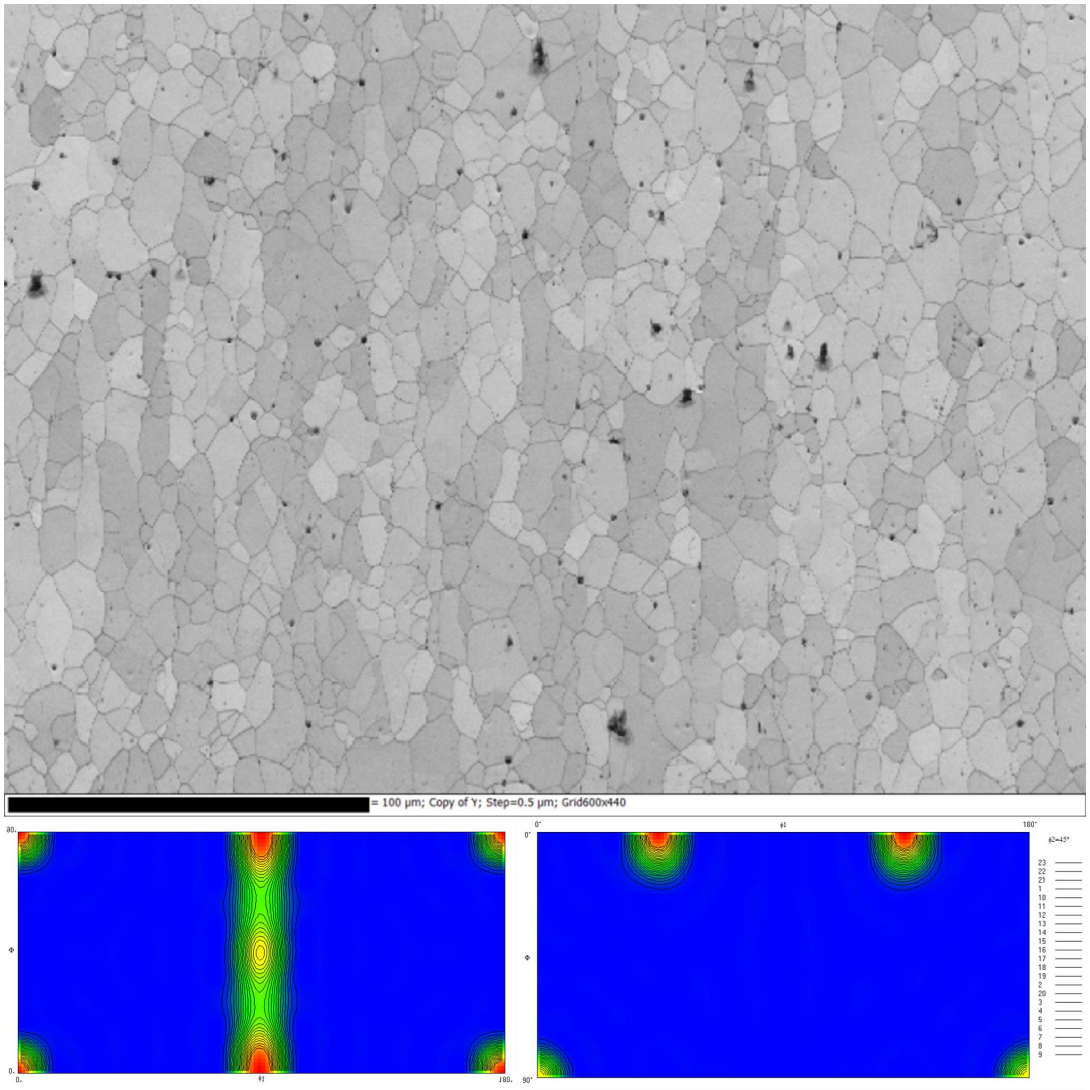

Figure 3.6 (a) Band contrast maps of the starting material before HPT processing and (b) ODFs at the sections of ϕ_2=0° and 45°.

In the case of single crystal, pole figure is a useful and simple representation to demonstrate the texture evolution in HPT. In the present study, the (111) pole figures were detected for Al single crystals. ODF is another clear representation. The analysis of the texture evolution based on ODFs will be undertaken in this thesis for polycrystalline Al.

The bands contrast maps and the ODF sections of ϕ_2=0° and 45°of the starting polycrystalline Al are shown in Fig. 3.6. It is found that the fully recrystallized structure is dominant but a small portion of the extrusion texture component (Rotated Cube, i.e. C component in simple shear mode) is also observed after annealing. The grains with an average grain size of ~ 11 µm are observed at this initial stage.

3.5 Strain distribution

3.5.1 Thickness of HPT processed specimen

As shown in Fig. 3.7, the diameter of the deformed sample increases to around 10.8 mm from the initial diameter of about 10 mm, which indicates that there is slight horizontal flow of the deformed material along the diametric direction.

As shown in Fig. 3.7 (a), the cross section of the as-received disc, which was cut along the plane of its cylinder axis and diameter, has a rectangular shape. The central thickness of the sample processed by HPT is thicker than that at the edge of the sample (Fig. 3.7 b).

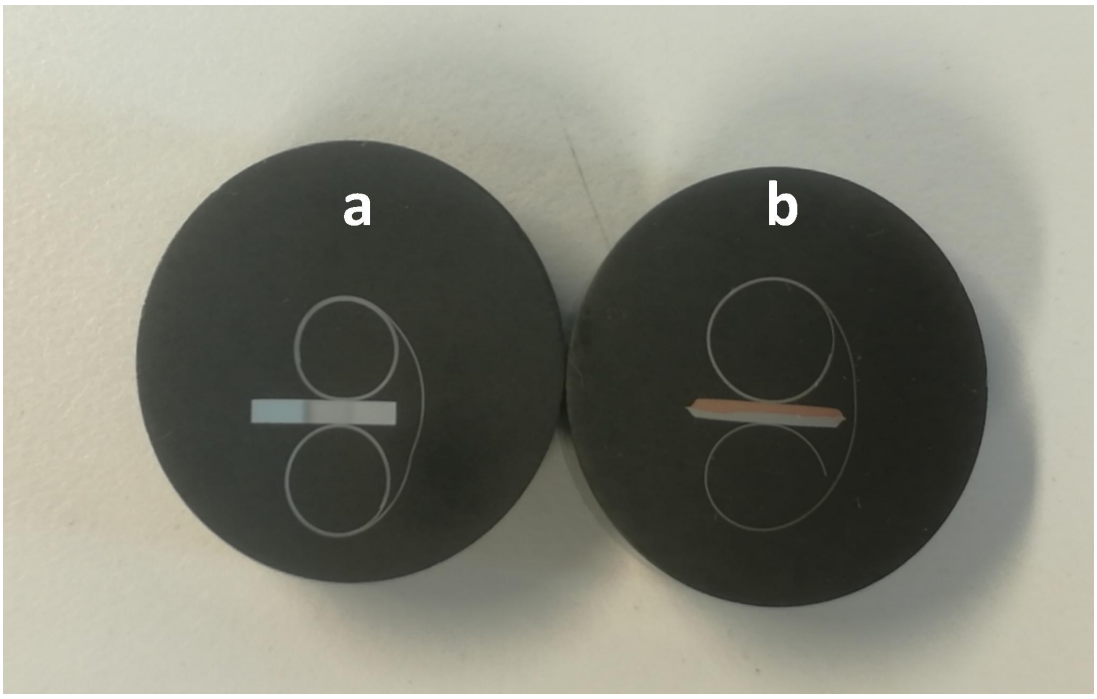

Figure 3.7 Cross section view of as-received (a) and deformed samples (b) cut along the plane of the cylinder axis and the diameter.

Fig. 3.8 shows the thickness distribution of the HPT processed specimen along the RD. The maximum thickness at the disc centre decreases from the initial thickness of ~1.5 mm to ~1.45 mm after HPT. As the distance from the centre increases, the decrease in thickness is moderate at the beginning and is accelerated when the distance is larger than 3 mm.

When the distance from the centre is greater than 4.5 mm, the thickness decreases dramatically. This is because the material flows outward through the gap between two anvils.

In the present study two areas located at the distances of 2 mm and 4 mm from the disc centre are selected for the analysis in order to avoid the area which is affected by the outflow significantly.

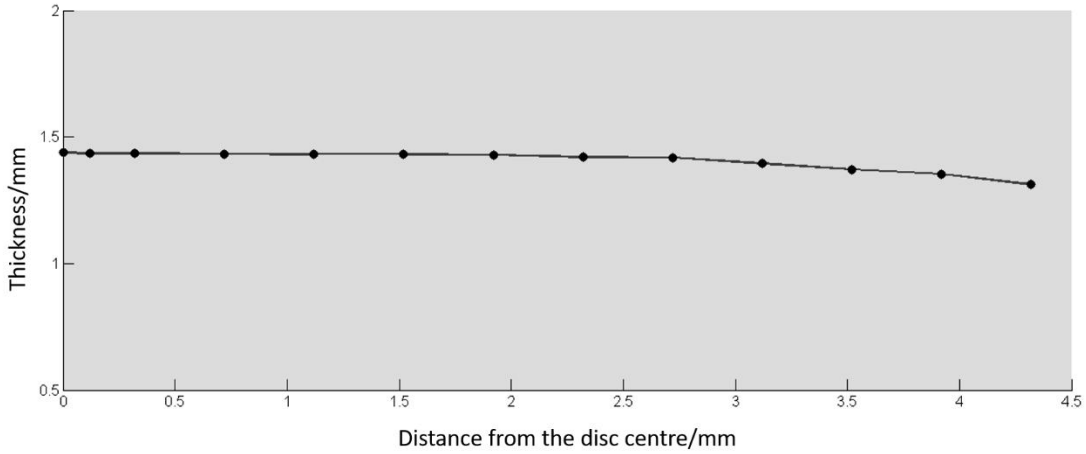

Figure 3.8 Thickness distribution in the HPT processed disc as a function of the distance from the disc centre

3.5.2 Shear strain and equivalent shear strain of HPT deformation

Table 3.3 Shear strain values at different locations of the samples for different rotation angles

	Rotation angle								
Position	15°	30°	45°	90°	180°	360°	720°	1080°	1800°
M	0.37	0.73	1.10	2.20	4.40	8.80	17.60	26.40	44.00
E	0.78	1.55	2.33	4.66	9.32	18.63	37.26	55.89	93.15

It is well known that the material deformation mode in HPT can be assumed to be simple shear. Due to the particular geometry, the distribution of the shear strain is symmetrical along the cylinder axis. As stated before, the shear strain can be calculated by Eqn. (2.1). In Table 3.3, the calculated shear strains at the M-position and E-position of the HPT samples with various rotation angles (15°-1800°) are demonstrated. The disc thickness is assumed to be independent of the HPT revolutions in the calculation of the shear strain.

Eqns. (2.2)-(2.4) can be used to calculate the equivalent train. As a fast, clear and simple estimation method, Eqn. (2.2) is the most widely adopted equation to calculate the equivalent strain for HPT, and is supported by many numerical simulations [244, 245]. In the present study, Eqn. (2.2) is employed to estimate the equivalent strain during HPT at different locations and

revolutions. The calculated equivalent strains are given in Table 3.4.

Table 3.4 Equivalent strains calculated by Eqn. (1) at different locations of the samples for different rotation revolutions.

	Rotation angle								
Position	15°	30°	45°	90°	180°	360°	720°	1080°	1800°
M	0.21	0.42	0.64	1.27	2.54	5.08	10.16	15.24	25.40
E	0.45	0.90	1.34	2.69	5.38	10.76	21.51	32.27	53.78

Chapter 4 High pressure torsion of commercial purity aluminium

As one of the most effective methods of SPD to acquire UFG or nc materials, HPT has been extensively studied for various metals and alloys by experiments [246-248] and simulations [249, 250], such as Al and alloys [226, 251-254], Cu and alloys [12, 99, 255-257], Ni and alloys [258-260], Ti alloy [161, 261, 262], Mg and alloys [263-265], steels [266, 267] and other alloys [268-273].

Because of numerous slip systems, materials with FCC structure have superior ductility and thus are used widely in industry. Aluminium is a typical FCC metal with high SFE, so that Al and its alloys are the most widely studied materials for HPT. It is well known that materials with fine grains generally possess excellent properties like high strength [249, 274, 275], improved ductility [16], superplasticity [263, 273, 276] and so on. A series of characteristics of Aluminium and its alloys processed by HPT have been reported [277-280]. In order to reveal the potential mechanisms inducing excellent properties, a great number of previous studies focused on microstructure [56, 78], texture evolution [281, 282] and grain refinement [283, 284] of pure Al and Al alloys deformed by HPT.

In this chapter, HPT was carried out on commercial purity aluminium at room temperature from low angle of 15° rotation to 5 revolutions (1800° rotation). Microstructures and texture in the specimens processed by HPT were observed via EBSD. Then hardness tests were conducted to evaluate the evolution of mechanical properties.

4.1 Experiment procedure

The material used in the present work was commercial purity (CP) Aluminium containing Al of 99.7 wt% purity The annealed discs used as starting materials were processed by HPT under a pressure of ~6.16 GPa at room temperature. In order to cover a wide range of the shear strain, HPT with 9 different rotation angles was conducted: 15° (1/24 turn), 30° (1/12 turn), 45° (1/8 turn), 90° (1/4 turn), 180° (1/2 turn), 360° (1 turn), 720°(2 turns), 1080° (3 turns) and 1800° (5 turns).

Microstructure and texture of the HPT processed CP Aluminium were investigated by EBSD observation. The EBSD measurements were conducted on an axial cut plane (SD plane) at the middle (M-position, at a distance of 2 mm away from the disc centre) and edge (E-position, at a distance of 4 mm away from the disc centre). In order to study the gradient in microstructure and texture through the thickness of the HPT specimens, 5 points are selected

at M and E positions which are referred to as M1, M2, M3, M4, M5 and E1, E2, E3, E4, E5, respectively, arranged from the top surface to the bottom surface of the deformed disc. The EBSD measurement areas marked as M1-M5 and E1-E5 are shown schematically in Fig. 4.1.

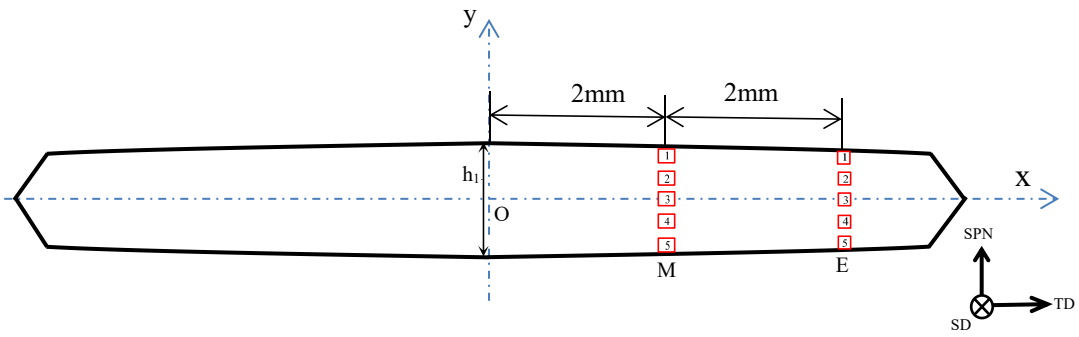

Figure 4.1 axial section (side view) of a HPT deformed disc. The observed points are depicted by red rectangles: M1, M2, M3, M4, M5 at M-position, and E1, E2, E3, E4, E5 at E-position from top to bottom, respectively.

For the Vickers hardness measurements, the SD-planes were polished. The measurement was conducted using a Struers Emco-Test DuraScan-70 equipped with Vickers indenter. In the hardness tests, the applied load was 0.025 kg. The microhardness was measured across the diameter of the disc with a step of 0.5 mm from one edge to another edge. As depicted schematically in Fig. 4.2, four hardness tests were conducted at each location and the average of the four hardness will be used in the analysis.

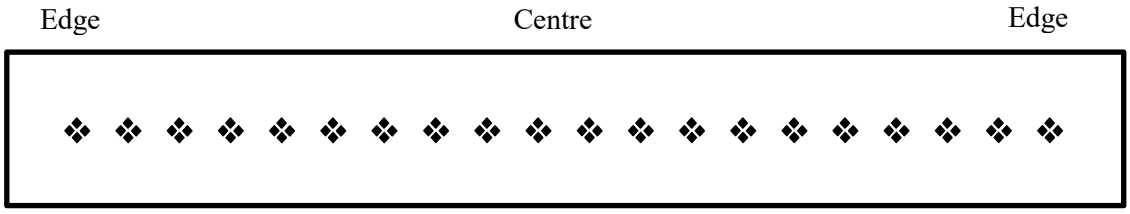

Figure 4.2 Schematic illustration of points conducted hardness measurements along the diameter of the disc after HPT. Each value of hardness is the average of the 4 neighboring measurement points.

4.2 CP Aluminium deformed by HPT

4.2.1 Microstructure evolution of CP Al during HPT at the M-position

The as-received rods were deformed by extrusion along the SPN direction of the HPT sample coordinate system, so that the initial grains of the HPT samples were elongated along the

SPN direction. After annealing the interior part of grains becomes clean. However, a portion of grains still keep the elongated shape along the SPN direction inevitably and fully equiaxed grains have not been achieved. Texture is predominated by the cube component and a small portion of the residual Rotated Cube component still remains.

The EBSD maps in Fig. 4.3 demonstrate the microstructure of the specimens after HPT with the rotation angles of 15°, 30° and 45° at the M positions. The colour of an individual grain in the EBSD map represents the SPN direction of the sample coordinate system relative to the grain orientation. The colour hue within a grain indicates the developing substructures inside the grain [78, 150]. HAGBs are highlighted with solid black lines and LAGBs are denoted by solid grey lines in the EBSD map. The panels from the top to the bottom in Fig.4.3 correspond to the areas M1-M5 respectively.

As shown in Figs. 4.3 (a)-(e), at all five M-locations after the HPT rotation angle of 15° (γ=0.37), the initial grain shapes generally remain because the deformation mainly results from the compression and the 15° rotation doesn't bring significant shear deformation into the sample. The deformations only change the sub-structures. For instance, the colours inside the gains are not unique anymore. Specifically, the gold colour emerges from the unique red colour. The onset of the colour spread within grains indicates that there is distortion in microstructure induced by the imposed strain.

Geometrically necessary boundaries (GNBs) and incidental dislocation boundaries (IDBs) play an important role in the evolution of the sub-grain boundary structures during plastic deformation. GNBs are the boundaries of the lamellar cell blocks and they generally have straight boundaries[285], whereas IDBs are given rise from the statistical trapping of the glide dislocations and have curved boundaries [286]. The dislocation walls and microbands which are typical characteristics of the microstructure at low strain, while the lamellar cell blocks consisting of GNBs and IDBs tend to be generated under large strain[286]. The cell blocks generally contain one grain in the width and at least three grains in the length, which is pretty similar to the feature of the microstructure observed in Fig. 4.3(a)-(e).

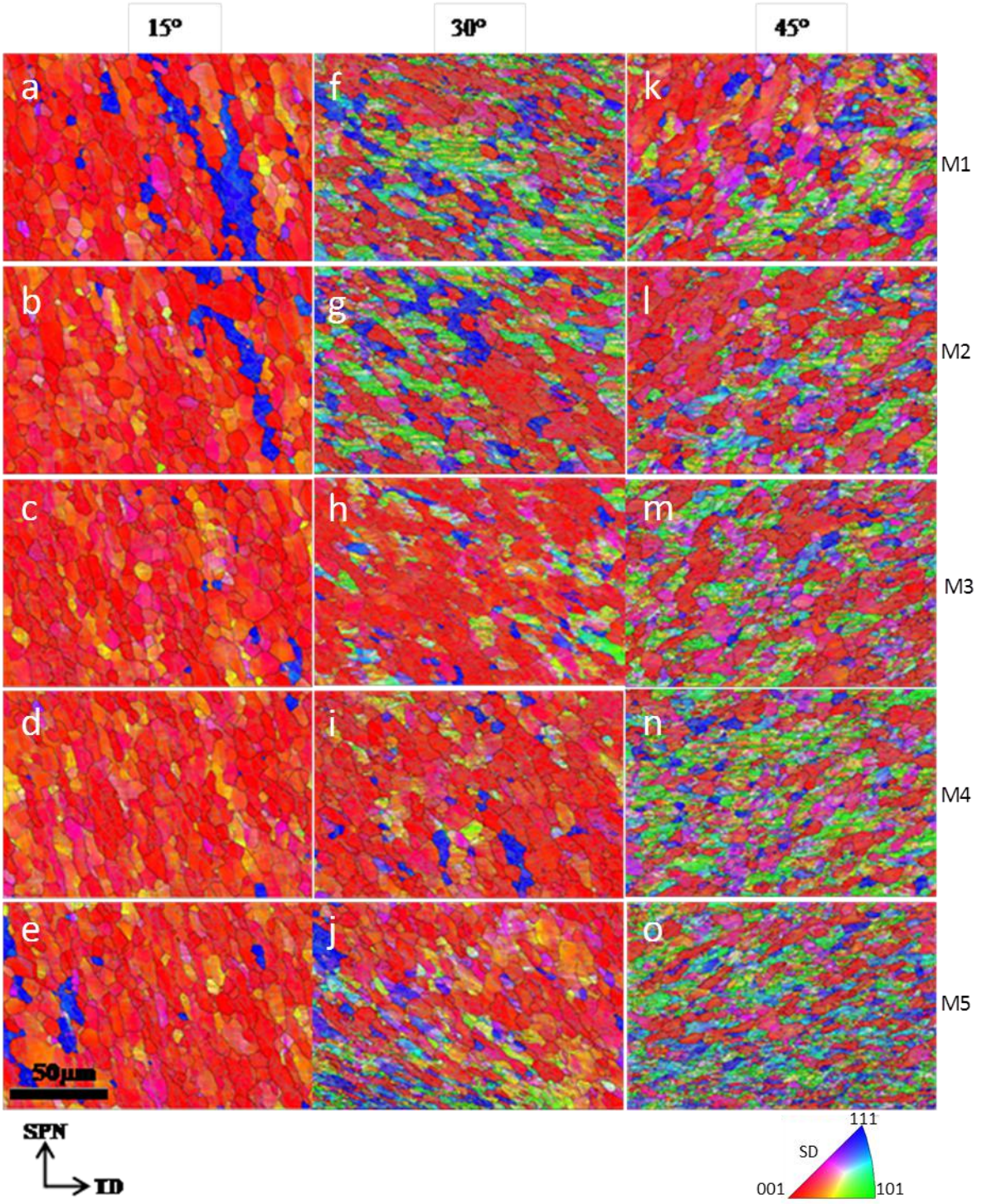

Figure 4.3 EBSD orientation and boundary maps of CP Aluminium after HPT with the rotation angles of 15°, 30° and 45° at M-position.

Fig. 4.4 is a magnified EBSD map at M3 (Fig. 4.3c). Although the morphology of many grains remains the same as the annealed grains, the colour spread is a notable indication of distortion within Grain A as shown in Fig. 4.4. The colour spread (i.e. orientation spread) is a qualitatively representative characteristic of GNDs [287, 288]. It can therefore be concluded that

the intragranular geometrically necessary dislocations (GNDs) have been generated at this stage (θ=15°) where the plastic strain is relatively low.

Fig. 4.4 (b) and (c) demonstrate the misorientation profiles along the solid blue lines within Grain A and Grain B marked in Fig. 4.4 (a), respectively. In Fig. 4.4 (b), the misorientation profile reveals the appearance of GNDs and substructures inside Grain A. Within Grain B, the misorientation angle of a large area is less than 2° and the intragranular colour is unique in this area. These features denote that the corresponding distortion is slight in this area.

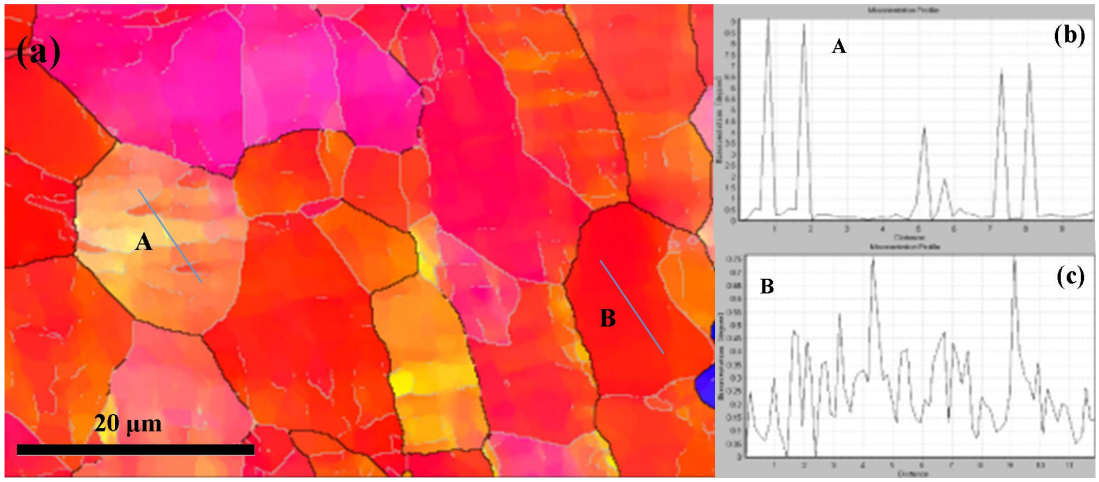

Figure 4.4 Magnified EBSD map (a) of Fig. 4.3(c), i.e. 15M3. Intragranular misorientaion of subgrain A (b) and subgrain B (c).

After the 30° rotation (γ=0.73), as shown in Fig. 4.3 (f) - (j), several noticeable changes start to occur due to the increase of the shear strain although the initial grain shape can still be seen in part of the map. Grain refinements have been observed at all 5 selected positions in the sample with the 30° rotation. In addition, there is an obvious gradient of microstructure along the thickness of the disc. As shown in Fig. 4.3 (j), the M5 position seems to have undergone severe shear deformation. It can be seen that the grain size at the bottom of M5 is drastically smaller than that at the top of M5.

The colour of the grain represents the SPN direction of the sample coordinate system relative to the specific crystallographic direction. The colours of the grains are identical to their colours in IPF. Theoretically, the red colour in the EBSD maps stands for {100} <u v w> fibre, typically consisting of fully recrystallized structure and rotated cube component. The {100} <u v w> fibre is still predominant in the sample deformed by the 15° rotation, which denotes that the crystallographic orientation has been changed barely after the preliminary

deformation equivalent to the 15° rotation. However as the rotation increases to 30°, a wider range of colours emerges from the uniform red colour. Specifically, more green and blue colour areas representing the {110} and {111} <u v w> fibres respectively emerge from the initial {100} <u v w> fibre. Due to friction between the anvil and the sample, the bottom surfaces of the disc are subjected to more plastic strain. This is in good agreement with observations from the M5 EBSD maps (Fig. 4.3 j).

Periodic alternation in colour can be observed in Fig. 4.3 (k) - (o) after the 45° rotation (γ=1.10). Grain rotation is one of the mechanisms to induce the change of microstructure and texture during plastic deformation. Grains tend to rotate to the stable textures. A fraction of the original crystallographic orientation, i.e. {100} <u v w> fibre, continues to decrease, whereas an amount of other fibres increases remarkably. Simultaneously, the colour spread is more homogeneous.

At this strain level (45° rotation), the initial shape of grains is difficult to distinguish from the EBSD maps except for a few areas where the appearance of microstructure is similar to that in the previous strain stage (30° rotation). Grain structures are elongated along the SD, so that the initial structures are converted partially to the lamellar structures. The microstructures in the vicinity of the sample upper surface (M1) are more heterogeneous than those near the sample bottom surface (M5). According to the conventional theory, the applied strain is uniform across the thickness of the HPT process sample. However, the present microstructure observation indicates that this conclusion may be not correct. In practice the disc is deformed by the rotating anvil, thus the shear strain transfers from one surface to the other surface along the thickness progressively, resulting in a strain gradient along the thickness at the low strain stages (15°~45° rotation).

Fig. 4.5 (a) shows a magnified EBSD map of M3 after HPT with the rotation angle of 30°. The increase of the strain leads to the great dislocation propagation. Subsequently the dislocation tangle and agglomeration give rise to the formation of the sub-grain boundaries. In Fig. 4.5 (a), the density of the sub-grain structure increases dramatically. It should be noted that most of the discontinued grey lines have transformed into the continuous grey lines. As for HAGBs, the discontinued black lines inside the grains appear at this stage because the misorientation angles of several sub-structures increase to over 15° by absorbing the propagative dislocations during HPT processing. It is interestingly found that most of the intragranular discontinued HAGBs distributes along the TD direction, such as the black lines

within Grains A, B and C indicated by white symbols in Fig. 4.5 (a). In fact, these discontinued GBs generated during HPT tend to distribute parallel to the shear plane because of the geometrical requirement. The possible mechanism is similar to the formation mechanism of GNBs in the rolling process.

Fig. 4.5 (b) shows a magnified EBSD map at the M3 position after the 45° rotation. A higher density of the sub-structures and HAGBs inside the grains can be seen as the shear strain increases. In contrast to Fig. 4.5 (a), a large fraction of the continuous sub-grain boundaries rather than the discontinued sub-grain boundaries predominate in the map. The crystallographic orientation is heterogeneously distributed and the initial parent grains still do not vanish, which indicates that the complete grain refinement has not been achieved so far. As explained before, the colour in the EBSD map stands for the corresponding orientation of the grain. It is interestingly found that the agglomerates of the substructures with close orientations are surrounded by LAGBs in Grain D. The interior of these agglomerates is not clear since the colour gradient exists. These sub-grains are apparently generated from the fragmentation of the original grain. Eventually they would be turned into new grains surrounded by HAGBs as the shear strain increases further.

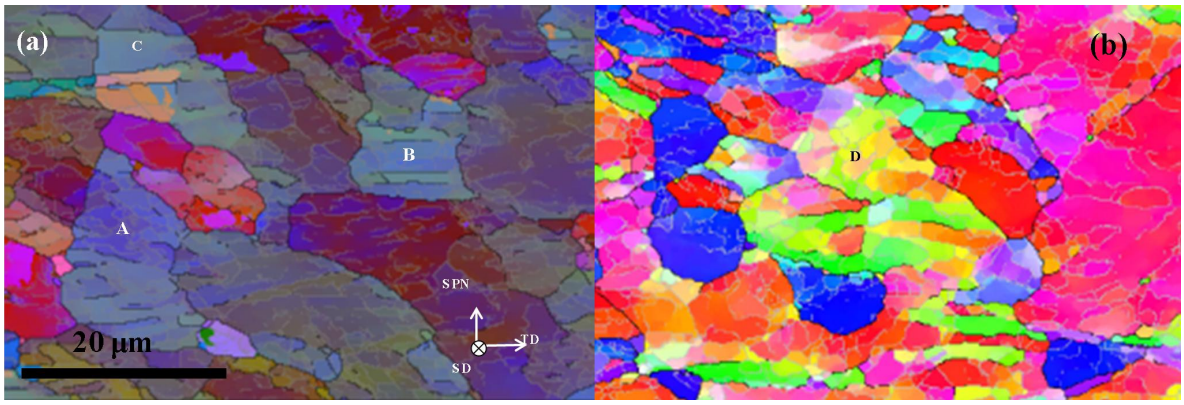

Figure 4.5 Magnified EBSD maps of (a) Fig. 4.3 (h) after the 30° rotation M3 and (b) Fig. 4.3 (m) after the 45° rotation at the M3 position.

The EBSD maps in Fig. 4.6 denote the microstructures of the deformed discs after the rotation of 90°, 180° and 360° at the M-locations. It should be mentioned that they have the same scale on the EBSD maps.

With increasing deformation to the 90° rotation (γ=2.20), the coarse parent grains, which are visible during the lower strain stages, disappear completely. As shown in the relatively low magnification EBSD maps in Fig. 4.6, the distribution of colours is quite homogenous,

especially the fraction of the blue colour areas increases remarkably. More and more new substructures surrounded by LAGBs are generated from the fragmentation of the parent grains. When the density of HAGBs in the grain interior continues to increase with the imposed strain, a growing number of LAGBs surrounding the substructures are converted into HAGBs, and subsequently the discontinued HAGBs are transferred into the continuous HAGBs. As a result, the new grains which are separated fully by HAGBs are born from the sub-structures. However, the fraction of LAGBs is larger than that of HAGBs in the samples with the 90° rotation.

At the accumulated shear strain of ~4.4, equivalent to the 180 ° rotation, surprisingly the changes in the morphology and colour distribution are fairly small in general, even though the shear strain has been significantly increased by several times when the rotation angle increases from 90° to 180 °. The only exception is M5 with the 180° rotation (Fig. 4.6 j) where obviously the finer grain size and the higher density of HAGBs are observed. Generally the grain sizes at bottom areas are smaller than other areas at low strain level stage, which suggests more severe deformation occurred in this area and the gradients along thickness at these stages.

As to crystallographic orientation, the difference in the colour spread at M5 implies that the {110} <u v w> fibre would play a more important role compared with other M positions after the 180° rotation.

When the rotation angle increases to 360° (γ=8.80), there are sharp changes in morphology and preferred orientation. The clusters of the grains with the red colour decrease sharply while the agglomerate with the blue colour increase significantly in contrast to the previous deformation stage. This means a great number of the {100} <u v w> fibre has converted into the {110} <u v w> fibre at this stage. The conclusion will be further discussed later.

The average grain size continues to decline greatly. More new grains are generated from the fragmentation of the initial structures. They prefer to emerge at the border of the initial structures. But the small and equaxied grains are also observed within the original structures.

It can be seen from Fig. 4.6 that the density of the intragranular HAGBs of the green grains is extremely larger than that of the grains with the red colour. The average grain size of the green grains is smaller than that of the red grains at this stage where the shear strain of γ=8.80 is applied. This phenomenon is an indication that the grain fragmentation has a preferred

orientation, namely the fragmentation during HPT prefers to take place in the {111} <u v w> fibre during this deformation stage.

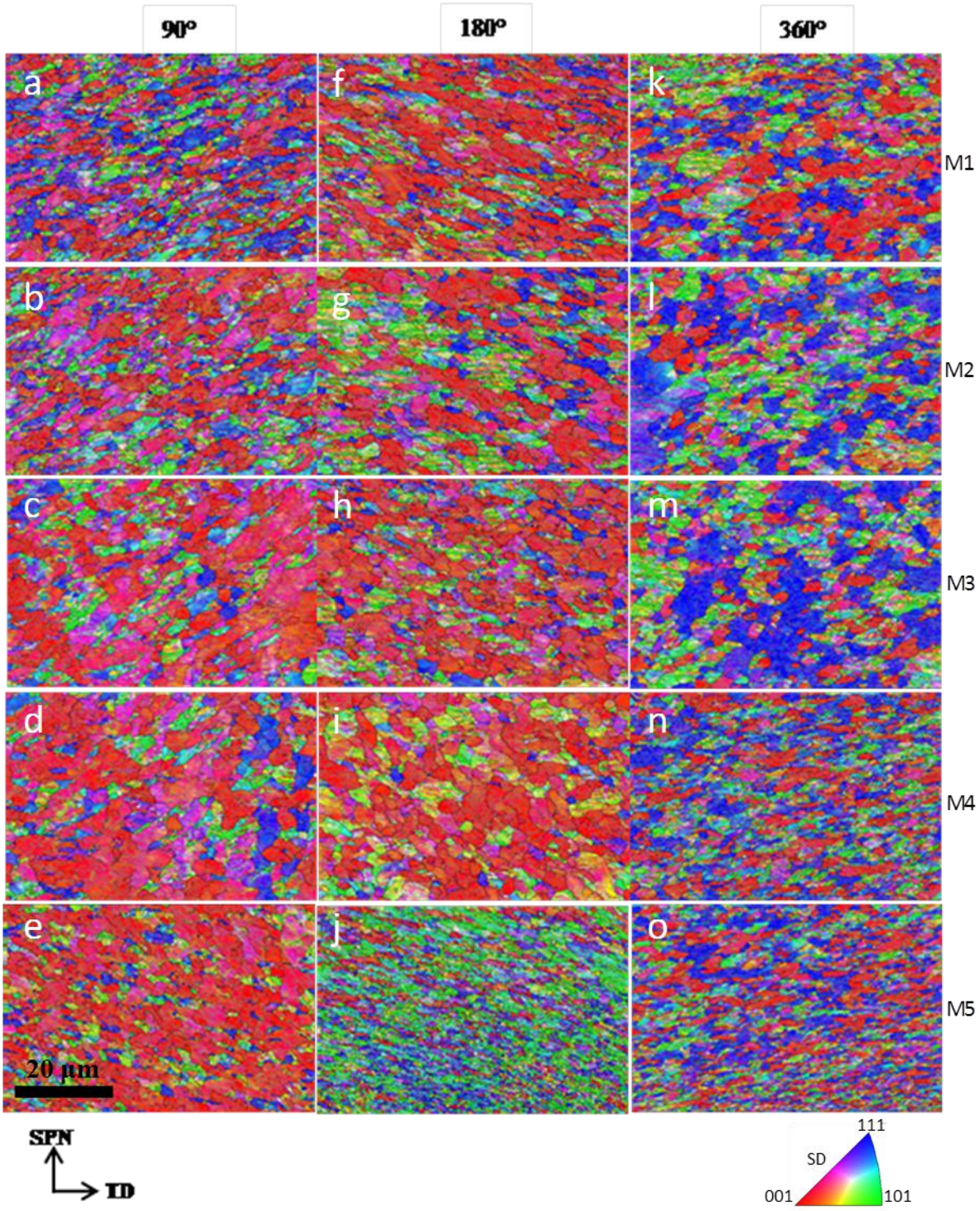

Figure 4.6 EBSD orientation of CP Aluminium after HPT with the rotation angles of 90°, 180° and 360° at M-positions. At each angle 5 points were measured along the thickness: M1, M2, M3, M4 and M5 (from top to bottom).

The EBSD maps in Fig. 4.7 represent the microstructures of the deformed discs after the rotations of 720°, 1080° and 1800° at M-positions. It should be noted that they have the same scales on the EBSD maps of 1080° and 1800°. At the accumulated strain of γ=17.6 (equivalent to 720° rotation), the distribution of crystallographic orientations is pretty homogenous. The area of agglomerates with close orientations is decreasing compared with the results of γ=8.80. The fragmentation tends to happen frequently within the clusters of {111} <u v w> fibre during HPT. At this strain level, a coexistence of coarse and fine grains is detected. This mean that the saturation of grain refinement has not been achieved.

With increasing deformation to the 1080° rotation (γ=26.4), the grain size decreases significantly to the near-nanometre level. The shape of grains is not in the form of typical lamellar structure in Fig 4.7 (f)-(j). More and more grains tend to become equiaxed. Although a great amount of LAGBs can still be seen inside the grains, the fraction of HGABs becomes higher than the fraction of LAGBs. Most of the intragranular sub-structures are the continuous LAGBs rather than the discontinued LAGBs. As the imposed shear strain increases, more discontinued LAGBs are converted to HGABs continuously. As a result, new grains surrounded by HAGBs are generated.

At the accumulated shear strain γ of 44.0 (equivalent to the 1800° rotation), the characteristics of the microstructures suggest that the grains have been highly refined. As can be seen in Fig 4.7 (k)-(o), most of the grain interiors are clean but a few LAGBs are still observed. When the shear strain reaches this level, the microstructure gradient along the thickness is no longer found. The microstructure distribution is pretty homogenous in all areas.

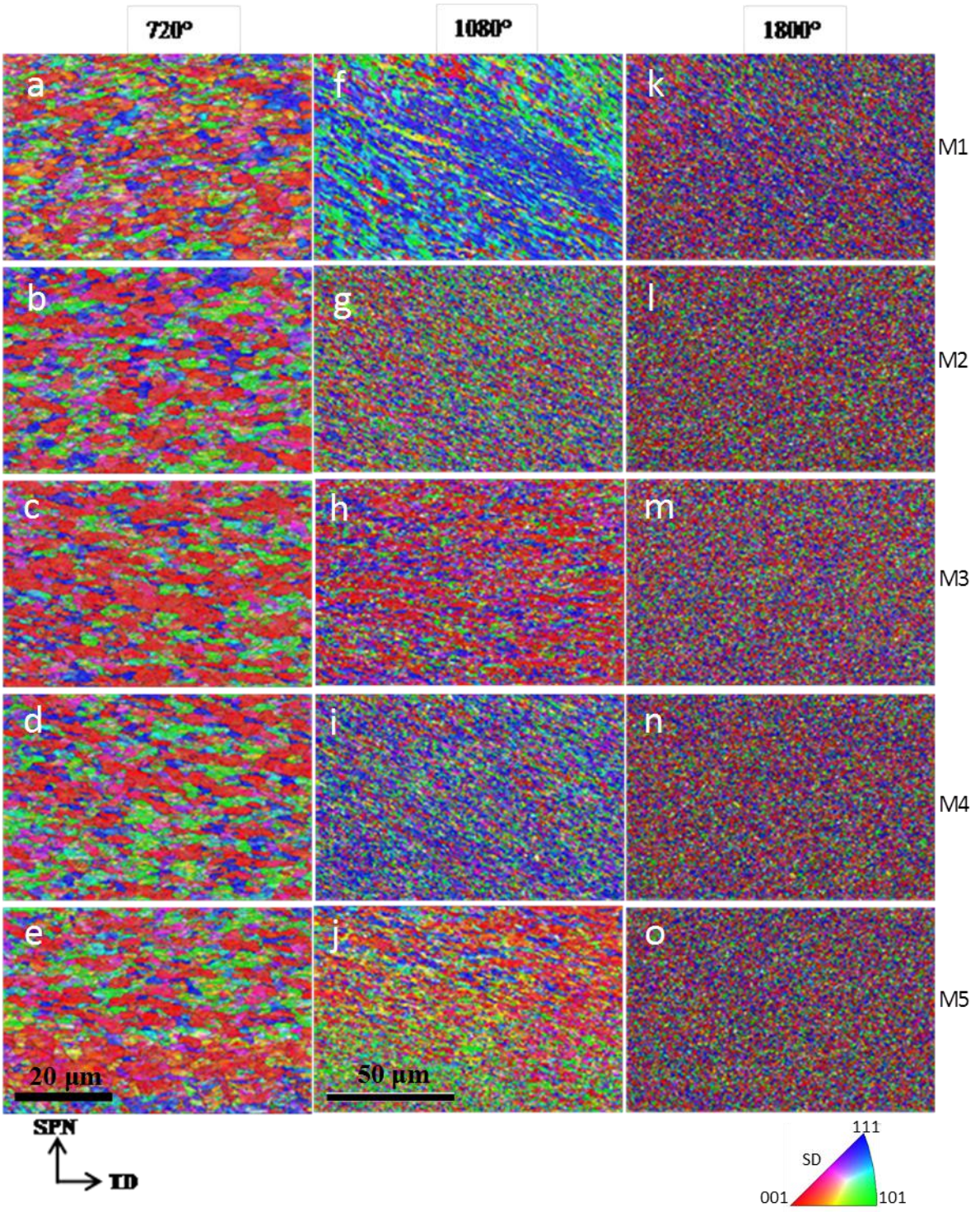

Figure 4.7 EBSD orientation of CP Aluminium after HPT with the rotation angles of 720°, 1080° and 1800° at M-positions. At each angle 5 points were measured along the thickness: M1, M2, M3, M4 and M5 (from top to bottom).

In HPT the evolution of the microstructure mainly consists of the grain fragmentation and refinement. The effect of strains on three parameters representing the characteristics of grain

fragmentation and refinement, i.e. grain size, aspect ratio of grain and misorientation distribution, are quantitatively shown in Figs. 4.8, 4.9 and 4.10, respectively.

The grain size depends highly on the definition of HAGBs. It is widely considered that HAGB refers to the GB with a misorientation angle of ≥15°.

As shown in Fig 4.8, the average grain size of the annealed disc is about 11 μm. In the light of the mean aspect ratio of grains, as explained earlier, part of initial grains after annealing are elongated along the SPN direction with the average aspect ratio of about 2.55, as given in Fig 4.9.

At the shear strain γ of 0.37 (15° rotation), the average grain sizes at the M1- M4 positions (Fig. 4.3 (a)-(e)) decrease modestly to around 10.5 μm. However the grain size at M5 is 9.18 μm, which is obviously smaller than the grain sizes in the other areas. It is noted that the HPT sample is deformed by a two-step procedure. The disc is first deformed by a high compressive pressure of ~6.16 GPa, and then by a rotation of 15°. The marginal decreases at M1- M4 are due to the compression before the torsional deformation. The large decrease in the grain size at M5 may be due to the relatively large shear deformation near the bottom surface. All aspect ratios decrease from ~2.55 to ~2.20 after a 15^{o} HPT rotation, as shown in Fig. 4.9. The elongations of the grains along the SPN direction become small after the compression. At this stage, the misorientation angle distribution is dominated by the substructures with the misorientation angles of less than 2°, which corresponds to the propagation of GNDs as indicated in Fig. 4.4.

As the shear strain increases to 0.73 (30° rotation) the grain size decreases to the range of 6-7 μm. The variation of the grain size is small except at M4. The grain size at M5 is smaller than the grain sizes at other locations due to the same reason as for the 15° rotation. The corresponding aspect ratio also changes significantly to 2.5~2.8. This increase in the aspect ratio can be attributed to the elongation of the grains under shear strain. In terms of misorientation angle distribution, the fraction of the substructures with misorientation angle of less than 2° decreases but a great number of LAGBs appear, since LAGBs are formed by the aggregation of the dislocations at this stage. The fraction of HAGBs doesn't change, indicating that few HAGBs are formed at this strain level. With increasing deformation to the 45° rotation (γ=1.10), the grain sizes drop greatly to around 5 μm. However the aspect ratio shows no great change at the same stage. Simultaneously, the density of the substructures with the misorientation angle of less than 5° continues to decrease, and HAGBs grow up to a

higher level in contrast to the sample subjected to the 30° rotation. These parameters are in good agreement with observations on the microstructures reported in Section 4.21. In summary, part of the discontinued sub-grain boundaries are converted into continuous sub-grain boundaries, thereby a number of new grains emerge from their parent grains. As a result the average grain sizes decrease at this strain level. Concurrently, the parent grains are elongated during HPT deformation. The balance of new grains and elongated grains causes the stable aspect ratio at this stage.

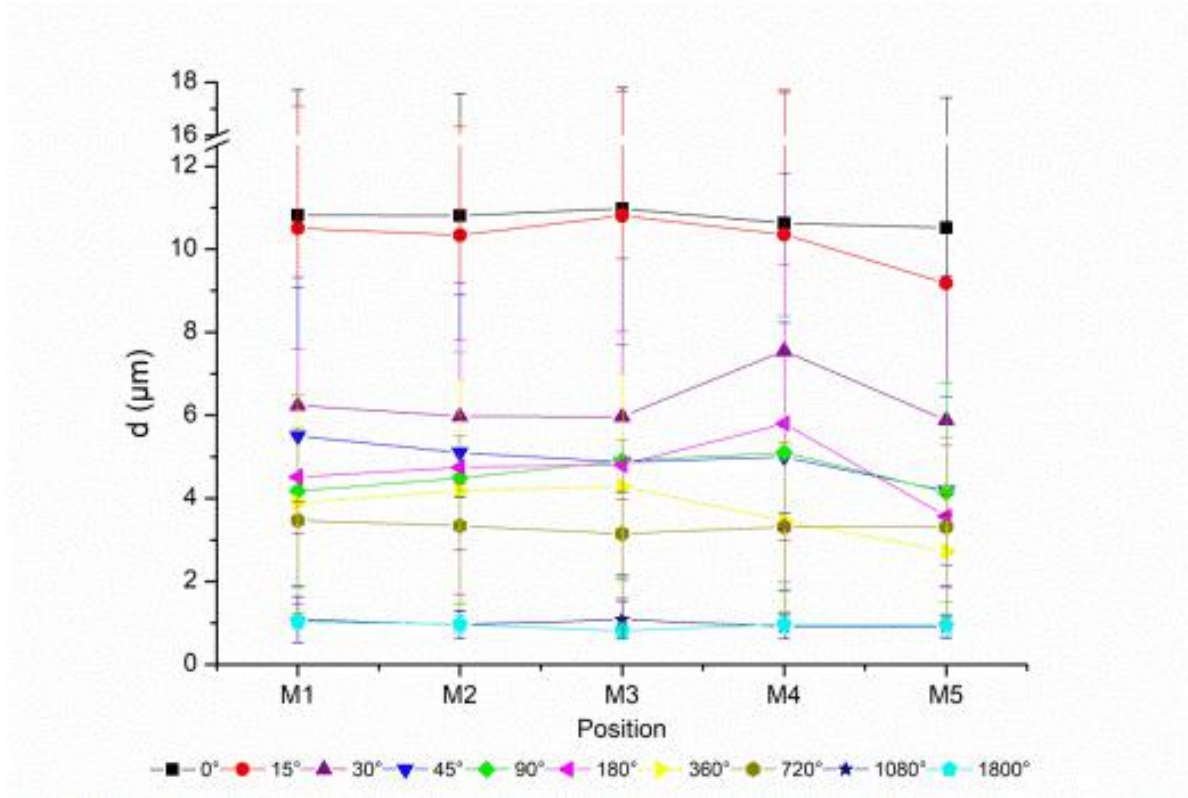

Figure 4.8 Grain size of CP Aluminium after HPT with the rotation angles of 0°, 15°, 30°, 45°, 90°, 180°, 360°, 720°, 1080°, 1800° at M-positions. The black line indicates the grain sizes at the as-received condition.

At the accumulated shear strain of 2.20 (90° rotation), the average grain sizes slightly decrease, and the average aspect ratio declines from above 2.5 to below 2.5 after the 90° rotation. At the accumulated shear strain of 4.40 (180° rotation), the average grain sizes are stable even though a double shear strain has been imposed compared to the 90° rotation. Concurrently, the aspect ratio rises again to about 2.81. In the light of the misorientation angle, the fraction of the substructures with the misorientation angles of <2° increases after the 90° rotation, but descends again after the 180° rotation. These microstructural features

suggest that as the shear strain increases to 2.20, new grains are born, causing the decrease in the grain size and aspect ratio. In the meantime, a great number of dislocations propagate inside the new and parent grains with the increase of shear strain, which gives rise to the increase in substructure with misorientation angle of less than 2°. As the shear strain ascends to 4.4, the dislocations generated at the previous deformation stage are absorbed by LAGBs and HAGBs. Grains are elongated but no substantial grain fragmentation is observed at this strain stage.

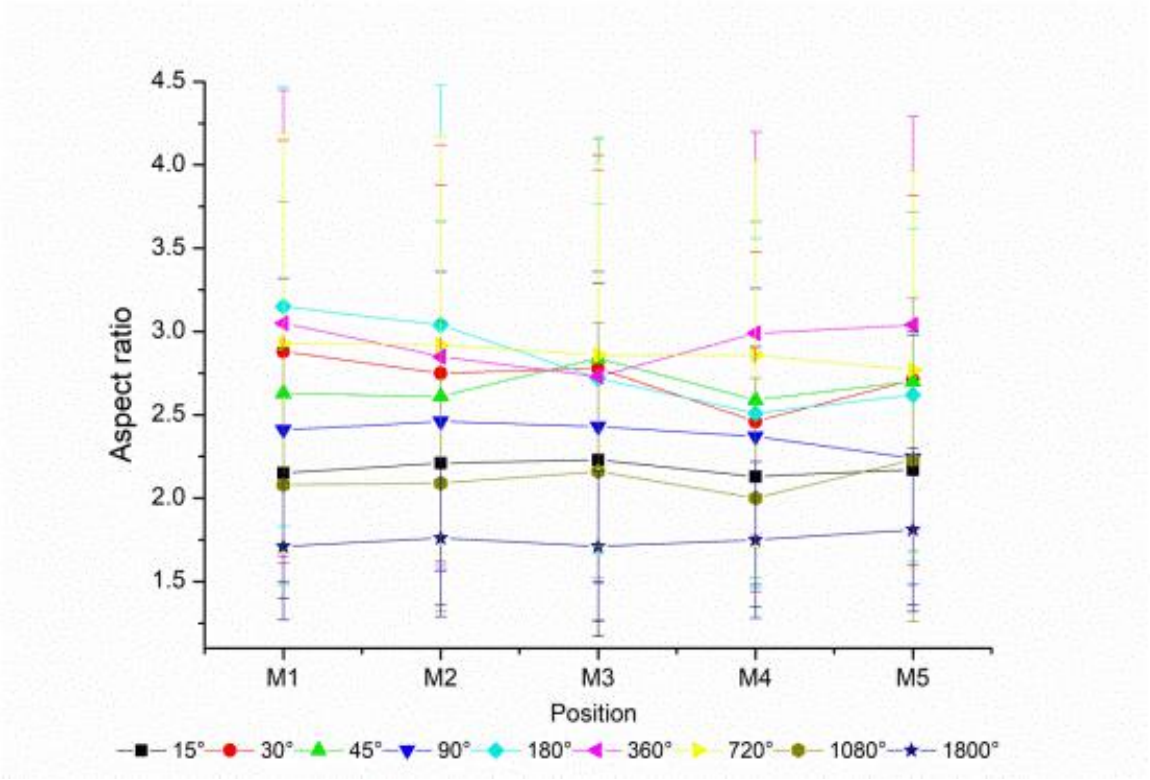

Figure 4.9 Aspect ratio of grains after HPT with the rotation angles of 15°, 30°, 45°, 90°, 180°, 360°, 720°, 1080° and 1800° at M-positions.

An increase in the strain up to γ=8.80 and 17.60 (360° and 720° rotations) causes further grain refinement. The grain size decreases into the range of 3-4 μm after the 360° rotation. But the increase in the shear strain does not result in a great change in the aspect ratio. The reason for this can be attributed to the offset of the fragmentations. During these stages, the densities of the dislocations and HAGBs increase compared to the 180° rotation, but LAGBs have a descending trend. More specifically, the propagation of the dislocations and formation of HAGBs at the expense of LAGBs are facilitated.

There are sharp changes in morphology at the shear strain of γ=26.4 and 44.0 (1080° and 1800° rotations). The grain size decreases to the order of 1 μm. The differences in grain size for all the areas are pretty small, while the difference in aspect ratio found in Fig 4.9 is around 2.10 after the 1080° rotation and about 1.75 after the 1800° rotation. The fraction of HAGBs increases rapidly at the expense of the dislocation density and LAGBs. The misorientation angle distribution for the 1800° rotation is similar to the theoretical random distribution, i.e. so-called Mackenzie plots.

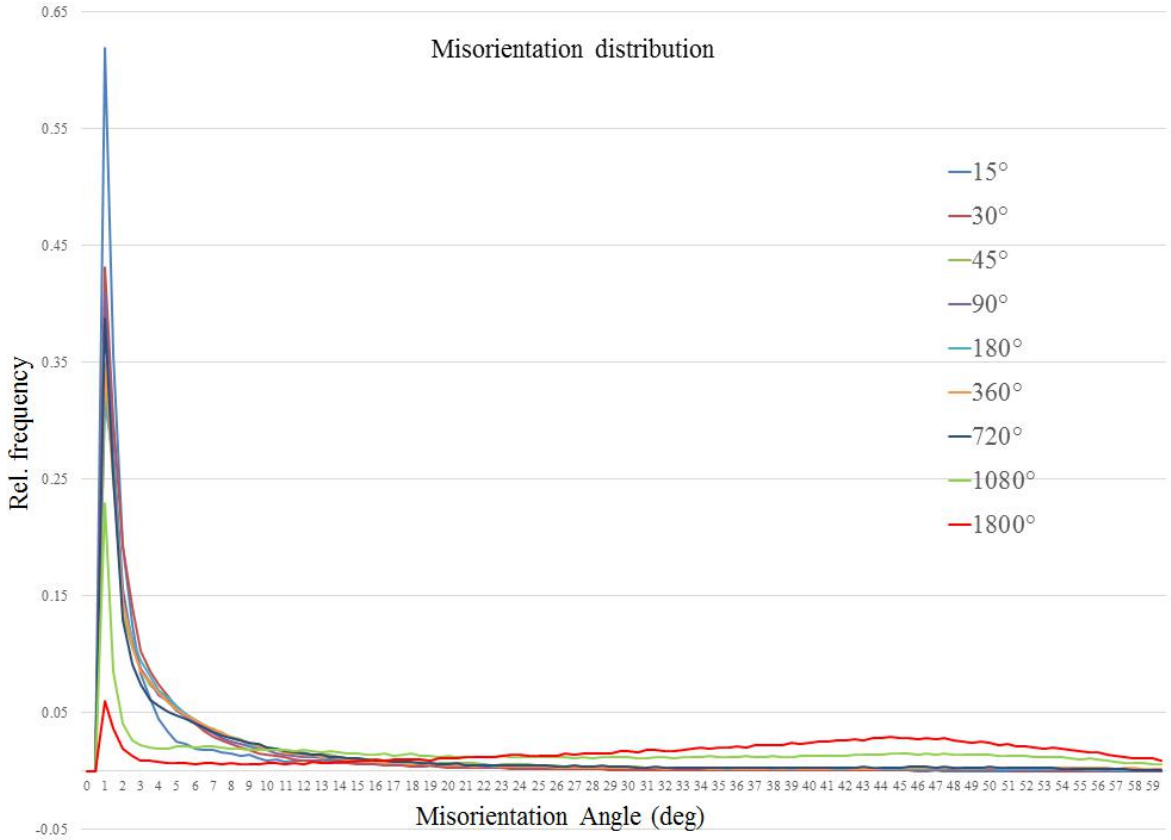

Figure 4.10 Misorientation of CP Aluminium after HPT with the rotation angles of 0°, 15°, 30°, 45°, 90°, 180°, 360°, 720°, 1080° and 1800° at the M3 positions.

4.2.2 Microstructure evolution of CP Al during HPT deformation at E-position

The EBSDs maps measured at the positions near the sample edge (E-position) where is 4 mm away from the centre of the disc are discussed in this section. At each rotation angle, 5 points were measured along the disc thickness on the SD plane.

The EBSD maps in Fig 4.11 represent the microstructures of the deformed samples after the HPT rotations of 15°, 30° and 45° at five E positions. The corresponding shear strains γ are 0.78, 1.55 and 2.33, respectively. The EBSD maps in the figure have the same scale.

It should be mentioned that the shear strains at the E-positions are larger than those at the M-positions under the same rotation angle. It can be seen in Fig 4.11 (a) - (e) that the grain shape after the 15° rotation changes very slightly although the remarkable microstructure change has happened inside the grains.

Wider colour range indicates that more serious distortion has taken place at this deformation stage. But the {100} <u v w> fibre still mainly predominates. This indicates that as the imposed strain increases, the dislocation propagation gives rise to more opportunity of their mutual reaction to form the dislocation tangles and walls. Subsequently the accumulation of the dislocation tangles and walls leads to the substructures observed on the EBSD maps. In addition, a number of the new-born grains appear at the border of their parent grains. The detailed inspection show that there is a microstructure gradient along the sample thickness. After the 15° rotation the grain shape at E1 is similar to that of the as-received specimens but the grain shapes at E2-E5 are distorted.

At the shear strain γ of up to 1.55 (30° rotation), the change in morphology is significantly great. The parent grains almost disappear but the periodic colour spread appears in most areas on the EBSD maps. As can be seen in Fig 4.11 (f)-(j), the band shaped structures are elongated and are surrounded by HGABs. The interior part of the band shaped structure has a high density of LAGB. The microstructure gradient along the sample thickness is also seen at this strain stage. This means that the applied strain along the disc thickness is non-uniform. It is reasonable to anticipate that when the low anvil drives the rotation by friction at the bottom surface, the bottom part of the disc deforms first and the top part deforms latter during the low strain stage.

At the shear strain of γ=2.33 (equivalent to 45° rotation) (Fig 4.11 (k)-(o)), part of the intragranular LAGBs observed at the previous deformation stage is transformed into HAGBs due to the increase of the shear strain. As a result, the band shaped grains surrounded by HAGBs are subdivided into smaller cell structures and the grain fragmentation proceeds further. It should be noted that this procedure is inevitably accompanied by the increase in the dislocation density inside the grains.

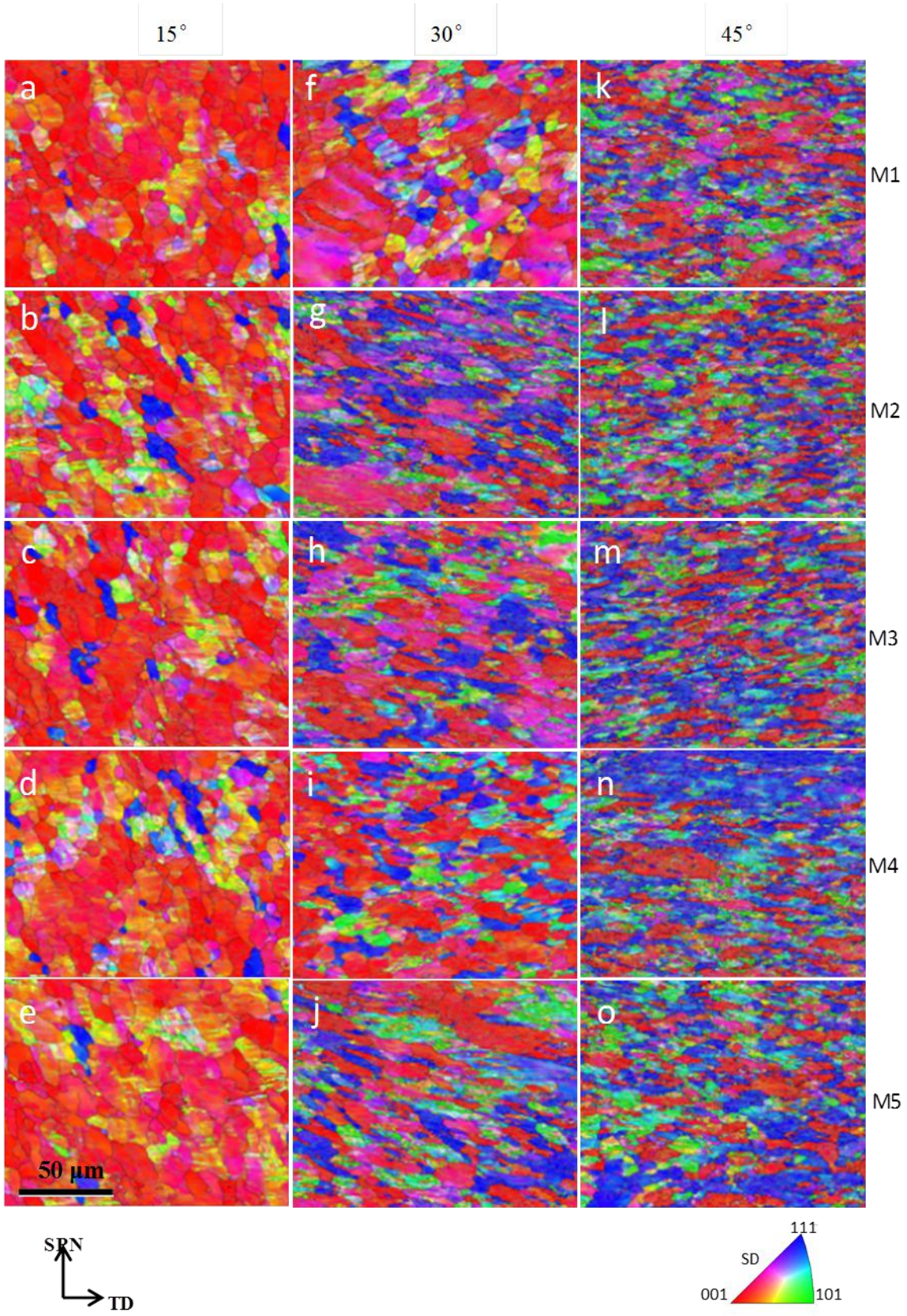

Figure 4.11 EBSD maps of CP Aluminium after HPT with the rotation angles of 15°, 30° and 45° at E-positions. At each angle 5 points were measured along the thickness: E1, E2, E3, E4 and E5 (from top to bottom).

As demonstrated in Fig 4.12, with increasing deformation to the 90° rotation (γ=4.66) and 180° rotation (γ=9.32), the degree of the grain refinement increases progressively in Fig 4.12 (a)-(j). Highly elongated structures are still dominant in morphology for all measured positions. Surprisingly, parent grains without the elongated structure are still observed at these two deformation stages. This is mainly due to the influence of the initial orientation. However a great number of new small grains emerge inside their parent grains with the different orientation colours on the EBSD map.

As the shear strain increases to γ=18.63 (360° rotation), as shown in Fig 4.12 (k)-(o), more LAGBs are transferred constantly into HAGBs. Then the substructures separated by newly generated HAGBs are converted into new grains. At this deformation stage, a large number of relatively equaixed and small grains have born from the subdivision of the elongated structures observed at the previous deformation stage. The crystallographic orientation distribution is generally homogeneous while the effect of some original grains still remains at two measurement positions: M4 and M5.

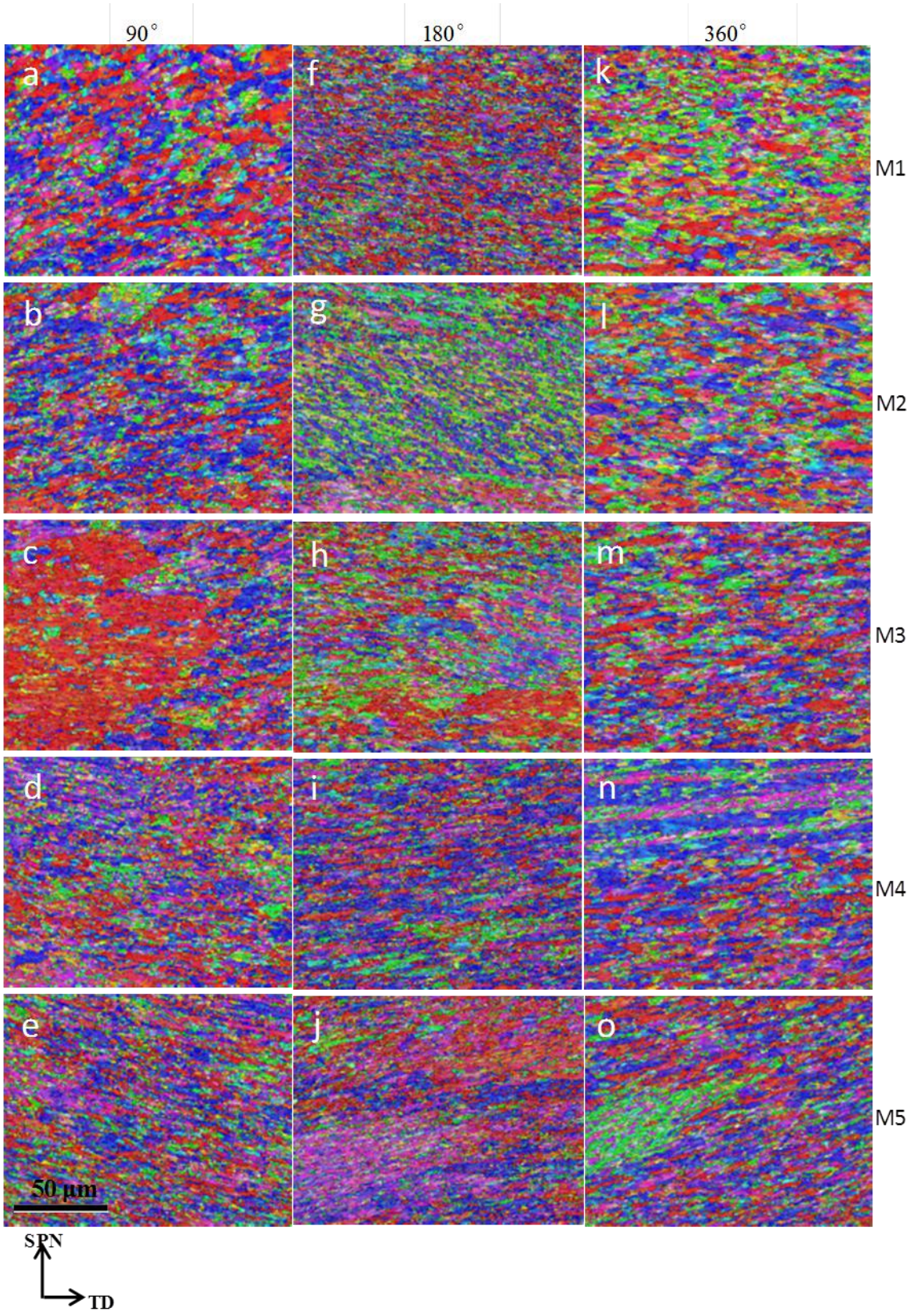

Figure 4.12 EBSD orientation of CP Aluminium after HPT with the rotation angles of 90°, 180°, 360° at E-positions. At each angle 5 points were measured along the thickness: E1, E2, E3, E4 and E5 (from top to bottom).

The EBSD maps in Fig. 4.13 represent the microstructures of the deformed discs after the rotations of 720°, 1080° and 1800° at E-positions respectively. It should be noted that the scale bar for 720° rotations is different to the scale bar for 1080° and 1800° rotations on the EBSD maps.

As the shear strain increases to γ=37.26 (equivalent to 720° rotation), the density of intragranular dislocations decreases sharply. Although a lot of LAGBs can still be observed within the grains, the interiors of the grains become cleaner and thus the colour spread within the grains tends to be homogeneous. This indicates that the accumulation of the intragranular dislocations has happened. The grain size shows a significant change compared to the previous deformation stage. It is interesting to find that the grain size at E5 is extraordinarily smaller than those at the other E positions. The grains at E5 are fairly equaxied because of the higher strain applied to this area. At E1-E4, a great amount of new grains is generated from the lamellar grains observed during the previous stage. However, the completely homogeneous microstructure and orientation has not been seen at this deformation stage, implying the strain saturation has not been achieved so far. It should be noted that the grain sizes shown in Figure 4.13 (e) are obviously smaller than those in (f) - (i). According to simple shear mode, the shear strain in all layers should be equivalent. But there are strain gradients along thickness in practice and the bottom layers are undergone more strain in most cases even after early stages. The similar situation is also observed in Figure 4.6 (j).

When the shear strain reaches γ=55.89 and 93.15 (1080° and 1800° rotations), the morphology and the colour spread during these two deformation stages are remarkably identical. This implies that the saturation of the grain refinement has been achieved.

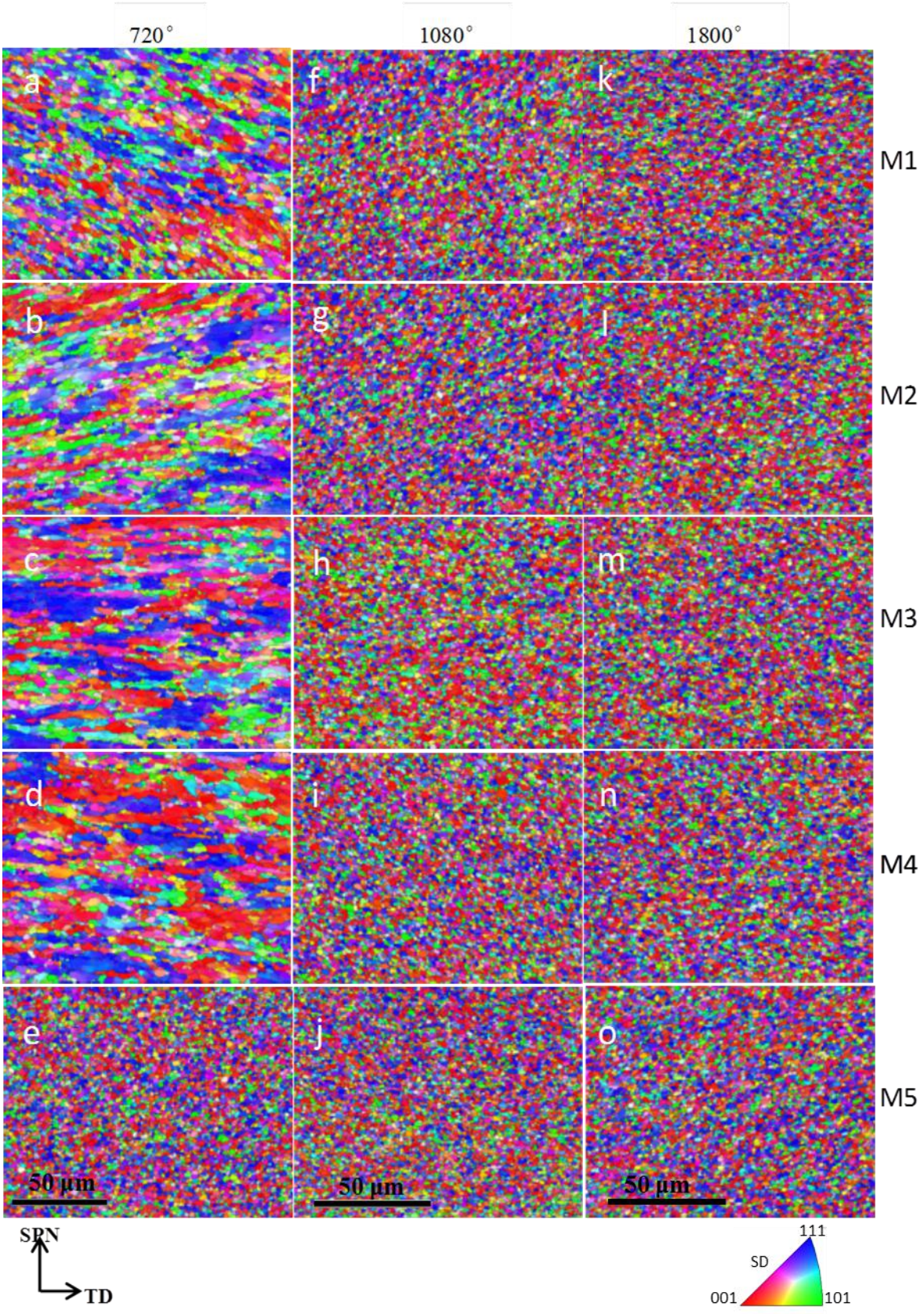

Figure 4.13 EBSD orientation of CP Aluminium after HPT with the rotation angles of 720°, 1080°, 1800° at E-positions. At each angle 5 points were measured along the thickness: E1, E2, E3, E4 and E5 (from top to bottom).

Grain size, aspect ratio of grains and misorientation distribution are quantitatively analysed in this section for E-positions.

In the EBSD analysis software Channel 5, two approaches are available to measure the grain size: grain area approach and the circle equivalent diameter approach. The grain area approach may aggravate the divergence between the big parent grains and the small new-born grains. Therefore the circle equivalent diameter is used in this section to characterise the grain size.

Figs. 4.14 and 4.15 show the average grain sizes and average aspect ratio of the grains at five locations (E1~E5) for different rotation angles. Fig. 4.16 shows the misorientation angle distributions at the E3 position for various rotation angles.

The average grain size of initial sample is the same with that in Fig. 4.8. It can be seen from Fig. 4.14 that the average grain size decreases sharply from the initial value of ~ 11 μm after annealing to the range of 5.3~6.5 μm after deformed by the 15° HPT rotation. The large error bar in Fig. 4.14 indicates that the grain size scatters significantly at this low strain level, which is a typical feature of the grain size under the low strain. As can be seen in Fig. 4.15, the average aspect ratio decreases moderately from around 2.5 at the annealed state to about 2.1 at the shear strain level of 0.78. This is mainly associated with the applied compression before the HPT rotation. In the light of the misorientation angle distribution, as shown in Fig. 4.16, the fraction of HAGBs is low and the LAGBs dominates, suggesting that the high dislocation density and sub-structure are exhibited at this deformation stage with a rotation angle of 15°.

At the accumulated shear strain γ of 1.55 (30° torsion), a great number of LAGBs are converted into HAGBs, causing the generation of new, small grains. As a result, the grain size has been reduced to approximate 3 μm. The corresponding aspect ratio increases to the maximum value of about 3 after 30° rotation. As the strain increases to the level equivalent to 45° rotation (γ=2.33), the fragmentation of lamellar structures gives rise to grain refinement and a decrease of aspect ratio in the meantime.

As shown in Fig 4.14, the grain sizes after the 30° and 45° HPT rotations are similar. However, there is a slight difference in the misorientation angle distribution. After the 30° rotation, there is a critical angle of 4°, below which the relative frequency significantly

decreases with decreasing misorientation angle. It is also observed that the fraction of substructures with the misorientation angle of less than 4° decreases after the 30° rotation.

As the rotation angle increases to 45°, the critical mirorientation angle shifts to 5°. The feature that the critical angle increases with the shear strain indicates that more dislocations and LAGBs with the relatively low misorientation angles are transferred into LAGBs with the relatively high misorientation angles and HAGBs at these two deformation stages.

Both the average grain size and average aspect ratio decrease to about 2 μm and 2.5 respectively after the 90° rotation (i.e. γ=4.66). Actually, this can be attributed to the grain fragmentation. The lamellar structures generated during the previous deformation stage are subdivided into small grains, indicating that this strain level is a significant point in the grain refinement. From the misorientation angle distribution curves shown in Fig. 416, it can be seen that the critical orientation angle grows to 6° and the fraction of substructures with the misorientation angle of less than 6° is reduced modestly.

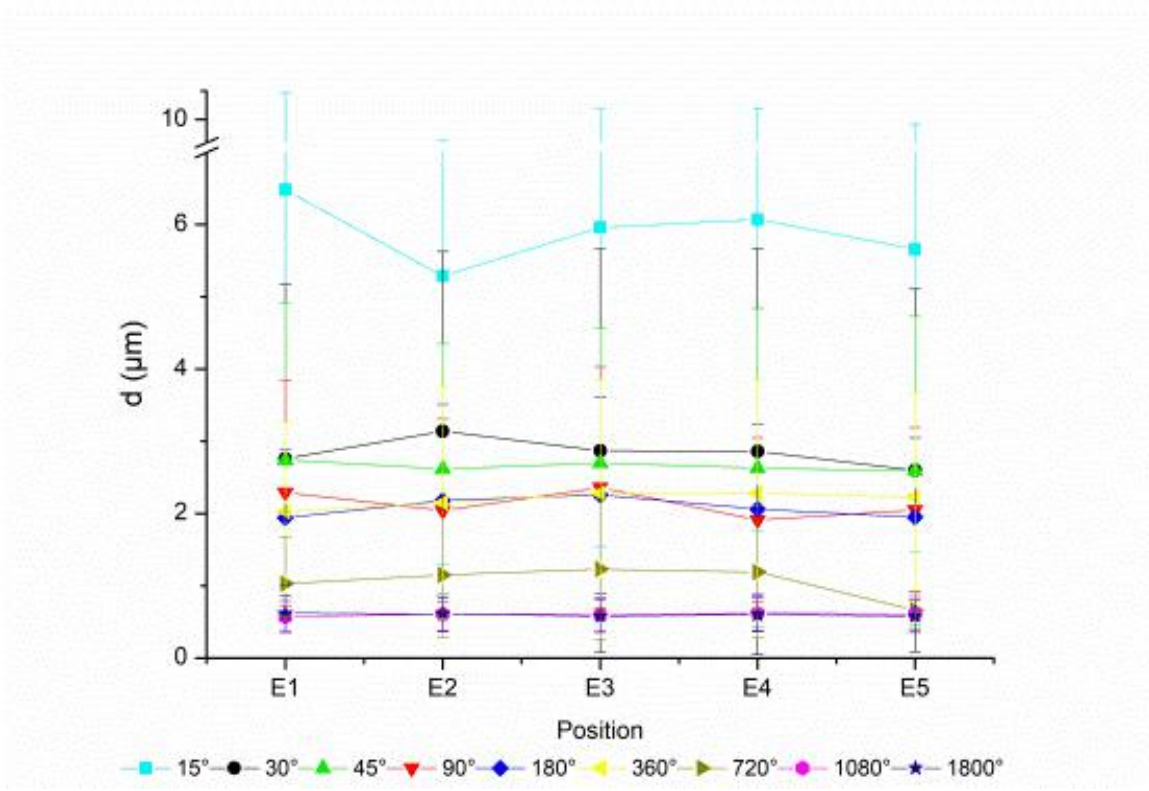

Figure 4.14 Grain size of CP Aluminium after HPT with the rotation angles of 0°, 15°, 30°, 45°, 90°, 180°, 360°, 720°, 1080°, 1800° at E-positions.

As the shear strain increases to 9.32 (180° rotation) and 18.63 (360° rotation), the grain size becomes stabilized within a narrow range and is not able to be further refined with increase in

shear strain within these deformation stages. It is noteworthy that the relationship between the grain size and the shear strain is a non-linear function.

Even though the grain sizes after the 180° rotation and the 360° rotations are similar, the microstructural evolutions are obviously different at these two stages. The aspect ratio rises dramatically after the 180° rotation, which is due to the elongation of new grains born from the grain fragmentation during the previous deformation stage. The density of substructures decline consistently because the absorption of the dislocations by grain boundaries is larger than the generation of new dislocations. The similar grain size (diameter of equivalent circle) and increased aspect ratio indicate a notable change in grain shape but there is the marginal grain fragmentation at this strain level. The grain size and aspect ratio maintain the same level after the 360° rotation. It is interesting to see that the fraction of substructures with the misorientation angles of ≤ 5° no longer drops after the 360° rotation. It shows a rising trend during this deformation stage, in contrast to the trends observed during the previous deformation stages. These microstructural characteristics imply that there is no apparent change in grain shape, but the propagation of dislocations and substructures with the misorientation angles ≤ 5° are promoted remarkably.

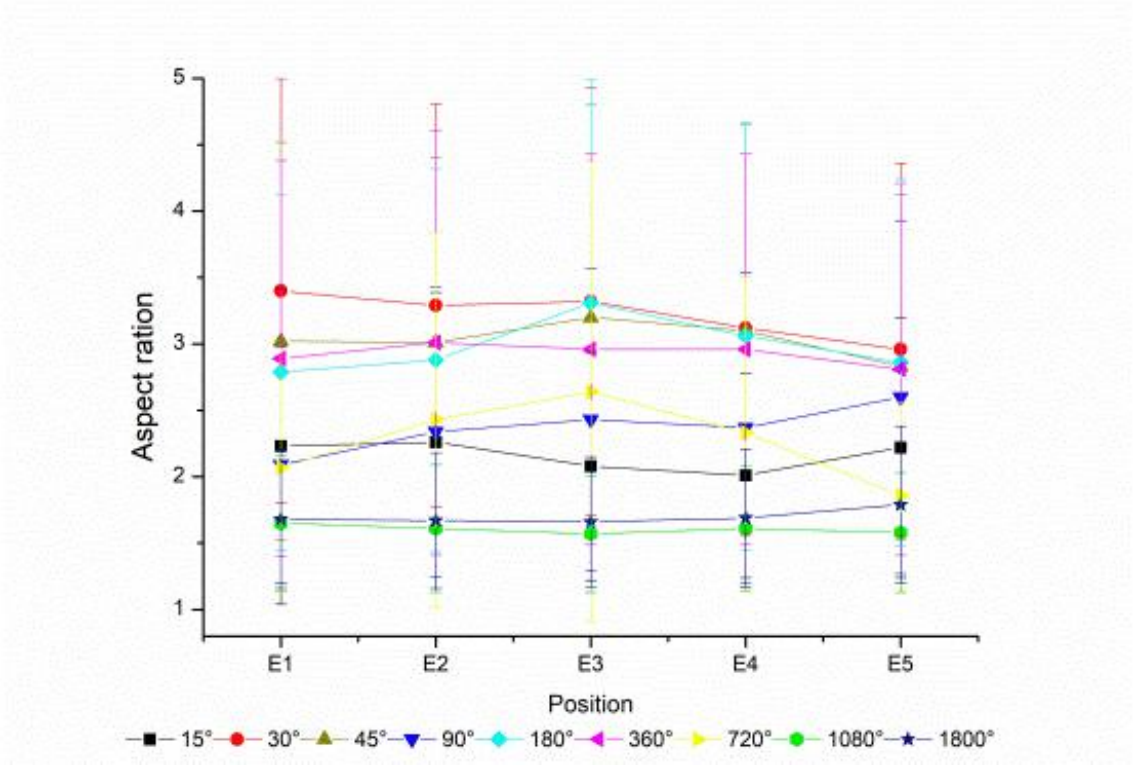

Figure 4.15 Aspect ratio of grains after HPT with the rotation angles of 15°, 30°, 45°, 90°, 180°, 360°, 720°, 1080° and 1800° at E-positions.

As the shear strain increases to γ=37.26 (720° rotation), it is easily found that a great number of new grains are formed since the surrounding LAGBs are converted into HAGBs. This causes both the grain size and aspect ratio to decrease obviously. The dislocation density goes up to the same level as for the 30° rotation but the density of substructures with the misorientation angles of 2°≤θ≤8.5° is less than that for the 30° rotation. This indicates that the dislocation propagation is accelerated and a large number of LAGBs have been transferred into HAGBs at this strain level.

As the shear strain increases to 55.89 (1080° rotation) and 93.15 (1800° rotation), the saturations of grain size and aspect ratio have been achieved. All grain sizes fall into nanometre level (about 500 nm) and the aspect ratios level out at near 1.6, which validate that HPT is a promising method to produce UFG an nc materials. By comparison with the Mackenzie distribution, it can be found that the misorientation distribution at the very high strain level approaches a random state.

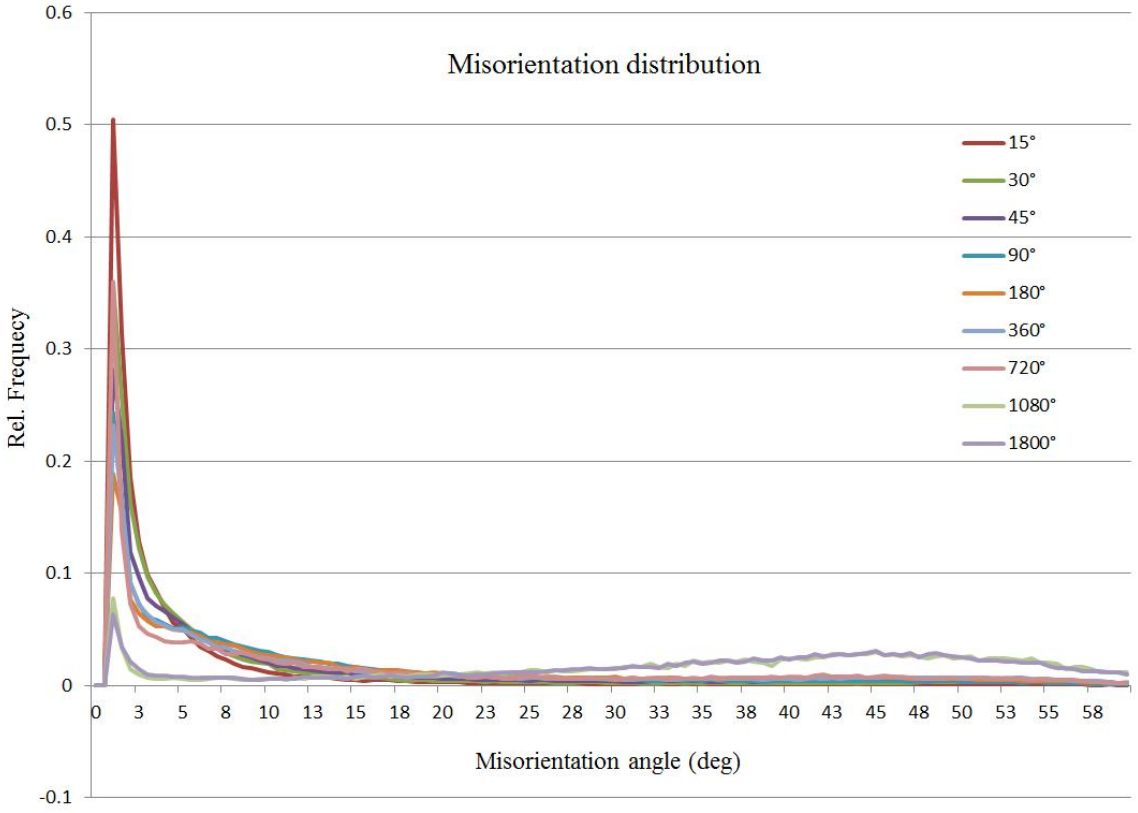

Figure 4.16 Misorientation distribution of CP Aluminium after HPT with the rotation angles of 0°, 15°, 30°, 45°, 90°, 180°, 360°, 720°, 1080° and 1800° at the E3 position.

By comparison, it is found that the grain refinement is not linked well with the magnitude of the shear strain. Specifically, the grains are finer at E-positions than those at M-positions

under the same shear strain. At M-positions, the significant grain fragmentations are observed in the shear strain ranges of $0.37 < \gamma < 1.10$ and $4.40 < \gamma < 26.4$. However at E-positions, the considerable grain fragmentations are found in the shear strain ranges of $0.78 < \gamma < 4.66$ and $18.63 < \gamma < 55.89$. It can be concluded that the shear strain is not the only determinant of the grain size, and the effect of the adjacent materials also plays a significant role in grain refinement.

4.3 Hardness of HPT processed CP Al

The hardness distributions across the diameters of the HPT deformed CP Al specimens after different rotation angles are shown in Fig. 4.17. The black line denotes the hardness of the annealed sample. It is found that the distribution of hardness is pretty homogenous for the annealed sample, which is in good agreement with the microstructure described previously. The difference between the centre and the edge of the disc in not obvious. The average hardness of the annealed sample is about 25.5HV

It should be mentioned that the distance=0 denotes the centre of the deformed disc. However the lowest hardness value sometimes may be not located at the central point especially in the cases of very low shear strain, which can possibly be attributed to the misalignment between the cylinder axis of the disc and the rotation axis of the anvils. The other reason can be attributed to the complex material flow in HPT.

It is clearly found that the hardness at all measuring points increase dramatically after the the 15° rotation. The distribution of the hardness across the disc diameter becomes inhomogeneous. The higher hardness is observed at the edges of the disc, whereas the relatively low hardness is located at the centre of the disc. This is clearly due to the inhomogeneous distribution of the applied shear strain across the disc diameter. However, at some positions with the low shear strain, such as the measured points at the disc peripheries with less than 30° rotations and at the disc centres, the hardness values are not consistent strictly with the corresponding shear strains. The reason for this is probably due to the complex material flow during HPT at the low straining stages.

At the rotation of 1800°, the hardness increases significantly. The average hardness is 64.3HV. When the distance from the centre changes from 1 mm to 5 mm, the hardness varies within a smaller range of 65-69 HV, which indicates that the saturation of the hardness has been nearly achieved at these areas. Although the hardness at the central area rises with the

rotation angle because of the effect from the adjacent areas, there is still an obvious valley at the disc centre even after the 1800° rotation. This result is in agreement with a previous study [66].

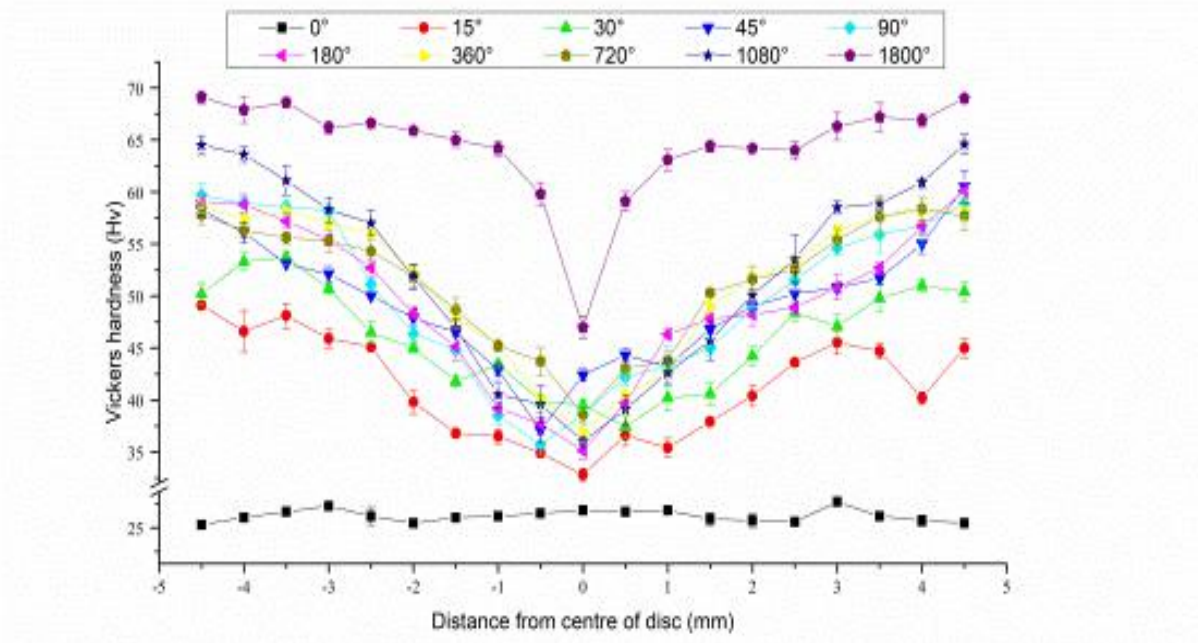

Figure 4.17 Vickers hardness as a function of the distance from the disc centre after 15°, 30°, 45°, 90°, 180°, 360°, 720°, 1080° and 1800° rotations. The black line shows the hardness of the annealed sample.

Fig. 4.18 shows the measured hardness as a function of the equivalent strain for the M positions and E positions. The hardness at the M and E positions follow the same trends, however, it should be noted that the hardness at the two positions have different values even at the same equivalent strain, which indicates the distribution of dislocations in deformed materials is not only affected by shear strain, but also depend on the conditions of adjacent grains. The sharply increasing harness corresponds to the stages where the average grain sizes decrease dramatically. At the preparatory stages for the grain refinement, the hardness at the M positions and E positions declines slightly. Hardness increases again with the strain after the equivalent strain is greater than 20 for the M positions and the E positions.

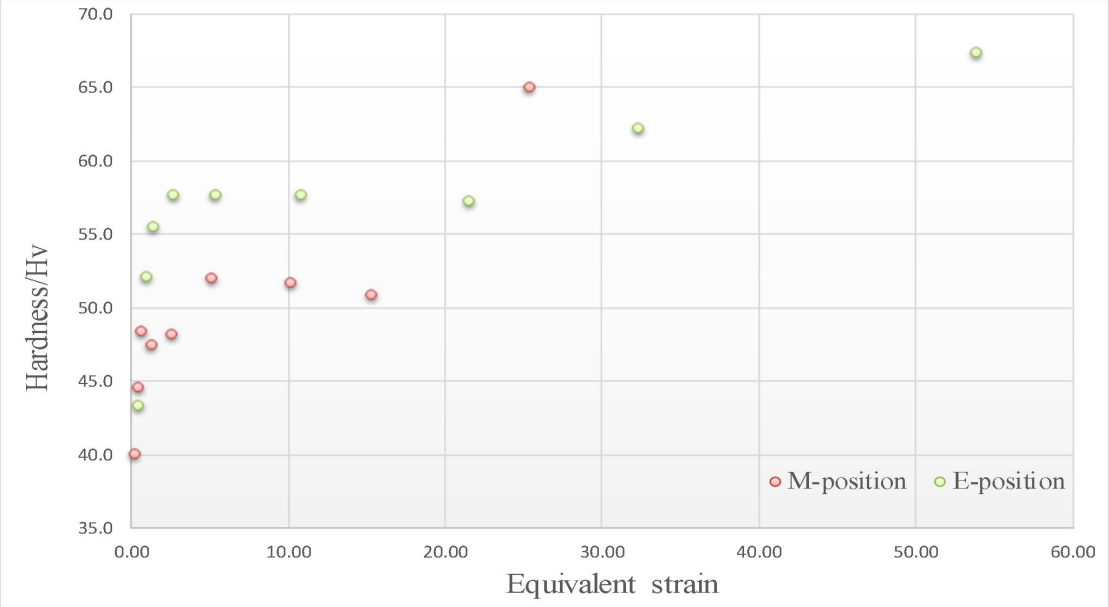

Figure 4.18 Average hardness plotted against equivalent strain for the data points at M-position and E-position. Equivalent strain was calculated from Eqn (2.2).

4.4 Texture evolution of CP Al during HPT deformation

4.4.1 Texture evolution of CP Al during HPT deformation at M-position

In Section 4.2, evolution of the microstructure of CP Al during HPT has been described in detail. The evolution of texture will be discussed in this section. Texture is essentially a cluster of the crystallographic orientations with close Euler angles. Different to other SPDs, such as plane strain deformation in ARB, material flow during HPT is more complex because the SD is constantly changing relative to the grain orientation during HPT. Due to this specific geometrical nature, textures are barely stabilised during HPT.

It is widely considered that the simple shear is a predominated deformation mode in HPT [142, 289]. The section of ODFs with φ_2=45 is used to study the texture evolution because all relevant ideal texture components for the simple shear deformation can be demonstrated in this section.

Fig. 4.19 demonstrates the texture evolution at the M-positions of the deformed discs after up to 1800° rotation. At each rotation angle 5 points were measured along the disc thickness. Cube crystallographic orientation and all ideal texture components of A/A_b, A^*_1, A^*_2, B/B_b and C are marked at the top of this figure. The ODF of the annealed sample is shown in Fig. 3.6.

At the early deformation stage with a very low shear strain of 0.37 (equivalent to 15° rotation), the textures of the annealed sample have significant effects on the textures of the deformed disc. It is found that the Cube component and the C component (i.e. Rotated Cube component) predominate at this stage. It is noteworthy to know that the texture gradient along the disc thickness is obvious. The strength of the Cube component decreases from the upper surface to the bottom surface of the disc whereas the C component has an opposite trend. The above results indicate that part of the Cube texture component has been transformed into the C component.

At the rotation angle of 30° (γ=0.73), the Cube component sustains whereas the C component tends to disappear. When the rotation angle increases to 45° (γ=1.10) , the HPT deformation causes significant change in texture. The Cube component becomes weak, especially at the bottom areas, and the Cube orientation almost vanishes, and the weak orientations occupies the positions close to the ideal B/B_b component. According to the Taylor theory, for the small strains applied to the equiaxed original grains, the Taylor full constraint condition should be satisfied [289]. Under these conditions, the texture components with high Taylor factor, such as the Cube and C orientations, are not stable [142]. Therefore the Cube and C texture components tend to vanish at these low strain stages.

A further increase of the rotation to 90° (γ=2.20) results in some newly developed textures. The development of textures is in good agreement with the microstructure evolution; in other words the grain refinement and dislocation propagations are observed at this strain level. With increasing deformation to the 180° rotation (γ=4.40), there is a slight change in texture. During this stage, the grains are elongated whereas the serious fragmentation of grains is barely observed. It is found that the C ideal orientation becomes a strong texture once again. As the shear strain increases to the medium level (γ=4.40), grains are elongated dramatically. In such condition, the full constraint Taylor mode is not valid anymore and is replaced by the Taylor relaxed strain constraints (RC) mode [289]. Thus the stable C texture component under this condition is strengthened. A significant texture gradient across the disc thickness is found at these stages, namely the intensity of the C component is higher at the areas near the bottom of the HPT deformed disc.

At the rotation angle of 360° (γ=8.80), almost all ideal simple shear orientations are present. According to previous microstructural observations, both the drastic grain fragmentation and grain elongation are found at this strain level. As explained before, the re-strengthening of the

C texture component can be attributed to the elongation of the grains at this stage. The grain fragmentation should be responsible for the prevalence of other textures. Actually the grain fragmentation arises from the diverging rotation of sub-grains inside the parent grains during the plastic deformation. A great number of new-born grains with small aspect ratios are generated from their rotations towards stable textures, which will reduce the Taylor factor. As a result, the texture components of A/A_b, A^*_1 and A^*_2 with low Taylor factors are formed.

With increasing deformation to the 720° rotation angle (γ=17.6), the A/A_b, A^*_1 and A^*_2 texture components observed at the previous deformation stage have evolved into considerably weaker textures while the HPT deformation promotes the intensity of B/B_b ideal orientations. A further increase of the shear strain to γ=2.20 (1080° rotation) is a transition stage where the B/B_b texture components become strong. This is possibly due to the continuous recrystallisation in Al at high plastic strain [289]. When the material is deformed by the 1800° rotation (γ=44.0), a typical orientation distribution of the simple shear mode at high strain level can be seen with the predominance of the B texture components (including C component) and the less strong A components. The stability of the C ideal orientation will be discussed later.

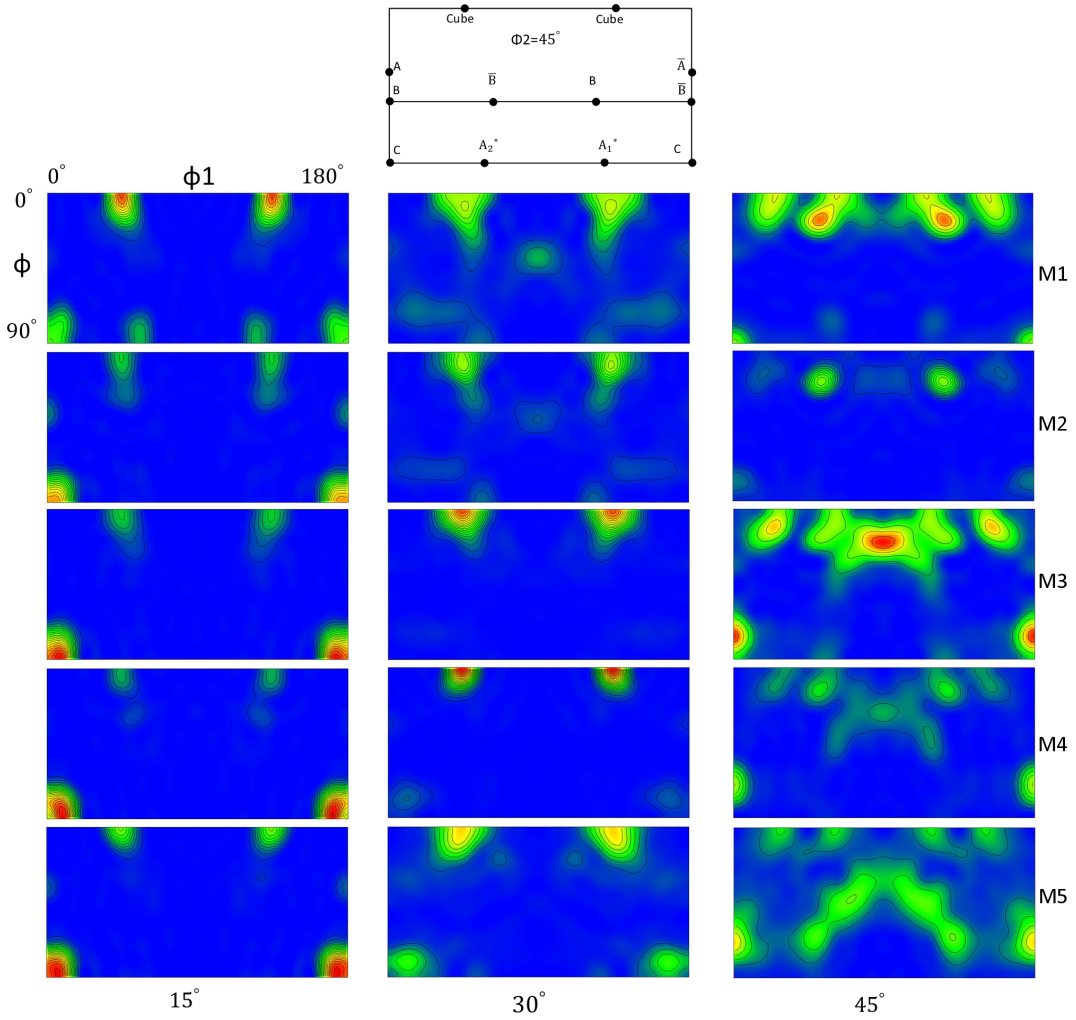
Cube
Cube
Φ2=45°
A
B
B̄
B
Ā
B̄
C
A2*
A1*
C
0°
ϕ1
180°
0°
ϕ
90°
M1
M2
M3
M4
M5
15°
30°
45°

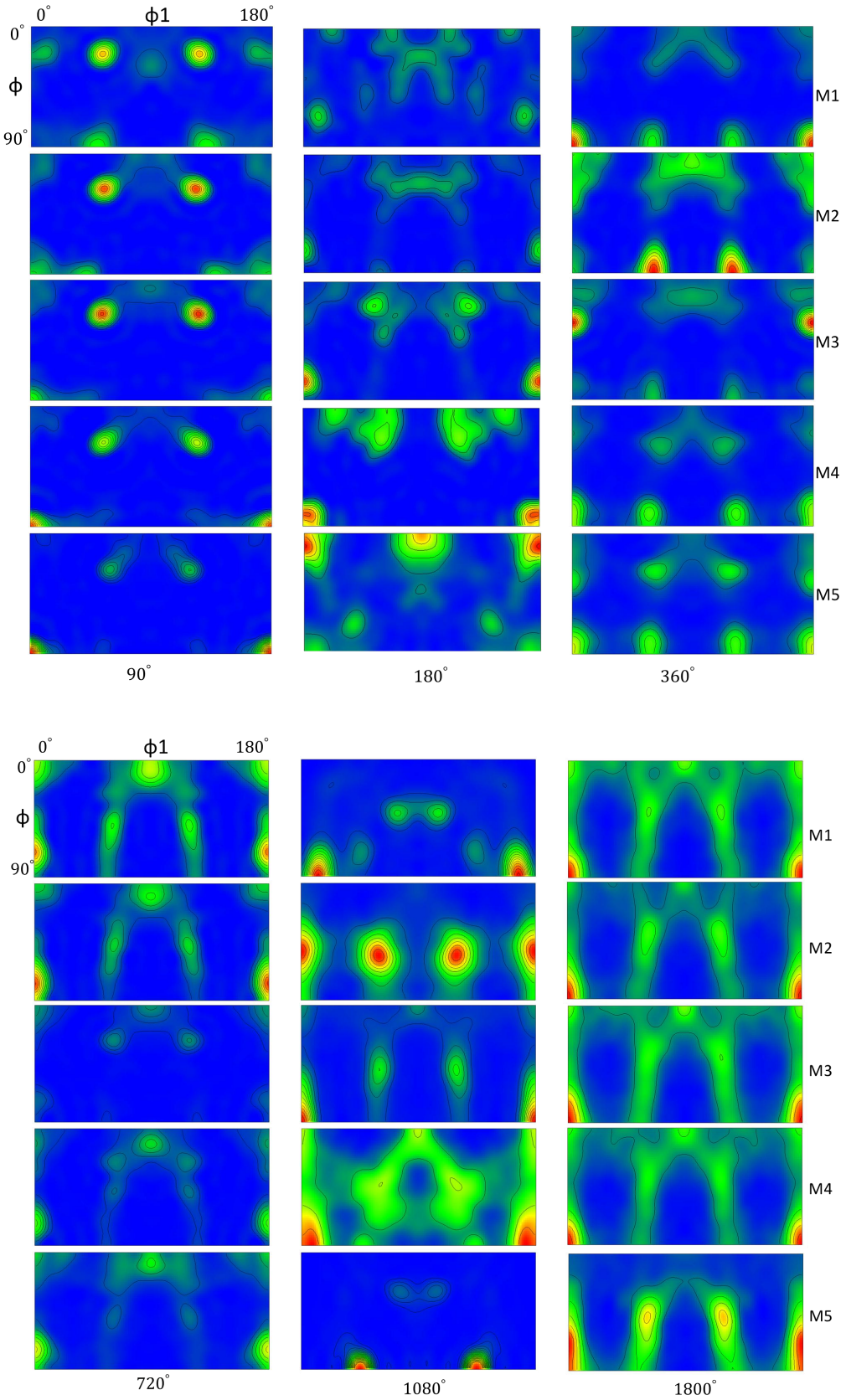

Figure 4.19 ODF maps of CP Aluminium after HPT rotations of 15°, 30°, 45°, 90°, 180°, 360°,720°, 1080° and 1800° at M-positions. At each angle 5 points were measured along the thickness: M1, M2, M3, M4 and M5 (from top to bottom).

4.4.2 Texture evolution of CP Al during HPT deformation at E-position

Fig. 4.20 demonstrates the evolutions of textures at five E-positions after different rotation angles. The original textures in the annealed sample, dominated by the Cube component and the residual extrusion texture (C component), can still be observed on the ODF maps of the sample subjected to the 15° rotation (γ=0.78). But these original textures gradually disappear with the increase of the shear strain.

At the rotation angle of 30° (γ=1.55), textures after the 15° rotation have been replaced by newly developed textures of B/B_b. The B/B_b texture components tend to spread to the ideal A^*_1 and A^*_2 orientation positions at the bottom areas. When the rotation angle increases to 45° (γ= 2.33), most of the B/B_b texture components have already been transformed into the components of C, A^*_1 and A^*_2. The reconcentration of the C component might be contributed to the grains elongation at this strain level.

Due to the 2/m symmetry of the HPT deformed specimen, the monoclinic sample symmetry is applied to HPT. As a result, the symmetrically equivalent components A/A_b and B/B_b should have the identical intensity in the section of ODFs with φ_2=45 in theory. However, slight intensity difference in these symmetrically equivalent components at low strain stages has been observed. This is probably due to incomplete development of the simple shear texture during these stages.

With increasing deformation to the 90° rotation (γ=4.66) and the 180° rotation (γ=17.6), the prevalence of the C, A^*_1 and A^*_2 texture components has been gradually replaced by the newly developed B/B_b texture components with high intensities. The fragmentation of the lamellar structures resulting in the generation of relatively small grains is most likely responsible for the decrease of the ideal C orientation.

As the shear strain increases, the new-born grains are elongated once again. As a result, the C texture component with high intensity predominates after the 360° rotation (γ=18.63). The key textures at this deformation stage are similar to the textures after the 45°rotation. It is found that the microstructures at these two stages are similar, namely the great elongated cell structures are dominant although the grain sizes are different. In addition to the strong C texture component, the weak A^*_1, A^*_2 and B/B_b components are found during this deformation stage.

At the rotation angle of 720° (γ=37.26) textures concentrate on the C, and B/B_b components. According to the previous observations in Section 4.24, saturation of the grain size has been achieved after the 1080° rotation (γ=55.89). It is known that for a high SFE FCC material, the typical simple shear textures are composed of a strong B fibre (including the C texture component) and a less strong A fibre [240], which is in good agreement with the observations in the present study. Textures observed after the 1080° rotation are weakened after the rotation angle increases to 1800° (γ=93.15). Generally further deformation causes greatly divergent orientation rotation. As a result, the orientation spread is promoted and textures at this stage do not change too much.

The texture evolutions at the M positions and E positions can be divided into similar stages. At the beginning, the initial textures (Cube and C component) have considerable influence. With the development of deformation, the weak B/B_b components appear at the expense of the initial Cube and C components. The C, A^*_1 and A^*_2 components prevail during the next stage. As the shear strain increases, the B/B_b components are found again. Finally, the typical simple shear textures with the strong B components and less A components are observed at the stage with the grain refinement saturation. The texture components at the M and E positions are different under the same shear strain. It is concluded that the texture evolution is not just a function of the shear strain, but is also effected by the neighbouring materials.

It is believed that the material flow is complicated in HPT. The constant change of the SD hinders the formation of stable textures. Therefore, it is reasonable to conclude that the simple shear textures periodically change with the formation and disappearance of the ideal components. This phenomenon is observed by simulations [176, 290] and experiments [129, 291]. However, this study found that from a certain strain level onwards (γ=55.89 at the disc edge), textures in the HPT deformed sample do not evolve with the increase of the shear strain anymore. This texture stability is in good agreement with the previous experimental observation [150]. In addition, it was reported [129, 176, 292] that the C texture component is relatively stable during the HPT deformation, and is capable of being sustained up to high equivalent strain ε of ~4 [176] . But in this study the C texture component is stable under the equivalent strain ε of~ 53.78 (γ=93.15).

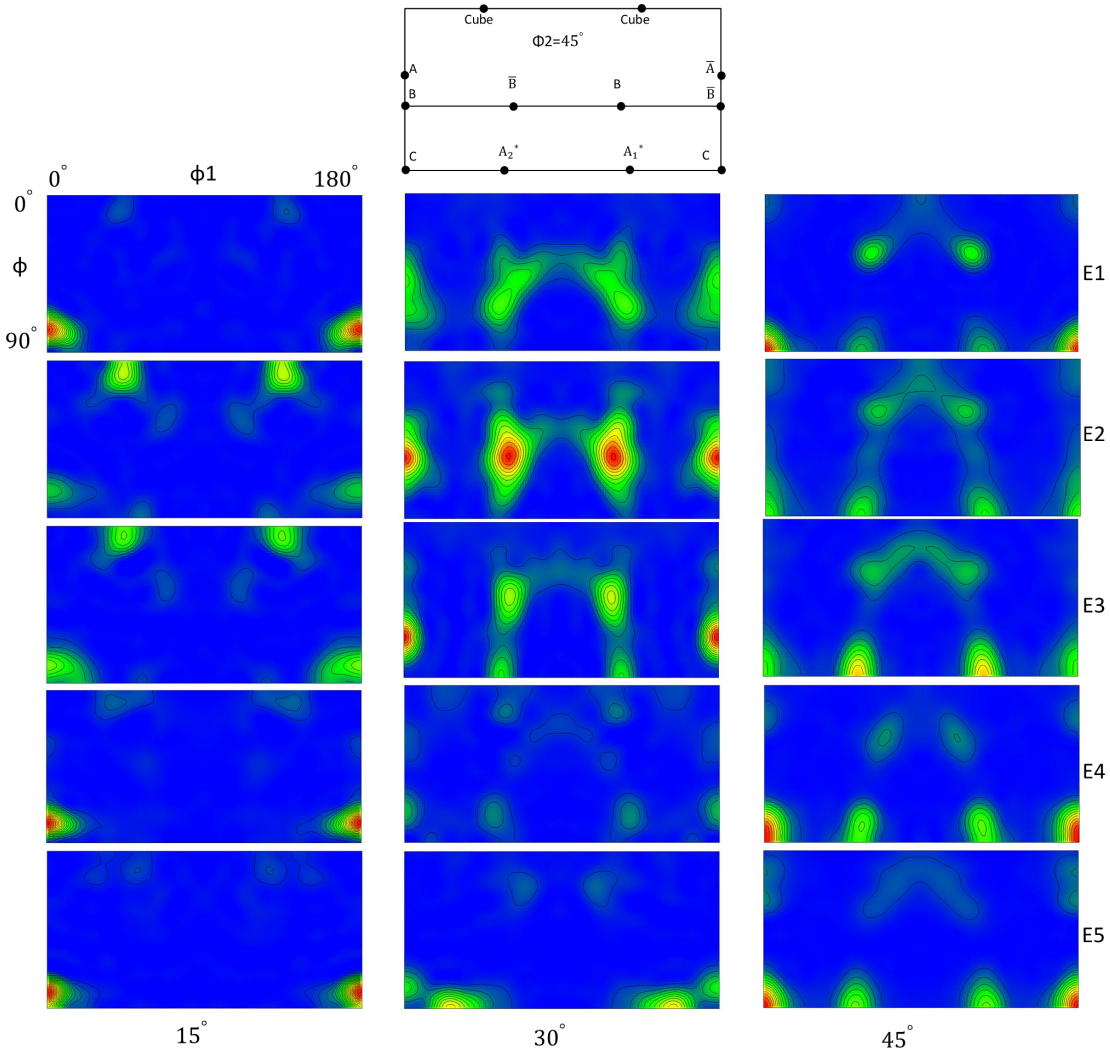
Cube
Cube
Φ2=45°
A
B
B̄
B
Ā
B̄
C
A2*
A1*
C
0°
ϕ1
180°
0°
ϕ
90°
E1
E2
E3
E4
E5
15°
30°
45°

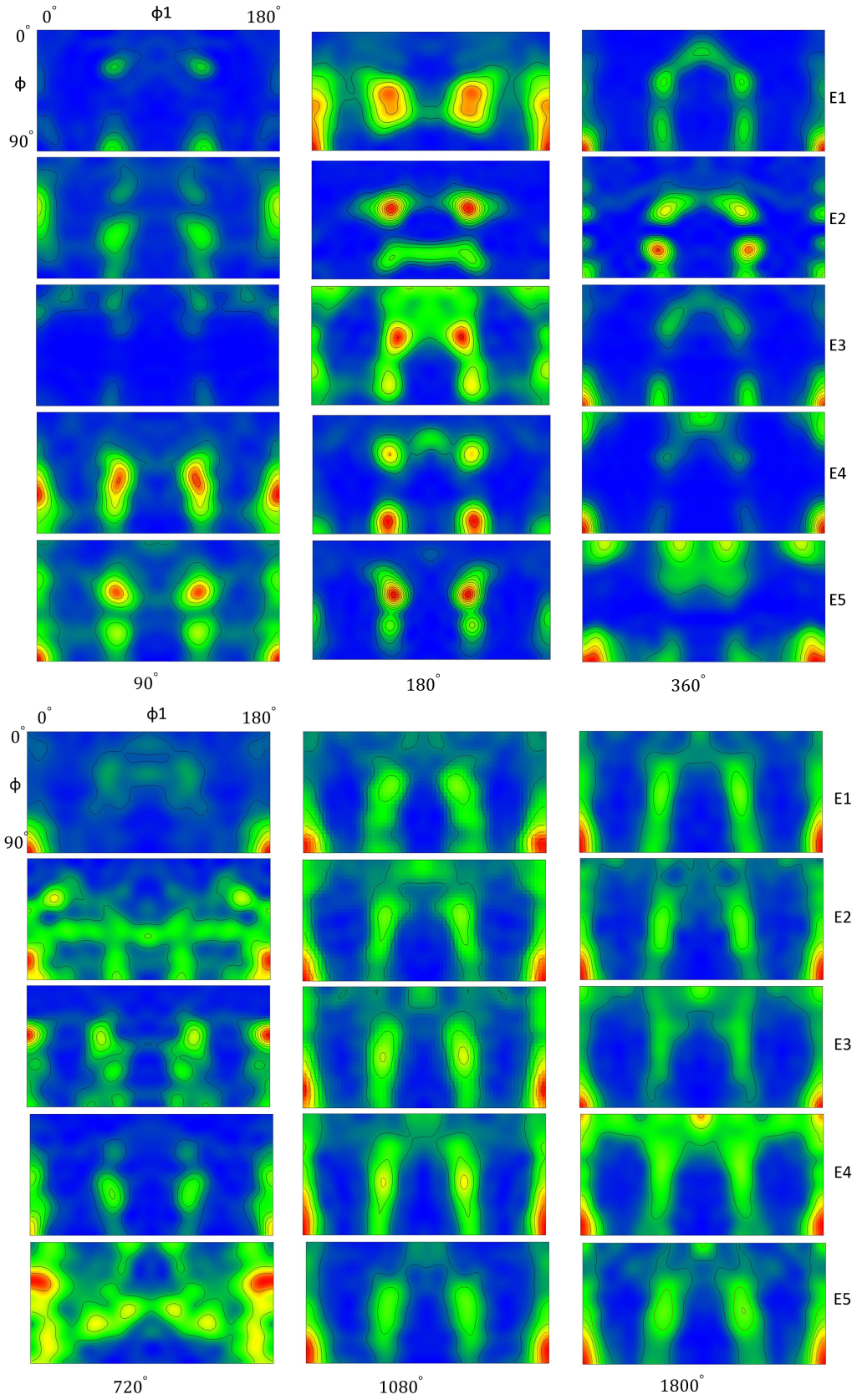

Figure 4.20 Texture of CP Aluminium after the torsion of 15°, 30°, 45°, 90°, 180°, 360°,720°, 1080° and 1800°, at E-position of deformed discs. At each angle 5 points were measured along the thickness: E1, E2, E3, E4 and E5 (from top to bottom).

4.5 Summary

In this chapter, the evolution of microstructural characteristics, textures and hardness of the HPT processed CP Aluminium were studied. The research findings can be summarised as follows:

(1) Grain refinement is not a linear function of the shear strain in HPT. Significant grain refinement mainly takes place during two stages. One stage is in the shear strain range of ~0.4＜γ ＜1.5, where the dislocations are highly active. The accumulation of the dislocations results in the formation of LAGBs. Finally HAGBs are converted from LAGBs by the continued dislocation absorption. Another stage is observed in the shear strain γ range of ~18-55 where the grain refinement is attributed to the fragmentation of the lamellar structures. Between these two stages, grains are elongated without the fragmentation. After the shear strain γ of ~55 at the disc edge, the saturation of the grain refinement has been achieved.

(2) The distribution of hardness is inhomogeneous throughout the diameter of the disc after the HPT deformation. It is observed that the central hardness is significantly lower than the hardness at the periphery of the disc. This result supports the conclusion that the HPT deformation cannot produce fully homogeneous microstructures even after a large number of revolutions [66]. As a material with low SFE, the softening phenomenon in the hardness of commercial purity Aluminium is barely found in this study.

(3) Textures of the annealed sample have a dramatic influence on the texture evolution during HPT at low levels of shear strain up to about 1, whereas during high shear strain stages, the initial textures have no effect on the observed textures. The typical texture components in the HPT deformed CP Al are the {111} fibres (A^*_1, A^*_2 and A/A_b) and the <110> fibres (B/B_b and C). These fibres are formed and vanish periodically due to the intrinsic instability of the material flow. Generally, the A/A_b ideal orientations tend to appear during the stage which has a great number of structures with the low aspect ratio, whereas the C texture component is associated with the presence of the elongated grains. The C component is relatively stable and is able to be maintained during the stages with very high shear strain.

(4) The gradients of microstructure and texture along thickness have not been report in past studies. Obvious gradients of microstructure and texture across the disc thickness are observed for the low applied strains. At the early stage of deformation, the low anvil of HPT machine drives the bottom surface of the disc rotating while the upper anvil is still stationary.

As a result, the materials in the bottom areas flow prior to that in the upper areas. However, the microstructural and textural gradients vanish at the high stain stages.

Chapter 5 High pressure torsion of stacked CP aluminium

It is well know that HPT is capable of producing UG materials or nanocrystallines. Conventionally, dislocation activities dominate the plastic deformation mechanism for pure Al at room temperature. Dislocation nucleation occurs within grains and at GBs and the dislocations glide on the slip plane along the slip direction to produce plastic deformation when the resolved shear stress exceeds a critical value. According to this mechanism, it is reasonable to speculate that fine grains will result in high material strength because the high density of GBs associated with the fine grains act as barriers to prevent the onset of the dislocation slip. However, in practice softening has been observed in many studies when the grain size decreases below a certain value [179-181], which suggests that different mechanisms are responsible for the plastic deformation in this grain size range [192].

It is generally considered that GB mediated processes, such as GB migration and grain rotation, are the alternative mechanisms. The grain size is the critical variable. It is reported that the grain coalescence induced by GB rotation prevails in polycrystalline materials with average size of tens of nanometres, while GB migration dominates in UFG materials [225]. In order to explore the potential mechanism of the grain rotation, nc polycrystalline materials with initial grain size of the order of several tens of nanometres were used as starting specimens in indentation [203, 224], uniaxial loading [235, 236], tensile [204, 228, 237] and HPT [225-227, 238] [205] at room temperature. During these studies, the stress, not the strain [233] and diffusion [224], increases the average grain sizes to approximate 100 nm due to the grain rotation and coalescence.

Many in-situ experiments [192, 203, 293] conducted at room temperature found that the GB migration rather than the grain rotation plays an important role in sub-micrometre grain size range. However, because of the limitation of in-situ experiment and the sample geometry, only thin films were employed. The grain structures may be relaxed and the GB structures may change during the sample preparation, resulting in the influence on the results. So far no GB migration during HPT has been reported. Therefore an opening question is raised: is there any GB migration during HPT in bulk UGF materials? If yes, what is the potential mechanism responsible for it?

In this chapter, the experiments were designed to investigate the GB mediated processes during HPT: Two discs were stacked and carefully aligned with each other, followed by HPT

deformation. The interface of two stacked discs was employed as a reference to analyse the GB mediated processes. In addition, the microstructural and textural evolutions in the HPT processed two-layer samples are investigated in this chapter. These results will be compared with those of the one-layer HPT deformed samples to study the difference of deformation behaviours between one-layer and two-layer mode.

5.1 Experiment procedure

Commercial purity Aluminium rods consisting of Al of 99.7 wt% were used in this study. The rod was produced by extrusion and had a diameter of 15 mm. In order to fit the cavities of the HPT dies, the diameter of the extruded rod was reduced to 10 mm by lathing. Subsequently, the rods were sliced into the discs with the thickness of ~0.85 mm by wire cutting.

Annealing of these discs was undertaken at a temperature of 300℃ for 2 hrs in atmosphere, and then these samples were placed at room temperature for complete air-cooling. The average grain size of the annealed samples is approximately 11 μm.

The oxide layers on the contact surfaces of two discs were removed by grinding using Struers AccuStop, which is a sample holder and can provide excellent reproducibility for the thickness reduction. The deformed layer resulting from the wire cutting and the layer contaminated by silicon carbide during grinding were removed by means of a stainless steel wire brush. Eventually, the specimen thickness was reduced to around 0.75 mm. It is noteworthy that the total thickness of the two stacked discs was approximately 1.5 mm which is moderately larger than the depth of the cavity between the two anvils. This ensured that the cavity was able to be fully filled with the deformed materials, thereby the extremely high pressure and friction imposed on the specimens can be achieved during the HPT deformation.

Two identical sizes of the discs were stacked in the cavity between the two anvils. Their cylinder axes were aligned with each other. The stacked specimen was deformed by the constrained HPT mode at a constant and slow rotation speed of ~0.5 rpm at room temperature to prevent the heat effect. The upper anvil was fixed whereas the lower anvil was moved up towards upper anvil to provide a compressive pressure of ~6.16 GPa. The rotational deformation was carried out by rotating the lower anvil by 15°, 30°, 45°, 90°, 180°, 360°, 720°, 1080° and 1800°.

The GB migration, microstructural and textural evolution during HPT were studied by means of the EBSD characterization using the JEOL JSM-7001F FEGSEM equipment. The observed TD-SPN plane was polished to mirror-like surface by electrolytic polishing.

When the distance to the centre is greater than 4.5 mm, the thickness of sample decreases dramatically. As a result, for the microstructural and textural characterization, the measured points located at two positions, namely 2mm (M-position) and 4mm (E-position) away from the cylinder axis respectively are selected in this study. 3 points were selected at each layer along the thickness of the HPT deformed discs. Therefore, there were totally 6 measurement points at the M and E positions respectively, marked as M1, M2, M3, M4, M5, M6 and E1, E2, E3, E4, E5, E6 arranged from the top to the bottom of the deformed disc, as marked by the red dashed rectangles in Fig. 5.1. And the sizes of these points refer to table 3.1. In terms of the observation of the GB migration, the EBSD characterization will be conducted around the interface between the two stacked discs. All EBSD maps shown in this chapter are viewed from the SD (or TD-SPN) plane.

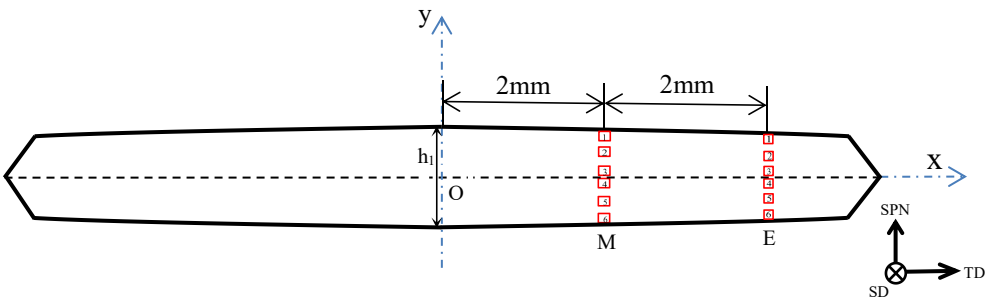

Figure 5.1 Axial section (side view) of a HPT deformed disc. The measurement points are depicted by red rectangles: M1, M2, M3, M4, M5 and M6 at the middle positions of the disc and E1, E2, E3, E4, E5, E6 near the edge of the disc.

The testing parameters of the Vickers hardness measurements on the deformed discs are the same as those used in Chpater 4 except that the hardness was measured for each of two stacked discs, as shown schematically in Fig. 5.2. There are 19 measurement locations along the disc diameter at each layer. At each measurement location, four hardness tests were conducted and the hardness used in the following analysis is the average of four measured values.

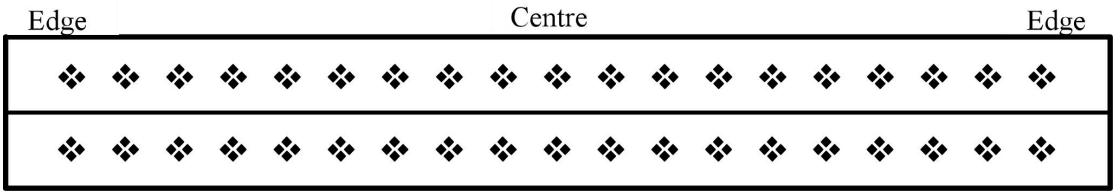

Figure 5.2 Schematic illustration of locations for hardness measurements along the diameter of the disc after HPT. Hardness used in the analysis is the average of of 4 measured hardness.

5.2 Microstructural evolution of stacked CP Aluminium during HPT

5.2.1 Microstructural evolution at M-position

Fig. 5.3 demonstrates the EBSD maps of the HPT deformed specimens after the rotation angles of 15°, 30° and 45°. The initial status of microstructure has a considerable effect on the microstructure at the early deformation with the rotation angle of 15° (shear strain of γ=0.37). The original grain shapes are largely sustained at most areas, whereas a great number of substructures emerge inside the grains. It should be mentioned that most substructures are the discontinued substructures at this stage. The formation of the substructures can be attributed to the tangles of dislocations. A great number of the dislocations is generated at the onset of the HPT deformation. As the deformation proceeds, the dislocations are tangled to form dislocation walls.

Subsequently, these dislocation walls are transformed into the substructures with misorientation angles of $2° \leq \theta < 15°$ by absorbing more dislocations. It is well known that the colours of grains on the EBSD maps are associated with their crystallographic orientations. At this stage, the distribution of the intragranular colour is no longer homogeneous. The colour spread within the grains suggests that these grains are distorted by the shear strain resulting from the HPT deformation.

Although the shear strain is very low during this stage with the 15° rotation angle, it is clearly found that there are remarkable discrepancies between the upper disc (M1-M3) and the lower disc (M4-M6). As shown in Fig. 5.3, the densities of substructures within M4-M6 are obviously higher than those inside M1-M3. The abnormal microstructure of M4 possibly contributes to the secondary recrystallization happened during annealing. At the onset of deformation, the extremely coarse grain generated from the secondary recrystallization is fragmented and many new grains are born from the parent grains.

At the rotation angle of 30° (γ=0.73), the deformation in both discs is more severe than the previous stage. Wider colour ranges are observed on the EBSD maps, especially the proportion of the green colour which represents the {111} <u v w> fibre increases significantly. The density of the substructures inside the grains ascends dramatically with the increase of the imposed shear strain, and the most discontinued substructures have been transformed into the continuous substructures. It should be noted that the initial grain shapes are still remained in the upper disc while they begin to vanish in the lower disc at this stain level.

The initial grains are not able to be identified from the EBSD maps after the 45° rotation angle (γ=1.10). As the imposed shear strain increases to this level, grains are elongated along the flow lines due to the geometrical nature of the simple shear deformation[56]. Grains are changed from the regular potato-like shapes to the irregular shapes. Parts of these jagged grains protrude into their neighbouring grains. Slip systems are activated and the crystal lattices spun during HPT. As a result, a lot of new, equaxied and small grains emerge within their parent grains and at the grain boundaries, which will cause the increase in the GB misorientation angle. In addition, several continuous HAGBs denoted by the solid black lines have been changed to the discontinued HAGBs. The density of the substructures increases drastically compared to the previous deformation stage.

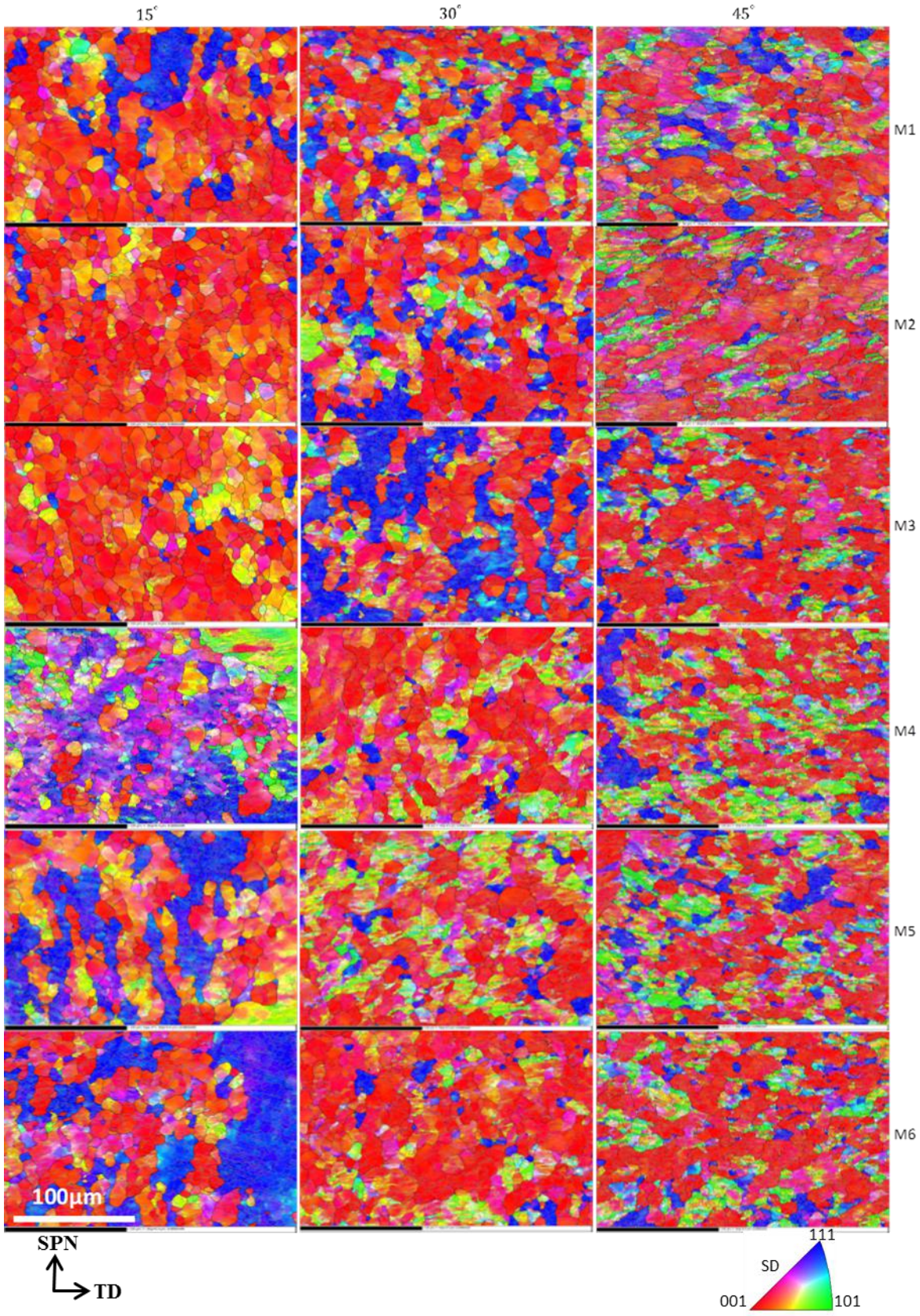

Figure 5.3 EBSD maps of two-layer disc after HPT with the rotation angles of 15°, 30° and 45° at M-positions.

As shown in Fig. 5.4, with increasing deformation to the rotation angle of 90° (γ=2.20), the gains are significantly refined. Concurrently, the elongation of the grains is enlarged to a high level. In the light of the morphology observed on the EBSD maps, the colours distribution seems to be more homogeneous. Periodic colour spread can be observed at this stage. There is slight difference in the colour distributions between the upper disc and the lower disc. The portion of the {111} <u v w> fibre is higher in the upper disc than that in the lower disc, whereas the {110} <u v w> fibre in the lower disc is stronger than that in the upper disc, suggesting that the upper disc and the lower disc have different dominant textures. It is surprisingly found that two coarse grains still exist at the M4 position.

At the rotation angles of 180° (γ= 4.40) and 360° (γ=8.80), there are no great changes in the morphology of the deformed specimen in comparison with the previous stage. It seems that the evolution of microstructure is not a linear function of the HPT shear strain. It is reasonable to postulate that there may be some steady-state stages over the full strain range. There won't be significant changes in the morphology within these steady state stages even if the shear strain has been raised by a factor of 4 from the 90° rotation angle to the 360° rotation angle. It has been observed that the colour range in the upper disc is different to that in the lower disc. This discrepancy maybe results from the contact surface slip at the low strain stages. In addition, some coarse grains originating from annealing are still found in several areas, but new grains have born within these grains.

The lamellar structure is a microstructural feature in the HPT processed sample. However, it should be noted that this lamellar structure is only the projection of actual grains on the observed SD plane. The 3-dimensional shapes of real grains are shrunk along the SPN direction and stretched in the SD and TD directions during HPT. That means that the 3D shape of the grains actually looks like a bun. Under the simple shear deformation mode, the flow lines of the materials tend to be parallel to the shear plane with the increase of the imposed shear strain.

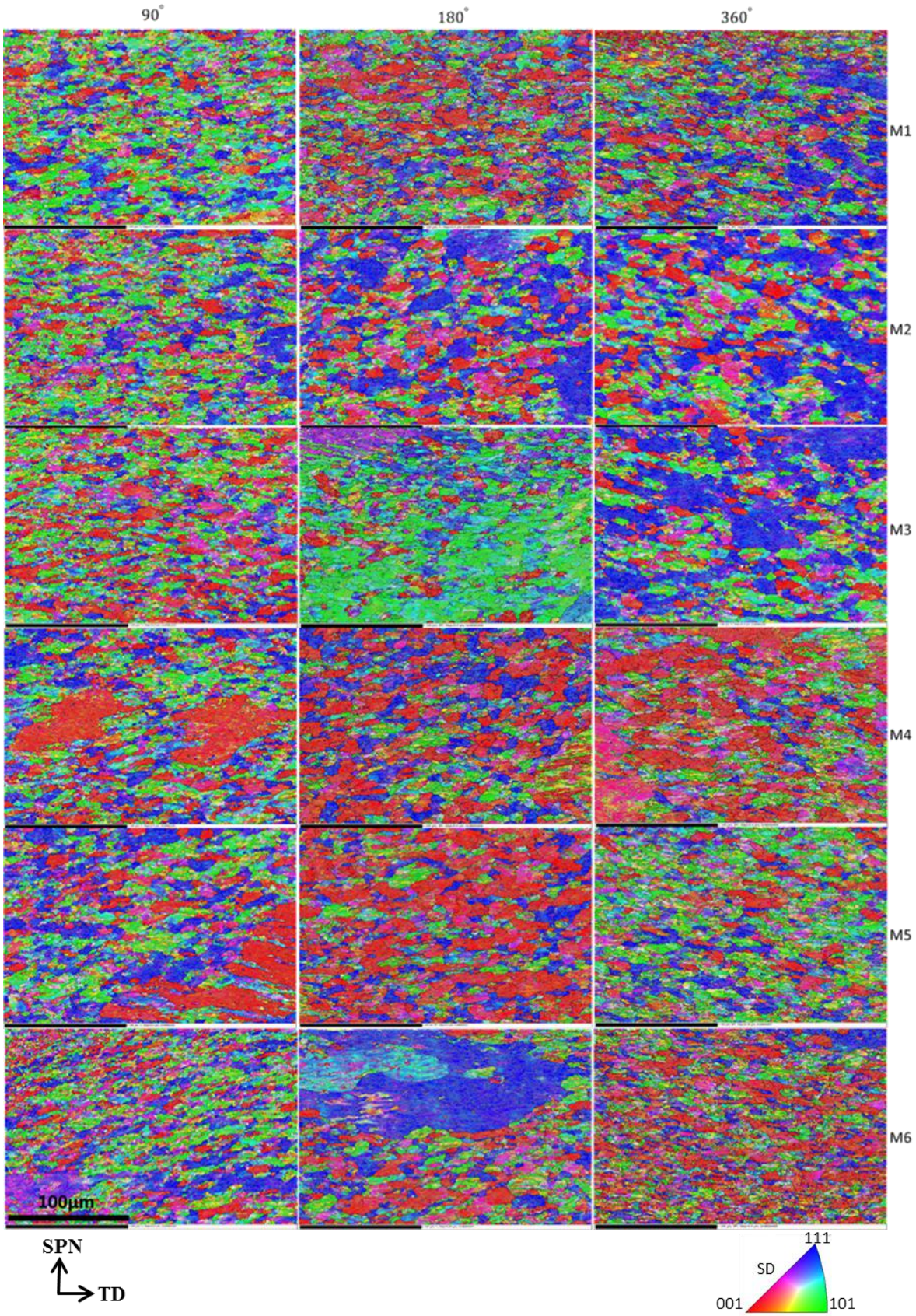

Figure 5.4 EBSD maps of two-layer disc after HPT with the rotation angles of 90°, 180° and 360° at the M-positions.

Fig. 5.5 shows the EBSD maps of the deformed specimens after HPT with the rotation angles of 720°, 1080° and 1800° at the M positions. At the shear strain of γ=17.6 (equivalent to 720° rotation angle), the coarse grains have completely disappeared. It is found that the grain size decreases considerably to a small level and significant grain refinement has been achieved. Interestingly, the grain size of two stacked discs at this stage is greatly finer than the grain size of the one-layer specimen after the same 720° rotation. As described in Chapter 4, the coexistence of the coarse and fine grains at the same position of the one-layer disc was observed after the 720° rotation. In terms of crystallographic orientations, the homogeneous colour spread instead of the periodic colour spread predominates on the EBSD maps. However, the flow directions of the material can still be identified, especially in the upper disc. For instance, at the M1 and M2 positions, the elongated direction of the structures indicates one of the material flow directions.

As the shear strain increases to γ=26.4 and 44.0 (i.e. 1080° and 1800° rotation angles) the similar morphologies can be observed in all measurement areas. This is different to the observation for the one-layer HPT deformed discs under the same strain conditions. The traces of the material flow cannot be detected from the EBSD maps anymore and all the grains become more equiaxed due to the high plastic deformation. HAGB instead of LAGB are dominant during these stages and almost all GBs are continuous. However the proportion of the residual LAGBs is not small, indicating that the saturation of the grain refinement has not yet been achieved.

In terms of microstructure gradient along the sample thickness, it is surprisingly found that although there are discrepancies between the upper and lower discs, the difference of morphology within each disc tends to be minimised during the two-layer HPT deformation. That means that using the two-layer disc instead of the one-layer disc as the starting specimens is able to stabilise the complex material flow during HPT. This point of view will be discussed later.

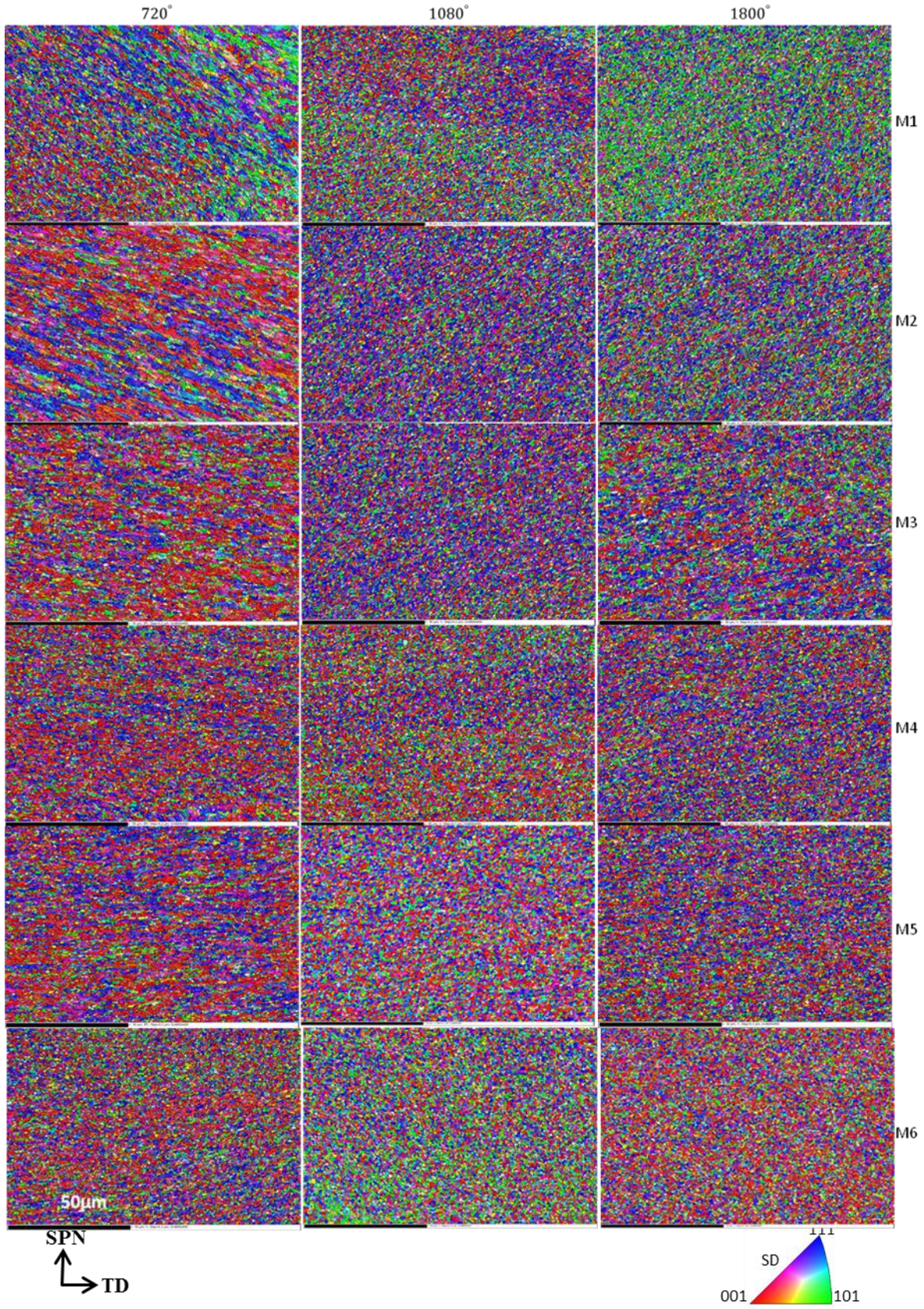

Figure 5.5 EBSD maps of two-layer disc after HPT with the rotation angles of 720°, 1080° and 1800° at the M-positions.

In order to further study HPT grain fragmentation and refinement, the quantitative characteristics including grain size, grain aspect ratio and misorientation angle distribution are analysed. Figs. 5.6, 5.7 and 5.8/5.9 show the distributions of the average grain size, the average aspect ratio and the misorientation angles for various HPT rotation angles, respectively. As stated before, the average grain size of the starting materials is about 11μm. The initial average aspect ratio of the grains is about 2.55.

At the rotation angle of 15°, the average aspect ratio of the grains decreases below 2 in most areas due to the compression along the SPN direction. The average grain size decreases slightly to the range of 9-10 μm. This modest decline in the grain size is mainly attributed to the small increment of the shear strain. However, it is known from Chapter 4 that the grain refinement is not a linear function of the shear strain. A small increment in shear strain does not necessarily correspond to a slight grain refinement. As demonstrated in Fig. 5.8 and Fig. 5.9, the density of the substructures with misorientation angle of less than 2° is extremely high while the percentages of LAGBs and HAGBs are very low in both upper disc and lower disc, indicating that the propagation of dislocations is promoted and there is no change in HAGBs.

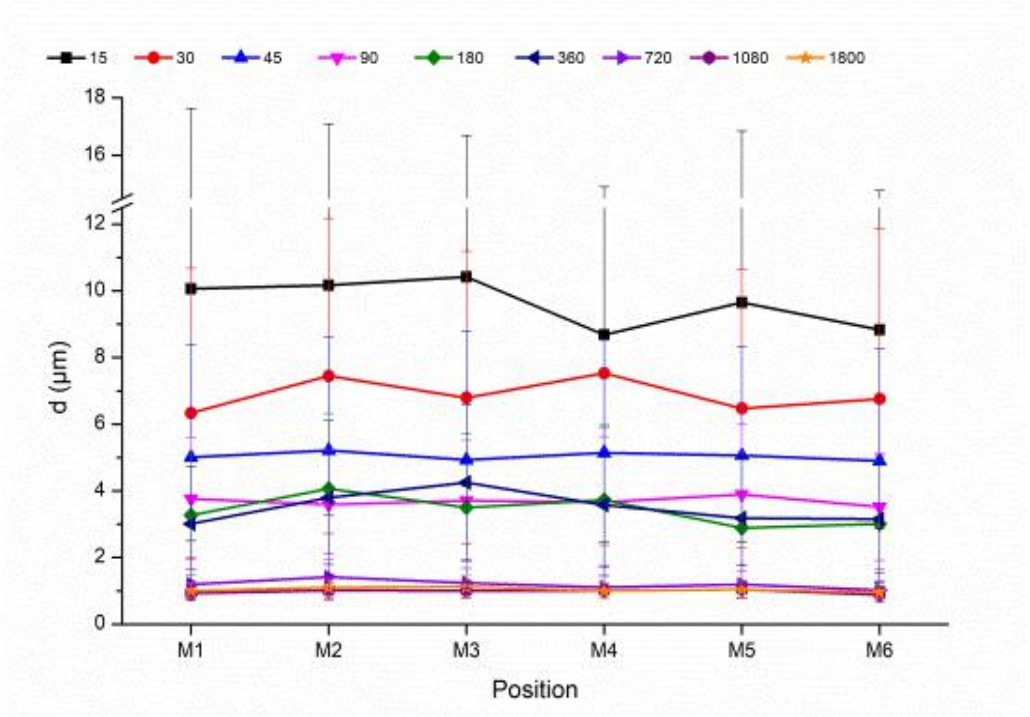

Figure 5.6 Grain size distributions of two-layer disc after HPT with the rotation angles of 0°, 15°, 30°, 45°, 90°, 180°, 360°, 720°, 1080° and 1800° at the M-positions.

As the rotation angle increases to 30°, 45° and 90° (γ= 0.73, 1.10 and 2.2 respectively) a similar trend on the evolution of the grain size has been observed. The average grain size decreases from approximately 6.9 μm at the rotation angle of 30° to about 5.0 μm at the rotation angle of 45°, then to 3.7 μm at the rotation angle of 90°. According to Fig. 5.8 and Fig. 5.9, after the 30° and 45° rotations, the dislocation density deceases consistently with the rotation angle, while the fraction of the substructures with $2°\leq\theta<15°$ ascends, denoting that the dislocations are significantly transformed into the LAGBs. After the 90° rotation, both the densities of the dislocations and LAGBs with $2°\leq\theta<6.5°$ are lower than the previous stage, whereas the numbers of LAGBs with $6.5°\leq\theta<15°$ and HAGBs increase. This suggests that the dislocations have been absorbed by LAGBs and HAGBs. It has been found that the grain aspect ratio increases with the shear strain during these three deformation stages, indicating that the grains are elongated to form the lamellar structures.

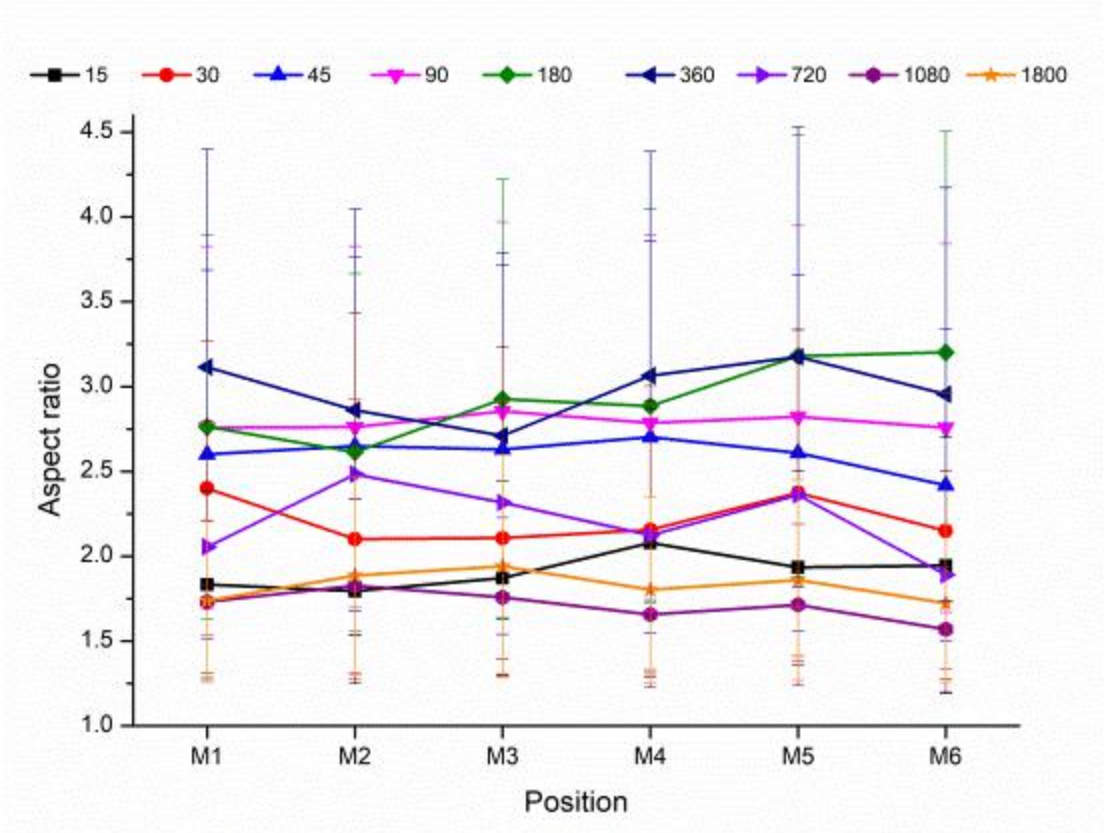

Figure 5.7 Aspect ratio of two-layer disc after HPT with the rotation angles of 15°, 30°, 45°, 90°, 180°, 360°, 720°, 1080° and 1800° at the M-positions.

In the shear strain range of 0.73-2.20, the variation in the average grain size is significantly smaller than that for the one-layer disc under the same condition. This means that compared

to the one-layer disc the two-layer disc is able to stabilise the material flow during the HPT deformation.

At the rotation angle of 180° (γ=9.32), both grain refinement and aspect ratios increase slightly. This situation is similar to previous three stages. Actually this deformation stage is located at the end of the previous trend. However, the latent changes have already started. It is found that the density of the substructures with $0 \leq \theta < 6.5°$ increases, denoting that the dislocation generation is faster than the dislocation absorption. The similar behaviour on the misorientation angle is also observed after the 360° rotation (γ =18.63). Concurrently the grain sizes and aspect ratio are stable within a narrow range. Thus this stage is another preparatory stage for the further grain refinement.

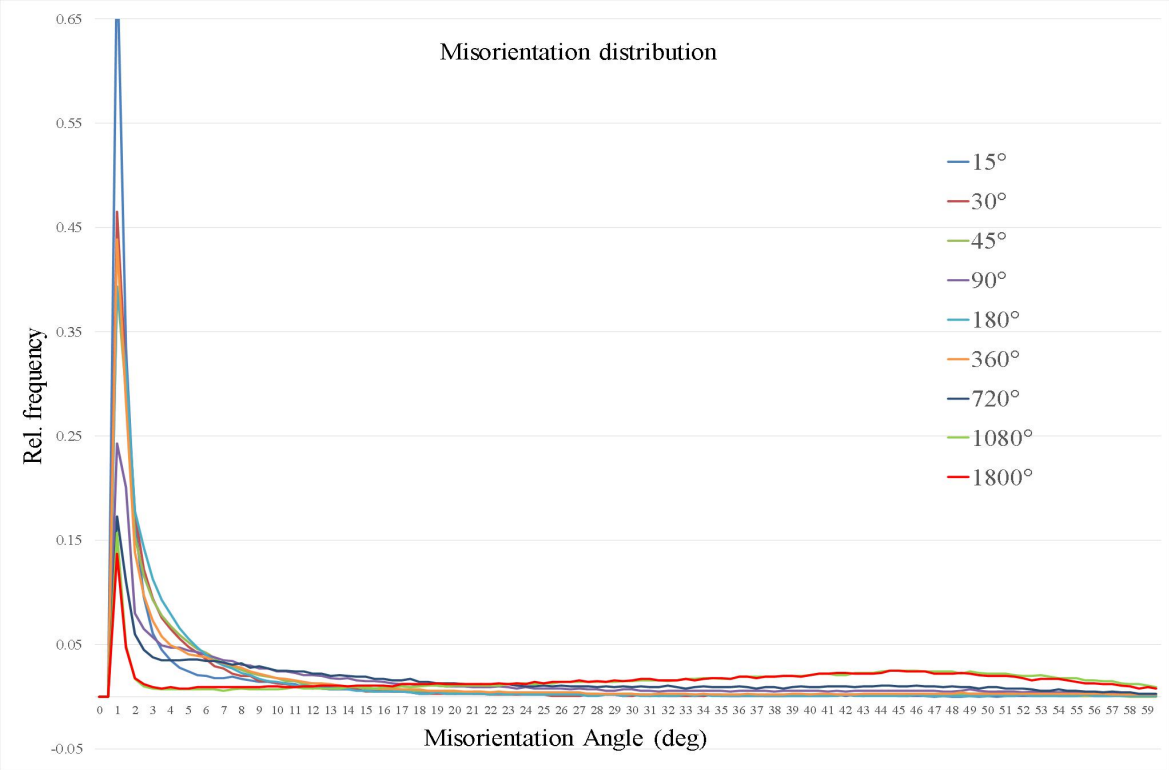

Figure 5.8 Misorientation angle distribution of two-layer disc after HPT with the rotation angles of 0°, 15°, 30°, 45°, 90°, 180°, 360°, 720°, 1080° and 1800° at the M2 position.

Dramatic grain refinement has been found when the shear strain γ reaches 37.26 (720° rotation). A large amount of the substructures have been converted into new grains. It should be noted that in contrast to the one-layer HPT deformed disc where the average grain size is about 3.3 μm, the grain size of the two-layer disc is refined close to nanometre as early as the 720° rotation at the M positions.

The average grain sizes of the order of 1 μm are stable at the accumulated shear strain of γ=26.4 and 44.0 (corresponding to 1080° and 1800° rotations, respectively). According to the previous observations, it is known that HPT is capable of obtaining grains with the average grain size of ~500 nm. However, there is not any further change in grain size although the shear strain increases by 1.7 times (from 26.4 to 44.0) after the rotation angle of 1800°. A stable aspect ratio can be seen for the rotation angles of 1080° and 1800°. It appears that the aspect ratio levels out at about 1.7. The percentage of HAGBs has been significantly increased, indicating that HAGBs are dominant at these strain levels.

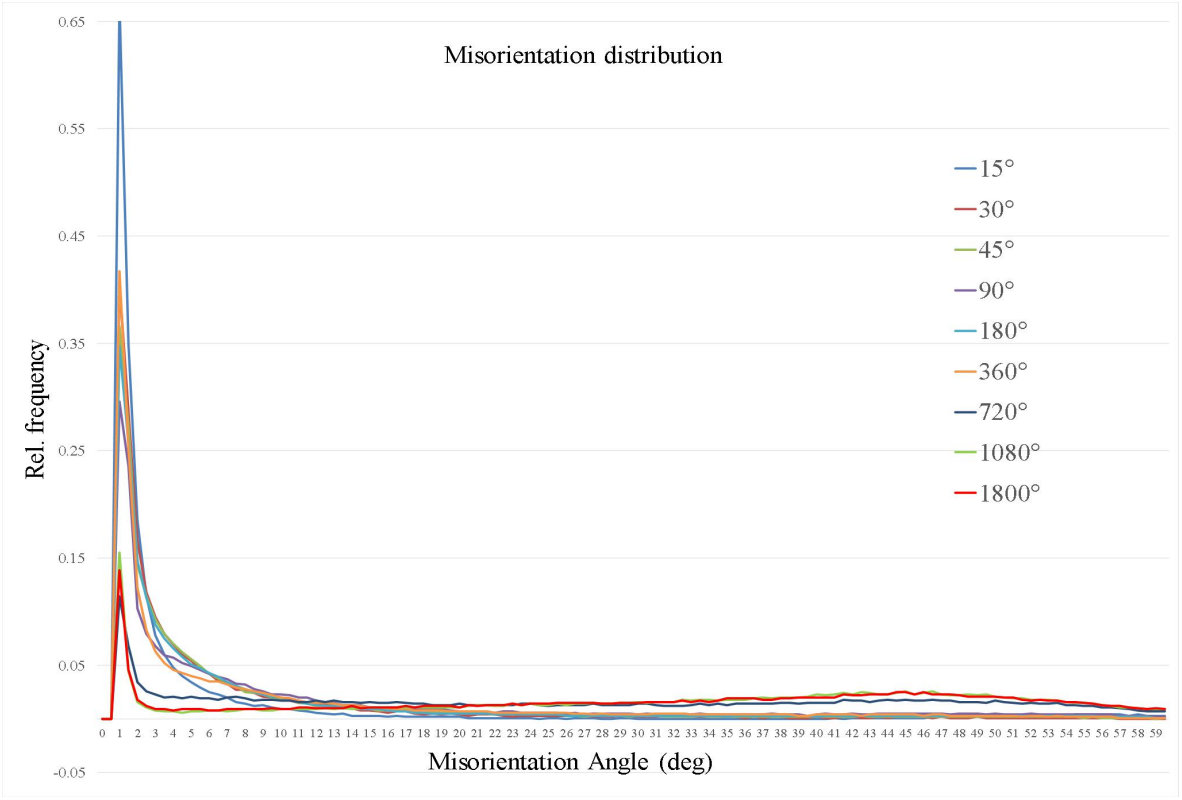

Figure 5.9 Misorientation angle distribution of two-layer disc after HPT with the rotation angles of 0°, 15°, 30°, 45°, 90°, 180°, 360°, 720°, 1080° and 1800° at the M5 position.

5.2.2 Microstructure evolution at E-position

The microstructure evolutions at the E-positions (4mm away from the disc centre) of the two-layer HPT deformed discs are analysed. Three points were measured within each of two stacked discs to reveal the distribution of microstructure along the sample thickness. These observed results will be compared with the results of the one-layer HPT deformed discs under the same conditions to achieve a deeper understanding of the complex material flow during HPT.

Fig. 5.10 shows the EBSD maps of the HPT deformed discs after HPT with the rotation angles of 15°, 30° and 45° at the E positions, corresponding to the shear strain γ of 0.78, 1.55 and 2.33, respectively. All EBSD maps shown in this figure have the same scale.

From the study in Chapter 4, it is found that the microstructure gradient exists along the thickness of the one-layer HPT deformed disc at the low and medium strain levels. For the two-layer disc, the variation in microstructure declines significantly. The gradient inside each of two layers tends to vanish at all these three stages.

Both continuous and discontinued LAGBs exist at the shear strain γ of up to 0.78 (15° rotation). More HAGBs are transformed from LAGBs by continuous dislocation absorption with the increase of the shear strain. A great number of new grains are generated when they are surrounded by the continuous HAGBs. It is noteworthy that the initial grain shapes remain and the lamellar structures are not observed. This means that the drastic grain refinement due to the increase of HAGBs occurs prior to the grain elongation at these stages.

It is observed from Fig. 5.10 that the fractions of the green colour ({110} <u v w> fibre) and the blue colour ({111} <u v w> fibre) are higher at the M1-M3 positions since these areas undergo larger shear strain. Generally, the activated slip systems, the lattice spin and the growth rates of the different texture components are discrepant during the plastic deformation. The diverging rotation rates and directions inevitably result in the grain fragmentation and refinement. As a result, different texture components generally possess different grain sizes. According to the statistical analysis by Channel 5, the grain size of the {110} <u v w> fibre is smaller than the grain size of the other two fibres at the low strain stage of HPT.

With the ongoing HPT deformation, the grain elongation has begun and the lamellar structures appear. Many small grains are found inside the initial grains but a great number of new grains emerge at the grain boundaries because the GB with the large misorientation angle is able to provide more likelihood of generating continuous HAGBs.

It is found that the coarse and fine grains coexist. These relatively equaxied fine grains have a negative effect on the aspect ratio at this stage. This trend is seen at two deformation stages where the accumulated shear strain γ is 1.55 (30° rotation) and 2.33 (45° rotation), respectively. The distribution of the periodic colour spread becomes more homogeneous in all areas and their shapes are irregular with jagged protrusions. It is observed that the {110} <u v w> fibre has the smallest grain size, suggesting that the fibre is more likely to be fragmented.

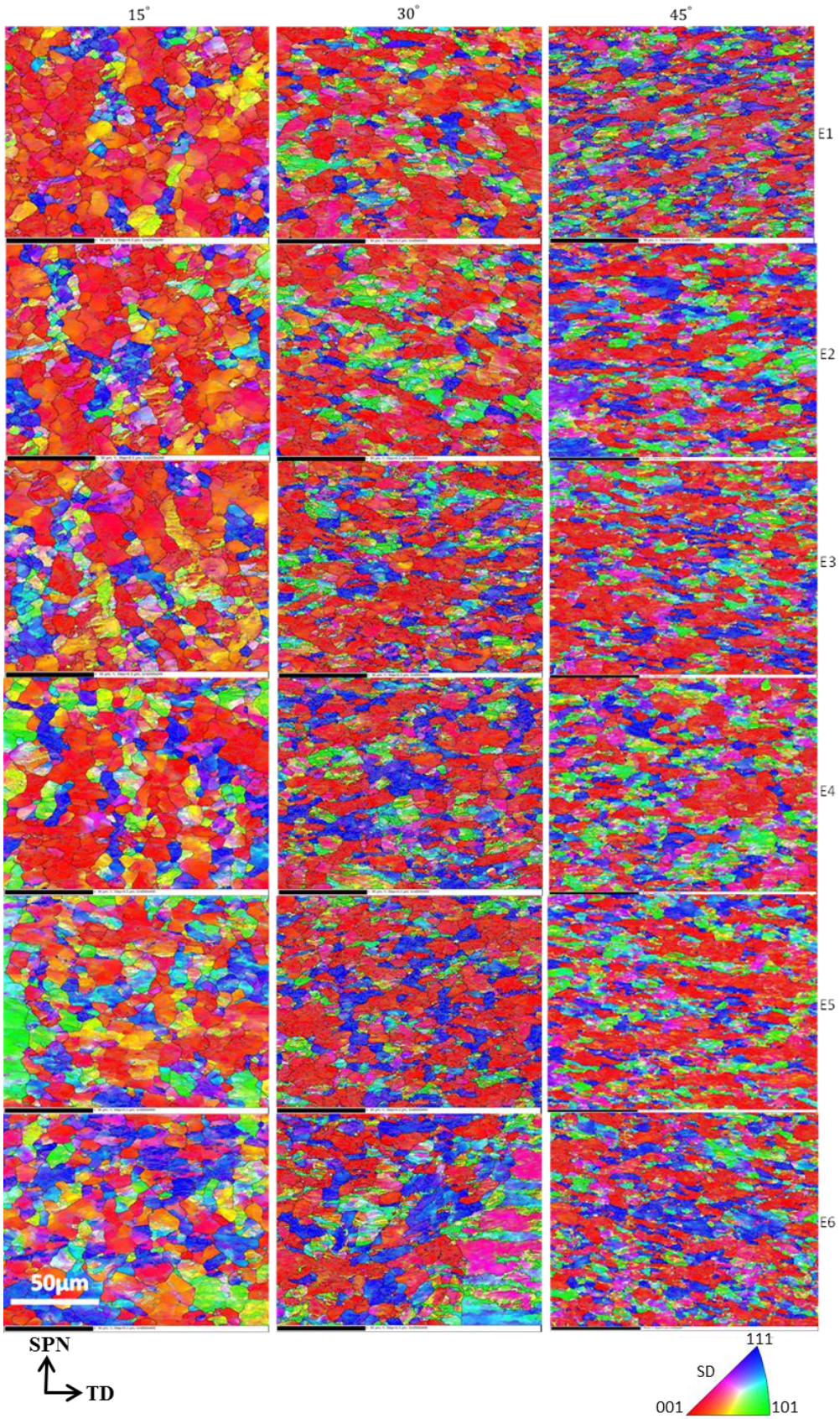

Figure 5.10 EBSD maps of two-layer disc after HPT with the rotation angles of 15°, 30° and 45° at the E-positions.

Fig. 5.11 shows the EBSD maps of the HPT deformed discs after the rotations of 90°, 180° and 360° at the E positions. With increasing deformation to the 90° rotation (γ=4.66), the morphologies are different compared with the previous three stages. At this stage, the elongated grains with the relatively large volume are divided into smaller volume lamellar-shaped grains because of the fragmentation of the parent grains. As a result the lamellar shaped grains are still in the majority. However it is observed that the average aspect ratio decreases. All EBSD measurements were conducted on the SD-plane. It is reasonable to assume that the initial grain is a sphere. Under the simple shear deformation, the material flow line β tends to align with the direction of the shear deformation [294], as shown in Fig. 5.12. With the increase of HPT deformation, the axis of the grain along the TD direction keeps constant in ideal condition which does not take the effects of the neighbouring grains into account, whereas the thickness of the grain parallel to the SPN direction declines. As a result, the grain size projected on the SD plane (i.e. EBSD maps) decreases.

At the rotation angle of 90°, the coarse grains have been fragmented. However, the effect of the initial grains on the crystallographic orientations can still be detected at the E5 position of the deformed two-layer specimen. The morphologies and distribution of the grain orientation after the 180° rotation (γ=9.32) and 360° rotation (γ=18.63) are similar to the previous stage. It has been known that the average size of the lamellar grains levels off at a certain level.

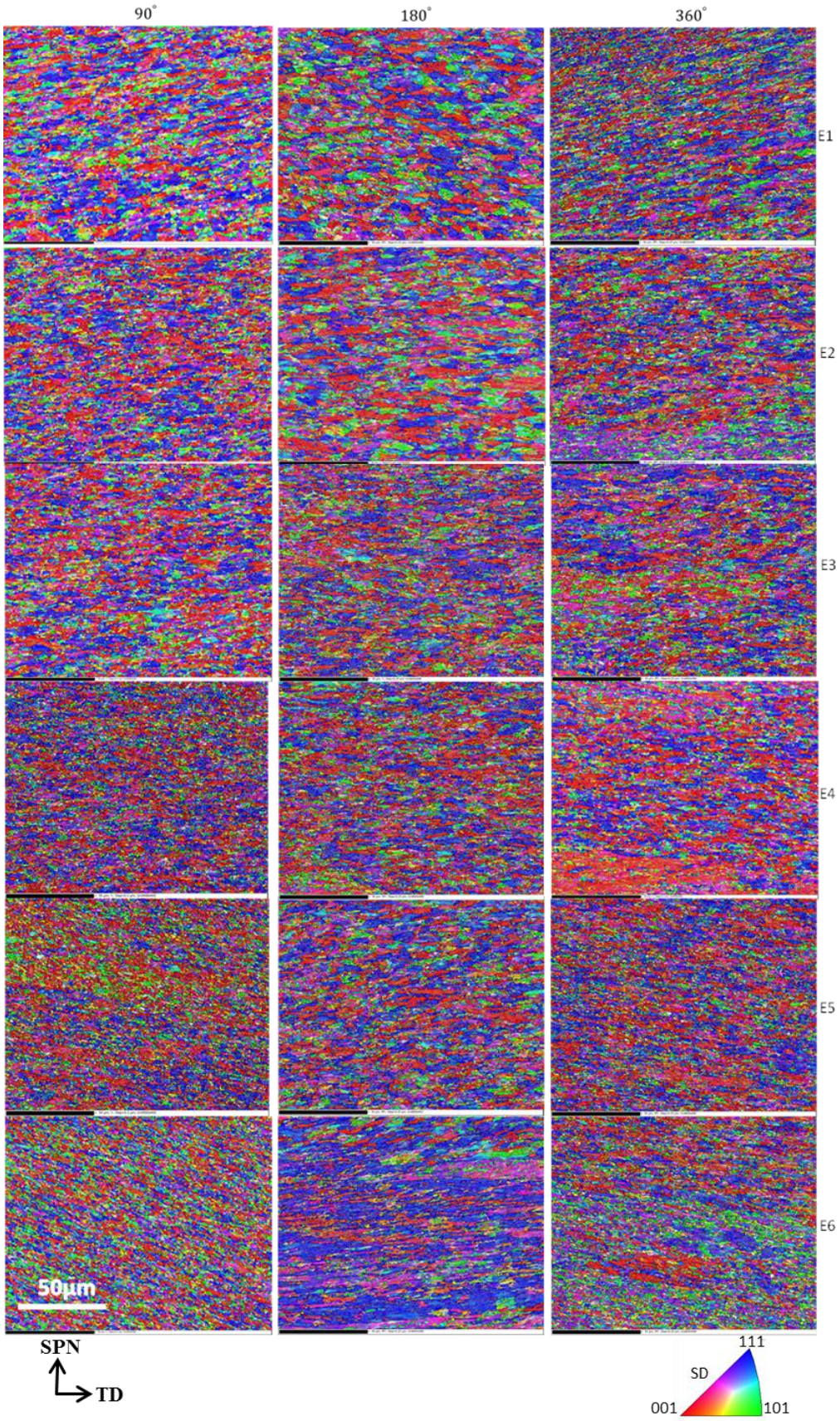

Figure 5.11 EBSD maps of two-layer disc after HPT with the rotation angles of 90°, 180° and 360° at the E positions.

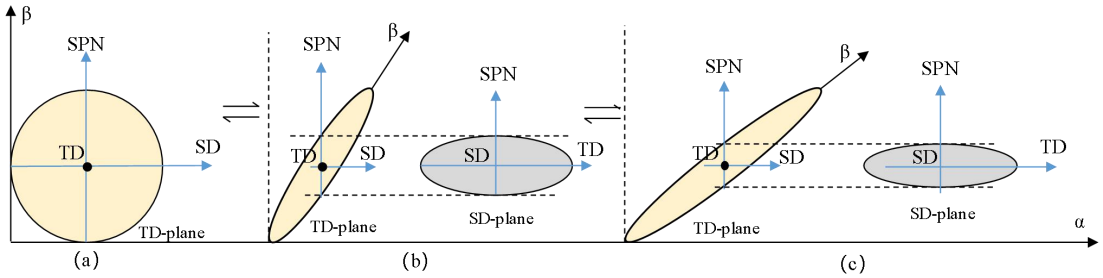

Figure 5.12 Schematic demonstration of the grain shape change under simple shear mode: (a) initial grain shape; (b) gain shape after lower deformation; (c) gain shape after larger deformation.

In contrast to the cases with the 90°-360° rotations where the lamellar structures are in the majority, the equaxied grains prevail after the 720° rotation (γ=37.26). As demonstrated in Fig. 5.13, with the increase of the shear strain, the lamellar grains are fragmented into the finer grains. Finally, the small and equaxied grains replace the lamellar grains and preponderate in all areas. It should be noted that the grain sizes of the two-layer disc after the 720° rotation are significantly finer than the grain size in the one-layer disc. The microstructure distributions are homogeneous at these three stages, and the grain size appears to have reached the saturation.

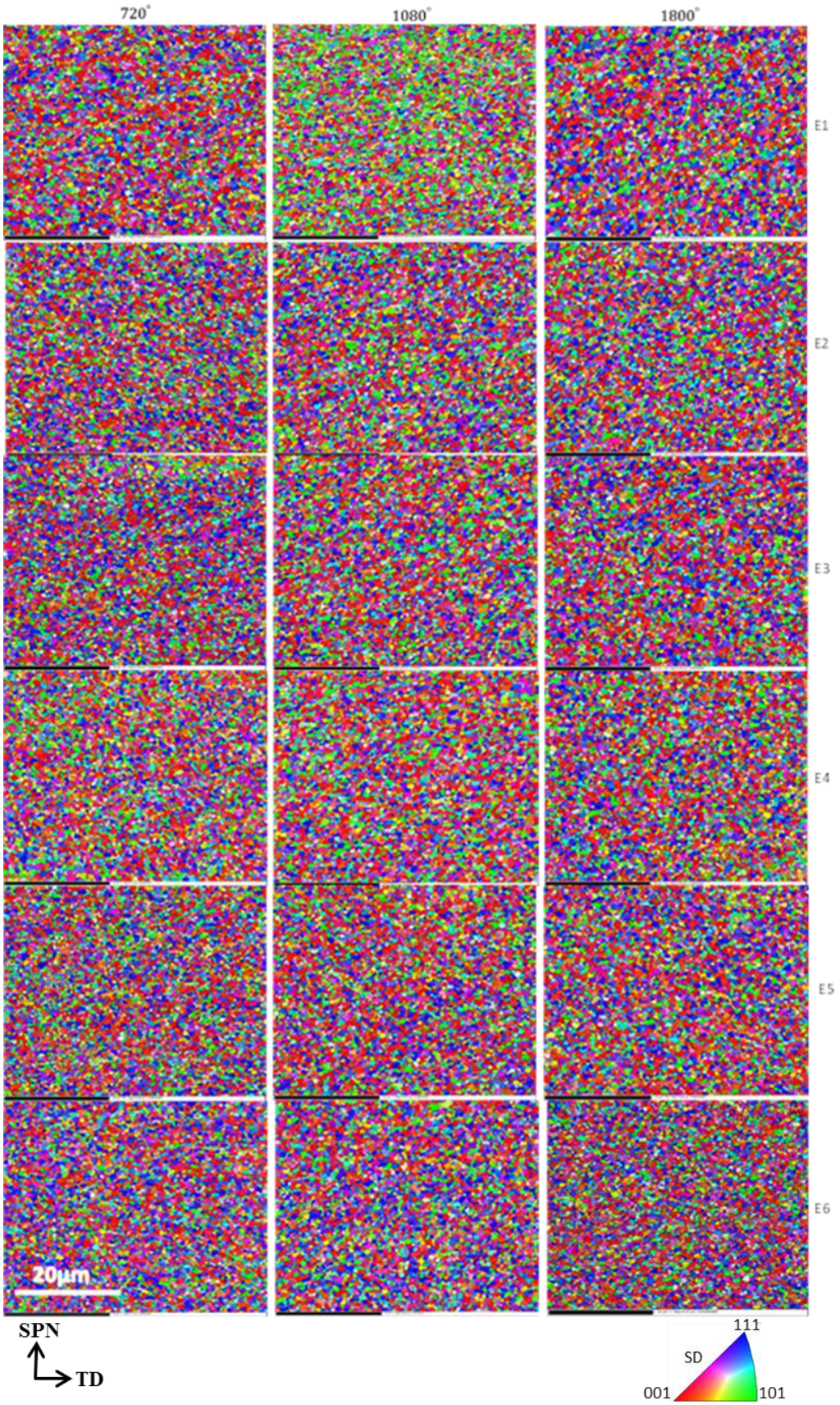

Figure 5.13 EBSD maps of two-layer disc after HPT with the rotation angles of 720°, 1080° and 1800° at the E-positions.

Figs. 5.14, 5.15 and 5.16 show the distributions of the grain size, the grain aspect ratio and the misorientation angle of the deformed two-layer stacked discs at six positions for various rotation angles.

As shown in Fig 5.14, the dependence of the grain size on the HPT deformation can be divided into four major stages. The first stage, from the 15° rotation to 90° rotation, exhibits a consecutively decreased trend of the grain size. During this stage, the average grain size drops dramatically from about ~ 11 μm for the annealed rod to less than 2 μm after the 90° rotation. The largest decrease in grain size has been achieved at the first stage.

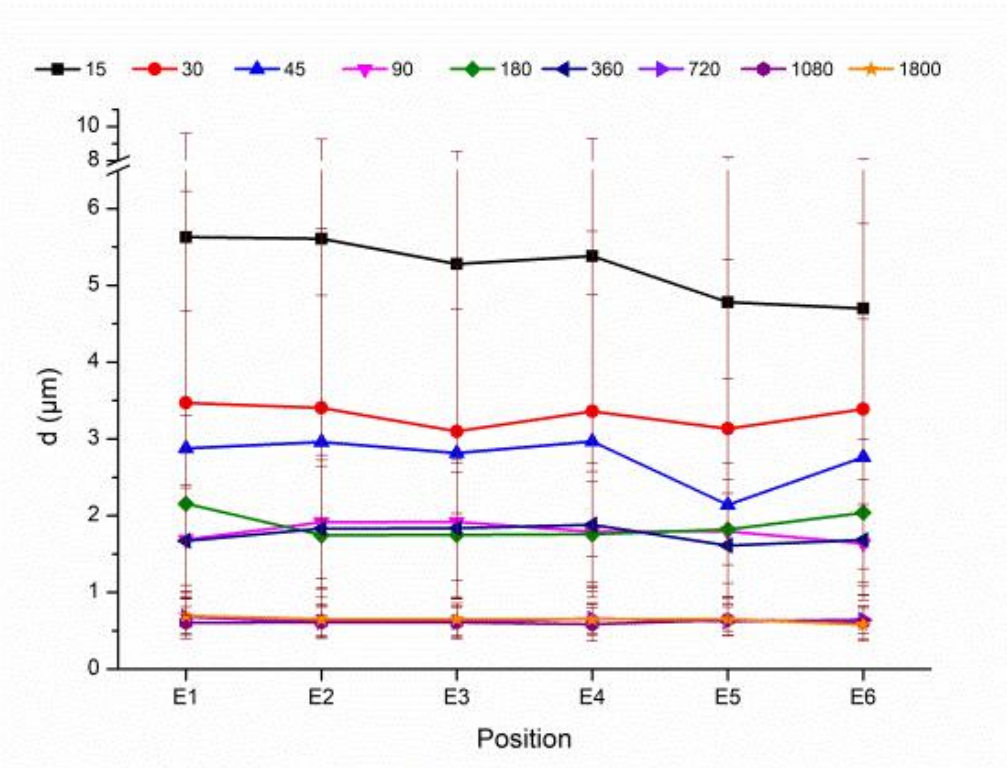

Figure 5.14 Grain size of two-layer disc after HPT with the rotation angles of 0°, 15°, 30°, 45°, 90°, 180°, 360°, 720°, 1080°, 1800° at the E positions.

For aspect ratio, the corresponding trend is different to that of the grain size and it is more complicated during the first stage. After the 15° rotation, the average aspect ratio decreases from 2.55 to about 2.24. Subsequently, the grains are elongated to form the large-volume lamellar structures as the shear strains γ increase to 1.55 (30° rotation) and 2.33 (45° rotation). Finally the fragmentation of the large volume lamellar structures into smaller volume lamellar structures reverses the ascend trend, and the average aspect ratio decreases from 2.84 to 2.46 after the 90° rotation.

It should be mentioned that the geometry of the two-layer disc results in particular microstructural features relevant to the grain size and the aspect ratio at the middle and edge positions after the 15° rotation. At this start-up stage, the grain size in the lower disc is obviously smaller than that in the upper disc. Concurrently the opposite situation is seen for the aspect ratio.

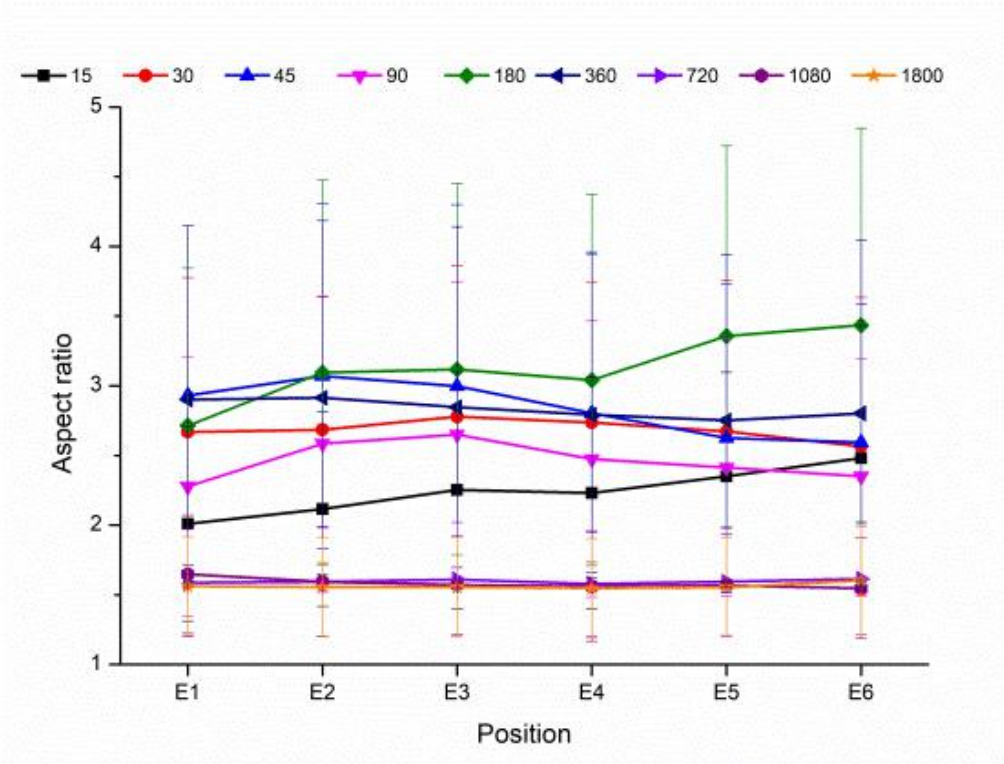

Figure 5.15 Aspect ratio of grains after HPT with the rotation angles of 15°, 30°, 45°, 90°, 180°, 360°, 720°, 1080° and 1800° at the E positions.

As shown in Fig 5.16 and Fig 5.17, the dislocation density (misorientation angle of ＜2°) at M5 is significantly larger than that at M2. However, the discrepancy in the dislocation density for the two-layer samples tends to disappear after the 30°, 45° and 90° rotations. During these three rotations, the fraction of the dislocation decreases drastically because the dislocations have transformed into LAGBs and HAGBs.

At the second deformation stage with the shear strain γ of 9.32 (180° rotation) and 18.63 (360° rotation), the grain size is stabilised at around 1.8 μm although the shear strain has increased by 13.97 (from 90° rotation to 360° rotation), which is in good agreement with the observations on microstructure. During this period, the dislocation densities at M2 and M5 rise again, indicating that the dislocations accumulate within the new-born small volume

lamellar structures. The average aspect ratio increases to 3.24 after the 180° rotation because the small volume structures are elongated without great fragmentation as the HPT shear strain increases. Then the average aspect ratio decreases to 2.83 after the 360° rotation, indicating a new round of the grain refinement.

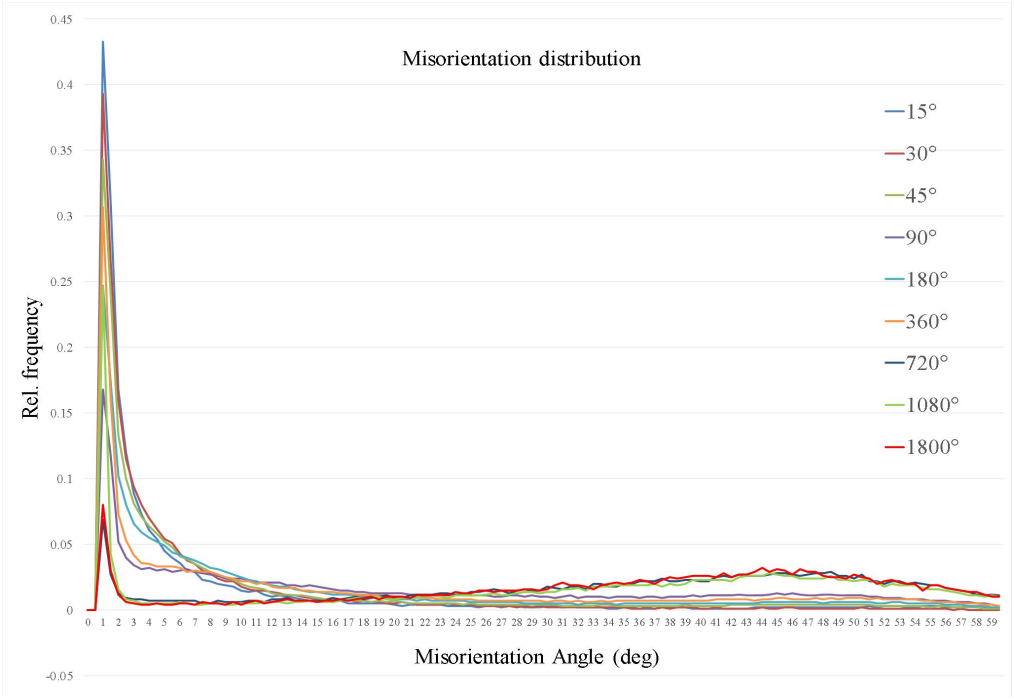

Figure 5.16 Misorientation angle distribution of two-layer disc after HPT with the rotation angles of 0°, 15°, 30°, 45°, 90°, 180°, 360°, 720°, 1080° and 1800° at the E2 position.

The shear strain increases from 18.63 (360° rotation) to 37.26 (720° rotation) at the third stage. The second significant grain refinement happens during this period. The average grain size decreases from 1.75 μm to 0.62 μm. From this stage afterwards the nanoscale grains are obtained via HPT and the gain refinement reaches the saturation. Accordingly the considerable grain refinement gives rise to the remarkable decline in the mean aspect ratio from 2.83 to 1.60. The fraction of HAGBs climbs notably at the expense of dislocations and LAGBs.

The final stage is observed in the samples after the 1080° (γ=55.89) and 1800° (γ=93.15) rotations. At this stage, the grain size is stable at the nanoscale. The aspect ratio levels off at about 1.58. It should be noted that after the 1080° rotation, the dislocation density at E2 and E5 increase exceptionally close to the level after the 180° rotation while the imperceptible decrease is observed in the fractions of HAGBs. This phenomenon is different to the normal trend of the dislocation density [295] at the M positions. This possibly denotes the onset of

grain coalescence. Generally it is rarely observed that the dislocation density increases within the nc grains during plastic deformation because of the dimensional limitations of the nc grains [181, 296-299]. It was reported that HPT results in an increase in the dislocation density in nc Ni–Fe alloy because of the grain coalescence caused by the grain rotation[238, 300]. With the development of coalescence, the sub-grain boundaries between neighbouring grains gradually disappear and the dislocations located at the sub-grain boundaries slip away through sub-grains, which results in the increased density of the intragranular dislocations. With the shear strain γ increases to 93.15, the high dislocation density within the nc grains is not stable and the dislocations tend to slip and be absorbed by the GBs under the applied force, and the coalescence of the sub-grains has been achieved. As a result, the dislocation density drops to a very low level, and the grain size increases slightly. From now on, the misorientation angle distribution is close to the Mackenzie distribution.

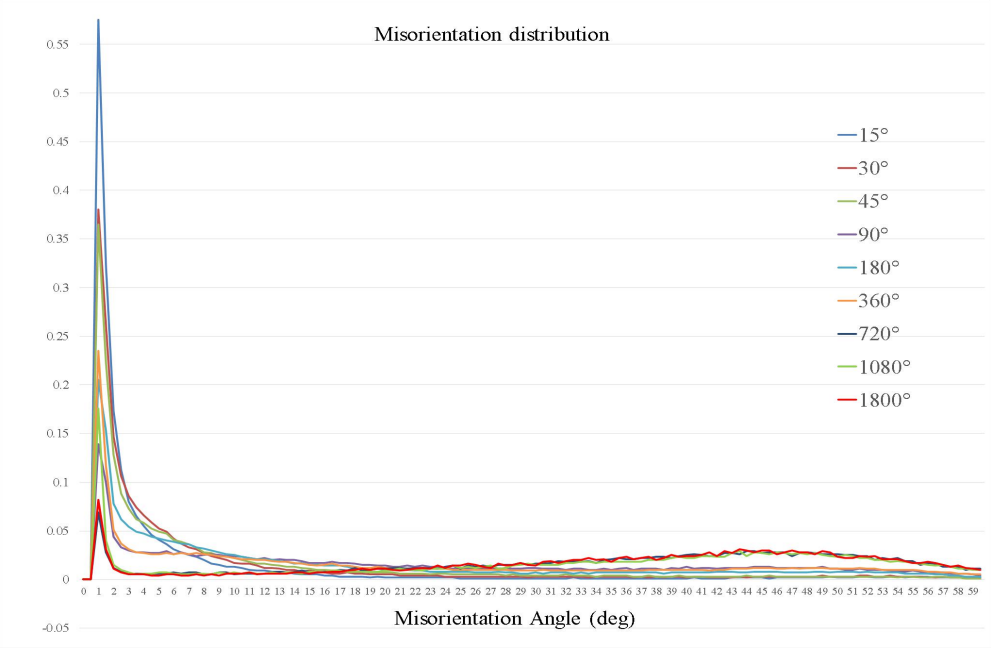

Figure 5.17 Misorientation of CP Aluminium after HPT with the rotation angles of 0°, 15°, 30°, 45°, 90°, 180°, 360°, 720°, 1080° and 1800° at the E5 position.

As shown in Fig. 5.18, the standard deviations for the average grain sizes of the one-layer and two-layer discs are compared to quantitatively characterise the stability of the material flow and the microstructural gradient. A large standard deviation generally denotes the significant gradient along the disc thickness.

In Fig. 5.18 (a), it is obviously observed that the standard deviation of the two-layer disc is lower than that of the one-layer disc, except at the rotation angle of 15°, indicating that the

two-layer disc instead of the one-layer disc is able to stabilise the material flow and has the smaller gradient along the sample thickness at the M-position. As the shear strain increases to a high level, the standard deviation is minimised and the gradient of microstructure tends to vanish eventually. The standard deviations for the E positions are demonstrated in Fig. 5.18 (b). Generally speaking, the standard deviation of the one-layer disc is slightly greater than that of its counterpart. The spiking value of the two-layer disc at E positions after the 45° rotation results from the abnormal grain size at E5. The value of the two-layer disc is close to that of the one-layer disc if the grain size at E5 is removed.

It is interestingly found that both trends in Fig 5.18 (a) and (b) are in good agreement with the microstructural evolution. As studied before, the microstructure evolution can be divided into several stages, such as grain refinement stages and preparation stages, during the whole HPT deformation from the initial state to the saturation state. At the stage of grain refinement, the parent grains are fragmented into smaller and more equiaxed grains, which will lead to more homogenous morphology and then reduce the gradient of the grain size along the sample thickness. At the preparation stage the grains are elongated into the lamellar structures without fragmentation. The complicated material flow affected by adjacent grains gives rise to different elongation degrees, which accelerates the grain size gradient.

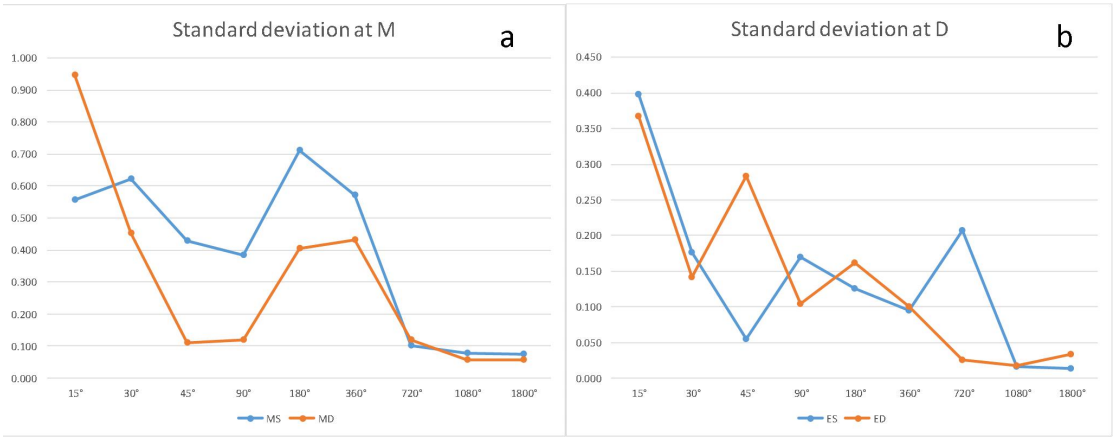

Figure 5.18 Standard deviation of grain size at M (a) and E (b) positions after HPT with the rotation angles of 15°, 30°, 45°, 90°, 180°, 360°, 720°, 1080° and 1800°. MS: M-position of one-layer discs; MD: M-position of two-layer discs; ES: E-position of one-layer discs; and ED: E-position of two-layer discs.

In summary, the two-layer disc instead of the one-layer disc is capable of stabilising the material flow and decreasing the gradient along the sample thickness during HPT, especially at M positions.

5.3 Hardness of HPT processed stacked CP Al

The distributions of Vickers hardness of the upper and lower disc after different revolutions up to 5 turns are shown in Fig 5.19 and Fig 5. 20, respectively.

The black line in Fig. 5.19 represents the hardness of the annealed materials. It is found that with the increase of revolutions, the hardness at the edge of the disc grows up faster than that at the centre of the disc. As a result, the distribution of hardness across the diameter becomes inhomogeneous. It should be noted that for the upper disc, the hardness at the disc centre seems to not be affected by the adjacent regions, so that the hardness can be considered as the hardness after the compression prior to the torsional deformation. In both upper and lower disc, the lowest hardness exists at the centre of the disc at the medium and high strain levels. Some exceptions are only observed after the 15° and 30° rotations.

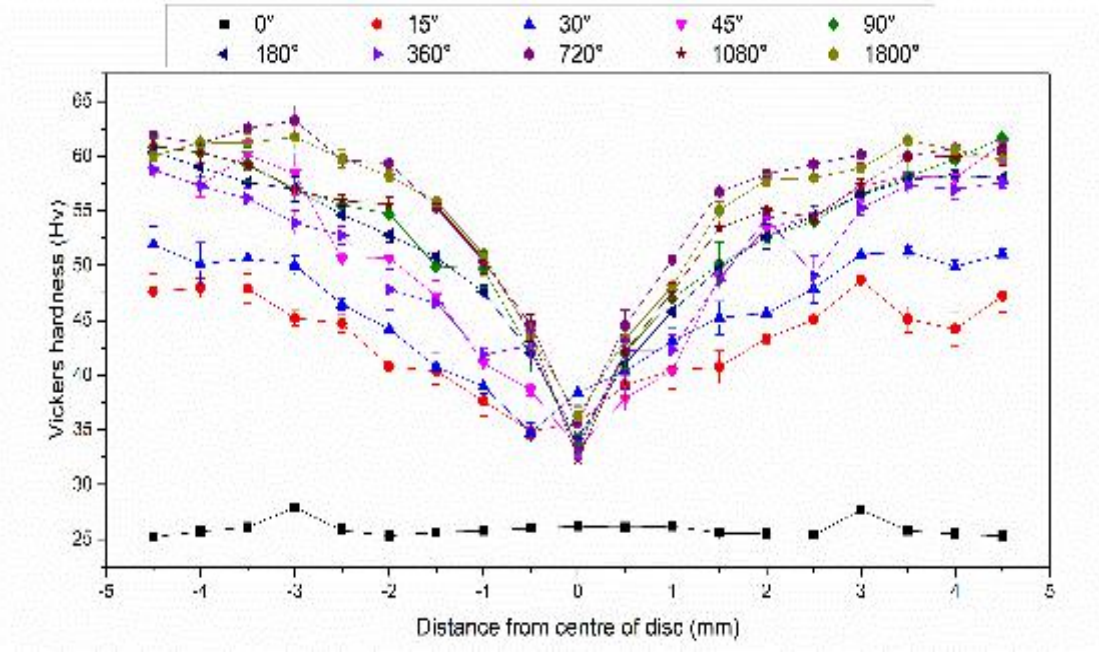

Figure 5.19 Distribution of Vickers hardness of the upper disc at different distances from the centres of the discs processed by HPT with the rotation angles of 15°, 30°, 45°, 90°, 180°, 360°, 720°, 1080° and 1800°. The black line indicates the hardness of the annealed specimens.

Actually, the increase of hardness is consistent with the microstructural evolution and can be also divided into several stages. After the rotations of 15°, 30°, 45° and 90°, the hardness increases greatly with the rise of the shear strain, whereas the hardness stops growing or even softening is detected at the rotation angles of 180° and 360° where the densities of HAGBs

decrease compared with that after the 90° rotation. Afterwards, the hardness at both upper disc and lower discs increase until the saturation has been achieved. Generally, the hardness values of the two-layer discs are slightly greater than the hardness of the one-layer disc at the medium strain level, especially after the 720° rotation.

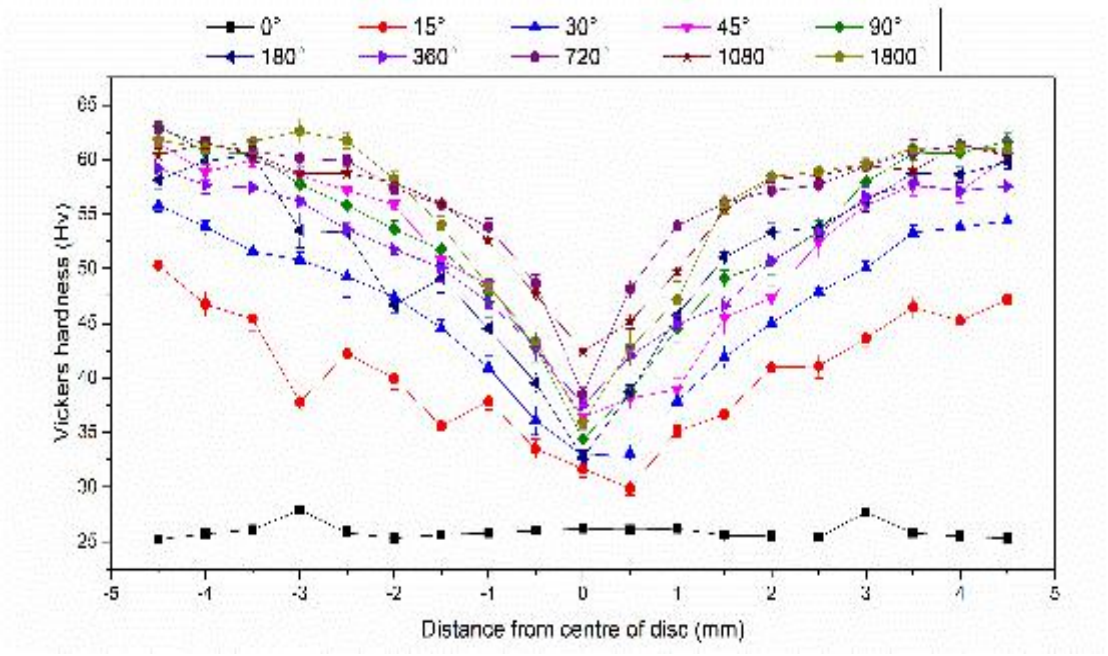

Figure 5.20 Distribution of Vickers hardness of the lower disc at different distance from the centres of the discs processed by HPT with the rotation angles of 15°, 30°, 45°, 90°, 180°, 360°, 720°, 1080° and 1800°. The black line indicates the hardness of the annealed specimens.

5.4 Texture evolution of stacked CP Al during HPT

5.4.1 Texture evolution at M-position

It is well known that the crystallographic slip is the major plastic deformation mechanism for pure Aluminium. Textures of the deformed specimens are essentially the preferred distribution of the orientations. ODFs with φ_2=45° are employed to demonstrate the texture evolution.

Fig. 5.21 illustrates the textures evolutions at the M positions of the deformed two-layer discs after the 15°-45° rotations. It is known that textures at the low strain stages are significantly influenced by the original textures of the starting materials. Strong C and Cube texture components prevail at the stage of the 15° rotation. It is noteworthy that the texture components at M1 are almost identical to the orientations of the annealed material. When the deformation increases to the 30° rotation, the Cube component starts to transform into the C

component. The Cube component then becomes weaker whereas the C component becomes stronger.

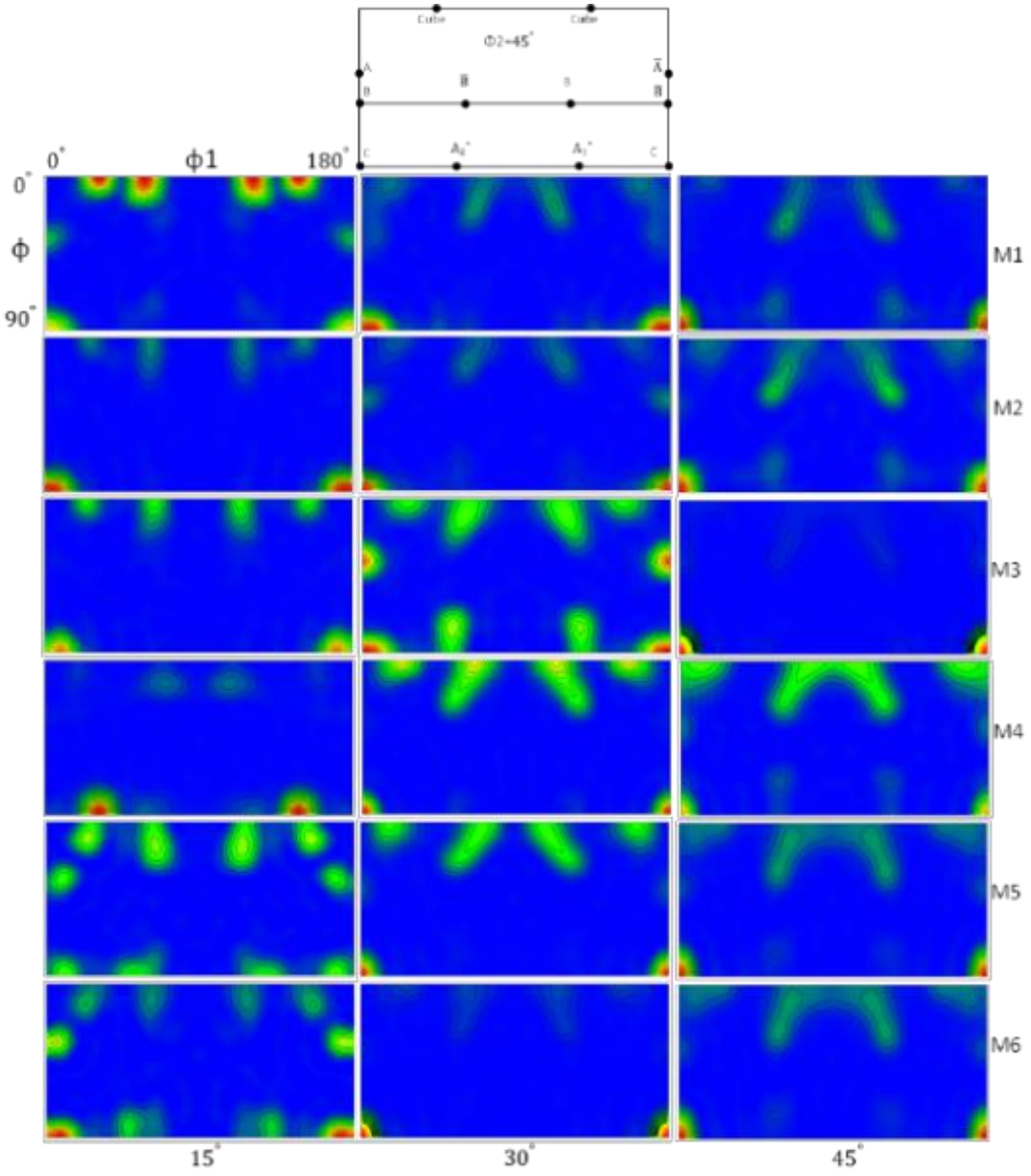

Figure 5.21 ODF sections with ϕ_2=45° of two-layer discs after HPT with the rotation angles of 15°, 30° and 45° at M positions.

HPT deformation with the rotation angle of 45° is a transition deformation stage between the 30° rotation and the 90° rotation. At this stage, in addition to the C component, the texture components of A^*_1 and A^*_2 start to appear. It is known that the C component results from the 45° rotation of the Cube component around the SPN axis. It is the most stable component among the ideal orientations during HPT [143, 176] . It should be mentioned that the intensity of the C component remains at a strong level at these medium strain stages. In the meantime the

grain aspect ratio increases drastically. This phenomenon is consistent with the prediction of the Taylor model [142, 289], namely the C ideal orientation is predominant when the grains are elongated at the medium strains.

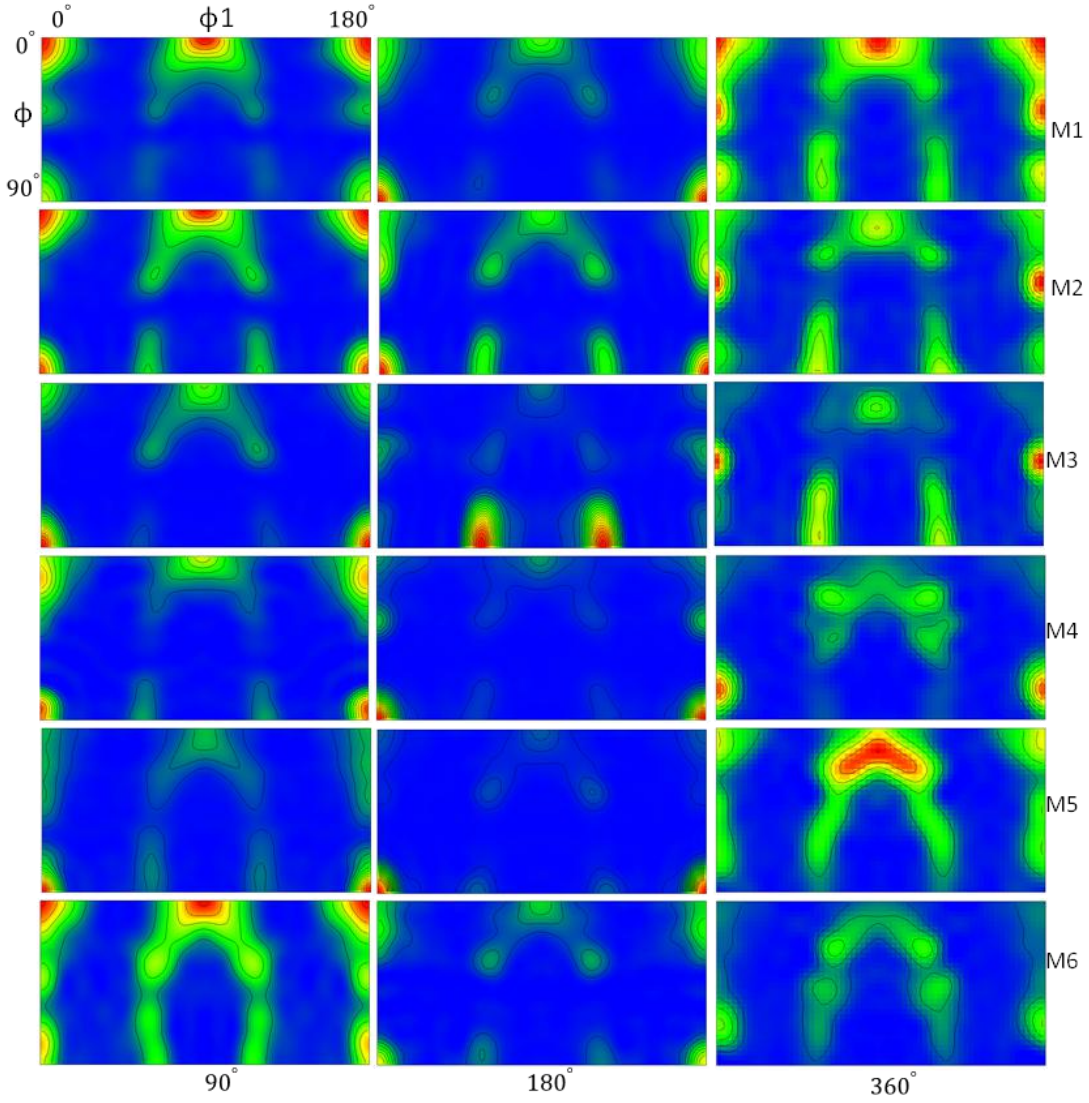

Figure 5.22 ODF sections with ϕ_2=45° of two-layer discs after HPT with the rotation angles of 90°, 180° and 360° at the M positions.

At the rotation angle of 180°, the texture components of A^*_1 and A^*_2 sustain. As shown in Fig. 5.22, the emergence of the new developed A/A_b texture components is simultaneously accompanied with the weakening C orientation. As the rotation further increases to 360°, the C orientation has almost vanished. The texture components of A/A_b and B/B_b are visible in the ODF section. After the 720° rotation, the typical orientation distributions are shown in Fig. 5.23. The C texture component predominates and the other pronounced textures can be observed. The texture gradients along the sample thickness generally disappears at these

stages. The similar orientation distributions are also observed for the 1080° and 1800° rotations, suggesting that these texture components are stable at very high plastic strain. The results are in good agreement with the previous experiments [78, 150].

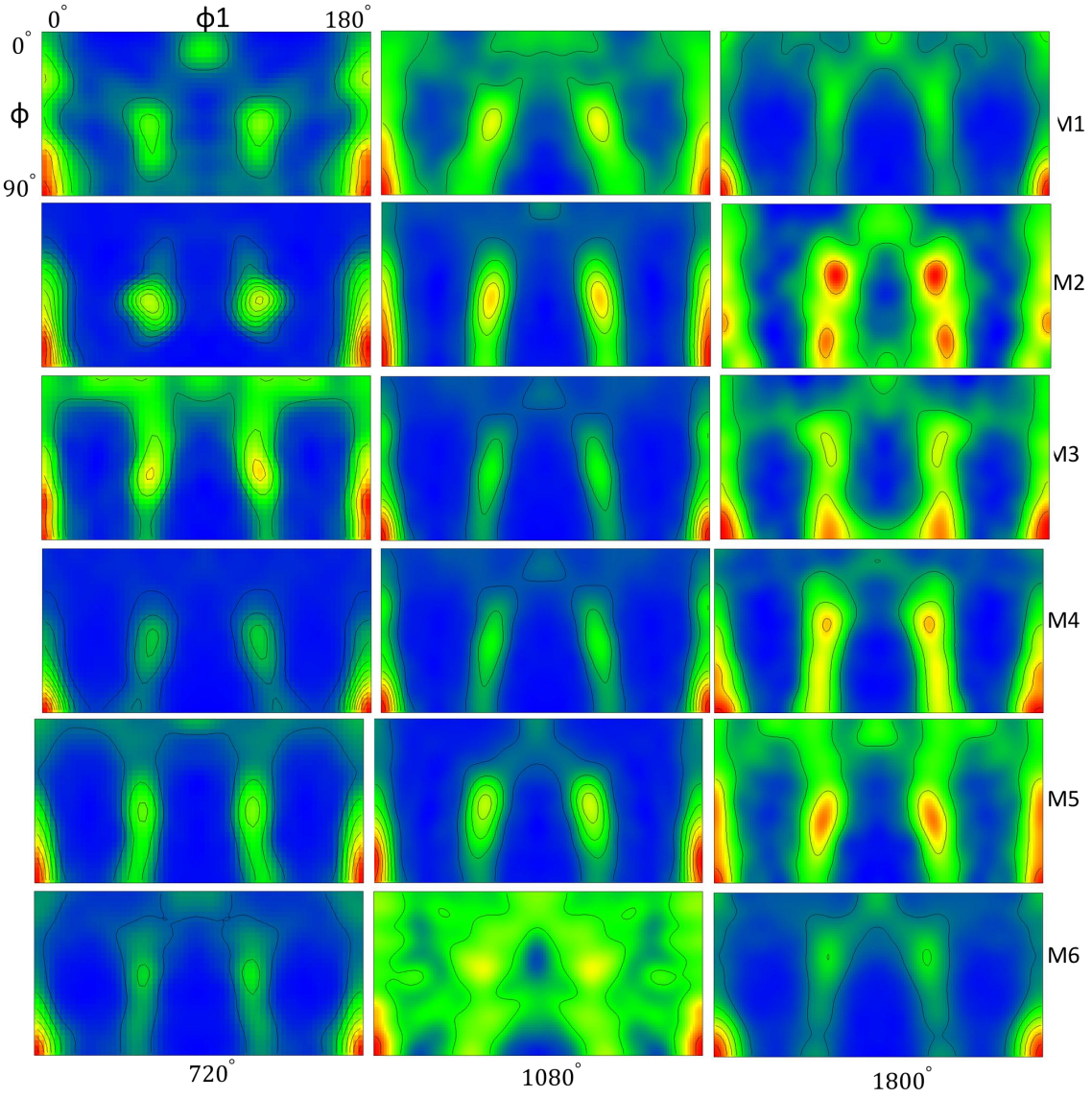

Figure 5.23 ODF sections with ϕ_2=45° of two-layer discs after HPT with the rotation angles of 720°, 1080° and 1800° at the M positions.

5.4.2 Texture evolution at E-position

Fig. 5.24 illustrates the texture evolution at the E positions after the 15°-30° rotations. At the 15° rotation, the residual traces of the initial textures can be observed. The C texture component prevails while the Cube orientation generated from annealing has evolved to a weak texture. The intensity of the Cube orientation declines from E1 to E6. Concurrently a

reversed trend of the A^*_1 and A^*_2 texture components is shown after the rotation angle of 30°, where the A^*_1 and A^*_2 orientations are strengthened gradually from the top to the bottom of the disc. In addition, the B/B_b components begin to appear. With the increase of deformation to the 45° rotation, the textures occupying the positions of ideal B/B_b, A^*_1 and A^*_2 are steadily strengthened. A slight gradient on the A^*_1 and A^*_2 components is detected along the sample thickness: with the increase of the shear strain, all components gradually move up. For example, the A^*_1 and A^*_2 components are rotated towards B/B_b in the lower disc but they remain at the ideal positions in the upper disc.

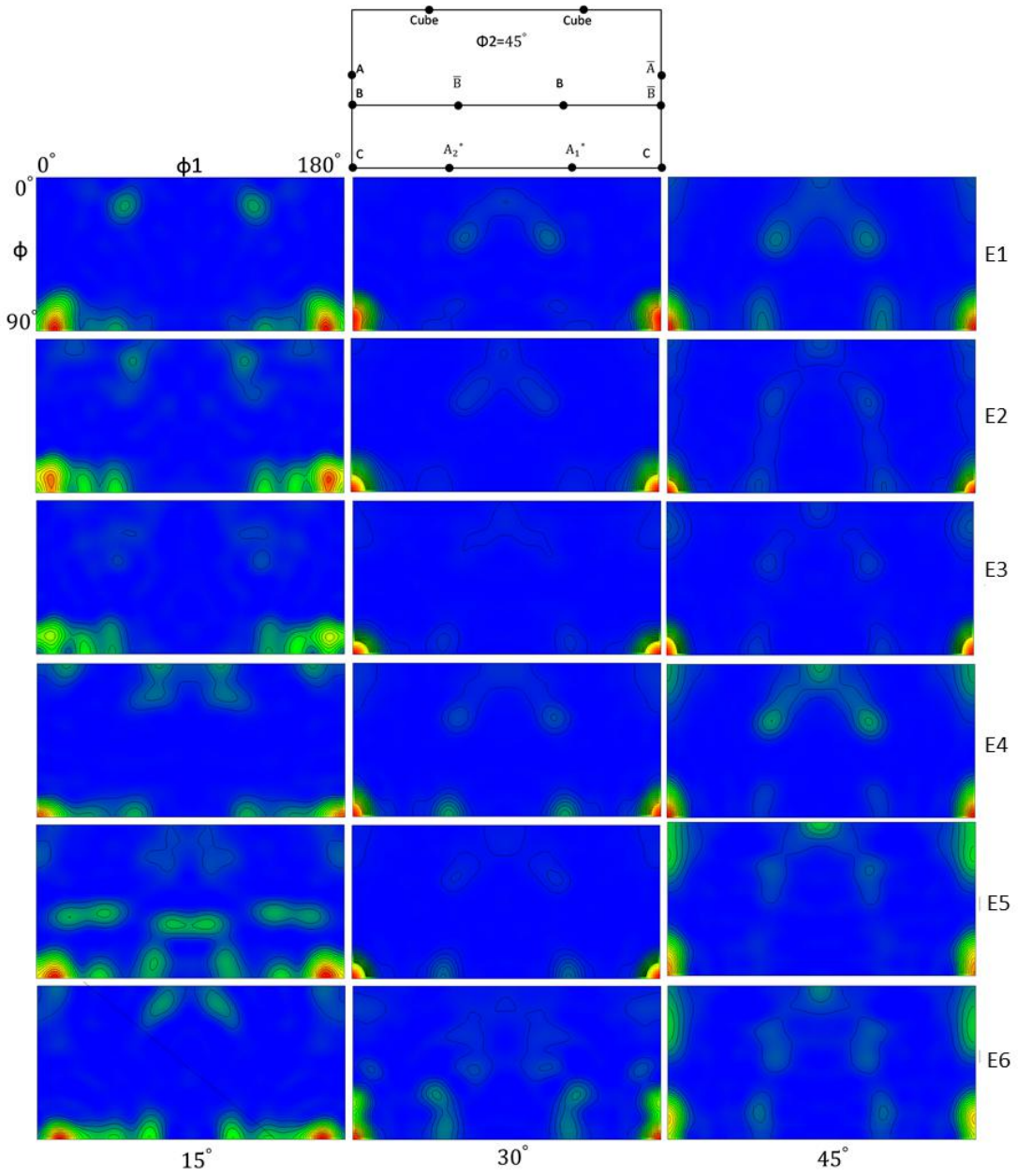

Figure 5.24 ODF sections with ϕ_2=45° of two-layer discs after HPT with the rotation angles of 15°, 30° at the E positions.

As shown in Fig. 5.25, with increasing deformation to the 90° rotation, although almost all components are strengthened, the moving up trend continues. As a result, the strong B/B_b orientations are formed at the expense of the A^*_1 and A^*_2 components at M5 and M6. Concurrently, the A/A_b orientations emerge at the same position. In the other areas, the texture components progressively move up along the sample thickness from M1 to M4. It should be mentioned that the intensity of the texture components is significantly stronger than the previous stages. At this stage, the initial parent grains disappear by considerable fragmentation into the smaller elongated structures. These new structures are born during the fragmentation with the favourable orientations, resulting in the stronger texture components.

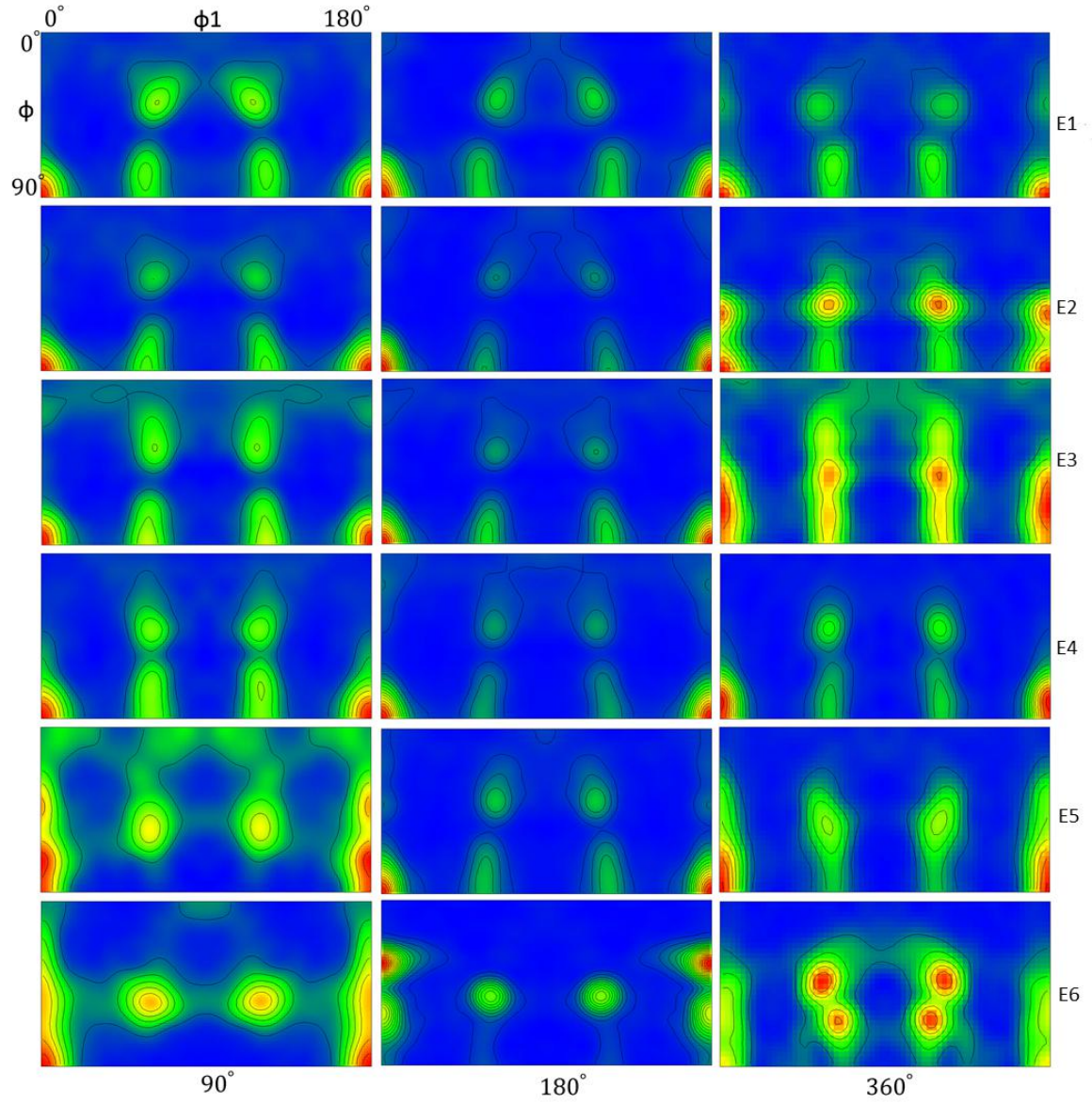

Figure 5.25 ODF sections with ϕ_2=45° of two-layer discs after HPT with the rotation angles of 90°, 180° and 360° at the E positions.

After the 180° rotation, the continued deformation weakens the strong texture components formed in the previous stage because of the constant change of the SD during HPT. The texture essentially results from a large number of grains with close crystallographic orientations. The strong components at the medium strain level with the 90° rotation are mainly given rise by the crystallographic slip and spin during the fragmentation. Therefore they are not stable texture components in simple shear. The moving up trend observed in the previous stage stops in the upper disc but continues moderately in the lower disc.

After the 360° rotation, the same texture components with last stage are re-strengthened. As stated before, the grains are elongated without great fragmentation at this stage. Therefore, the simple shear rather than the fragmentation is responsible for restrengthening of the texture components. The texture components formed at this stage will not change dramatically at high strain level.

Fig. 5.26 demonstrates the typical textures of the simple shear after HPT deformation of 2, 3 and 5 revolutions. It is well known that the typical simple shear textures of Al consist of a strong B fibre (C is a particular B texture component) and a less strong A fibre [240], which is consistent with the present study. The typical simple shear textures are generally stable even when the shear strain reaches the very high level.

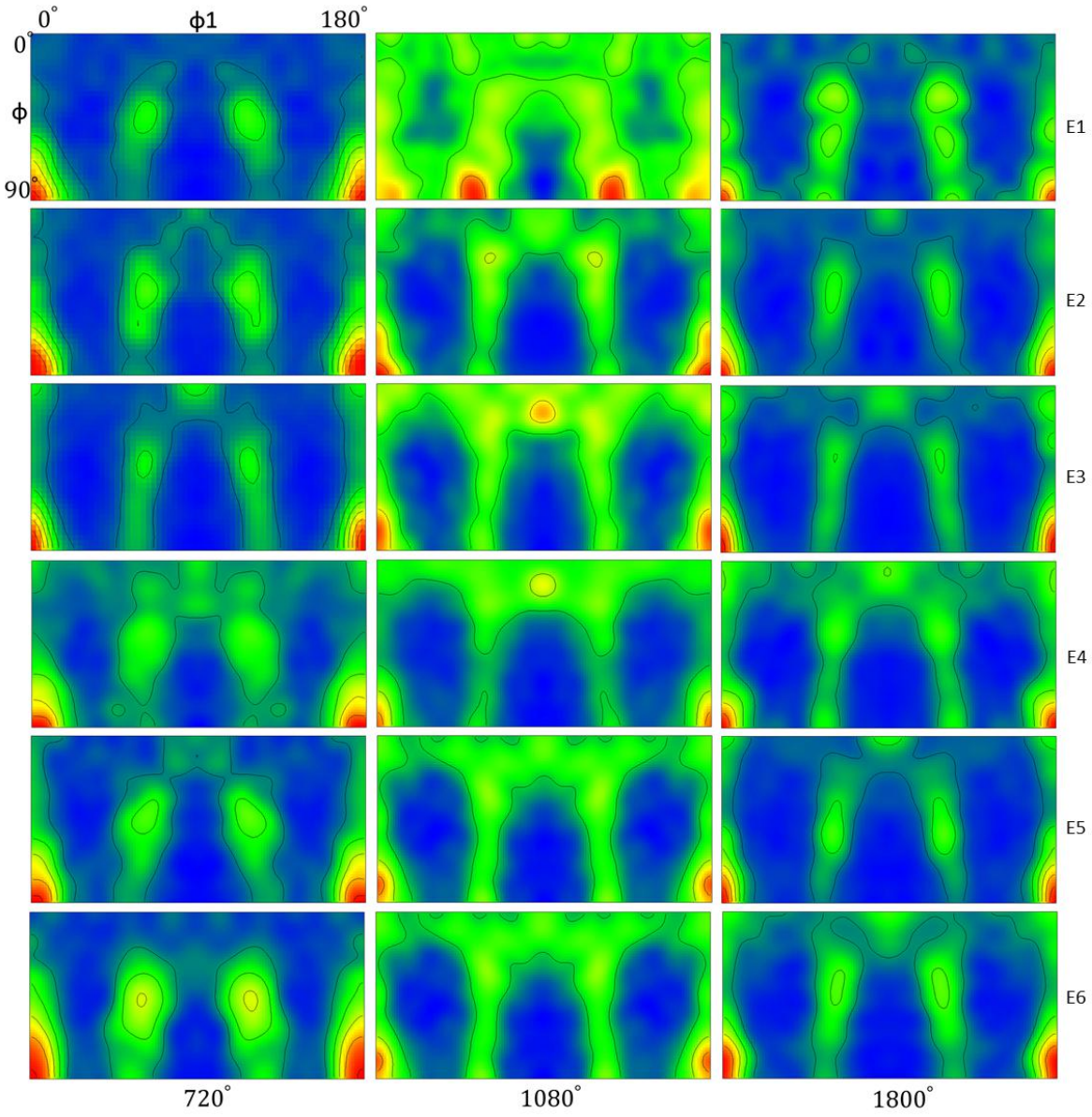

Figure 5.26 ODF sections with ϕ_2=45° of two-layer discs after HPT with the rotation angles of 720°, 1080° and 1800° at the E positions.

5.5 Shear-induced GB mediated processes during HPT

Grain boundaries and interface between the upper disc and the lower disc have higher energies than interiors of the grains. As a result the significant surface topology can result from electro-polishing. Secondary electron (SE) imaging is surface sensitive so that it can provides higher resolution and more detail about the surface topography rather than backscattered electron imaging [301]. Generally in the EBSD equipment, six diodes around the EBSD detector phosphor screen act as a complementary imaging system to the EBSD technique, called fore-scatter detector (FSD) system. Among them, two upper and two side

diodes are able to offer information about density and atomic number. The orientation contrast signal can be provided by two other lower positions diodes. Two different orientations can now be differentiated based on contrast [302, 303].

Fig. 5.27 shows the imaging of an area near the edge of the disc deformed by the 1080° rotation. In Fig. 5.27 (a) the interface between the upper disc and the lower disc is enclosed by a yellow rectangle. In Fig. 5.27 (b), it seems that two grains, labelled G1 and G2/G3, migrate across the interface between the upper disc and the lower disc. It is found from Figs. 5.27 (c) and (d) that the grain G2/G3 in the SE image actually is composed of two grains G2 and G3 whereas G1 is an individual grain. It should be noted that the common boundary between G2 and G3 is actually the interface of two discs and evidently stops the motions of G2 and G3 towards each other. A dent caused by electro-polishing is located at the bottom left of G1, which denotes the intersection of the interface and G1. Therefore, the grain migration across the interface only occurs in G1. The grain size of G1 is about 800 x 1000 nm. The irregular shape of G4 suggests its shrinkage at the left side during HPT accompanied with the enlargement of G1. From the thermodynamic perspective, the enlargement of grains is attributed to their favourably responding crystallographic orientations to the shear stress, thereby minimising the system and free energy [304].

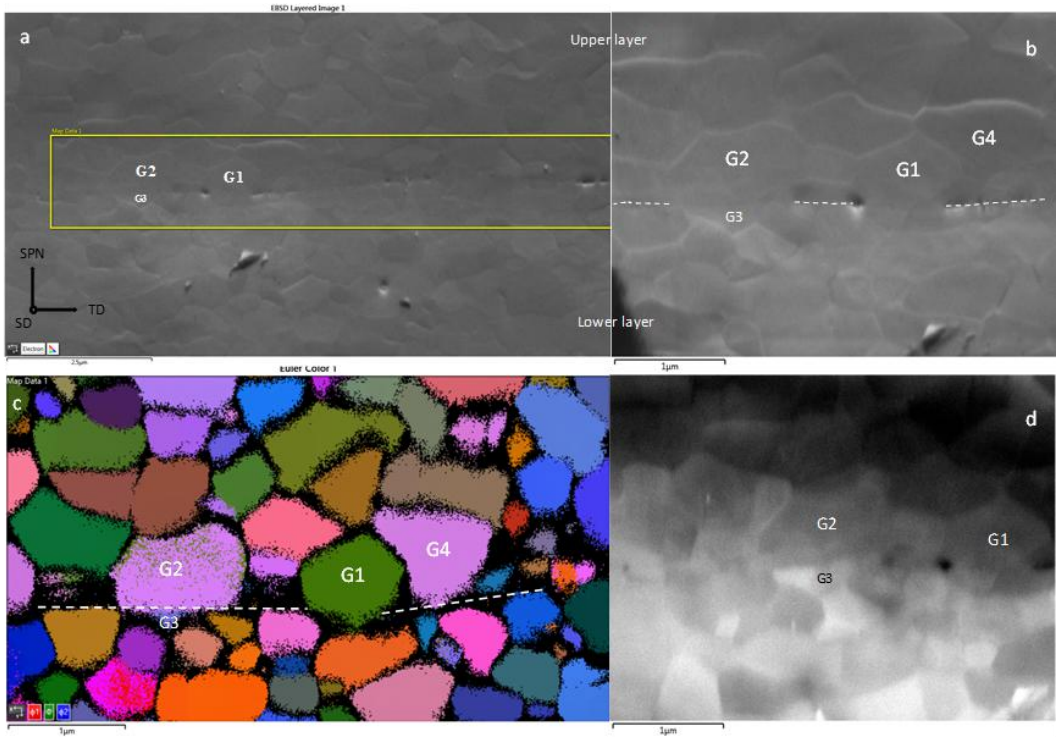

Figure 5.27 (a) SE image of an area near the edge of the HPT sample; (b) magnified SE image of grains G1, G2 and G3 in (a); (c) IPF maps of the same grains in (b); (d) FSD image of the same grains

in (b).

Another example is found at the vicinity of the peripheral area of the specimen deformed by the 1080° rotation. As shown in Fig 5.28 (a), the projection of the interface between two discs on the SD-plane is clearly demonstrated by a straight line inclined to the horizontal direction (i.e. TD direction). Noteworthy, because of the complicated material flow during HPT, the interface is not a flat plane and it fluctuates with respect to the SPN direction. The straight line is broken by the protruding G1, which is an individual grain with the close intracrystalline orientation confirmed by the FSD image (Fig.5.28 d) and the all Euler maps (Fig. 5.28(e)). In Fig. 5.28 (d) the common grain boundaries of G4/G5 and G6/G7 are obviously parts of the interface between the two discs. As shown in the magnified SE image (Fig. 5.28 (c)) G1 with the grain size of around 500x400 nm extends across the interface from the upper disc towards G2 in the lower disc. In addition, the small grain size and the shrunken shape of G3 indicates its shrinkage during the plastic deformation. At this stage, not all grain shapes are equiaxed. Most of the grains, such as G2, have a long axis along the SD direction and a short axis parallel to the SPN direction, which proves that the aspect ratio at the saturation stage is not one.

In comparison with its surrounding grains, the grain size of G1 in Fig. 5.27 is larger than the average grain size and reaches the upper limit of the grain size produced by HPT at this stage, whereas G1 in Fig. 5.28 is obviously smaller than most of its surrounding grains, indicating that the GB migration can induce the grain expansion or shrinkage under the same shear stress condition [192, 209]. The GB migration is only observed in several grains, indicating that the GB migration possibly occurs for the preferential boundaries.

Grain coalescence caused by the grain rotation is not found in this study, suggesting that the grain rotation is negligible during the present experiment. Actually the grain rotation and shear-induced GB migration are based on different mechanisms. In the triple junction of tricrystal [200, 201, 204, 231], the gliding GB dislocations are divided into two climbing dislocations which will result in the grain rotation in the neighbouring grains. The grain rotation brings their crystallographic orientations closer, thereby decreasing their mutual misorentation angle. In the other mechanism proposed by Moldovan et al [202, 305], the diffusion induced grain rotation is valid at room temperature when the grain size is at nanoscale. The shear-induced GB migration involves the dislocation activities. The shear

stress assists the dislocations in overcoming energy barriers and causes the GB migration consisting of these dislocations moving perpendicular to the boundary plane [211].

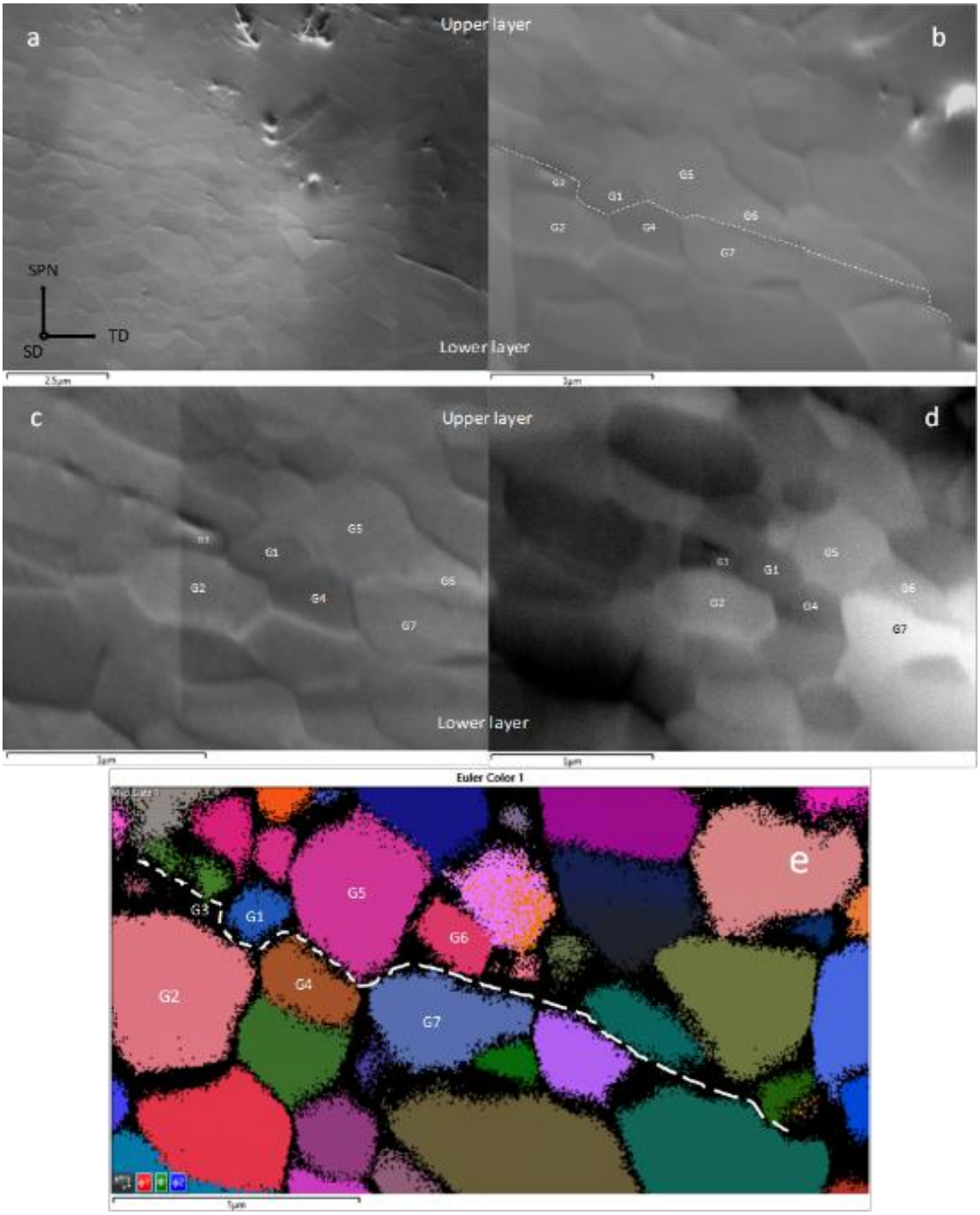

Figure 5.28 (a) SE image of interface at the edge of HPT sample; (b) magnified SE image of G1-G7; the interface of two layers is demonstrated by white long dash line; (c) magnified SE image of grain in (a); (d) FSD image of the same grains in (c); (e) all Euler maps of the same grains in (b).

5.6 Summary

(1) It has been found from the study in this chapter that the grain size doesn′t link well with the shear strain at the M and E positions, possibly indicating that the grain size doesn′t only depend on the imposed shear strain but also is affected by neighbouring materials. The grain refinements at both M and E positions can be generally divided into five stages from the original state to the saturated state.

(2) By comparing the grain size of the two-layer specimen to that of the one-layer specimen at the M and E positions, it is found that the value of the former is obviously smaller than the value of the latter at the medium strain stage ($2.20 < \gamma < 37.26$). As the shear strain increases to the high level, both the grain sizes of the two-layer specimen and one-layer specimen are stabilised at about 0.6 μm, which is the lower limit of the grain size produced by the present HPT experiments. In addition, the saturation of the grain refinement has been achieved earlier in the two-layer HPT deformation compared with the one-layer experiments. It is concluded that the two-layer HPT deformation is able to facilitate the grain refinement.

(3) The two-layer disc instead of the one-layer disc is capable of stabilising the material flow and decreasing the gradient along the sample thickness during HPT at the medium strain level. It is found that the trend of the standard deviation of the grain size declines at the stages of the grain refinement, while the trend ascends or is stable at the stages before the significant grain refinement.

(4) In contrast to the one-layer HPT deformation, although the texture gradient along the sample thickness still exist, the fluctuation of the texture components become less in the two-layer disc, which is in good agreement with the observations of microstructures. The initial textures influence the texture evolution until the 90° rotation.

(5) Strong evidences of the shear-induced GB migration are observed in the UFG Al produced by HPT. The GB migration is only found in several areas at the periphery of the specimen after the 1080 ° and 1800° rotations. The GB migration along the preferred orientation results in the shrinkage or expansion of particular grains under the applied shear deformation

Chapter 6 High pressure torsion of Al single crystal

In the polycrystalline materials, the deformation behaviour of an individual grain is affected by its neighbouring grains. To eliminate the influence of neighbouring grains and grain boundaries on the material deformation behaviour during HPT, single Aluminium crystals were used as starting materials to study the deformation mechanism at the low strain levels in this chapter.

Hafok and colleagues studied experimentally the HPT process of the nickel single crystals [128, 129]. However, their study did not reveal the texture and microstructure evolutions in the low strain range. In this study, the textures and microstructures at the centre (C-position), middle (M-position), and edge (E-position) positions of each disc deformed after various rotation angles are investigated.

Although the dislocation-based mechanism is dominant, GB migration has been observed in the UFG polycrystalline Al during HPT in Chapter 5. Actually GB migration is most likely found in the conditions where traditional dislocation activities are constrained [306]. There are several mechanisms to explain the GB migration phenomenon. It was considered that GB migration involves thermal processes such as recrystallization [291, 307], Coble creep [308, 309] (i.e. enhanced grain boundary diffusion) and DIGM [221, 310-312] (diffusion-induced grain boundary migration). However, it was found that GB migration is not a temperature-dependent process [223, 224] whereas it is sensitive to the external stress [209, 214, 237, 313]. As a result, the shear stress-induced GB motion [314], termed as the shear induced GB migration [207], has attracted the considerable interests.

Based on investigations of bi-crystals with symmetric tilt GB [210-212, 315] and twist GB [316], the DSC (displacement shift complete) dislocation model [312, 317-319] and Cahn model [207, 208, 320] were proposed to explain the shear induced GB migration. In the DSC dislocation model, GB migration is attributed to the sliding of the DSC dislocations driven by shear stress. For the sake of the geometrical compatibility of the DSC lattice, a step (termed disconnection) is generally accompanied with the DSC dislocations. The effect of the shear induced GB migration is quantitatively expressed by a shear induced factor which depends on the DSC Burgers vector and the step height. In the Cahn model, the symmetric tilt HAGBs have been considered as an array of edge dislocations. As a result, complex HAGBs have similar characteristics with LAGBs, which only have one set of the edge dislocation with the Burgers

vector perpendicular to the GB plane. Under shear stress, GB migration occurs by the gliding of the array of edge dislocations in the plane perpendicular to the tilt axis. Concurrently the motion of the dislocations causes a shear displacement parallel to the GB plane and perpendicular to the tilt axis. However, the two models are only applicable to particular cases because all these investigated GBs are in coincidence orientation relationships (DSC model) or symmetrical tilt boundaries (Cahn model). Many experiments [237, 304, 321] have been conducted to explore the underlying mechanism of shear induced GB migration in more general cases. A more general model [223, 234] was developed by Mompiou et al. for grain boundaries with random misorientation angles. This model was a pure geometrical model without any long-range diffusion. In this model, the change of grain shape was caused by local reorganisation of small groups of atoms.

Since HPT can provide extremely high shear strain in the sample, it is reasonably assumed that GB migration should occur during HPT. However, GB migration in HPT was rarely reported. In Chapter 5, the shear induced GB migrations have been detected in UFG material deformed by HPT. In nc and UFG materials, GB mediated processes including GB migration are generally promoted because the traditional dislocation actives are constrained by an extremely high volume of GBs. However, is there any GB migration in extra coarse-grained materials during the early deformation stage of HPT? If yes, does its underlying mechanism follow the shear induced GB migration models? In this chapter, in order to address these questions, two <100> single Al crystals are stacked to be deformed by HPT. The interface of the two stacked discs plays a role of reference to characterise the GB migration from one disc towards another disc.

6.1 Experiment procedure

High purity Aluminium single crystal discs purchased from MaTecK Material-Technologie & Kristalle GmbH, Germany, were employed as the starting samples in this study. All these discs had a diameter of 10 mm. The crystallographic orientation of single crystals along the axial direction of the disc is [0 0 1]. There were two groups of the disc samples: one group with the thickness of 1.5 mm used for one-layer HPT and the other group with the thickness of 0.75mm used for two-layer stacked HPT. The maximum thickness of the cavity between the HPT anvils was approximately 1.44 mm. As a result, some materials flowed out from the gaps between the two anvils.

The single Al crystal samples were processed by HPT under a pressure of ~6.16 GPa at room temperature. During HPT the lower anvil was rotated clockwise from the top view at a constantly slow speed of 0.5 rpm to minimize the heat effect. The one-layer discs were deformed by the rotations of 15° (1/16 turn), 30° (1/16 turn), 45° (1/8 turn) and 90° (1/4 turn) respectively The two-layer discs were deformed by larger rotation angles, i.e. 180° (1/2 turn) and 270° (3/4 turn) respectively.

As shown in Fig. 6.1, the [100] crystallographic orientation of a single crystal is indicated by a small notch on the side of the one-layer disc. Two radii (r1 and r2) parallel to the [100] crystallographic orientation were marked on the top surface and bottom surface respectively (Fig. 6.1(a)). After HPT, there was an angle θ between the two radii. It was found that the angle θ was approximately equal to the HPT rotation angle. This indicates that there was no relative movement between the sample and the anvils during HPT of the one-layer disc.

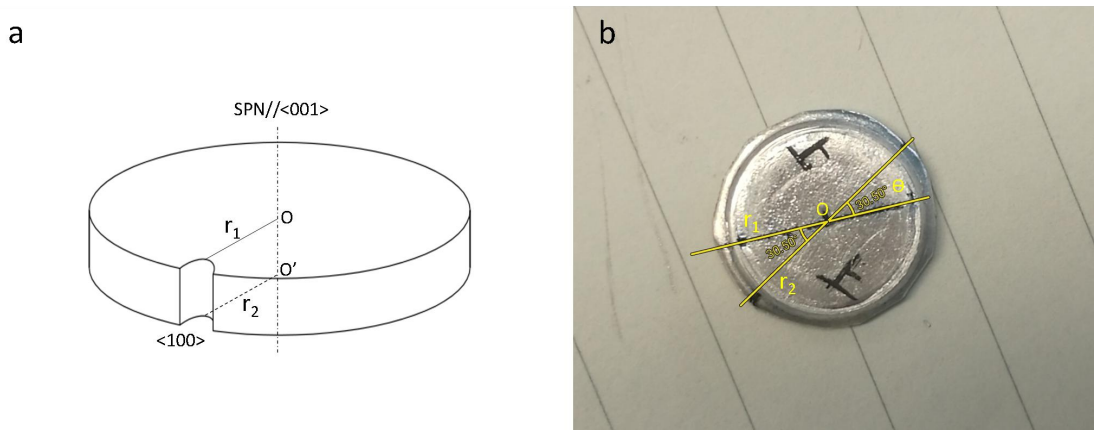

Figure 6.1 Schematic illustration of one-layer disc (a) before and (b) after HPT. Two radii parallel to the [100] crystallographic orientations were marked on the top surface (r_1) and bottom surface (r_2) respectively before HPT as shown in (a). The r_2 was rotated along the anticlockwise direction (from the top view) around the SPN axis by an angle of θ as shown in (b).

In the two-layer disc HPT, two discs were stacked and carefully aligned with each other. As shown in Fig. 6.1.2, two radii r_1 and r_2 parallel to the initial [100] crystallographic orientation were marked on the top surface of the upper disc and the bottom surface of the lower disc respectively. In order to study the influence of misorientation angle between two discs on GB migration, there was an angle of θ between r_1 and r_2 before HPT. θ was 45° for the HPT with the 180° rotation (named as 180°/45° sample) and 30° and 45° for the HPT with the 270° rotation (named as 270°/30° and 270°/45° samples), respectively.

After HPT, all deformed discs were cut along the r_1-SPN (i.e. TD-SPN) plane. The corresponding EBSD measurements on the one-layer discs were conducted on the cut plane at the C-position (at the disc centre), M-position (at a distance of 2 mm away from the disc centre) and E-position (at a distance of 4 mm away from the disc center) respectively. For the two-layer discs, EBSD measurements were carried out around the interface of two discs at the peripheral area to observe the shear induced GB migration. The angle θ (53.15%) after HPT was slightly larger than the initial 45° indicating a slight slip between the two stacked discs.

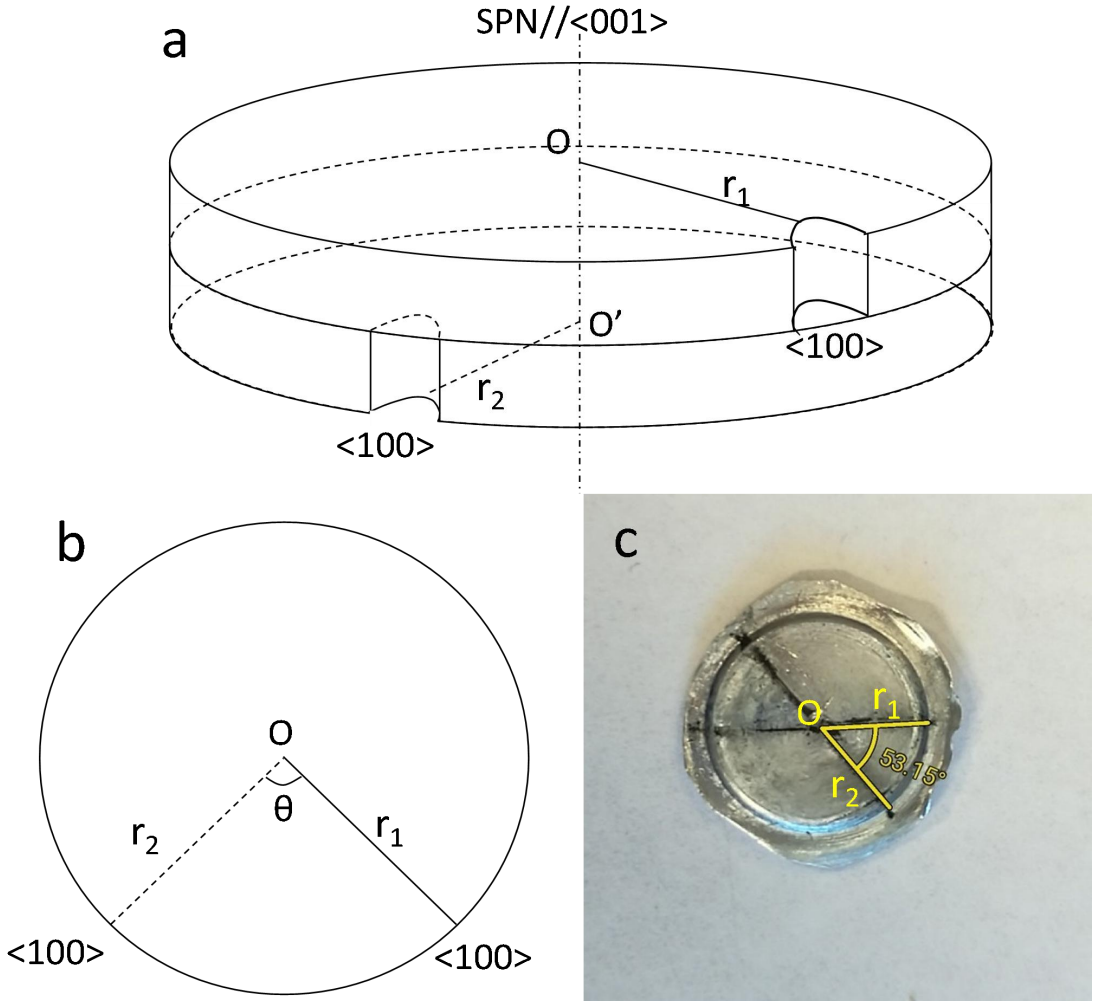

Figure 6.2 Schematic illustration of two-layer single crystal discs before (a)-(b) and after HPT (c). (a) Two radii of the disc parallel to the [100] crystallographic orientation were marked on the top surface of the upper disc (r_1) and the bottom surface of the lower disc (r_2) respectively. The angle of θ is the misorientation angle between initial r_1 and r_2 from top view (b and c).

6.2 Microstructure and texture of HPT deformed one-layer Al single crystal at E-position

Fig. 6.3 demonstrates the EBSD maps after the HPT rotations of (a) 15°, (b) 30°, (c) 45° and (d) 90° respectively at the E-positions on the SPN–r_1 plane. The grain colour denotes the SD direction of the sample coordinate system relative to the crystal coordinate system. The colour spread on the EBSD maps indicates the change of the crystallographic orientation. HAGBs are represented by solid black lines and LAGBs are denoted by solid grey lines on all EBSD maps.

After the 15° rotation, as shown in Fig. 6.3 (a), the single crystal at the E position has been fragmented into many pronouncedly coarse grains with the grain size of larger than 500 μm. Any trace of the original single crystal cannot be detected. Several relatively small grains appear within or at the boundaries of these coarse grains. The average grain size is about 123 μm at this stage.

As shown in Fig. 6.3 (b), with the development of deformation (30° rotation), the grain refinement is constantly promoted and the average grain size is reduced to around 111 μm. Some small grains with the grain size of about tens of micrometres are formed. It can be seen that the grains at the bottom are generally smaller than those at the top.

With the development of the rotation to 45°, the average grain size decreases significantly to about 49 μm. The strain gradient along the RD gives rise to the corresponding gradient in grain size. As shown in Fig. 6.3 (c), a significant grain refinement is seen at the right-hand area which is close to the edge of the disc and subjected to relatively higher strain, whereas the considerably coarse grains are still found at the left-hand area. At the left-hand area, the band-shaped structures with the major axes roughly parallel to the RD are dominant. However the grains at the right hand area are generally more equiaxed and have a relatively low value of the aspect ratio.

As the HPT rotation increases to 90° the average grain size has been reduced to ~36 μm. It can still be seen that the grain size at the right-hand area is smaller than that at the left-hand area. The periodic colour spread in Fig. 6.3 (d) suggests a random orientation distribution.

With the rotation angle increasing from 15°, to 30°, 45° and 90°, the average grain size reduced from 123 μm, to 111 μm, 49 μm and 36 μm, respectively. It should be noted that the

average grain size reduced rapidly between the rotation angles of 30° and 45°. As stated in previous chapters, grain refinement is not a linear function of the shear strain in HPT. The deformation process can be divided into two kinds of stages, i.e. preparation stages and grain refinement stages. During preparation stages, the dislocations are considerably propagated without severe fragmentation, whereas during the grain refinement stages, the parent grains are fragmented into smaller grains. Therefore, it is concluded that the stage of rotation angle from 30° to 45° is a grain refinement stages.

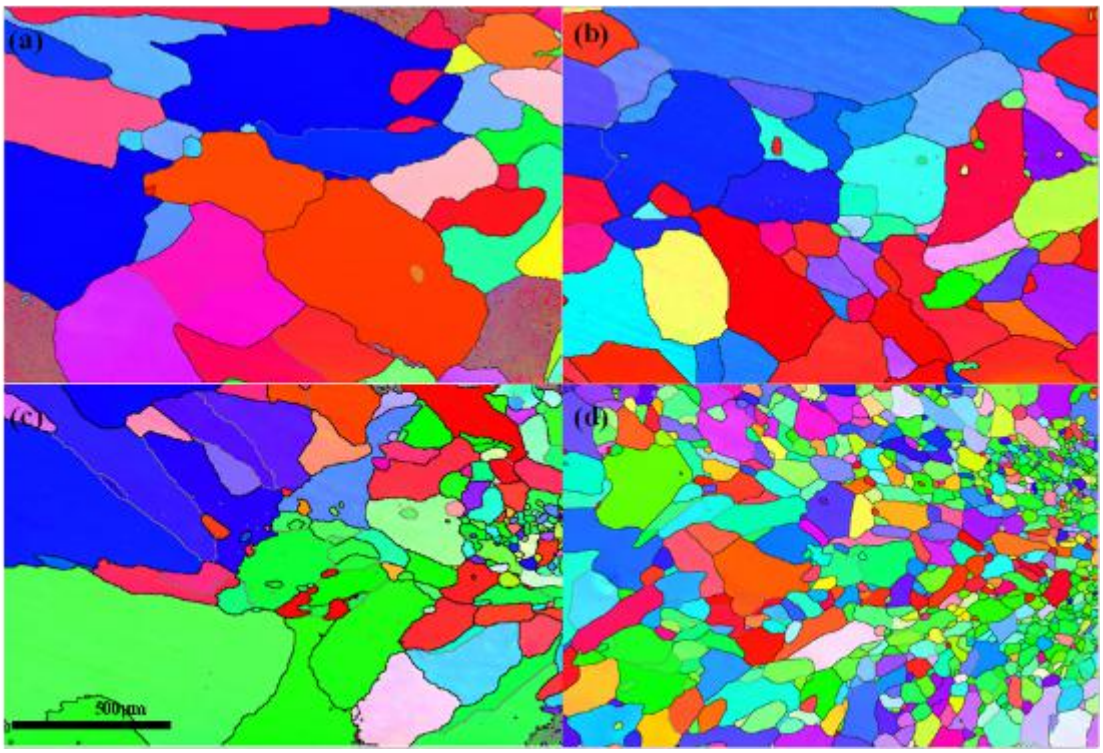

Figure 6.3 EBSD maps of <100> Al single crystal at E-position after HPT with the rotation angles of 15° (a), 30° (b), 45° (c) and 90° (d).

Fig. 6.4 illustrates the (111) pole figures at the E-position after the 15°, 30°, 45° and 90° rotations on. All ideal simple shear orientations are marked in Fig. 6.4 (a). After the 15° rotation, as shown in Fig. 6.4 (a), ideal simple shear components cannot be found. The initial cube component rotates around the SPN axis and it tends to evolve into two separate texture components. The volume fraction of the Cube component is 1.94% at this stage.

With the development of deformation to 30° rotation, the volume fraction of the A^*_2 texture component accounts for 0.64%. Simultaneously the volume fraction of the Cube component decreases slightly to 1.46%. As shown in Fig. 6.4 (b), the more diverging contour lines in comparison with Fig. 6.4 (a) imply the lower intensity of existing textures.

As the rotation angle increases to 45°, the volume fraction of the Cube component grows up to 2.96%. Several new components are detected at this stage. The volume fractions of the A/A_b, A^*_2 and C components take up 0.35%, 0.06% and 1.44% respectively.

After the 90° rotation, as shown in Fig. 6.4 (d), poles rotate away from the positions of the Cube and C components, resulting in the disappearance of the C component and the pronounced decline of the Cube component to the volume fraction of 0.17%. In addition, different trends for the A/A_b and A^*_2 components are observed. The volume fraction of the A/A_b component is stabilised at 0.35% while the A^*_2 component increases moderately to 0.14%.

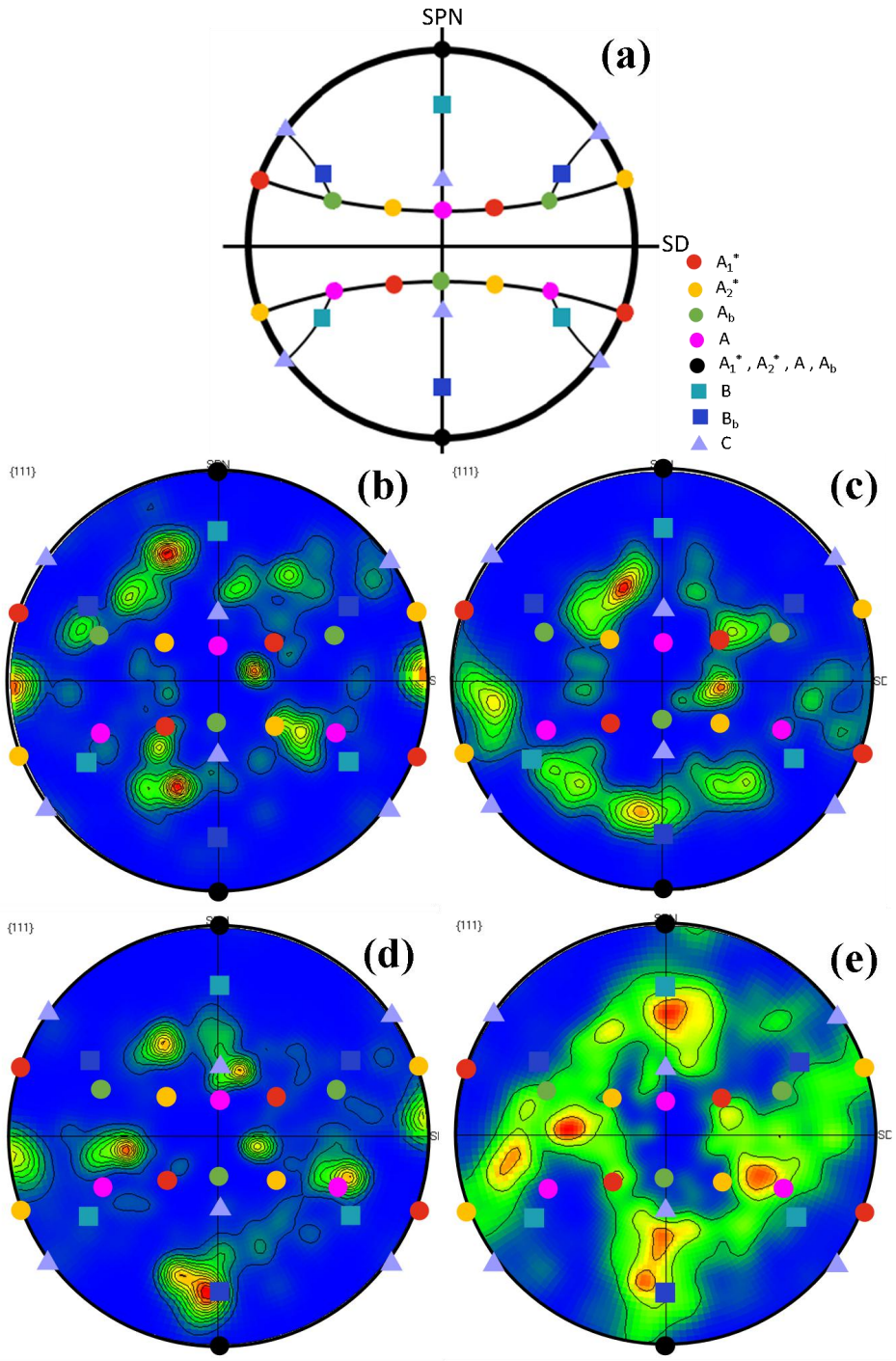

Figure 6.4 {111} pole figures of the <100> Al single crystal at E-position after HPT with the rotation angles of (a) 15°, (b) 30°, (c) 45° and (d) 90°. All ideal simple-shear textures are projected in (a)-(d).

6.3 Microstructure and texture of HPT deformed one-layer Al single crystal at M-position

Fig. 6.5 shows the EBSD maps after the HPT rotations of (a) 15°, (b) 30°, (c) 45° and (d) 90° respectively at the M-position on the SPN $-r_1$ plane. The distance from the disc centre

increases from the left-hand side to the right-hand side in each of the figures. As shown in Fig. 6.5 (a), at the low rotation angle of 15°, some gains with clean interior have been generated at the right-hand side of the picture. The rest area still remains in a similar orientation though this area is a little bit blurry, indicating that the small lattice rotations have occurred.

With the development of the rotation angle to 30°, more newborn grains in the form of band structures are observed in Fig. 6.5 (b). It is known that the applied strain increases from the left-hand side to the right-hand side of the picture. Comparison of Fig. 6.5 (a) and Fig. 6.5 (b) clearly shows that the grain generation/refinement propagates from the right-hand side to the left-hand side. One of the reasons for this is that the applied strain at the right-hand side is larger than that at the left-hand side. The other reason is that the existence of the smaller grains at the right-hand side promotes the grain generation/refinement at the left-hand side in order to meet the geometrical compatibility.

At the rotation angle of 45°, as shown in Fig. 6.5 (c), the grain generation further extends to the left-hand side of the picture. Sawtooth shaped grains can be observed in Fig. 6.5 (c). Actually these sawtooth shaped grains are a kind of band structures. With the development of the rotation angle to 90°, new-born grains cover the entire area in Fig. 6.5 (d). The area can be divided into three layers along the thickness. These layers have the band structures. The grains SG1-SG4 in the second layer were generated from the same parent band structure. It is noteworthy that all the major axes of the new grains incline to the RD. In addition, many small grains emerge inside parent grains (for example inside SG1) or at the grain boundaries (for instance between SG2 and SG3 and between SG3 andSG4).

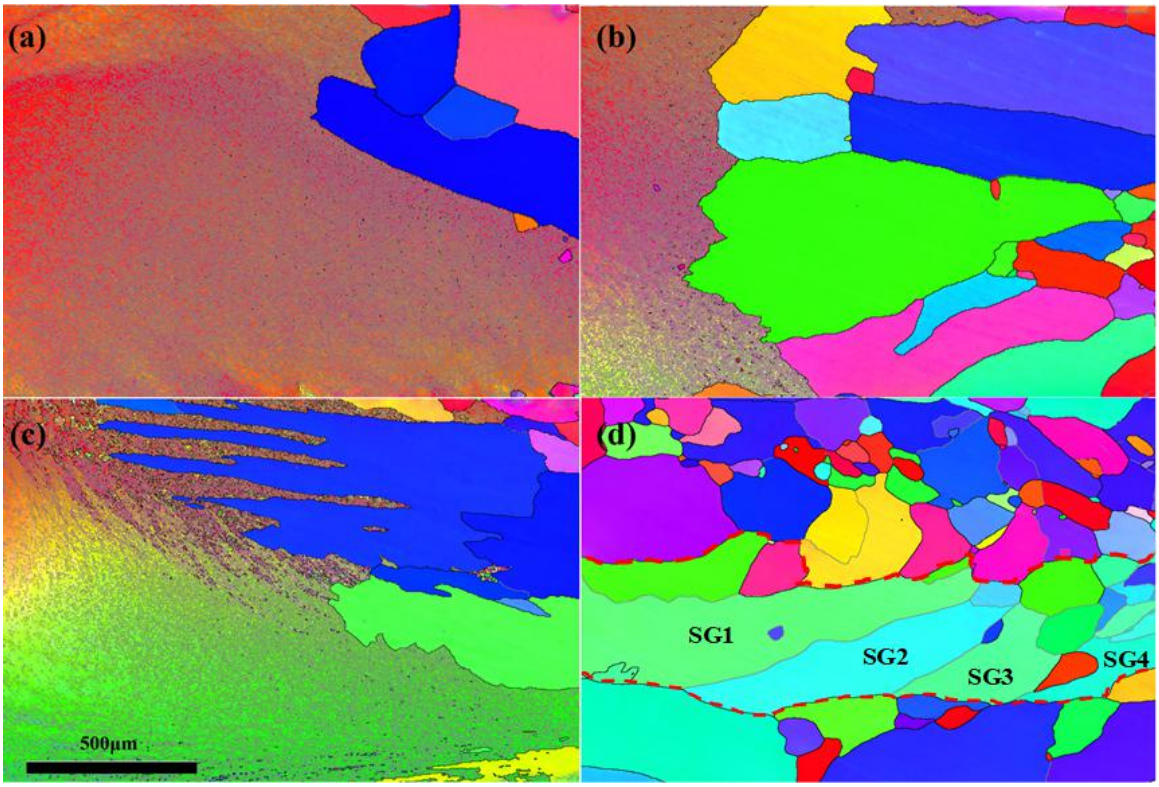

Figure 6.5 EBSD maps of <100> Al single crystal at M-position after the rotations of 15°, 30°, 45° and 90°.

Fig. 6.6 shows the the (111) pole figures at the M-position after 15°, 30°, 45° and 90° rotations respectively . All ideal simple-shear textures on the {111} pole figure are presented in Fig. 6.6 (a). After the 15° rotation, only a 6.43% volume fraction of the Cube component is found, indicating that the influence of the initial orientation on the current texture components has decreased to a low level. In Fig. 6.6 (b), poles are away from the ideal Cube position but have not seen any ideal simple-shear texture components.

With the development of the rotation to 30°, textural randomization is introduced by the grain generation as shown in Fig. 6.6 (c). Almost no ideal simple-shear textures can be detected except the Cube component (2.9%), suggesting that the preferred orientations of new-born grains are not that of ideal simple-shear components at this stage.

After the rotation angle of 45°, the C component predominates with the volume fraction of 23.2%. However, the C component originates from the lattice spin at the bottom areas rather than from the generation of new grains. Simultaneously the volume fraction of the Cube component decreases to a negligible level (1.12%).

After the 90° rotation, no large volume ideal texture can be observed. The presence of extremely low volume fraction of the A^*_1 component (only 0.2%) possibly comes from a small new grain. The fraction volume of the Cube component is stable at low level (1.55%).

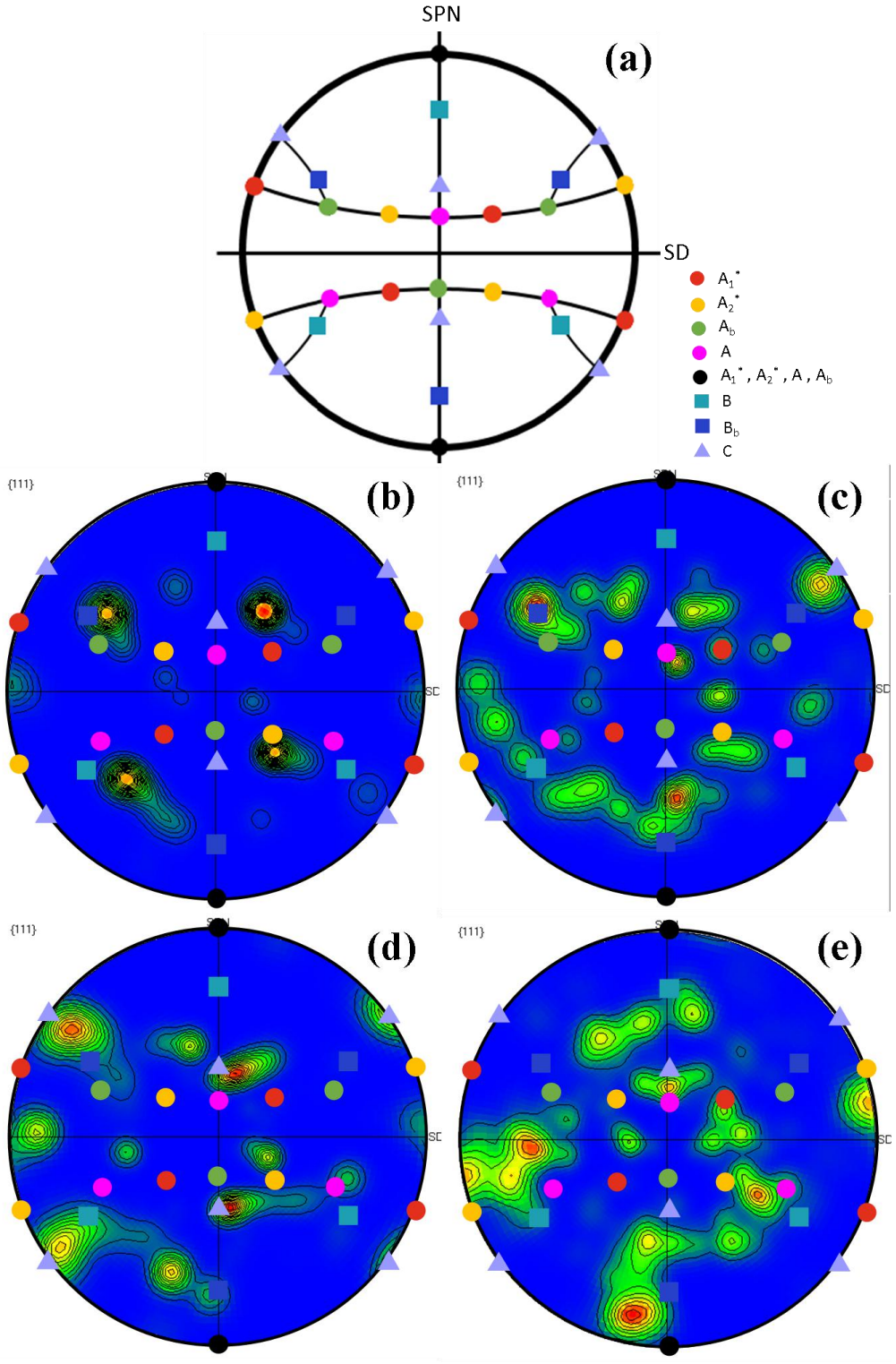

Figure 6.6 {111} pole figures of the <100> Al single crystal on the SPN-SD plane at M-position after rotations of (b) 15°, (c) 30°, (d) 45° and (e) 90°. All ideal simple-shear textures are projected in (b)-(e).

6.4 Microstructure and texture of HPT deformed one-layer Al single crystal at C-position

Fig. 6.7 shows four EBSD maps after the HPT rotations of (a) 15°, (b) 30°, (c) 45° and (d) 90°, respectively, at the C-position.

In Fig. 6.7 (a) with the rotation angle of 15° the most areas have the red colour on the EBSD map. This suggests that the initial [100]//SD orientation is sustained and the compressive pressure before the HPT rotation does not significantly change the crystallographic orientation at the central position. It is known that at the beginning of HPT the material at the bottom of the disc flows first with the rotation of the low anvil. As a result, the torsional deformation starts from the bottom layer, then gradually transfers to the top layer. The corresponding result is demonstrated by the colour gradient shown in Fig. 6.7 (a). Specifically, a touch of the green colour ([110]//SD) emerges at the bottom. At this stage, most of the intragranular sub-structures are the discontinued LAGBs. The density of LAGB at the edge area is obviously higher than that at the centre, which is in good agreement with the strain gradient along the RD.

The deformed region is enlarged with increasing rotation angle to 30° as shown in Fig. 6.7 (b). It is clearly found that the more initial [100] orientations convert into the [110] orientations progressively by the rotation with respect to the SPN direction. The central area in Fig. 6.7 (b) with the low density of sub-structure has become narrow. This is because the increasing shear strain gives rise to remarkable propagation of dislocations, resulting in more mutual dislocation tangles and walls. The absorption of the dislocations by dislocation walls leads to the formation of the sub-grain boundaries. The continued sub-structures have been found but the discontinued LAGBs are still dominant. In spite of increasing the shear strain, HAGBs have not been observed at this stage.

At the rotation angle of 45°, the crystallographic orientations in more than half of the areas have been rotated into the <110> {u v w} texture. The colour spread clearly demonstrates that the microstructure gradient does not just exist along the thickness but also along the RD. As the shear strain increases, the absorption of the dislocations by sub-structures will increase the misorientation angles of LAGBs, thereby the LAGBs are transformed into HAGBs. As a result, HAGBs appear at the top right of Fig. 6.7 (c) at this strain level.

New grains appear at both sides of Fig. 6.7 (d) with the rotation angle of 90°. However the low density of sub-structures still predominates at the centre of Fig. 6.7 (d). Low density of sub-structures can deduce low dislocation density in the same area. As a result, it is reasonably postulated that the low hardness value exists at the centre of the deformed disc, which is in good agreement with the experimental measurements in the previous studies [64-66, 322]. It should be noted that the interiors of new grains are very clear, indicating that the recovery has taken place at room temperature. Irregular grain shapes suggest no recrystallization occurrence at this stage. In terms of crystallographic orientation, with the increase of deformation at the centre of Fig. 6.7 (d) the green colour area moves up towards the top surface, and at the central bottom area new red colour emerges. However, the top layer keeps the initial orientations constantly so far.

The grain fragmentation is the result of increase in the fraction of continuous grain boundaries. Actually there are two types grain boundary in materials with medium to high SFE after plastic deformation, i.e. GNBs and IDBs. The GNDs are derived from the strain gradient in materials undergone nonhomogeneous plastic deformation and accommodate the misorientation angles of neighbouring grains which result from the deformation with different slip activities. The IDBs is generated by mutual trapping of dislocations. As shown in Figure 6.3, 6.5 and 6.7, it is clearly observed that at the areas with low plastic strain, for example at the C-position, although numerous dislocations are propagated during plastic deformation, most of the continuous GBs are GNDs. The grains bounded by GNDs generally have large grain size.

At M-position, with the increase of deformation, the onset of grain-grain interactions give rise to grain fragmentation at the GBs [322, 323]. The grains exert stress on their adjoining grains to produce new grains, thus most of the newly small grains are observed at GBs. In the meantime, several new sub-grains and grains are emerged within their parent grains, which should be attributed to the formation of IDBs. The growth of shear strain considerably promotes the propagation of dislocations. And the mutual dislocation tangle and agglomeration lead to the small intragranular grains. More small grains are born at E-position. As a consequence, grain sizes are of bimodal distributions.

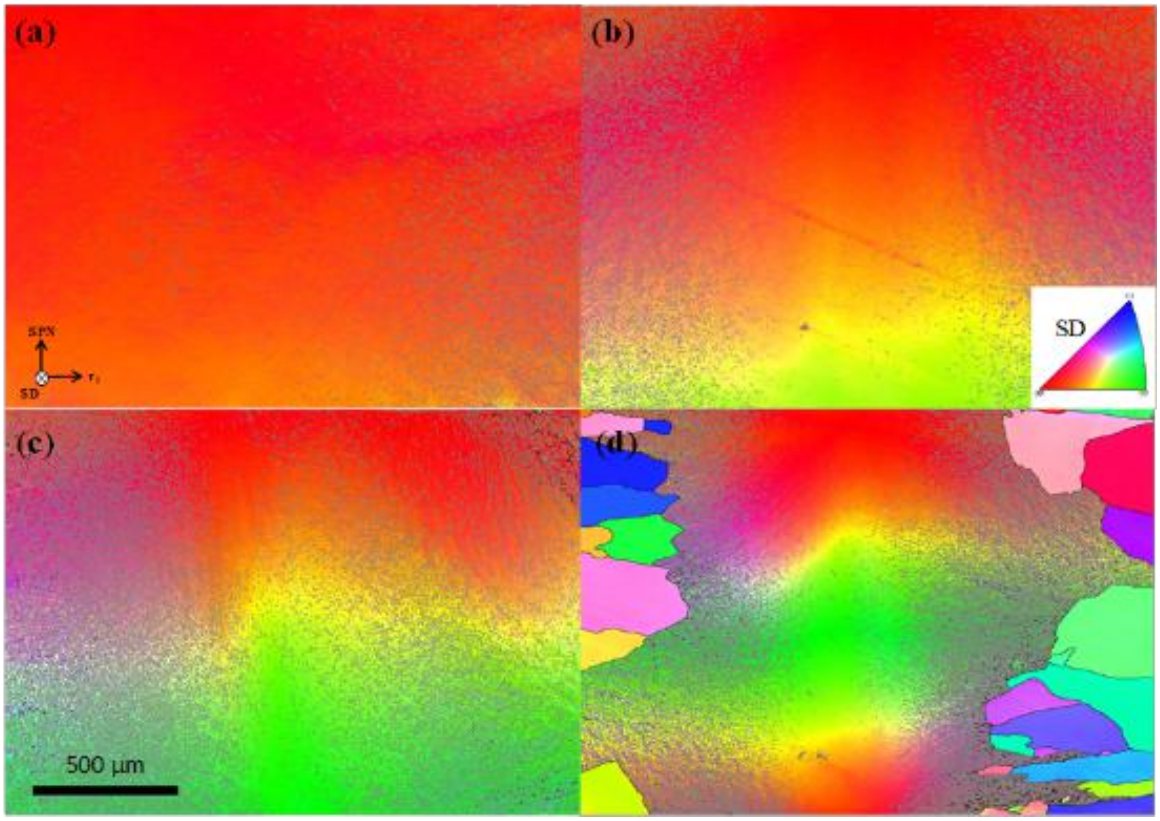

Figure 6.7 EBSD maps of <100> Al single crystal at C-position after HPT with the rotation angles of (a) 15°, (b) 30°, (c) 45° and (d) 90°. The grains are coloured according to their crystallographic orientations relative to the SD direction.

Fig. 6.8 shows the misorientation angle distributions of the <100> single Al crystal after HPT with the rotation angles of 15°, 30°, 45° and 90° at the C-position. Because the fraction of HAGBs is extremely low, it does not take this into account in this figure. With the onset of the deformation, the dislocations propagate significantly, causing the increase in the fraction of structures with the misorientation angle of less than 2°. After the 30° rotation, more dislocations are aggregated to form the dislocation tangles and walls. As a result the fraction of the dislocations descends consistently. This decreasing trend continues to the 45° rotation. In addition, the densities of LAGBs ascend at the expense of the dislocation densities at these two stages. After the 90° rotation the relative frequency of dislocations and LAGBs with misorientation angle of larger than 6° increase in comparison with that at the previous stage, but the density of LAGBs with the misorientation angle of $2°<\theta<6°$ declines. This is possibly attributed to the recovery within the new-born grains.

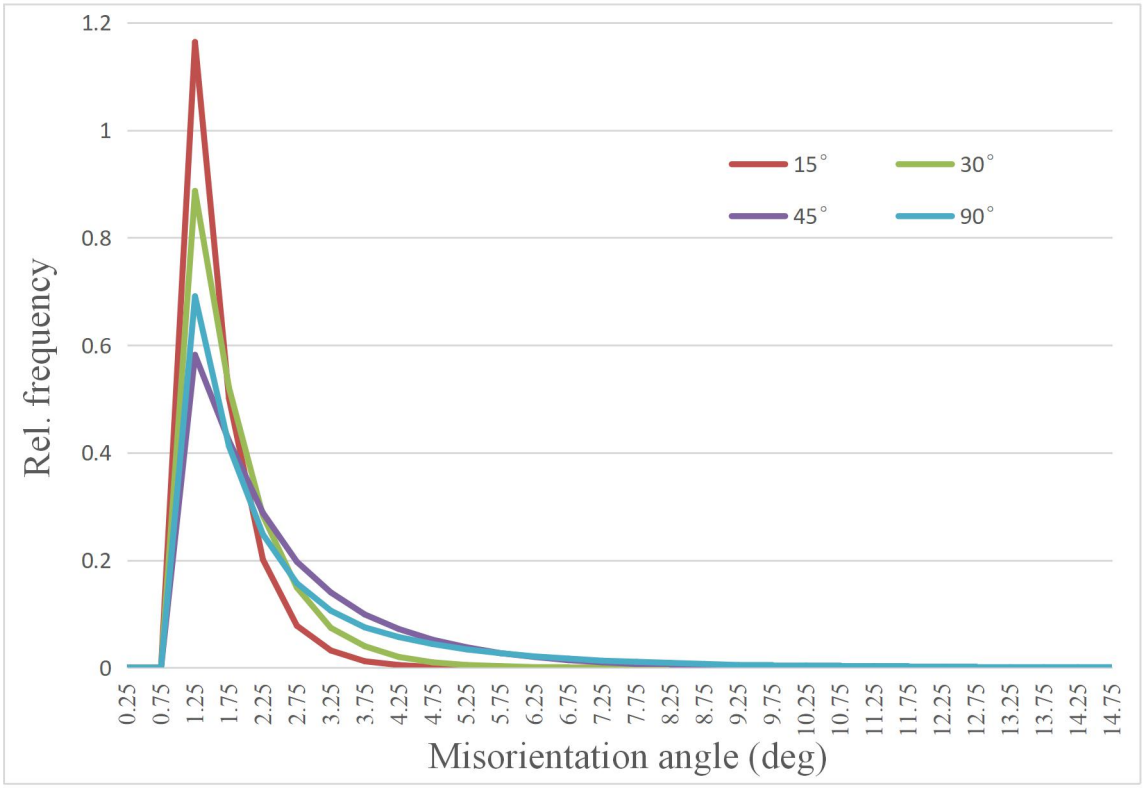

Figure 6.8 Misorientation angle distributions of <100> single Al crystal after HPT with the rotation angles of 15°, 30°, 45° and 90° at C-position.

Ideal textures are the favourable crystallographic orientations generated during plastic deformation. Fig. 6.9 shows the distributions of the simple-shear texture components at the C position after HPT with the rotation angles of 15°, 30°, 45° and 90°. It is found that only two components exhibit at all stages. The red colour represents the Cube texture component and the olive green colour denotes the C texture component. In this study the maximum deviation of these texture components is 10°. The 3D crystal cubes are superposed on the corresponding areas to demonstrate the orientations.

The Cube component prevails at the early deformation stage. At the bottom area (Position C) in Fig. 6.9 (a), after the 15° rotation, the orientation rotates away from the Cube orientation with respect to the SPN axis, whereas at the top area, such as Position A, the Cube component dominates. It is noted that the Cube component vanishes at Position B.

As the rotation angle increases to 30° the area with the Cube component shrinks. As shown in Fig. 6.9 (b), the Cube component only remains at the top area. The textural gradient can be observed along the RD. It is known that the C component can be obtained by rotating the Cube component around the SPN axis by 45°.

At the rotation angle of 45°, the C component appears in Position I at the central bottom of Fig. 6.9 (c). In addition, the area of the Cube orientation decreases continuously.

At the rotation angle of 90°, new Cube texture component emerges at the central bottom of Fig. 6.9 (d) and the C texture component moves up to Position L. The 3D crystal cubes at Positions (J)-(M) demonstrate clearly that the lattices rotate around the SPN axis at the centre of the disc and the rotation angle increases from the top surface to the bottom surface. These lattice rotations generate the band structure in the sample. It is found that at Position C the material flow is stably constrained within a layer. The lattices of these materials rotate around the SPN axis and their (010) planes are parallel to the SPN plane. The material flows are more complicated at the non-central areas such as Positions B and O where the (010) planes of these lattices incline to the SPN-plane. This is attributed to the concurrent lattice rotations with respect to the SPN and the TD directions. This kind of lattice spin can help the easy slip (111) plane align to the direction of the applied stress as far as possible, thereby leading to the activation of the slip systems.

According to the shear strain equation for HPT, the shear strain at the centre of the disc should sustain at zero constantly even after a great number of revolutions. In practice, as shown in Fig. 6.9, the materials at the centre of the disc are effected by the flow of adjacent materials. With the increase of HPT deformation, the affected areas are enlarged from the bottom area to the top area. It is deduced that eventually the material at the top area will be deformed when the sufficient revolutions are achieved.

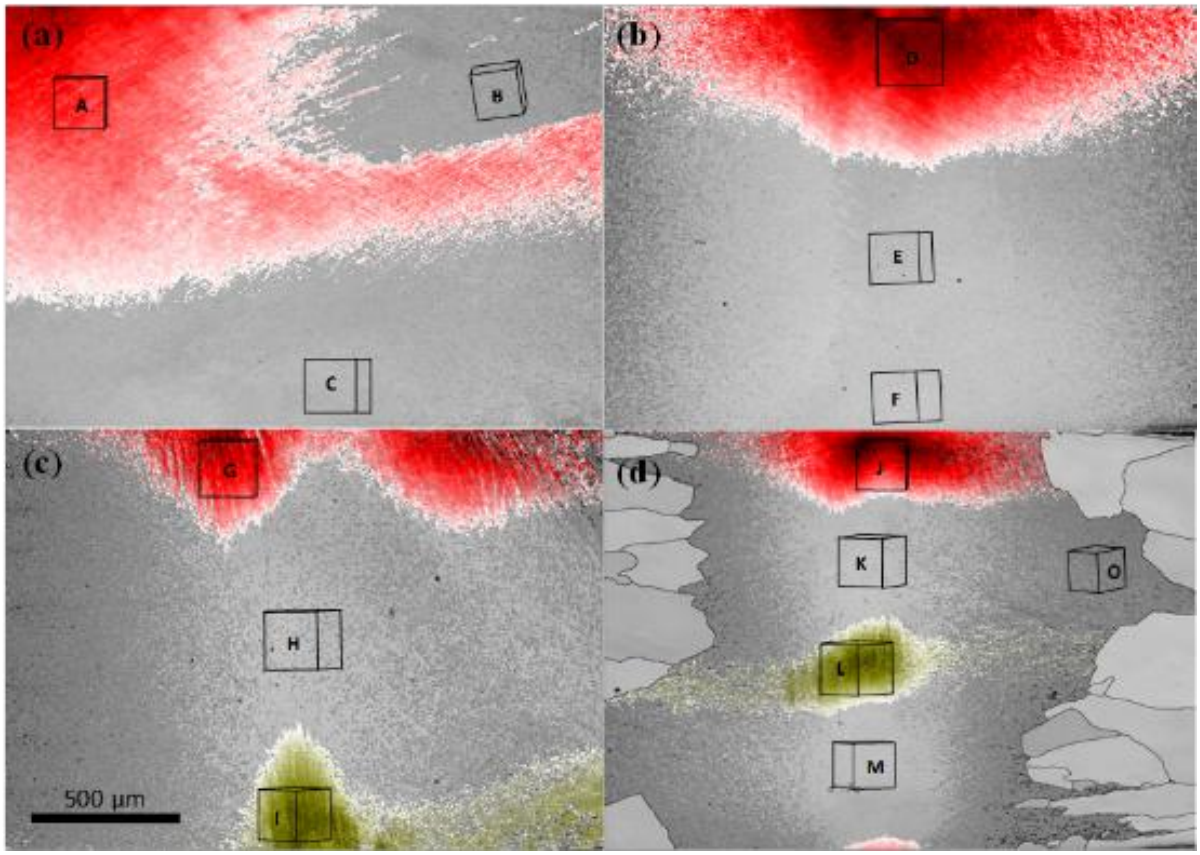

Figure 6.9 Ideal simple-shear texture components illustrated in EBSD maps of <100> Al single crystal at the C-position after the HPT rotations of (a) 15°, (b) 30°, (c) 45° and (d) 90°. Red and olive green colour denote the Cube and C texture component respectively. The 3D crystal cubes are superposed in the EBSD maps

Fig. 6.10 demonstrates the {111} pole figures at Position C after the HPT rotation angles of 15°, 30°, 45° and 90°. All ideal simple-shear textures on the {111} pole figure are presented in Fig. 6.10 (a). After the 15° rotation, the poles start to deviate from the positions of the Cube component. The high density of the contour lines in Fig. 6.10 (a) indicates that the strong texture exists at this stage. Fig. 6.11 denotes the volume fractions of all ideal components with a maximum deviation of 10° after different HPT rotation angles. It is found that the volume fraction of the Cube component decreases drastically from 100% in the as-received condition to 43% after the 15° rotation. Any ideal components cannot be detected at this stage.

With the development of the rotation angle to 30°, more diverging poles are observed in Fig. 6.10 (b). It is known that the grain distortion and fragmentation would possibly lead to a weaker texture because the unique orientation of the initial grain is divided into several

different orientations. The poles are further rotated away from the initial position. As a result the volume fraction of the Cube component decreases by approximatly 43%.

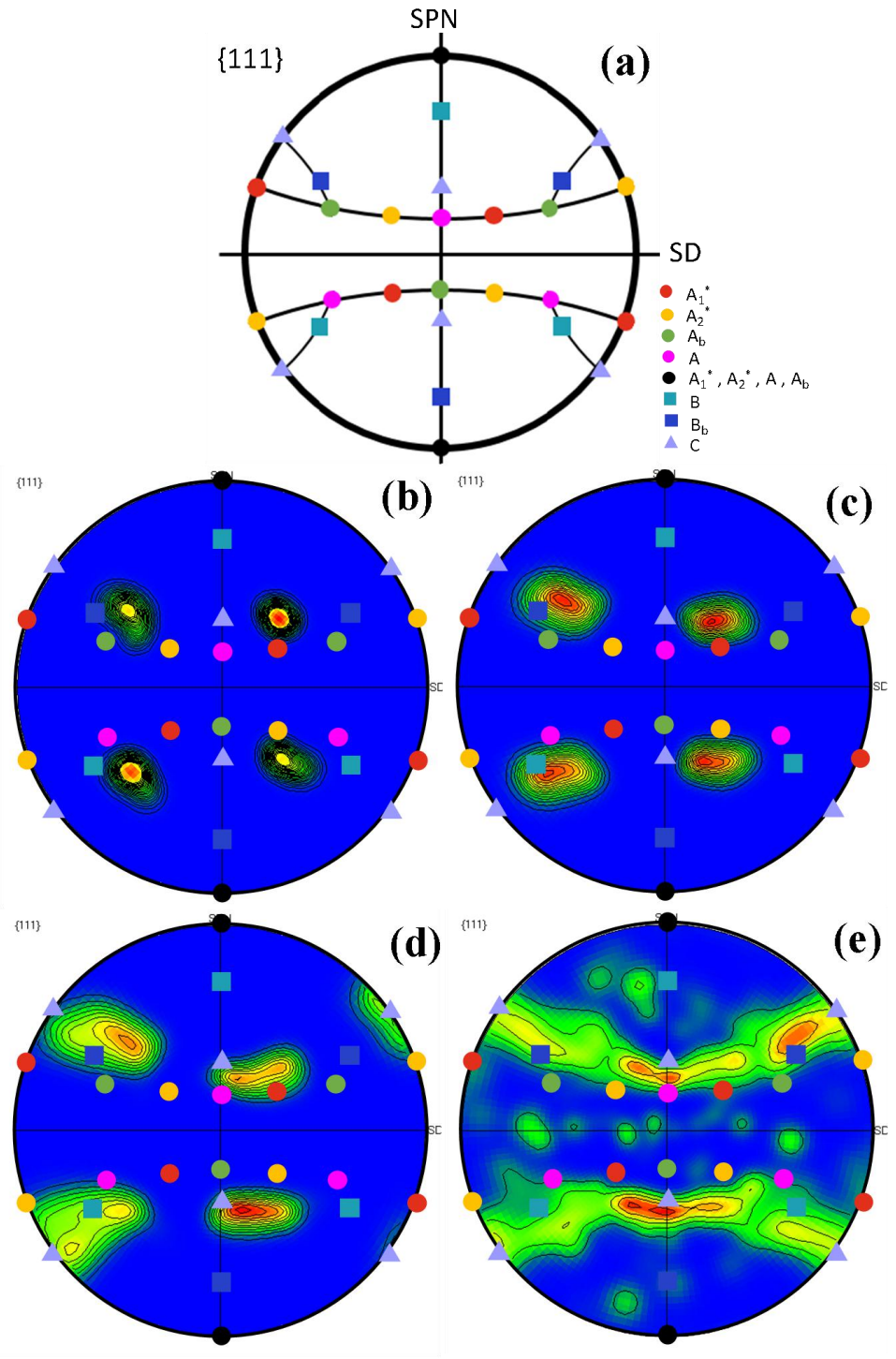

Figure 6.10 {111} pole figures of the <100> Al single crystal on the SPN-SD plane at Position C after rotation angles of (b) 15°, (c) 30°, (d) 45° and (e) 90°. All ideal simple-shear textures are demonstrated in (a) and projected in (b)-(e).

A continuous weakening on the Cube component is observed after the 45° rotation. But some poles are located at the ideal position of the C texture component, indicating the C component starts to emerge at this stage. The corresponding volume fractions of the Cube and C components are 12.4% and 9.24% respectively.

At the rotation angle of 90°, the commencement of the grain fragmentation promotes the formation of more random orientations. The weak Cube and C components dominate with the volume fractions of 8.6% and 8.11% respectively. Other ideal simple shear components are too weak to be detected.

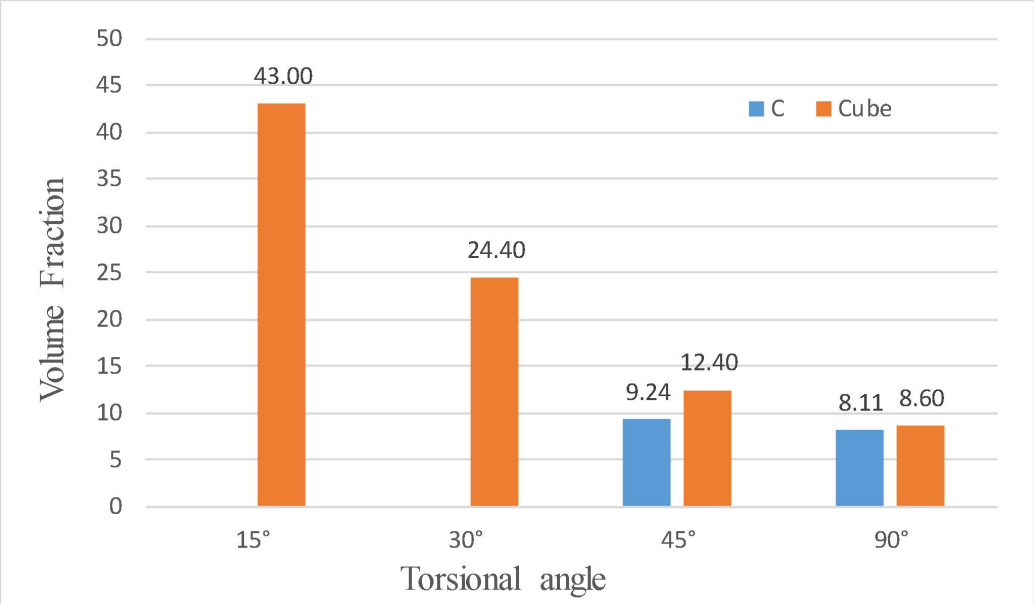

Figure 6.11 Volume fraction of different ideal simple-shear orientations after HPT rotations of 15°, 30°, 45° and 90° at C-position.

6.5 Shear-induced GB mediated processes during HPT

In the present study, the two-layer Al single crystals were used to study the stress-induced GB migration during HPT. Forward scatter detector (FSD) images and all Euler angle images were used to characterise the crystallographic orientations.

In this study, no GB migration has been found in the 180°/45° sample, indicating that the applied strain is one of the important parameters influencing the GB migration.

Fig. 6.12 shows one observation of the GB migration in the 270°/30° sample. The interface of two stacked discs, which is marked by a dashed line in the figure, play a role of reference to demonstrate GB migrations. It is clear that some GBs have migrated through the interface

between two stacked discs. The migrated GB and its neighbouring GBs are marked by numbers in Fig. 6.12. These GBs are the boundaries between four grains, named G1, G2, G3 and G4 respectively, as shown in Fig. 6.12. GB-1 and GB-2 are the boundaries between G1 and G2. These two GBs are ∑5 boundaries. After recovery, the insides of the G1-G4 become clear. Part of the internal stress relief results in a decrease of strain. Thus the relationship between G1-G2 could be considered as a bicrystal system. According to the calculation of bicrystal interface energy in Al [323], there is an energy valley in the energy-misorientation angle relationship at the ∑5 boundaries, indicating ∑5 is a relatively stable structure in Al. GB-3 is the boundary between G1 and G4, which is also a ∑5 boundary. GB-4 and GB-5 are located between G1 and G3. They are non-CSL HAGBs with the misorientation angle of about 45°.

It can be concluded from Fig. 6.12 that G1 grows towards G4 at the expense of G2, G3 and G4. As a result, GB-3 migrates from its initial position (indicated by a red dashed line in Fig. 6.12 (b)) to the current position. But the growth of G1 is blocked by G2, G3 and G4. GB-1 and GB-5 remains immovably at the position of the initial interface. GB- 2 and GB-4 are dragged by the migration of G1, causing the shrinkage of G2 and G3.

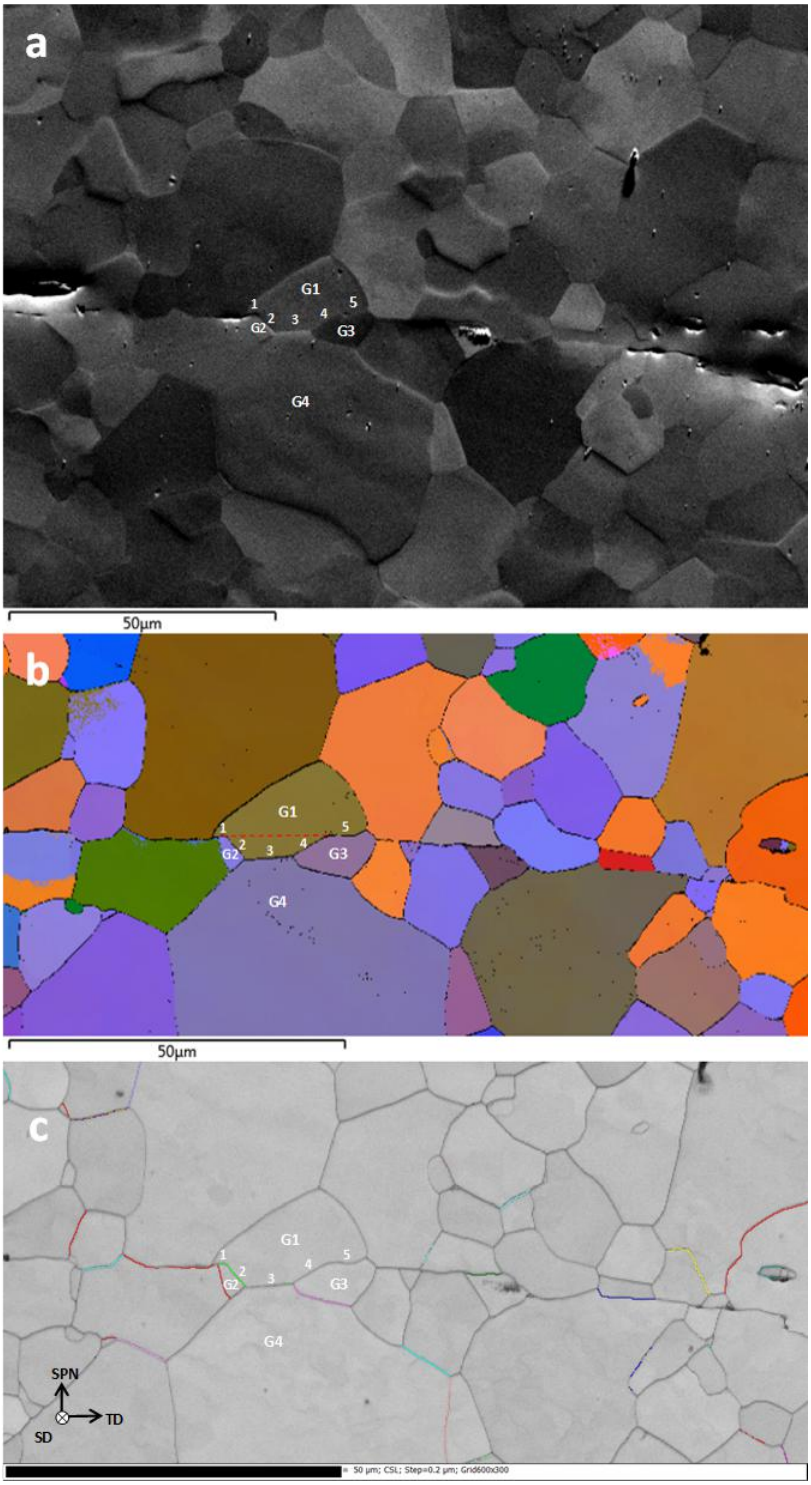

Figure 6.12 (a) FSD image around interface between two discs at the sample edge after 270° rotation; (b) Euler angle map; (c) CSL boundary map. The sense of shear and the observation plane are indicated in (c).

The migration distance of GB-1 at its left-hand side is greater than that at its right-hand side, which is possibly attributed to the different resistances of G2 and G3. The small length of GB-2 compared to the length of GB-4 leads to smaller resistance to the migration of GB-1.

Fig. 6.13 shows the other example of the GB migration observed in the 270°/45° sample. The interface between the two stacked discs is marked by a red dashed line. The relevant GBs and grains are marked in this figure. It is found that GB-1 between G1 and G2 is a ∑41a GB, while GB-2~GB-5 are HAGBs with non-CSL misorientaions. It can be concluded that G1 grows at the expense of G2, G3 and G5. GB-3 and GB-4 have high mobility. It is reasonably assumed that GB-3 and GB-4 are the same boundary. The boundary migrates towards G3, subsequently part of the boundary is stopped by G3 to form GB-3. The rest of the boundary continues to migrate towards G4 to generate GB-4. GB-2 and GB-5 are dragged by the migration of GB-3 and GB-4. GB-1 is impeded by G2 and stays at the initial interface position.

According to the simulation by Homer et al. ∑41a boundary has a high mobility of migration and ∑5 boundary can be mobile at room temperature. However, in this study, both the ∑41a and ∑5 boundaries are stationary while the non-CSL GB-3 in Fig. 6.12 and GB-3 and GB-4 in Fig. 6.13 migrate during HPT. Simulations of 388 GBs have demonstrated that the GB mobility was not correlated to any parameters including the disorientation angle, ∑ value, excess volume or boundary energy [324]. In addition, Rottmann et al. investigated 21 mobile GBs and 62 static GBs in the in situ straining experiment and could not find any criteria to separate the two group [325]. These conclusions are in good agreement with the observation in this study.

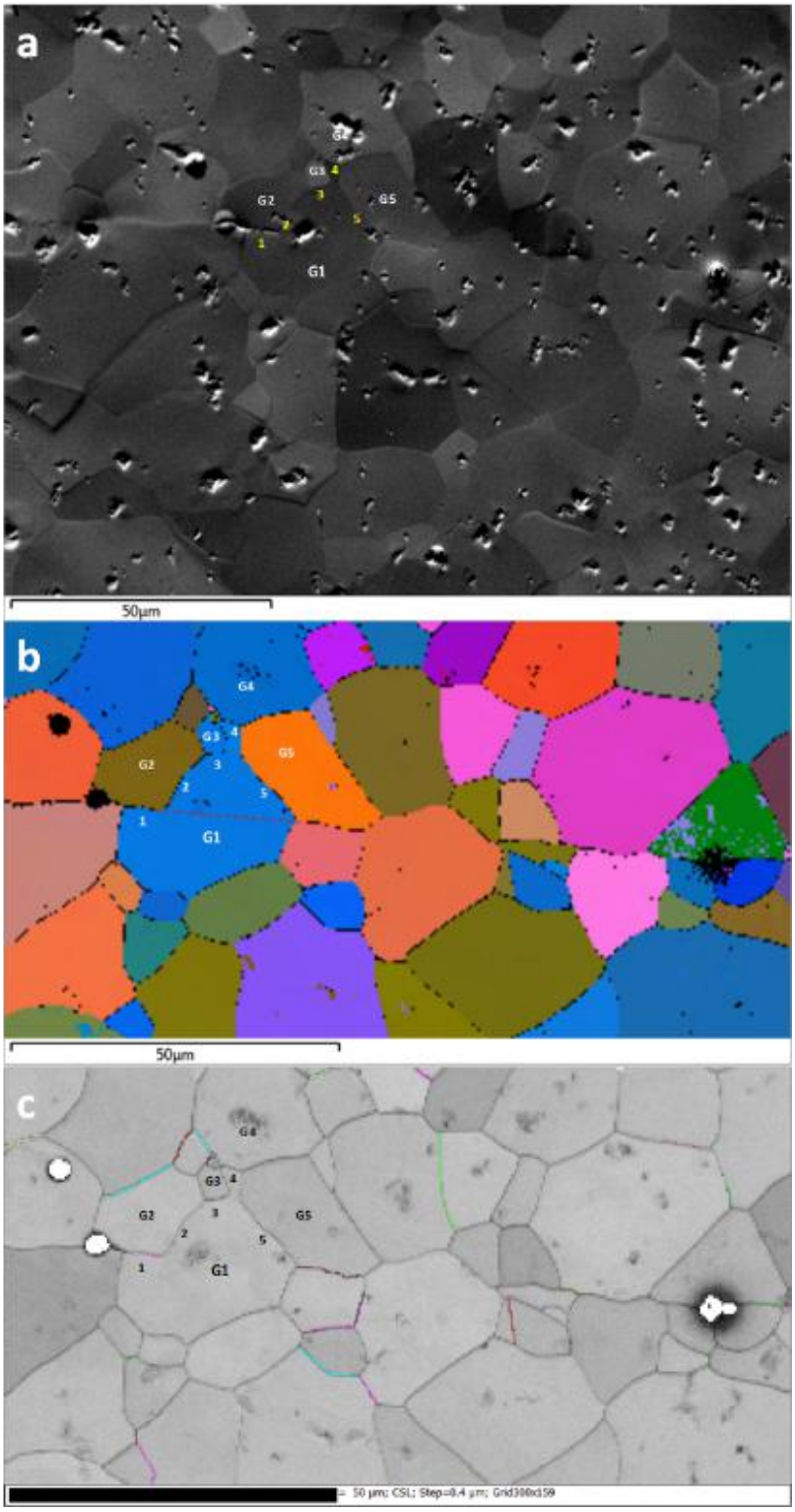

Figure 6.13 (a) FSD image of interface at the edge of HPT sample after 270°/45° torsion; (b) all Euler map of the selected area in (a).

6.6 Summary

(1) At the centre of the sample (C-position), the lattice rotation around the SPN axis is driven by adjacent materials. The deformation does not follow the typical simple shear mode. There is a significant strain gradient along the sample thickness. New grains emerge after the 90° rotation.

The band-shaped structures are dominant at the sample middle position (M-position). With the development of HPT, the band-shaped structures start to be fragmented. But the initial shapes of the band structures can still be identified after the 90° rotation.

At the position near the sample edge (E position), the relatively large strain gives rise to more equiaxed structures. With the increase of deformation, the average grain size is reduced to tens of micrometres.

(2) The Cube and C texture components play significant roles at the C position. The effect of the initial orientation is extremely high but it decreases drastically with the development of deformation. The volume fraction of the Cube texture component declines from 43% at the beginning of HPT to 8.60% at the final stage. After the 45° rotation a great amount of the C texture component appears and its volume fraction is stable during HPT.

At the M position, the development of fragmentation dramatically weakens the the influence of the initial orientation and finally results in a randomizing distribution of ideal texture components. With the increase of deformation, the remaining Cube component declines to a low level after the 45° rotation. Finally, only A^*_1 Cube components with low fractions can be observed.

At the E position, further fragmentation leads to the appearances of more ideal texture components. After the 30° rotation, the A^*_2 component emerges at the expense of the Cube component. But after the 45° rotation, the reverse trends on the A^*_2 and Cube component have been seen. Concurrently the C and A/A_b components are detected. After the 90° rotation the C component vanishes. The volume fractions of the A^*_2, A/A_b and Cube components are very low.

(3) The GB migration was not observed in the 180°/45° sample but found in the 270°/30° and 270°/45° samples. The magnitude of the applied strain could be one of the influencing

parameters on the GB migration. In this study, the GB migrations occur on the normal HAGBs, whereas the ∑41a and ∑5 GBs are stationary.

Chapter 7 Conclusions and recommendations for future work

7.1 Conclusions

In this study, one-layer and two-layer commercial purity polycrystalline aluminium, one-layer and two-layer high purity single crystal aluminium were processed by HPT. The distribution of hardness, microstructural and textural evolutions, and GB migration in the samples subject to various HPT rotation were investigated. The following conclusions can be drawn:

(1) The band-shaped structures predominate in all the HPT processed samples at the low and medium strain levels. With the increase of the shear strain, the band-shaped structures are fragmented into small grains. These small grains are elongated again to form the new band-shaped structures. At the high strain level, the new band-shaped structures are fragmented to generate the equiaxed grains. The evolution of microstructure can be generally divided into several steps: a) The dislocations propagate considerably; b) The original grains are elongated into the lamellar structures. In the meantime, the dislocations and LAGBs are converted into the continuous HAGBs. Thereby a great number of new grains are born and the lamellar structures are fragmented into smaller lamellar structures; c) New grains and smaller lamellar structures are elongated without a significant fragmentation. The density of the dislocations increases again; d) The numerous dislocations generated are transformed into LAGBs and HAGBs, which causes the pronounced grain refinement; d) The saturation of the grain refinement is achieved.

(2) Textures of the starting materials have a significant influence on the texture evolution during the early stage of HPT. At the saturation stage of the grain refinement, the effect of initial texture disappears. The texture evolution in Al single crystal is different to that in polycrystalline Al, indicating that the deformation behaviour is affected by its neighbouring grains and existing grain boundaries. By comparison with the one-layer polycrystalline Al, the B/B_b components cannot be found at the low shear strain level in the two-layer polycrystalline Al, denoting the different material flow behaviour between the one-layer sample and the two-layer sample. The typical simple shear textures with the strong type-B components and less strong type-A components are observed after the 1800° rotation in all polycrystalline Al. The texture evolutions at M-position and E-position can be divided into similar stages in polycrystalline Al. But the texture components at M-position and E-position are different even under the same deformation condition, suggesting that the texture evolution

is dependent on both the shear strain and the neighbouring materials.

(3) Significant grain refinements are achieved for all the HPT deformed specimens. In the one-layer and two layer polycrystalline Al, the average grain size of about 1 μm and 600 nm can be achieved at the M-positions and E-positions respectively after the 1800° rotation. The grains at both M- and E-positions are finer in the two-layer discs than those in the one-layer discs at the medium shear strain level, especially at the stage of the 720° rotation. The grain refinement is not linked well with the magnitude of the shear strain. The grain size is smaller at the E-positions than that at the M-positions, indicating the grain refinement is dependent of both the shear strain and the adjacent materials in HPT.

(4) The gradient in terms of hardness, grain size, morphology and texture along the RD are observed in all HPT processed specimens due to the inhomogeneous distribution of the shear strain. Although according to Eqn (2), the shear strain is identical along the thickness of the HPT processed specimens. However, the difference in grain size, morphology and texture along the sample thickness indicates that there is a strain gradient in the thickness direction at the low and medium strain levels. By comparison with the one-layer polycrystalline specimen, the two-layer polycrystalline specimen is capable of stabilising the material flow and decreasing the gradient along the sample thickness during HPT at the medium strain level. At the high strain level, the microstructural characteristics along the sample thickness become homogeneous.

(5) In the two-layer polycrystalline specimen, the shear-induced GB migration has been observed in the grains with the size of hundreds of nanometres after HPT with the rotation angles of 1080° and 1800°, whereas in the two-layer single crystals, the similar GB migration has been seen in extremely coarse grains with the grain size of larger than 25 μm after the 270° rotation. This indicates that the critical stress which is able to induce the GB migration is correlated with the grain size. In single crystals, the migrated GBs are the normal HAGBs, whereas the GB with the CSL structure are stationary.

7.2 Recommendation for future work

The following investigations are recommended to be conducted to continue the research from the present work.

(1) In this study, all works focused on the Al which is a typical FCC metal with high SFE. In the future, more works should be conducted on the FCC metals with low SFEs (such as Cu),

HCP metals (such as Mg) and BCC metals (such as Fe) to explore the underlying mechanism of the plastic deformation in HPT.

(2) 2D EBSD is only able to provide the orientation information of GBs with four degrees of freedom. In order to further study the shear induced GB migration, 3D EBSD should be carried out to obtain more crystallographic orientation information of GBs with all five degrees of freedom.

(3) More experiments should be conducted to study the influencing factors on the GB migration, such as the magnitude of the shear strain, the compressive pressure, the grain size and the CSL relationship.

(4) Numerical simulations should be carried out to investigate the GB migration in the UFG and coarse grained materials.

References

1. Hall, E., *The deformation and ageing of mild steel: III discussion of results.* Proceedings of the Physical Society. Section B, 1951. **64**(9): p. 747.
2. Petch, N., *The Cleavage Strengh of Polycrystals.* J. of the Iron and Steel Inst., 1953. **174**: p. 25-28.
3. Vorhauer, A. and R. Pippan, *On the homogeneity of deformation by high pressure torsion.* Scripta Materialia, 2004. **51**(9): p. 921-925.
4. Cao, Y., et al., *A visualization of shear strain in processing by high-pressure torsion.* 2010. **45**(3): p. 765-770.
5. Zhilyaev, A.P., T.R. McNelley, and T.G. Langdon, *Evolution of microstructure and microtexture in fcc metals during high-pressure torsion.* Journal of Materials Science, 2007. **42**(5): p. 1517-1528.
6. Zhilyaev, A.P., et al., *Microstructural evolution in commercial purity aluminum during high-pressure torsion.* Materials Science and Engineering: A, 2005. **410-411**: p. 277-280.
7. Horita, Z. and T.G. Langdon, *Microstructures and microhardness of an aluminum alloy and pure copper after processing by high-pressure torsion.* Materials Science and Engineering: A, 2005. **410-411**: p. 422-425.
8. Rosochowski, A. and L. Olejnik, *Finite element simulation of severe plastic deformation processes.* Proceedings of the Institution of Mechanical Engineers, Part L: Journal of Materials: Design and Applications, 2007. **221**(4): p. 187-196.
9. Tian, Y., et al., *Comparison of microstructures and mechanical properties of a Cu–Ag alloy processed using different severe plastic deformation modes.* Materials Science and Engineering: A, 2011. **528**(13-14): p. 4331-4336.
10. Sha, G., et al., *Strength, grain refinement and solute nanostructures of an Al–Mg–Si alloy (AA6060) processed by high-pressure torsion.* Acta Materialia, 2014. **63**: p. 169-179.
11. Edalati, K., T. Fujioka, and Z. Horita, *Microstructure and mechanical properties of pure Cu processed by high-pressure torsion.* Materials Science and Engineering: A, 2008. **497**(1): p. 168-173.
12. Lugo, N., et al., *Microstructures and mechanical properties of pure copper deformed severely by equal-channel angular pressing and high pressure torsion.* Materials Science and Engineering: A, 2008. **477**(1): p. 366-371.
13. Nie, M., et al., *The corrosion behaviour of commercial purity titanium processed by high-pressure torsion.* Journal of materials science, 2014. **49**(7): p. 2824-2831.
14. Balyanov, A., et al., *Corrosion resistance of ultra fine-grained Ti.* Scripta Materialia, 2004. **51**(3): p. 225-229.
15. Wang, X., et al., *Microhardness and corrosion properties of hypoeutectic Al–7Si alloy processed by high-pressure torsion.* Materials & Design, 2015. **83**: p. 193-202.
16. Zhilyaev, A.P., et al., *Experimental parameters influencing grain refinement and microstructural evolution during high-pressure torsion.* Acta Materialia, 2003. **51**(3): p. 753-765.
17. Valiev, R.Z. and T.G. Langdon, *Principles of equal-channel angular pressing as a processing tool for grain refinement.* Progress in materials science, 2006. **51**(7): p. 881-981.
18. Kim, W., et al., *Texture development and its effect on mechanical properties of an AZ61 Mg alloy fabricated by equal channel angular pressing.* Acta Materialia, 2003. **51**(11): p. 3293-3307.
19. Moon, B., H. Kim, and S. Hong, *Plastic flow and deformation homogeneity of 6061 Al during equal channel angular pressing.* Scripta materialia, 2002. **46**(2): p. 131-136.
20. Edalati, K., et al., *Significance of temperature increase in processing by high-pressure torsion.* Materials Science and Engineering: A, 2011. **528**(24): p. 7301-7305.
21. Sabbaghianrad, S., M. Kawasaki, and T.G. Langdon, *Microstructural evolution and the mechanical properties of an aluminum alloy processed by high-pressure torsion.* Journal of Materials Science, 2012. **47**(22): p. 7789-7795.
22. Yang, Z. and U. Welzel, *Microstructure–microhardness relation of nanostructured Ni produced by high-pressure torsion.* Materials Letters, 2005. **59**(27): p. 3406-3409.
23. Tóth, L., et al., *Severe plastic deformation of metals by high-pressure tube twisting.* Scripta Materialia, 2009. **60**(3): p. 175-177.
24. Arzaghi, M., et al., *Microstructure, texture and mechanical properties of aluminum processed by high-pressure tube twisting.* Acta materialia, 2012. **60**(11): p. 4393-4408.

25. Pougis, A., et al., *Stress and strain gradients in high-pressure tube twisting.* Scripta Materialia, 2012. **66**(10): p. 773-776.
26. Ghosh, A. and W. Huang, *Severe deformation based process for grain subdivision and resulting microstructures*, in *Investigations and applications of severe plastic deformation*. 2000, Springer. p. 29-36.
27. Huang, J., et al., *Development of repetitive corrugation and straightening.* Materials Science and Engineering: A, 2004. **371**(1-2): p. 35-39.
28. Rajinikanth, V., et al., *Effect of repetitive corrugation and straightening on Al and Al–0.25 Sc alloy.* Materials Letters, 2008. **62**(2): p. 301-304.
29. Pardis, N. and R. Ebrahimi, *Deformation behavior in Simple Shear Extrusion (SSE) as a new severe plastic deformation technique.* Materials Science and Engineering: A, 2009. **527**(1-2): p. 355-360.
30. Pardis, N. and R. Ebrahimi, *Different processing routes for deformation via simple shear extrusion (SSE).* Materials Science and Engineering: A, 2010. **527**(23): p. 6153-6156.
31. Tork, N.B., N. Pardis, and R. Ebrahimi, *Investigation on the feasibility of room temperature plastic deformation of pure magnesium by simple shear extrusion process.* Materials Science and Engineering: A, 2013. **560**: p. 34-39.
32. Beygelzimer, Y., et al., *Useful properties of twist extrusion.* Materials Science and Engineering: A, 2009. **503**(1-2): p. 14-17.
33. Beygelzimer, Y., et al., *Kinematics of metal flow during twist extrusion investigated with a new experimental method.* Journal of materials processing technology, 2009. **209**(7): p. 3650-3656.
34. Orlov, D., et al., *Microstructure evolution in pure Al processed with twist extrusion.* Materials Transactions, 2009. **50**(1): p. 96-100.
35. Jamaati, R. and M.R. Toroghinejad, *Manufacturing of high-strength aluminum/alumina composite by accumulative roll bonding.* Materials Science and Engineering: A, 2010. **527**(16-17): p. 4146-4151.
36. Pérez-Prado, M.T. and O. Ruano, *Grain refinement of Mg–Al–Zn alloys via accumulative roll bonding.* Scripta materialia, 2004. **51**(11): p. 1093-1097.
37. Jamaati, R., et al., *Investigation of nanostructured Al/Al2O3 composite produced by accumulative roll bonding process.* Materials & Design, 2012. **35**: p. 37-42.
38. Utsunomiya, H., et al., *Continuous grain refinement of aluminum strip by conshearing.* Materials Science and Engineering: A, 2004. **372**(1-2): p. 199-206.
39. Saito, Y., H. Utsunomiya, and H. Suzuki, *Proposal of novel continuous high straining process–development of conshearing process.* Advanced Technology of Plasticity, 1999. **3**: p. 2459-2464.
40. Aydogan, E., et al., *Effect of self-ion irradiation on the microstructural changes of alloy EK-181 in annealed and severely deformed conditions.* Journal of Nuclear Materials, 2017. **487**: p. 96-104.
41. El-Masry, M. and M. Abo-Elkhair. *ULTRAFINE-GRAINED MATERIALS PRODUCED BY SEVERE PLASTIC DEFORMATION*. in *Proceedings of the 17th Int. AMME Conference*. 2016.
42. Tsuji, N., et al., *Ultra-fine grained bulk steel produced by accumulative roll-bonding (ARB) process.* Scripta materialia, 1999. **40**(7): p. 795-800.
43. Languillaume, J., et al., *Microstructures and hardness of ultrafine-grained Ni3Al.* Acta Metallurgica Et Materialia, 1993. **41**(10): p. 2953-2962.
44. PW, B., *On torsion combined with compression.* J Appl Phys, 1943. **14**(273–283).
45. Zhilyaev, A.P. and T.G. Langdon, *Using high-pressure torsion for metal processing: Fundamentals and applications.* Progress in Materials Science, 2008. **53**(6): p. 893-979.
46. Zhilyaev, A., T. McNelley, and T. Langdon, *Evolution of microstructure and microtexture in fcc metals during high-pressure torsion.* Journal of materials science, 2007. **42**(5): p. 1517-1528.
47. Shrivastava, S.C., J.J. Jonas, and G. Canova, *Equivalent strain in large deformation torsion testing : Theoretical and practical considerations.* Journal of the Mechanics and Physics of Solids, 1982. **30**(1): p. 75-90.
48. Valiev, R.Z., et al., *Structure and deformaton behaviour of Armco iron subjected to severe plastic deformation.* Acta Materialia, 1996. **44**(12): p. 4705-4712.
49. Wetscher, F., et al., *TEM investigations of the structural evolution in a pearlitic steel deformed by high-pressure torsion.* Metallurgical and Materials Transactions A, 2006. **37**(6): p. 1963-1968.
50. Valiev, R.Z., et al., *Producing bulk ultrafine-grained materials by severe plastic deformation.* JOM, 2006. **58**(4): p. 33-39.
51. Stüwe, H.P., *Equivalent strains in severe plastic deformation.* Advanced Engineering Materials, 2003. **5**(5): p. 291-295.
52. Polakowski, N.H. and E.J. Ripling, *Strength and structure of engineering materials.* 1966.

53. Eichinger, A., *Handbuck der Werkstoffprüfung*. 1955, 2nd, Edited by: Siebel, E.
54. Degtyarev, M.V., et al., *Influence of the relaxation processes on the structure formation in pure metals and alloys under high-pressure torsion.* Acta Materialia, 2007. **55**(18): p. 6039-6050.
55. Efros, B.M., et al. *Phase transformations in ultrafine grained Fe and Fe-Mn alloys*. in *TMS Annual Meeting*. 2002.
56. Orlov, D., N. Kamikawa, and N. Tsuji, *High pressure torsion to refine grains in pure aluminum up to saturation: mechanisms of structure evolution and their dependence on strain.* Philosophical Magazine, 2012. **92**(18): p. 2329-2350.
57. Zhang, H.W., X. Huang, and N. Hansen, *Evolution of microstructural parameters and flow stresses toward limits in nickel deformed to ultra-high strains.* Acta Materialia, 2008. **56**(19): p. 5451-5465.
58. Huang, Y. and P.B. Prangnell, *The effect of cryogenic temperature and change in deformation mode on the limiting grain size in a severely deformed dilute aluminium alloy.* Acta Materialia, 2008. **56**(7): p. 1619-1632.
59. Pippan, R., et al., *Saturation of fragmentation during severe plastic deformation.* Annual Review of Materials Research, 2010. **40**: p. 319-343.
60. Cao, Y., et al., *Concurrent microstructural evolution of ferrite and austenite in a duplex stainless steel processed by high-pressure torsion.* Acta Materialia, 2014. **63**: p. 16-29.
61. Lee, H.-J., et al., *Evolution in hardness and texture of a ZK60A magnesium alloy processed by high-pressure torsion.* Materials Science and Engineering: A, 2015. **630**: p. 90-98.
62. Xu, C., Z. Horita, and T.G. Langdon, *Microstructural Evolution in Pure Aluminum in the Early Stages of Processing by High-Pressure Torsion.* MATERIALS TRANSACTIONS, 2010. **51**(1): p. 2-7.
63. Sakai, G., Z. Horita, and T.G. Langdon, *Grain refinement and superplasticity in an aluminum alloy processed by high-pressure torsion.* Materials Science and Engineering: A, 2005. **393**(1): p. 344-351.
64. Jiang, H., et al., *Microstructural evolution, microhardness and thermal stability of HPT-processed Cu.* Materials Science and Engineering A, 2000. **290**(1): p. 128-138.
65. Yang, Z. and U. Welzel, *Microstructure-microhardness relation of nanostructured Ni produced by high-pressure torsion.* Materials Letters, 2005. **59**(27): p. 3406-3409.
66. Tian, Y.Z., et al., *Microstructural evolution and mechanical properties of a two-phase Cu–Ag alloy processed by high-pressure torsion to ultrahigh strains.* Acta Materialia, 2011. **59**(7): p. 2783-2796.
67. Edalati, K. and Z. Horita, *Universal plot for hardness variation in pure metals processed by high-pressure torsion.* Materials transactions, 2010. **51**(5): p. 1051-1054.
68. An, X.H., et al., *Significance of stacking fault energy on microstructural evolution in Cu and Cu–Al alloys processed by high-pressure torsion.* Philosophical Magazine, 2011. **91**(25): p. 3307-3326.
69. Edalati, K. and Z. Horita, *Significance of homologous temperature in softening behavior and grain size of pure metals processed by high-pressure torsion.* Materials Science and Engineering A, 2011. **528**(25-26): p. 7514-7523.
70. Edalati, K., et al., *Softening of high purity aluminum and copper processed by high pressure torsion.* International Journal of Materials Research, 2009. **100**(12): p. 1668-1673.
71. Edalati, K., et al., *Allotropic phase transformation of pure zirconium by high-pressure torsion.* Materials Science and Engineering: A, 2009. **523**(1): p. 277-281.
72. Lee, S., K. Edalati, and Z. Horita, *Microstructures and Mechanical Properties of Pure V and Mo Processed by High-Pressure Torsion.* MATERIALS TRANSACTIONS, 2010. **51**(6): p. 1072-1079.
73. Xu, C., Z. Horita, and T.G. Langdon, *The evolution of homogeneity in processing by high-pressure torsion.* Acta Materialia, 2007. **55**(1): p. 203-212.
74. Ito, Y. and Z. Horita, *Microstructural evolution in pure aluminum processed by high-pressure torsion.* Materials Science and Engineering: A, 2009. **503**(1): p. 32-36.
75. Harai, Y., Y. Ito, and Z. Horita, *High-pressure torsion using ring specimens.* Scripta Materialia, 2008. **58**(6): p. 469-472.
76. Edalati, K., et al., *High-pressure torsion of pure magnesium: Evolution of mechanical properties, microstructures and hydrogen storage capacity with equivalent strain.* Scripta Materialia, 2011. **64**(9): p. 880-883.
77. Kawasaki, M., *Different models of hardness evolution in ultrafine-grained materials processed by high-pressure torsion.* Journal of Materials Science, 2014. **49**(1): p. 18-34.
78. Naghdy, S., et al., *Evolution of microstructure and texture in commercial pure aluminum subjected to high pressure torsion processing.* Materials Characterization, 2016. **120**: p. 285-294.

79. Wongsa-Ngam, J., et al., *Microstructural evolution and mechanical properties of a Cu-Zr alloy processed by high-pressure torsion.* Materials Science and Engineering A, 2011. **528**(25-26): p. 7715-7722.
80. Balogh, L., et al., *Influence of stacking-fault energy on microstructural characteristics of ultrafine-grain copper and copper-zinc alloys.* Acta Materialia, 2008. **56**(4): p. 809-820.
81. Khereddine, A.Y., et al., *An examination of microstructural evolution in a Cu–Ni–Si alloy processed by HPT and ECAP.* Materials Science and Engineering A, 2013. **576**: p. 149-155.
82. Zhang, N.X., et al., *Microstructural evolution in two-phase alloys processed by high-pressure torsion.* Journal of Materials Science, 2013. **48**(13): p. 4582-4591.
83. Cho, T.-S., et al., *Microstructural evolution and mechanical properties in a Zn–Al eutectoid alloy processed by high-pressure torsion.* Acta Materialia, 2014. **72**: p. 67-79.
84. Furukawa, M., et al., *Fabrication of submicrometer-grained Zn–22% Al by torsion straining.* Journal of Materials Research, 2011. **11**(9): p. 2128-2130.
85. Kawasaki, M., B. Ahn, and T.G. Langdon, *Significance of strain reversals in a two-phase alloy processed by high-pressure torsion.* Materials Science and Engineering: A, 2010. **527**(26): p. 7008-7016.
86. Ni, S., et al., *Strain hardening and softening in a nanocrystalline Ni–Fe alloy induced by severe plastic deformation.* 2011. **528**(9): p. 3398-3403.
87. Ni, S., et al., *Strain softening in nanocrystalline Ni–Fe alloy induced by large HPT revolutions.* 2011. **528**(13-14): p. 4807-4811.
88. Song, Y., et al., *Mechanical properties of copper after compression stage of high-pressure torsion.* Materials Science and Engineering: A, 2011. **528**(13): p. 4840-4844.
89. Gleiter, H. *Nanocrystalline Materials*. 1991. Berlin, Heidelberg: Springer Berlin Heidelberg.
90. Hu, C., et al., *Improving the intergranular corrosion resistance of 304 stainless steel by grain boundary network control.* Corrosion Science, 2011. **53**(5): p. 1880-1886.
91. Lu, L., et al., *Ultrahigh strength and high electrical conductivity in copper.* Science, 2004. **304**(5669): p. 422-426.
92. Cao, Y., et al., *Structural evolutions of metallic materials processed by severe plastic deformation.* Materials Science and Engineering: R: Reports, 2018. **133**: p. 1-59.
93. An, X.H., et al., *Enhanced strength–ductility synergy in nanostructured Cu and Cu–Al alloys processed by high-pressure torsion and subsequent annealing.* Scripta Materialia, 2012. **66**(5): p. 227-230.
94. Valiev, R., et al., *Paradox of strength and ductility in metals processed bysevere plastic deformation.* Journal of Materials Research, 2002. **17**(1): p. 5-8.
95. Balogh, L., et al., *Influence of stacking-fault energy on microstructural characteristics of ultrafine-grain copper and copper–zinc alloys.* Acta Materialia, 2008. **56**(4): p. 809-820.
96. Čížek, J., et al., *Evolution of defects in copper deformed by high-pressure torsion.* Acta Materialia, 2011. **59**(6): p. 2322-2329.
97. Zhilyaev, A., et al., *An evaluation of microstructure and microhardness in copper subjected to ultra-high strains.* Journal of Materials Science, 2008. **43**(23-24): p. 7451-7456.
98. Liao, X., et al., *Deformation twinning in nanocrystalline copper at room temperature and low strain rate.* 2004. **84**(4): p. 592-594.
99. Liao, X., et al., *Grain-size effect on the deformation mechanisms of nanostructured copper processed by high-pressure torsion.* Journal of applied physics, 2004. **96**(1): p. 636-640.
100. Islamgaliev, R., et al., *Deformation behavior of nanostructured aluminum alloy processed by severe plastic deformation.* Materials Science and Engineering: A, 2001. **319**: p. 877-881.
101. Oh-ishi, K., et al., *Fabrication and thermal stability of a nanocrystalline Ni–Al–Cr alloy: comparison with pure Cu and Ni.* Journal of materials research, 1999. **14**(11): p. 4200-4207.
102. !!! INVALID CITATION !!! {}.
103. Yamashita, A., et al., *Influence of pressing temperature on microstructural development in equal-channel angular pressing.* Materials Science and Engineering: A, 2000. **287**(1): p. 100-106.
104. Scharnweber, J., et al., *Texture, microstructure and mechanical properties of ultrafine grained aluminum produced by accumulative roll bonding.* Advanced Engineering Materials, 2010. **12**(10): p. 989-994.
105. Li, B.L., N. Tsuji, and N. Kamikawa, *Microstructure homogeneity in various metallic materials heavily deformed by accumulative roll-bonding.* Materials Science and Engineering: A, 2006. **423**(1): p. 331-342.

106. Rathmayr, G.B., A. Hohenwarter, and R. Pippan, *Influence of grain shape and orientation on the mechanical properties of high pressure torsion deformed nickel.* Materials Science and Engineering: A, 2013. **560**: p. 224-231.
107. Zhilyaev, A., et al., *Microhardness and microstructural evolution in pure nickel during high-pressure torsion.* Scripta materialia, 2001. **44**(12): p. 2753-2758.
108. Jia, D., K.T. Ramesh, and E. Ma, *Effects of nanocrystalline and ultrafine grain sizes on constitutive behavior and shear bands in iron.* Acta Materialia, 2003. **51**(12): p. 3495-3509.
109. Estrin, Y. and A. Vinogradov, *Extreme grain refinement by severe plastic deformation: A wealth of challenging science.* Acta Materialia, 2013. **61**(3): p. 782-817.
110. Mishra, A., et al., *Microstructural evolution in copper processed by severe plastic deformation.* Materials Science and Engineering: A, 2005. **410-411**: p. 290-298.
111. An, X.H., et al., *The influence of stacking fault energy on the mechanical properties of nanostructured Cu and Cu–Al alloys processed by high-pressure torsion.* Scripta Materialia, 2011. **64**(10): p. 954-957.
112. Hong, C.S., et al., *Nucleation and thickening of shear bands in nano-scale twin/matrix lamellae of a Cu–Al alloy processed by dynamic plastic deformation.* Acta Materialia, 2010. **58**(8): p. 3103-3116.
113. Wang, Y.B., et al., *The role of stacking faults and twin boundaries in grain refinement of a Cu–Zn alloy processed by high-pressure torsion.* Materials Science and Engineering: A, 2010. **527**(18): p. 4959-4966.
114. An, X., et al., *Influence of stacking-fault energy on the accommodation of severe shear strain in Cu-Al alloys during equal-channel angular pressing.* Journal of Materials Research, 2009. **24**(12): p. 3636-3646.
115. Baik, S.C., et al., *Dislocation density-based modeling of deformation behavior of aluminium under equal channel angular pressing.* Materials Science and Engineering: A, 2003. **351**(1): p. 86-97.
116. Belyakov, A., et al., *Grain refinement in copper under large strain deformation.* Philosophical Magazine A, 2001. **81**(11): p. 2629-2643.
117. Gourdet, S. and F. Montheillet, *An experimental study of the recrystallization mechanism during hot deformation of aluminium.* Materials Science and Engineering: A, 2000. **283**(1): p. 274-288.
118. Kaibyshev, R., et al., *Continuous dynamic recrystallization in an Al–Li–Mg–Sc alloy during equal-channel angular extrusion.* Materials Science and Engineering: A, 2005. **396**(1-2): p. 341-351.
119. Association, A., *Aluminum: properties and physical metallurgy*. 1984: ASM International.
120. Lee, S., et al., *Microstructures and mechanical properties of 6061 aluminum alloy processed by accumulative roll-bonding.* Materials Science and Engineering: A, 2002. **325**(1): p. 228-235.
121. Troeger, L. and E. Starke, *Microstructural and mechanical characterization of a superplastic 6xxx aluminum alloy.* Materials Science and Engineering: A, 2000. **277**(1): p. 102-113.
122. !!! INVALID CITATION !!!
123. Miyamoto, H., et al., *Microstructure and texture development of copper single crystals deformed by equal-channel angular pressing.* Philosophical magazine letters, 2004. **84**(4): p. 235-243.
124. Skrotzki, W., et al., *Texture after ECAP of a cube-oriented Ni single crystal.* Acta Materialia, 2008. **56**(14): p. 3439-3449.
125. Goran, D., et al., *Local texture and microstructure in cube-oriented nickel single crystal deformed by equal channel angular extrusion.* Philosophical Magazine, 2011. **91**(2): p. 281-299.
126. Alexandrov, I., M. Zhilina, and J. Bonarski, *Formation of texture inhomogeneity in severely plastically deformed copper.* Technical Sciences, 2006. **54**(2).
127. Hafok, M., et al. *HPT-deformation of copper and nickel single crystals*. in *Materials Science Forum*. 2006. Trans Tech Publ.
128. Hafok, M. and R. Pippan. *Comparison of single crystalline and polycrystalline behavior under high pressure torsion*. in *Materials science forum*. 2007. Trans Tech Publ.
129. Hafok, M. and R. Pippan, *High-pressure torsion applied to nickel single crystals.* Philosophical Magazine, 2008. **88**(12): p. 1857-1877.
130. Randle, V. and O. Engler, *Introduction to texture analysis: macrotexture, microtexture and orientation mapping*. 2000: CRC press.
131. Dorner, D., S. Zaefferer, and D. Raabe, *Retention of the Goss orientation between microbands during cold rolling of an Fe3%Si single crystal.* Acta Materialia, 2007. **55**(7): p. 2519-2530.
132. Engler, O. and J. Hirsch, *Polycrystal-plasticity simulation of six and eight ears in deep-drawn aluminum cups.* Materials Science and Engineering: A, 2007. **452-453**: p. 640-651.
133. Koblischka-Veneva, A., et al., *Microtexture of magnetite thin films of (001) and (111) orientations on MgO substrates studied by electron-backscatter diffraction.* Journal of Applied Physics, 2008. **103**(7): p. 07E505.

134. Obst, B., et al., *Application of electron backscatter diffraction in the SEM to textural problems of coated high-temperature superconductors: Dedicated to Professor Dr. Otmar Vöhringer on the occasion of his 65th birthday.* Zeitschrift für Metallkunde, 2003. **94**(5): p. 580-586.
135. Descartes, S., C. Desrayaud, and E. Rauch, *Inhomogeneous microstructural evolution of pure iron during high-pressure torsion.* Materials Science and Engineering: A, 2011. **528**(10-11): p. 3666-3675.
136. Hansen, J., J. Pospiech, and K. Lücke, *Tables for texture analysis of cubic crystals*. 1978: Springer.
137. INSTRUMENTS, O., *EBSD Explained: From data acquisition to advanced analysis*. 2015.
138. Rollett, A. *Texture, Microstructure and Anisotropy*. 2016; Available from: http://slideplayer.com/slide/9388142/.
139. Tóth, L., et al., *Texture development and length changes in copper bars subjected to free end torsion.* Texture, Stress, and Microstructure, 1992. **19**(4): p. 245-262.
140. Bunge, H.-J., *Zur darstellung allgemeiner texturen.* Zeitschrift fur metallkunde, 1965. **56**(12): p. 872-&.
141. Kawasaki, M., et al., *Using high-pressure torsion to process an aluminum–magnesium nanocomposite through diffusion bonding.* Journal of Materials Research, 2016. **31**(1): p. 88-99.
142. Canova, G.R., U.F. Kocks, and J.J. Jonas, *Theory of torsion texture development.* Acta Metallurgica, 1984. **32**(2): p. 211-226.
143. Montheillet, F., M. Cohen, and J.J. Jonas, *Axial stresses and texture development during the torsion testing of Al, Cu and α-Fe.* Acta Metallurgica, 1984. **32**(11): p. 2077-2089.
144. Toth, L.S., P. Gilormini, and J.J. Jonas, *Effect of rate sensitivity on the stability of torsion textures.* Acta Metallurgica, 1988. **36**(12): p. 3077-3091.
145. Toth, L., P. Gilormini, and J. Jonas, *Effect of rate sensitivity on the stability of torsion textures.* Acta Metallurgica, 1988. **36**(12): p. 3077-3091.
146. Enikeev, N.A., et al. *Observations of texture in large scale HPT-processed Cu*. in *Materials Science Forum*. 2008. Trans Tech Publ.
147. Tóth, L.S., K.W. Neale, and J.J. Jonas, *Stress response and persistence characteristics of the ideal orientations of shear textures.* Acta Metallurgica, 1989. **37**(8): p. 2197-2210.
148. Ghosh, P., O. Renk, and R. Pippan, *Microtexture analysis of restoration mechanisms during high pressure torsion of pure nickel.* Materials Science and Engineering: A, 2017. **684**: p. 101-109.
149. Neale, K.W., L.S. Tóth, and J.J. Jonas, *Large strain shear and torsion of rate-sensitive FCC polycrystals.* International Journal of Plasticity, 1990. **6**(1): p. 45-61.
150. Korznikova, E.A., et al., *Microstructural evolution and electro-resistivity in HPT nickel.* Materials Science and Engineering: A, 2012. **556**: p. 437-445.
151. Wang, S.C., et al., *Texture evolution by shear on two planes during ECAP of a high-strength aluminum alloy.* Acta Materialia, 2008. **56**(15): p. 3800-3809.
152. Jahedi, M., et al., *Texture evolution and enhanced grain refinement under high-pressure-double-torsion.* Materials Science and Engineering: A, 2014. **611**: p. 29-36.
153. Al-Fadhalah, K.J., et al., *Microstructure and microtexture in pure copper processed by high-pressure torsion.* Journal of Materials Science, 2013. **48**(13): p. 4563-4572.
154. Orlov, D., et al., *Texture evolution in pure aluminum subjected to monotonous and reversal straining in high-pressure torsion.* Scripta materialia, 2009. **60**(10): p. 893-896.
155. Chulist, R., et al., *Microstructure and texture in Ni50Mn29Ga21 deformed by high-pressure torsion.* Scripta Materialia, 2010. **62**(9): p. 650-653.
156. Dopita, M., et al., *Microstructure evolution of CuZr polycrystals processed by high-pressure torsion.* Journal of materials science, 2010. **45**(17): p. 4631-4644.
157. Huang, Y., et al., *Microstructure and texture evolution in a magnesium alloy during processing by high-pressure torsion.* Materials Research, 2013. **16**(3): p. 577-585.
158. Islamgaliev, R., et al., *Structure and Crystallographic Texture in the Cu-Cr-Ag Alloy Subjected to Severe Plastic Deformation.* Rev. Adv. Mater. Sci, 2014. **39**: p. 14-34.
159. Zhang, H., et al., *Thermal behavior of Ni (99.967% and 99.5% purity) deformed to an ultra-high strain by high pressure torsion.* Acta Materialia, 2010. **58**(5): p. 1698-1707.
160. Tränkner, C., et al. *Influence of deformation temperature on texture evolution in HPT deformed NiAl*. in *IOP Conference Series: Materials Science and Engineering*. 2014. IOP Publishing.
161. Kilmametov, A., et al., *The $\alpha \rightarrow \omega$ and $\beta \rightarrow \omega$ phase transformations in Ti–Fe alloys under high-pressure torsion*. Vol. 144. 2017.
162. Tränkner, C., et al. *Influence of hydrostatic pressure on texture evolution in HPT deformed NiAl*. in *IOP Conference Series: Materials Science and Engineering*. 2015. IOP Publishing.

163. Bonarski, B., et al., *Texture evolution of Mg during high-pressure torsion.* Journal of Materials Science, 2008. **43**(23-24): p. 7513.
164. Skrotzki, W., et al., *Torsion texture measurements with high-energy synchrotron radiation on NiAl.* Texture, Stress, and Microstructure, 2003. **35**(3-4): p. 163-173.
165. Ivanisenko, Y., et al., *Information on deformation mechanisms in nanocrystalline Pd–10% Au inferred from texture analysis.* Journal of materials science, 2010. **45**(17): p. 4571-4577.
166. Cao, G., et al., *High strain torsion of a TiAl-based alloy.* Materials Science and Engineering: A, 2008. **483**: p. 512-516.
167. Taylor, G.I., *Plastic strain in metals.* J. Inst. Metals, 1938. **62**: p. 307-324.
168. Kocks, U., *The relation between polycrystal deformation and single-crystal deformation.* Metallurgical and Materials Transactions B, 1970. **1**(5): p. 1121-1143.
169. Baczynski, J. and J. Jonas, *Texture development during the torsion testing of α-iron and two IF steels.* Acta Materialia, 1996. **44**(11): p. 4273-4288.
170. Klein, H., C. Esling, and H. Bunge, *Model Calculation of Cross Rolling Textures.* Texture, Stress, and Microstructure, 1991. **14**: p. 1079-1090.
171. Aifantis, E.C., *The physics of plastic deformation.* International Journal of Plasticity, 1987. **3**(3): p. 211-247.
172. Lowe, T., et al., *Analysis of the evolution of texture and axial stresses in FCC polycrystals subject to large strain shear.* Yielding, Damage, and Failure of Anisotropic Solids, 1987: p. 335-358.
173. Pippan, R., et al. *Advantages and limitations of HPT: a review*. in *Materials Science Forum*. 2008. Trans Tech Publ.
174. Lu, C., K. Tieu, and D. Wexler, *Significant enhancement of bond strength in the accumulative roll bonding process using nano-sized SiO2 particles.* Journal of Materials Processing Technology, 2009. **209**(10): p. 4830-4834.
175. Barnett, M. and F. Montheillet, *The generation of new high-angle boundaries in aluminium during hot torsion.* Acta materialia, 2002. **50**(9): p. 2285-2296.
176. Wei, P., et al., *A study on the texture evolution mechanism of nickel single crystal deformed by high pressure torsion.* Materials Science and Engineering: A, 2017. **684**: p. 239-248.
177. Toth, L., et al., *Length changes during free end torsion: a rate sensitive analysis.* International journal of plasticity, 1990. **6**(1): p. 83-108.
178. Beausir, B., L.S. Tóth, and K.W. Neale, *Ideal orientations and persistence characteristics of hexagonal close packed crystals in simple shear.* Acta Materialia, 2007. **55**(8): p. 2695-2705.
179. Meyers, M.A., A. Mishra, and D.J. Benson, *Mechanical properties of nanocrystalline materials.* Progress in Materials Science, 2006. **51**(4): p. 427-556.
180. Detor, A.J. and C.A. Schuh, *Tailoring and patterning the grain size of nanocrystalline alloys.* Acta Materialia, 2007. **55**(1): p. 371-379.
181. Shan, Z., et al., *Grain boundary-mediated plasticity in nanocrystalline nickel.* Science, 2004. **305**(5684): p. 654-657.
182. Chen, M., et al., *Deformation twinning in nanocrystalline aluminum.* Science, 2003. **300**(5623): p. 1275-1277.
183. Van Swygenhoven, H., *Grain boundaries and dislocations.* Science, 2002. **296**(5565): p. 66-67.
184. Schiøtz, J. and K.W. Jacobsen, *A maximum in the strength of nanocrystalline copper.* Science, 2003. **301**(5638): p. 1357-1359.
185. Yamakov, V., et al., *Deformation-mechanism map for nanocrystalline metals by molecular-dynamics simulation.* Nature materials, 2004. **3**(1): p. 43-47.
186. Schuh, C.A., T.G. Nieh, and T. Yamasaki, *Hall–Petch breakdown manifested in abrasive wear resistance of nanocrystalline nickel.* Scripta Materialia, 2002. **46**(10): p. 735-740.
187. Hu, J., et al., *Grain boundary stability governs hardening and softening in extremely fine nanograined metals.* Science, 2017. **355**(6331): p. 1292-1296.
188. Chen, B., et al., *Texture of nanocrystalline nickel: Probing the lower size limit of dislocation activity.* Science, 2012. **338**(6113): p. 1448-1451.
189. Chokshi, A.H., et al., *On the validity of the hall-petch relationship in nanocrystalline materials.* Scripta Metallurgica, 1989. **23**(10): p. 1679-1683.
190. Sanders, P.G., J.A. Eastman, and J.R. Weertman, *Elastic and tensile behavior of nanocrystalline copper and palladium.* Acta Materialia, 1997. **45**(10): p. 4019-4025.
191. Zhang, L., C. Lu, and K. Tieu, *A review on atomistic simulation of grain boundary behaviors in face-centered cubic metals.* Computational Materials Science, 2016. **118**: p. 180-191.

192. Legros, M., D.S. Gianola, and K.J. Hemker, *In situ TEM observations of fast grain-boundary motion in stressed nanocrystalline aluminum films.* Acta Materialia, 2008. **56**(14): p. 3380-3393.
193. Liao, X., et al., *Deformation mechanism in nanocrystalline Al: Partial dislocation slip.* Applied Physics Letters, 2003. **83**(4): p. 632-634.
194. Hughes, D. and N. Hansen, *Exploring the limit of dislocation based plasticity in nanostructured metals.* Physical review letters, 2014. **112**(13): p. 135504.
195. Schiotz, J., F.D. Di Tolla, and K.W. Jacobsen, *Softening of nanocrystalline metals at very small grain sizes.* Nature, 1998. **391**(6667): p. 561.
196. Yamakov, V., et al., *Dislocation processes in the deformation of nanocrystalline aluminium by molecular-dynamics simulation.* Nature materials, 2002. **1**(1): p. 45.
197. Knapp, J. and D. Follstaedt, *Hall–Petch relationship in pulsed-laser deposited nickel films.* Journal of materials research, 2004. **19**(1): p. 218-227.
198. Chen, J., L. Lu, and K. Lu, *Hardness and strain rate sensitivity of nanocrystalline Cu.* Scripta Materialia, 2006. **54**(11): p. 1913-1918.
199. Sergueeva, A., et al., *Cooperative grain boundary sliding in nanocrystalline materials.* Philosophical Magazine, 2006. **86**(36): p. 5797-5804.
200. Gutkin, M.Y., I. Ovid'ko, and N. Skiba, *Crossover from grain boundary sliding to rotational deformation in nanocrystalline materials.* Acta Materialia, 2003. **51**(14): p. 4059-4071.
201. Haslam, A.J., et al., *Mechanisms of grain growth in nanocrystalline fcc metals by molecular-dynamics simulation.* Materials Science and Engineering: A, 2001. **318**(1): p. 293-312.
202. Moldovan, D., et al., *Scaling behavior of grain-rotation-induced grain growth.* Physical review letters, 2002. **89**(20): p. 206101.
203. Jin, M., et al., *Direct observation of deformation-induced grain growth during the nanoindentation of ultrafine-grained Al at room temperature.* Acta Materialia, 2004. **52**(18): p. 5381-5387.
204. Wang, Y., et al., *Deformation-induced grain rotation and growth in nanocrystalline Ni.* Applied Physics Letters, 2008. **92**(1): p. 011903.
205. Wang, Y., et al., *Mechanism of grain growth during severe plastic deformation of a nanocrystalline Ni–Fe alloy.* Applied Physics Letters, 2009. **94**(1): p. 011908.
206. Yamasaki, T., Y. Demizu, and Y. Ogino. *Grain Rotation during Grain Growth of Polycrystalline Aluminium*. in *Materials Science Forum*. 1996. Trans Tech Publ.
207. Cahn, J.W., Y. Mishin, and A. Suzuki, *Coupling grain boundary motion to shear deformation.* Acta materialia, 2006. **54**(19): p. 4953-4975.
208. Cahn, J.W. and J.E. Taylor, *A unified approach to motion of grain boundaries, relative tangential translation along grain boundaries, and grain rotation.* Acta Materialia, 2004. **52**(16): p. 4887-4898.
209. Gorkaya, T., D.A. Molodov, and G. Gottstein, *Stress-driven migration of symmetrical< 100> tilt grain boundaries in Al bicrystals.* Acta Materialia, 2009. **57**(18): p. 5396-5405.
210. Homer, E.R., et al., *Phenomenology of shear-coupled grain boundary motion in symmetric tilt and general grain boundaries.* Acta Materialia, 2013. **61**(4): p. 1048-1060.
211. Molodov, D., V. Ivanov, and G. Gottstein, *Low angle tilt boundary migration coupled to shear deformation.* Acta Materialia, 2007. **55**(5): p. 1843-1848.
212. Sheikh-Ali, A., *Coupling of grain boundary sliding and migration within the range of boundary specialness.* Acta Materialia, 2010. **58**(19): p. 6249-6255.
213. Zhang, L., et al., *Molecular dynamics study on the atomic mechanisms of coupling motion of [0 0 1] symmetric tilt grain boundaries in copper bicrystal.* Materials Research Express, 2014. **1**(1): p. 015019.
214. Winning, M., G. Gottstein, and L.S. Shvindlerman, *Migration of grain boundaries under the influence of an external shear stress.* Materials Science and Engineering: A, 2001. **317**(1): p. 17-20.
215. Winning, M., G. Gottstein, and L.S. Shvindlerman, *On the mechanisms of grain boundary migration.* Acta Materialia, 2002. **50**(2): p. 353-363.
216. Winning, M., *Motion of 〈1 0 0〉-tilt grain boundaries.* Acta Materialia, 2003. **51**(20): p. 6465-6475.
217. Balluffi, R. and J. Cahn, *Mechanism for diffusion induced grain boundary migration.* Acta Metallurgica, 1981. **29**(3): p. 493-500.
218. Hillert, M., *On the driving force for diffusion induced grain boundary migration.* Scripta metallurgica, 1983. **17**(2): p. 237-240.
219. Atkinson, H.V., *Overview no. 65.* Acta Metallurgica, 1988. **36**(3): p. 469-491.
220. Bréchet, Y.J.M. and G.R. Purdy, *On the possibility of DIGM-assisted abnormal grain growth.* Scripta Materialia, 2006. **54**(12): p. 2009-2011.

221. Balluffi, R.W. and J.W. Cahn, *Mechanism for diffusion induced grain boundary migration.* Acta Metallurgica, 1981. **29**(3): p. 493-500.
222. Gottstein, G. and L. Shvindlerman, *Grain boundary migration in metals. CRC Series in Materials Science and Technology*. 1999, Boca Raton, FL: CRC Press.
223. Mompiou, F., D. Caillard, and M. Legros, *Grain boundary shear–migration coupling—I. In situ TEM straining experiments in Al polycrystals.* Acta Materialia, 2009. **57**(7): p. 2198-2209.
224. Zhang, K., J. Weertman, and J. Eastman, *Rapid stress-driven grain coarsening in nanocrystalline Cu at ambient and cryogenic temperatures.* Applied Physics Letters, 2005. **87**(6): p. 061921.
225. Wen, H., et al., *High-pressure torsion-induced grain growth and detwinning in cryomilled Cu powders.* Philosophical Magazine, 2010. **90**(34): p. 4541-4550.
226. Zhilyaev, A., et al., *Particle and grain growth in an Al–Si alloy during high-pressure torsion.* Scripta materialia, 2007. **57**(8): p. 763-765.
227. Liao, X., et al., *High-pressure torsion-induced grain growth in electrodeposited nanocrystalline Ni.* Applied Physics Letters, 2006. **88**(2): p. 021909.
228. Rupert, T., et al., *Experimental observations of stress-driven grain boundary migration.* Science, 2009. **326**(5960): p. 1686-1690.
229. Wan, L., W. Han, and K. Chen, *Bi-crystallographic lattice structure directs grain boundary motion under shear stress.* Scientific reports, 2015. **5**.
230. Zhang, H., et al., *Atomic motion during the migration of general [001] tilt grain boundaries in Ni.* Acta materialia, 2007. **55**(13): p. 4527-4533.
231. Haslam, A., et al., *Stress-enhanced grain growth in a nanocrystalline material by molecular-dynamics simulation.* Acta Materialia, 2003. **51**(7): p. 2097-2112.
232. Winning, M. and A.D. Rollett, *Transition between low and high angle grain boundaries.* Acta materialia, 2005. **53**(10): p. 2901-2907.
233. Gianola, D., et al., *Increased strain rate sensitivity due to stress-coupled grain growth in nanocrystalline Al.* Scripta Materialia, 2006. **55**(7): p. 649-652.
234. Caillard, D., F. Mompiou, and M. Legros, *Grain-boundary shear-migration coupling. II. Geometrical model for general boundaries.* Acta Materialia, 2009. **57**(8): p. 2390-2402.
235. Fan, G., et al., *Orientation-dependent grain growth in a bulk nanocrystalline alloy during the uniaxial compressive deformation.* Applied Physics Letters, 2006. **88**(17): p. 171914.
236. Fan, G., et al., *Grain growth in a bulk nanocrystalline Co alloy during tensile plastic deformation.* Scripta Materialia, 2006. **54**(12): p. 2137-2141.
237. Gianola, D., et al., *Stress-assisted discontinuous grain growth and its effect on the deformation behavior of nanocrystalline aluminum thin films.* Acta Materialia, 2006. **54**(8): p. 2253-2263.
238. Ni, S., et al., *Grain growth and dislocation density evolution in a nanocrystalline Ni–Fe alloy induced by high-pressure torsion.* Scripta Materialia, 2011. **64**(4): p. 327-330.
239. Korznikova, E., et al., *Microstructural evolution and electro-resistivity in HPT nickel.* Materials Science and Engineering: A, 2012. **556**: p. 437-445.
240. Kocks, U.F., C.N. Tomé, and H.-R. Wenk, *Texture and anisotropy: preferred orientations in polycrystals and their effect on materials properties*. 2000: Cambridge university press.
241. Bravais, A., *On the systems formed by points regularly distributed on a plane or in space*. 1949: Crystallographic Society of America.
242. Van Houtte, P., *In Preferred Orientations in Deformed Metals and Rocks. An Introduction of Modern Texture Analysis, Vol. ed.: H.-R. Wenk*. 1985, Academic Press, New York.
243. Kleber, W., et al., *Einführung in die Kristallographie*. 2010: Oldenbourg Verlag.
244. Kim, H.S., et al., *Deformation behavior of copper during a high pressure torsion process.* Journal of Materials Processing Technology, 2003. **142**(2): p. 334-337.
245. Shrivastava, S., J. Jonas, and G. Canova, *Equivalent strain in large deformation torsion testing: theoretical and practical considerations.* Journal of the Mechanics and Physics of Solids, 1982. **30**(1-2): p. 75-90.
246. Lukyanova, E.A., et al., *Strengthening of age-hardenable WE43 magnesium alloy processed by high pressure torsion.* Materials Letters, 2016. **170**: p. 5-9.
247. Edalati, K., et al., *Effect of temperature rise on microstructural evolution during high-pressure torsion.* Materials Science and Engineering: A, 2018. **714**: p. 167-171.
248. Yu, P.F., et al., *Effects of high pressure torsion on microstructures and properties of an Al0.1CoCrFeNi high-entropy alloy.* Materials Science and Engineering: A, 2016. **655**: p. 283-291.

249. Figueiredo, R.B., et al., *Using finite element modeling to examine the temperature distribution in quasi-constrained high-pressure torsion.* Acta Materialia, 2012. **60**(6-7): p. 3190-3198.
250. Kamrani, M., V.I. Levitas, and B. Feng, *FEM simulation of large deformation of copper in the quasi-constrain high-pressure-torsion setup.* Materials Science and Engineering: A, 2017. **705**: p. 219-230.
251. Kawasaki, M., et al., *The development of hardness homogeneity in pure aluminum and aluminum alloy disks processed by high-pressure torsion.* Materials Science and Engineering: A, 2011. **529**: p. 345-351.
252. Bazarnik, P., et al., *Enhanced grain refinement and microhardness by hybrid processing using hydrostatic extrusion and high-pressure torsion.* Materials Science and Engineering: A, 2018. **712**: p. 513-520.
253. Chen, Y., et al., *Stored energy and microstructures in nanostructured Al-Cu-Mg alloy processed by high-pressure torsion.* 2016.
254. Alhajeri, S.N., et al., *Microstructure and microhardness of an Al-6061 metal matrix composite processed by high-pressure torsion.* Materials Characterization, 2016. **118**: p. 270-278.
255. Straumal, B., et al., *Competition between precipitation and dissolution in Cu–Ag alloys under high pressure torsion.* Acta Materialia, 2017. **122**: p. 60-71.
256. Straumal, B., et al., *Phase transitions in Cu-based alloys under high pressure torsion.* Journal of Alloys and Compounds, 2017. **707**: p. 20-26.
257. Bachmaier, A., et al., *Tailoring the magnetic properties of nanocrystalline Cu-Co alloys prepared by high-pressure torsion and isothermal annealing.* Journal of Alloys and Compounds, 2017. **725**: p. 744-749.
258. Kapoor, G., et al., *Effect of Mo addition on the microstructure and hardness of ultrafine-grained Ni alloys processed by a combination of cryorolling and high-pressure torsion.* Materials Science and Engineering: A, 2017. **688**: p. 92-100.
259. Kapoor, G., et al., *Influence of Mo alloying on the thermal stability and hardness of ultrafine-grained Ni processed by high-pressure torsion.* Journal of Materials Research and Technology, 2017. **6**(4): p. 361-368.
260. Kapp, M.W., et al., *Cyclically induced grain growth within shear bands investigated in UFG Ni by cyclic high pressure torsion.* Journal of Materials Research, 2017. **32**(23): p. 4317-4326.
261. Haraguchi, R., et al., *Electrical resistivity mapping of titanium and zirconium discs processed by high-pressure torsion for homogeneity and phase transformation evaluation.* Journal of Materials Science, 2017. **52**(11): p. 6778-6788.
262. Yang, C., et al., *Evidence for a transition in deformation mechanism in nanocrystalline pure titanium processed by high-pressure torsion.* Philosophical Magazine, 2016. **96**(16): p. 1632-1642.
263. Alizadeh, R., et al., *Superplasticity of a nano-grained Mg–Gd–Y–Zr alloy processed by high-pressure torsion.* Materials Science and Engineering: A, 2016. **651**: p. 786-794.
264. Gajdics, M., et al., *Characterization of a nanocrystalline Mg–Ni alloy processed by high-pressure torsion during hydrogenation and dehydrogenation.* International Journal of Hydrogen Energy, 2016. **41**(23): p. 9803-9809.
265. Tang, L., et al., *Localized deformation via multiple twinning in a Mg–Gd–Y–Zr alloy processed by high-pressure torsion.* Materials Science and Engineering: A, 2016. **677**: p. 68-75.
266. Gubicza, J., et al., *Microstructure, phase composition and hardness evolution in 316L stainless steel processed by high-pressure torsion.* Materials Science and Engineering: A, 2016. **657**: p. 215-223.
267. Marulanda Cardona, D.M., et al., *Effects on hardness and microstructure of AISI 1020 low-carbon steel processed by high-pressure torsion.* Journal of Materials Research and Technology, 2017. **6**(4): p. 355-360.
268. Edalati, K. and Z. Horita, *Significance of homologous temperature in softening behavior and grain size of pure metals processed by high-pressure torsion.* Materials Science and Engineering: A, 2011. **528**(25): p. 7514-7523.
269. Harai, Y., et al., *Microstructural and mechanical characteristics of AZ61 magnesium alloy processed by high-pressure torsion.* Materials transactions, 2008. **49**(1): p. 76-83.
270. Perez-Prado, M., et al., *Bulk nanocrystalline ω-Zr by high-pressure torsion.* Scripta Materialia, 2008. **58**(3): p. 219-222.
271. Chinh, N.Q., et al., *Influence of Zn content on the microstructure and mechanical performance of ultrafine-grained Al–Zn alloys processed by high-pressure torsion.* Materials Letters, 2017. **186**: p. 334-337.
272. Fukushima, Y., et al., *High-resolution transmission electron microscopy analysis of bulk nanograined silicon processed by high-pressure torsion.* Materials Characterization, 2017. **129**: p. 163-168.

273. Shahmir, H., et al., *Evidence for superplasticity in a CoCrFeNiMn high-entropy alloy processed by high-pressure torsion.* Materials Science and Engineering: A, 2017. **685**: p. 342-348.
274. Lee, H.-J., et al., *Significance of grain refinement on microstructure and mechanical properties of an Al-3% Mg alloy processed by high-pressure torsion.* Journal of Alloys and Compounds, 2016. **686**: p. 998-1007.
275. Yoon, E.Y., et al., *Grain refinement and tensile strength of carbon nanotube-reinforced Cu matrix nanocomposites processed by high-pressure torsion.* Metals and Materials International, 2013. **19**(5): p. 927-932.
276. Matsunoshita, H., et al., *Ultrafine-grained magnesium–lithium alloy processed by high-pressure torsion: Low-temperature superplasticity and potential for hydroforming.* Materials Science and Engineering: A, 2015. **640**: p. 443-448.
277. Tugcu, K., et al., *Enhanced grain refinement of an Al–Mg–Si alloy by high-pressure torsion processing at 100 C.* Materials Science and Engineering: A, 2012. **552**: p. 415-418.
278. Cubero-Sesin, J.M. and Z. Horita, *Powder consolidation of Al–10 wt% Fe alloy by high-pressure torsion.* Materials Science and Engineering: A, 2012. **558**: p. 462-471.
279. Ashida, M., et al., *Production of Al/Al2O3 nanocomposites through consolidation by high-pressure torsion.* Materials Transactions, 2012. **53**(1): p. 13-16.
280. Mungole, T., et al., *Evolution of microhardness and microstructure in a cast Al–7% Si alloy during high-pressure torsion.* Journal of Materials Science, 2013. **48**(13): p. 4671-4680.
281. Kocich, R., et al., *Texture, deformation twinning and hardening in a newly developed Mg–Dy–Al–Zn–Zr alloy processed with high pressure torsion.* Materials & Design, 2016. **90**: p. 1092-1099.
282. Chadha, K., P.P. Bhattacharjee, and M. Jahazi, *The effect of strain reversal during high pressure torsion on the microstructure evolution and texture of aluminum alloys*, in *Characterization of Minerals, Metals, and Materials 2015*. 2015, Springer. p. 107-114.
283. Loucif, A., et al., *Ultrafine grains and the Hall–Petch relationship in an Al–Mg–Si alloy processed by high-pressure torsion.* Materials Science and Engineering: A, 2012. **532**: p. 139-145.
284. Alhamidi, A. and Z. Horita, *Grain refinement and high strain rate superplasticity in alumunium 2024 alloy processed by high-pressure torsion.* Materials Science and Engineering: A, 2015. **622**: p. 139-145.
285. Liu, Q. and N. Hansen, *Geometrically necessary boundaries and incidental dislocation boundaries formed during cold deformation.* Scripta metallurgica et materialia, 1995. **32**(8).
286. Hughes, D.A. and N. Hansen, *Microstructure and strength of nickel at large strains.* Acta Materialia, 2000. **48**(11): p. 2985-3004.
287. Orlov, D., et al., *Role of strain reversal in grain refinement by severe plastic deformation.* Materials Science and Engineering: A, 2009. **499**(1): p. 427-433.
288. Molinari, A. and L.S. Tóth, *Tuning a self consistent viscoplastic model by finite element results—I. Modeling.* Acta Metallurgica et Materialia, 1994. **42**(7): p. 2453-2458.
289. Montheillet, F., P. Gilormini, and J. Jonas, *Relation between axial stresses and texture development during torsion testing: a simplified theory.* Acta Metallurgica, 1985. **33**(4): p. 705-717.
290. Cho, J.-Y., et al., *The Influence of AH-26 and zinc oxide-eugenol root canal sealer on the shear bond strength of composite resin to dentin.* Journal of Korean Academy of Conservative Dentistry, 2006. **31**(3): p. 147-152.
291. Humphreys, F.J. and M. Hatherly, *Recrystallization and related annealing phenomena*. 2012: Elsevier.
292. Hughes, D.A., et al. *Stacking fault energy and microstructure effects on torsion texture evolution*. in *Proceedings of the Royal Society of London A: Mathematical, Physical and Engineering Sciences*. 2000. The Royal Society.
293. Minor, A., et al., *Direct observations of incipient plasticity during nanoindentation of Al.* Journal of Materials research, 2004. **19**(1): p. 176-182.
294. Liu, Q., D. Juul Jensen, and N. Hansen, *Effect of grain orientation on deformation structure in cold-rolled polycrystalline aluminium.* Acta Materialia, 1998. **46**(16): p. 5819-5838.
295. Dalla Torre, F., et al., *Microstructures and properties of copper processed by equal channel angular extrusion for 1–16 passes.* Acta Materialia, 2004. **52**(16): p. 4819-4832.
296. Yamakov, V., et al., *Length-scale effects in the nucleation of extended dislocations in nanocrystalline Al by molecular-dynamics simulation.* Acta Materialia, 2001. **49**(14): p. 2713-2722.
297. Legros, M., et al., *Microsample tensile testing of nanocrystalline metals.* Philosophical Magazine A, 2000. **80**(4): p. 1017-1026.
298. Budrovic, Z., et al., *Plastic deformation with reversible peak broadening in nanocrystalline nickel.* Science, 2004. **304**(5668): p. 273-276.

299. Li, L., et al., *Simultaneous reductions of dislocation and twin densities with grain growth during cold rolling in a nanocrystalline Ni–Fe alloy.* Scripta Materialia, 2009. **60**(5): p. 317-320.
300. Wang, Y., et al., *Dislocation density evolution during high pressure torsion of a nanocrystalline Ni–Fe alloy.* Applied Physics Letters, 2009. **94**(9): p. 091911.
301. Wright, S.I., et al., *Electron imaging with an EBSD detector.* Ultramicroscopy, 2015. **148**: p. 132-145.
302. Prior, D.J., et al., *Orientation contrast imaging of microstructures in rocks using forescatter detectors in the scanning electron microscope*. 1996, De Gruyter.
303. Day, A. and T. Quested, *A comparison of grain imaging and measurement using horizontal orientation and colour orientation contrast imaging, electron backscatter pattern and optical methods.* Journal of Microscopy, 1999. **195**(3): p. 186-196.
304. Jin, M., et al., *Direct observation of deformation-induced grain growth during the nanoindentation of ultrafine-grained Al at room temperature.* Acta Materialia, 2004. **52**(18): p. 5381-5387.
305. Moldovan, D., D. Wolf, and S.R. Phillpot, *Theory of diffusion-accommodated grain rotation in columnar polycrystalline microstructures.* Acta Materialia, 2001. **49**(17): p. 3521-3532.
306. Van Swygenhoven, H., P.M. Derlet, and A.G. Frøseth, *Nucleation and propagation of dislocations in nanocrystalline fcc metals.* Acta Materialia, 2006. **54**(7): p. 1975-1983.
307. Sakai, T., et al., *Dynamic and post-dynamic recrystallization under hot, cold and severe plastic deformation conditions.* Progress in Materials Science, 2014. **60**: p. 130-207.
308. Yamakov, V., et al., *Grain-boundary diffusion creep in nanocrystalline palladium by molecular-dynamics simulation.* Acta Materialia, 2002. **50**(1): p. 61-73.
309. Coble, R., *A model for boundary diffusion controlled creep in polycrystalline materials.* Journal of applied physics, 1963. **34**(6): p. 1679-1682.
310. Hillert, M. and G.R. Purdy, *Chemically induced grain boundary migration.* Acta Metallurgica, 1978. **26**(2): p. 333-340.
311. Yoon, D.Y., *Theories and observations of chemically induced interface migration.* International Materials Reviews, 1995. **40**(4): p. 149-179.
312. Babcock, S.E. and R.W. Balluffi, *Grain boundary kinetics—II. In situ observations of the role of grain boundary dislocations in high-angle boundary migration.* Acta Metallurgica, 1989. **37**(9): p. 2367-2376.
313. Winning, M., G. Gottstein, and L.S. Shvindlerman, *Stress induced grain boundary motion.* Acta Materialia, 2001. **49**(2): p. 211-219.
314. Li, C.H., et al., *Stress-induced movement of crystal boundaries.* Acta Metallurgica, 1953. **1**(2): p. 223-229.
315. Wan, L. and S. Wang, *Shear response of the Σ 9(110){221} symmetric tilt grain boundary in fcc metals studied by atomistic simulation methods.* Physical Review B, 2010. **82**(21): p. 214112.
316. Gorkaya, T., et al., *Concurrent grain boundary motion and grain rotation under an applied stress.* Acta Materialia, 2011. **59**(14): p. 5674-5680.
317. Babcock, S. and R.W. Balluffi, *Grain boundary kinetics—I. In situ observations of coupled grain boundary dislocation motion, crystal translation and boundary displacement.* Acta Metallurgica, 1989. **37**(9): p. 2357-2365.
318. Rae, C. and D. Smith, *On the mechanisms of grain boundary migration.* Philosophical Magazine A, 1980. **41**(4): p. 477-492.
319. Fukutomi, H., et al., *Sliding behavior of coincidence grain boundaries deviating from ideal symmetric tilt relationship.* Acta Metallurgica et Materialia, 1991. **39**(7): p. 1445-1448.
320. Cahn, J.W., Y. Mishin, and A. Suzuki, *Duality of dislocation content of grain boundaries.* Philosophical Magazine, 2006. **86**(25-26): p. 3965-3980.
321. Fan, G.J., et al., *Uniaxial tensile plastic deformation and grain growth of bulk nanocrystalline alloys.* Acta Materialia, 2006. **54**(18): p. 4781-4792.
322. Sakai, G., Z. Horita, and T.G. Langdon, *Grain refinement and superplasticity in an aluminum alloy processed by high-pressure torsion.* Materials Science and Engineering A, 2005. **393**(1-2): p. 344-351.
323. Spearot, D.E., K.I. Jacob, and D.L. McDowell, *Nucleation of dislocations from [001] bicrystal interfaces in aluminum.* Acta Materialia, 2005. **53**(13): p. 3579-3589.
324. Olmsted, D.L., E.A. Holm, and S.M. Foiles, *Survey of computed grain boundary properties in face-centered cubic metals—II: Grain boundary mobility.* Acta Materialia, 2009. **57**(13): p. 3704-3713.
325. Rottmann, P.F. and K.J. Hemker, *Experimental quantification of mechanically induced boundary migration in nanocrystalline copper films.* Acta Materialia, 2017. **140**: p. 46-55.

References